Strange New Worlds:

Development of Active Nuclear Technologies and Techniques

for Planetary Science Applications

by

Lena Elizabeth Heffern

A Dissertation Presented in Partial Fulfillment
of the Requirements for the Degree
Doctor of Philosophy

Approved April 2022 by the
Graduate Supervisory Committee:

Craig Hardgrove, Chair
Lindy Elkins-Tanton
Ann Parsons
Laurence Garvie
Keith Holbert
James Lyons

ARIZONA STATE UNIVERSITY

August 2022

ABSTRACT

Information about the elemental composition of a planetary surface can be determined using nuclear instrumentation such as gamma-ray and neutron spectrometers (GRNS). High-energy Galactic Cosmic Rays (GCRs) resulting from cosmic super novae isotropically bombard the surfaces of planetary bodies in space. When GCRs interact with a body's surface, they can liberate neutrons in a process called spallation, resulting in neutrons and gamma rays being emitted from the planet's surface; how GCRs and source particles (i.e. active neutron generators) interact with nearby nuclei defines the nuclear environment. In this work I describe the development of nuclear detection systems and techniques for future orbital and landed missions, as well as the implications of nuclear environments on a non-silicate (icy) planetary body.

This work aids in the development of future NASA and international missions by presenting many of the capabilities and limitations of nuclear detection systems for a variety of planetary bodies (Earth, the Moon, metallic asteroids, icy moons). From bench top experiments to theoretical simulations, from geochemical hypotheses to instrument calibrations—nuclear planetary science is a challenging and rapidly expanding multidisciplinary field. In this work (1) I describe ground-truth verification of the neutron die-away method using a new type of elpasolite (Cs_2YLiCl_6:Ce) scintillator, (2) I explore the potential use of temporal neutron measurements on the surface of Titan through Monte-Carlo simulation models, and (3) I report on the experimental spatial efficiency and calibration details of the miniature neutron spectrometer (Mini-NS) on board the NASA LunaH-Map mission. This work presents a subset of planetary nuclear science and its many challenges in humanity's ongoing effort to explore strange new worlds.

DEDICATION

For Kelsey.

"No one ever made a difference by being like anyone else."

– P.T. Barnum

For the healthcare workers.

*And for the 1,035,903 Americans who passed away due to the COVID-19 pandemic
and the 6,332,125 additional people who lost their lives worldwide
from December 2019 to June 2022.*

ACKNOWLEDGMENTS

making me laugh even in the hardest times.

Thank you to Tom Gosnell from Lawrence Livermore National Laboratory for kickstarting my career with an amazing opportunity. Thank you to Dr. Morgan Burks for the many project opportunities and mentorship over the years. Thank you to Dr. Jonathan Dreyer for your friendship and continued encouragement, advice, and guidance. Thank you to Dr. Vladimir Mozen for the many stories while taking long data sets, and for your selfless collection of data. Thank you to Marianne for resoldering my mistakes. To my collaborators at APL, CUA, & PSI, thank you to Dr. David Lawrence, Dr. Patrick Peplowski, Dr. John Goldsten, Dr. Tom Prettyman, & Dr. Richard Starr for guidance & encouragement.

From Arizona State University, thank you to Sierra F., Kevin H., Genevieve S., Alyssa S., Alex P., Lucia P., Ed B., Ashley H., Lee B., Morgan S., Steven D., Sean C., Travis G., Stephen W., and Hannah K. for being an amazing group of friends and colleagues. Thank you to Dr. Laurence Garvie, Dr. Keith Holbert, Dr. Jim Lyons, and Dr. Dave Williams (LLAP) for your advice and support.

Thank you to my partner, Jon Von Garich, for being supportive, organized, caring (especially with our dog, Bones), and loving, and for always making me want to laugh. I love that you encourage me without hesitation in everything that I do.

To my long-time, best friends Amanda Ray, Ryan Larson, Kirsten Cook, Jamie Wilson, Amber Williams, Ally Davis, Sean McArthur, and Joel Bluemel, thank you for your continued support throughout my life, I wouldn't be here without y'all.

To Kelsey O'Leary, for whom this dissertation is dedicated, thank you for your unbreakable friendship and compassion, your laughter, wit, & wild antics will live on through us as we fly kites over rolling green hills on hot summer days. So it goes.

Finally, thank you to all the other people who helped me along the way.

TABLE OF CONTENTS

LIST OF TABLES

LIST OF FIGURES

xi

Chapter 1

INTRODUCTION

1.1 Prologue

Gamma-ray and neutron spectrometers (GRNS) have a long history of use in planetary science missions ranging from Mercury to the asteroid belt (Surkov *et al.*, 1987; Feldman *et al.*, 1998; Lawrence *et al.*, 2013; Peplowski, 2016; Wilson *et al.*, 2017; Prettyman *et al.*, 2019b; Gabriel *et al.*, 2018). These missions have resulted in data sets that have furthered our ability to explore the solar system, helping to continue answering three of the central scientific problems of our time: 1) the origin and evolution of our earth, sun, and planets; 2) the origin and evolution of life; and 3) the dynamic processes that shape the environment (Adler & Trombka, 1970).

1.2 Science Background

1.2.1 Galactic Cosmic Rays

High-energy Galactic Cosmic Rays (GCRs) resulting from super novae isotropically penetrate the surface of solar system objects that have little or no atmosphere. When GCRs interact with a body's surface, they can liberate neutrons from nuclei within the surface material in a process called *spallation*. These liberated neutrons can then immediately escape back into space, or they can continue on to interact with elemental nuclei within a surface resulting in the emission of gamma-rays, neutrons of lower energies (moderation), or other particles. Neutron interactions resulting in gamma-rays consist primarily of neutron absorption (capture and delayed gamma rays) and inelastic collisions (prompt gamma rays); other naturally occurring ra-

1

dioactive elements (K, Th, and U) on the surface can emit gamma-rays as well. Using gamma-ray and neutron spectrometers, we can detect and measure the bulk elemental abundances of a planetary body's surface (Reedy, 1978).

1.2.2   Neutron Physics

Neutron energies are typically broken into categories: 1) High-energy neutrons, which are ∼10 MeV or greater; 2) fast neutrons, which range from around 500 keV to 10 MeV; 3) slow neutrons, which range from ∼ 500 eV to 500 keV; 4) epithermal neutrons, which range from ∼ 0.025 eV to 500 eV; 5) thermal neutrons, which are at thermal equilibrium with their environment (typically 0.025 eV on Earth); and cold neutrons, which range from 0 to ∼0.025 eV (Prettyman et al., 2006; Knoll, 2010; Heilbronn, 2015). The incident neutron energy, activation/bombardment duration time, and area materials (including target, detectors, neutron source, and room materials) dictate the resulting measured gamma-ray spectrum. Neutrons interact with nuclei in material through processes such as inelastic scattering, neutron capture, and delayed neutron activation. The energy and decay time of the resulting measured gamma rays are characteristic of the interaction processes and the target nuclei. The number of gamma rays produced by these reactions is proportional to the concentration of the elements and the incident flux of neutrons (Nowicki et al., 2017).

Neutron interactions consist primarily of inelastic scattering, neutron capture, and delayed neutron activation. An inelastic scattering interaction (e.g. n, n'γ) consists of a neutron with sufficient energy (threshold energy) that strikes a nucleus, transferring energy and activating that nucleus into an excited, unstable, short-lived energy state. In order to reach a stable state, the excited nucleus will quickly emit radiation, usually in the form of a prompt gamma ray. The initial neutron *scatters* from the nucleus at a lower energy. In order to cause an inelastic interaction, the neutron must have a

higher energy than the reaction threshold in the nucleus ($\sim$1 – 6 MeV). When using a neutron generator, inelastic events (n, n X) occur before the high-energy neutrons emitted from the neutron generator have had sufficient time to lose most of their energy (thermalize). Neutron capture events (e.g. n, γ) occur when a neutron has a sufficiently low enough energy (cold, thermal, epithermal) to be *absorbed* by the nucleus. The energy of the neutron is deposited into the nucleus, creating a compound nucleus that is often in an excited state, a diagram of this process is seen in Figure 1.1. There are several ways for this compound nucleus to deexcite, including the emission of secondary charged particles (e.g. α and β-decay) and uncharged particles (e.g. gamma rays). The initial emission of a photon from the first metastable absorption state is termed a capture gamma ray; the metastable nucleus then deexcites via emission of a secondary charged particle to another, usually unstable state, and upon reaching a stable ground state emits another uncharged photon termed a delayed gamma ray (Knoll, 2010; Nowicki *et al.*, 2017; Heilbronn, 2015). Other processes that must be considered are related to nuclear resonances for both neutron scattering and absorption cross sections.

Neutron cross sections can be thought of as the probability of occurrence of a specific interaction (e.g. absorption) with a specific nucleus (e.g. ^{59}Co) for a specific incident neutron energy (e.g. a thermal neutron). The probability that a neutron is absorbed by an elemental nucleus is called the microscopic neutron absorption cross section (σ_a). The probability that a neutron is scattered by an elemental nuclei is called the microscopic neutron scattering cross section (σ_s). In a planetary surface, the total effect of the microscopic cross sections of each element combine to produce the macroscopic neutron cross section, which dictates the resulting neutron energy spectrum after initial neutrons interact within that surface. The macroscopic neutron absorption (Σ_a) and scattering (Σ_s) cross sections can be defined as follows (Beckurts
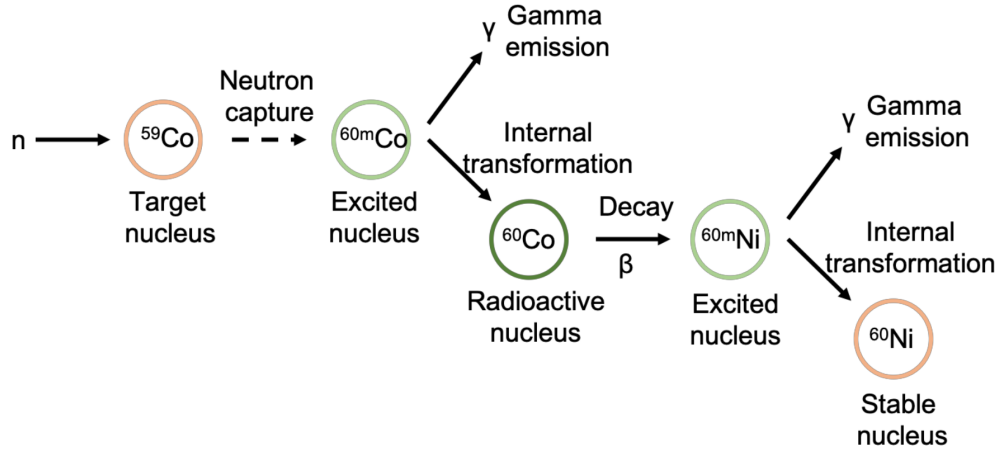
Figure 1.1: Nuclear process diagram showing the stages of neutron activation, including neutron capture and delayed gamma emission using activation of ^{59}Co as an example target nucleus.

and Wirtz, 1964):

$$\Sigma_n = \sum_{i=1}^{N} \frac{\sigma_i N_A m_i}{a_i} \qquad (1.1)$$

where Σ_n is either the macroscopic neutron absorption or scattering cross section, σ_i is the associated microscopic neutron cross section (absorption or scattering, in barns, at a specific neutron energy), N_A is Avogadro's number ($6.0221408e + 23/mol$), m_i is the mass fraction of element i (unitless), and a_i is the atomic mass of element i (in units of grams) summed over the number of elements, N, contained in the surface. The macroscopic neutron cross sections are an indicator of the presence of certain elements within the subsurface (Hardgrove *et al.*, 2011; Kerner *et al.*, 2020).

1.2.3 Active Neutron Sources

When a planetary body has a dense atmosphere or when measurement integration times require a short duration ($\lesssim$ 1 hr) the use of an active neutron source can be

advantageous for nuclear planetary spectroscopy measurements. Spontaneous sources (e.g. ^{252}Cf) can continuously fission in a decay process that emits a wide energy spectrum of neutrons. Alpha neutron sources (e.g. AmBe, PuBe) consist of a radioisotope that alpha decays (e.g. ^{241}Am, ^{241}Pu) mixed with a lighter element (e.g. Be). Neutron generators use electric and magnetic fields to accelerate isotopes of deuterium (^{2}H) towards either a deuterium or tritium (^{3}H) target, causing a fusion reaction that generates specific peak energies of fast neutrons – 14.1 MeV for deuterium-tritium (DT) and 2.54 MeV for deuterium-deuterium (DD). These neutron generators can be operated in a pulsed mode, allowing for temporal data acquisition of both neutrons and gamma rays (Hardgrove *et al.*, 2011; Parsons *et al.*, 2013).

1.3 The Voyages of GRNS Instrumentation

1.3.1 Earth

Active nuclear techniques have been used for decades in nuclear nonproliferation and safeguards-applications, as well as geologic applications in hydrogeology, hydrology, agriculture, environmental science, and mining (Knoll, 2010; Ferronsky, 2015; Vertes, 1998). Neutron and gamma-ray spectrometers have been used to develop these active techniques alongside neutron generators.

Safeguards applications include detection of special nuclear materials (SNM) and explosives via prompt gamma-ray neutron activation analysis (PGNAA) in airport and ground boarders, as well as detection of fissile nuclide SNM (^{233}U, ^{235}U, ^{239}Pu) via neutron die-away analysis of secondary fissions of nuclides that emit prompt or delayed neutrons (Knoll, 2010; Vertes, 1998). Active techniques have been used in hazardous waste storage facilities, active nuclear power plants, and enrichment facilities to monitor activity levels and for leak detection and identification (Knoll, 2010;

Ferronsky, 2015).

Although ^{235}U is often associated with special nuclear materials it is also a prevalent terrestrial background nuclide. This nuclide, along with others and non-fissile isotopes, are often targeted for extraction in mining applications. The oil well logging industry uses active nuclear techniques to determine the elemental content and geologic context of various target areas both above and below the surface. In well and borehole logging, an instrument package consisting of a neutron source (spontaneous fission source or neutron generator) and a gamma-ray spectrometer (GRS) and/or a neutron spectrometer (NS) are lowered into the well or borehole in a single hermetically sealed sonde which can be moved at various rates and positions within a geologic formation. Ore analysis for mining typically uses active nuclear methods for investigating ore deposits in-situ and for rapid analysis of large grains or inclusions. In environmental science, active techniques are used to study the biogeochemistry of plants, given that plants, which take up metals in the soil they grow in, can reveal anomalous concentrations of metals (Vertes, 1998).

Current Earth applications of GRNS, specifically, help to facilitate raising the technical readiness level of GRNS for space applications. Handheld nuclear instruments already have a strong heritage of being successfully adapted to planetary science applications; e.g. the GRNS on the NASA Lunar Prospector mission consisted of a set of commercially available ^{3}He tubes and a standard NaI scintillator, whereas the NASA Psyche mission will carry the same ^{3}He tubes and a GRS that shares development with the Falcon handheld from ORTEC (Lawrence *et al.*, 2020; Burks *et al.*, 2020).

1.3.2 Where No Man Has Gone Before: Project Apollo

The first GRNS science results from another planetary body came from the Apollo missions to Earth's Moon. The Apollo 15 and 16 command modules both carried a boom-mounted NaI(Tl) GRS that was capable of mapping and measuring major elemental abundances from orbit (Harrington *et al.*, 1974). Over 20% of the Moon's surface was mapped during these two missions, resulting in information about the Fe, Ti, and Th contents of the Moon. Returned rock and soil samples from the Apollo 11 – 17 landing sites and the Luna sample return missions helped to validate and provide ground-truth to orbital data from the GRNS on Apollo 15 and 16. These GRNS elemental abundance maps allowed scientists to better understand the composition of the lunar mare and the lunar highlands (Metzger *et al.*, 1973).

1.3.3 The Venera and VeGa Probes to Venus

The Venera probes consist of 16 spacecraft probes that launched between 1961 to 1983. In 1985 the Venus-Halley mission returned to Venus with the VeGa 1 and 2 probes to study both Venus and Halley's comet. The first use of a landed GRS on another planet was during the Venera missions. The science objective for the Venera and VeGa probes was to study the geochemistry of the atmosphere and surface of the planet via landed missions. Venera 9 and 10 carried a NaI(Tl) GRS that was able to measure major radioactive elements in the vicinity of the landing site (Surkov, 1977). VeGa 1 and 2 carried a similar GRS, a CsI scintillator (Surkov *et al.*, 1986). Both sets of probes resulted in the conclusion that the K, Th, and U content of Venetian rocks is similar to those between theolitic and alkaline terrestrial basalts. This suggests that much of Venus' surface is the product of moderate differentiation of its primary substance (Surkov *et al.*, 1987).

1.3.4 Lunar Prospector Revisits the Moon

The Apollo 15 and 16 missions were able to map elemental abundances using a GRS for over 20% of the Moon's surface. In 1998 the Lunar Prospector mission arrived to lunar orbit and has since mapped the entire Moon using a GRNS. The overall surface resolution of the Lunar Prospector GRNS is ∼100 km at its standard science orbit of ∼100 km. The GRS on board Lunar Prospector consisted of a cylindrical bismuth germanate oxide (BGO) crystal surrounded by an anticoincidence shield (ACS) of borated plastic. The NS consisted of a pair of ^{3}He tubes (Feldman *et al.*, 1996). Lunar Prospector mapped out a variety of major elements on the Moon, including KREEP (rich in potassium, rare-earth element, and phosphorus) terrain which likely formed later in the crust and mantle, this helps to further support the hypothesis that there was once a lunar magma ocean (Lawrence *et al.*, 1998). Other results included the discovery of polar water-ice, likely trapped within permanently shadowed regions (PSRs), such as impact craters (Feldman *et al.*, 1998).

1.3.5 A Rendezvous with Asteroid 433 Eros

The Near Earth Asteroid Rendezvous (NEAR) spacecraft to the asteroid 433 Eros carried onboard an x-ray spectrometer and GRS with the objective of establishing a relationship between asteroids and meteorites, and determining whether or not Eros, an S-type asteroid, is the parent body of ordinary chondrites or other undifferentiated meteorite samples (Wetherill, 1985). The GRS onboard NEAR was a NaI(Tl) scintillator combined with a BGO ACS (Goldsten, 1998). Unfortunately, due to emergency mission orbit changes and the small size of the body, the orbital GRS data from the NaI(Tl) detector have been inconclusive. However, towards the end of the mission, science team members decided to land the NEAR spacecraft on Eros, resulting in

landed GRS dataset showing that the local composition of Eros is consistent with chondritic compositions, likely ordinary chondrites (Evans *et al.*, 2001). More recently, the NEAR BGO ACS (which is a GRS with high energy efficiency) data has been revisited and used to confirm that chondritic material is within the realm of compositions for Eros on a global scale (Peplowski, 2016).

1.3.6 2001: A Mars Odyssey

The Mars Odyssey spacecraft is currently still in orbit about the planet Mars and is operating as a primary mode of communication for NASA's surface explorers. The Mars Odyssey GRS (MOGRS) successfully completed its mission to globally map the major elemental abundances on Mars. The GRS onboard Odyssey consisted of a high-purity germanium (HPGe) spectrometer which has a very high energy resolution ($\leq$ 4 keV at 662 keV compared to NaI or CsI at $\sim$ 70 keV) but requires $\sim$ 80 K internal temperature to operate. The Mars Odyssey neutron spectrometer (MONS) consists of two systems, one with four segments of boron lithiated plastic (BLP) to detect thermal and epithermal neutrons, and another called the High Energy Neutron Detector (HEND) which measures fast neutrons (Boynton *et al.*, 2004). Measurements by MOGRS and MONS have resulted in the detection of abundant water ice at the poles and near subsurface water-equivalent hydrogen deposits along the equatorial regions of Mars; these findings suggest the presence of subsurface aquifers and support the hypothesis that recent periods of high orbital obliquity may have played a role in former periods of water stability on Mars (Feldman *et al.*, 2007; Wilson *et al.*, 2017). The MONS systems are still in operation, however in 2009 MOGRS become non-operational due to radiation damage.

1.3.7 Falling into Mercury with MESSENGER

The MErcury Surface, Space ENvironment, GEochemistry, and Ranging (MESSENGER) mission to the planet Mercury launched in 2004, but since the transit to Mercury requires an enormous change in velocity to overcome the Sun's gravity well, MESSENGER didn't enter orbit and begin taking data until 2011. MESSENGER eventually ended its successful mission with a deorbit into the planet in 2015. The objective of the GRNS onboard MESSENGER was to map the elemental abundances and average atomic mass of the surface. The mission carried a HPGe GRS with a BGO ACS and a sandwich of 3 lithiated glass scintillators for the NS (Goldsten et al., 2007). Higher than expected Fe and Ti abundances (likely Fe-Ti oxides) from the GRS measurements on MESSENGER suggest the presence of volcanic processes (Evans et al 2012). Extended mission low-orbit flybys resulted in neutron measurements showing suppressed neutron count rates in equatorial regions, this suppression is consistent with an enriched carbon crust, a likely explanation for Mercury's dark crustal color (Peplowski et al., 2015). Finally, the GRNS also showed evidence for the presence of water ice in PSRs at Mercury's poles (Lawrence et al., 2013).

1.3.8 Characterizing the Solar System's Earliest Eon with Dawn

The Dawn mission to asteroid belt objects (4) Vesta and (1) Ceres launched in 2007, orbiting Vesta first in 2011 for over a year, then proceeding on to orbit Ceres in 2015 where it is currently still in orbit. Dawn carried a GRNS, named GRaND (Gamma Ray and Neutron Detector), which includes over 21 sensors including a CdZnTe (CZT) semi-conductor GRS, a BGO anti-coincidence shield (ACS), and a lithium-loaded borosilicate glass phoswitch NS, amongst other sensors (Prettyman et al., 2003). One of Dawn's science objectives for Vesta, in relation to GRaND, was

to determine whether or not Vesta is the parent body for howardite-eucrite-diogenite (HED) meteorites. An objective for Ceres was to determine if it is the parent body of carbonaceous chondrites. Mission results from GRaND's GRS indicate that Vesta is likely the parent body for the HEDs, while neutron results suggest that global magmatic differentiation may have taken place (Prettyman *et al.*, 2012; McSween *et al.*, 2013). Recent results from Dawn show that Ceres' bulk geochemistry is broadly consistent with aqueously altered carbonaceous chondrites and that hydrogen consistent with water ice is globally abundant on Ceres' surface, most prominently at the poles (Prettyman *et al.*, 2019b; McSween Jr. *et al.*, 2018). Findings for both of these planetary bodies are helping to answer questions regarding planetary evolution, planetary origin, and mass transport in the Solar System.

1.3.9   *Exploring Mars' Subsurface with Curiosity*

To date, the only extraterrestrial mobile landed mission to ever use an active nuclear spectrometer system is the Mars Science Laboratory (MSL) rover, Curiosity. Curiosity carries the first roving NS, consisting of a set of ^{3}He tubes, along with a pulsed neutron generator (PNG) built by the Russian Space Agency (Roscosmos), the full system is called the Dynamic Albedo of Neutrons (DAN) instrument. The use of a PNG categorizes DAN as an active neutron instrument, meaning that instead of relying on galactic cosmic rays for the production of neutrons, DAN emits them in pulses into the planetary surface using a compact DT fusion reactor (Litvak *et al.*, 2008). Active neutron measurements can be used to rapidly ($\sim$ tens of minutes as opposed to months to years in orbit) characterize the H content and its depth within the top meter of planetary surfaces. Neutrons that interact with DAN's ^{3}He neutron detectors are time-resolved allowing for neutron die-away curves to be constructed. Throughout Curiosity's traverse in Gale Crater DAN has revealed H

enrichments, hydrated silica phases within fractures, and helped place constraints on hydrated amorphous phases (Gabriel *et al.*, 2018; Czarnecki *et al.*, 2020). Continued results from DAN have helped with understanding and interpreting processes that have formed and modified rocks on the surface of Mars.

1.3.10 Revisiting Mercury with BepiColombo

BepiColombo, a joint mission between the European Space Agency (ESA) and the Japanese Aerospace Exploration Agency (JAXA) launched October 20th of 2018 en route to Mercury. Once there, it will perform a comprehensive exploration of Mercury, focusing on global characterization of the planet through investigation of its interior, surface, exosphere, and magnetosphere (Benkhoff *et al.*, 2021). BepiColombo carries the Mercury Gamma and Neutron Spectrometer (MGNS), which consists of four neutron spectrometers and one gamma-ray spectrometer. The NS instrument is similar to that of the HEND onboard NASA's Mars Odyssey. The GRS consists of a 3-inch $CeBr_3(Ce)$ scintillator. MGNS will measure major soil-composing elements Si, O, C, Al, Na, Fe, Ca, S, Cl and natural radioactive elements K, Th, U from the planetary surface with a surface resolution of about 400 km (Mitrofanov *et al.*, 2010a; Benkhoff *et al.*, 2021).

1.3.11 More Visits to the Moon in Search of Polar Ice

As previously mentioned, the Lunar Prospector mission was able to orbit and globally map neutrons coming from the lunar surface. However, as also mentioned, the surface spatial resolution of the Lunar Prospector GRNS is ~ 100 km (at 100 km altitude). Craters in the south polar region of the Moon that are likely to harbor PSRs with water ice typically range in diameter from $0 - 70$ km (Elphic *et al.*, 2007). Although there have been low altitude flybys (35 km altitude resulting in 45 km spa-

tial resolution scale) with Lunar Prospector, missions to apply further constraints on the bulk hydrogen content of PSRs have been suggested. One such mission, which has been in lunar orbit since 2009 is the Lunar Reconnaissance Orbiter (LRO) which carries onboard a NS instrument called the Lunar Exploration Neutron Detector (LEND) consisting of collimated ^{3}He and stilbene detectors (Chin et al., 2007; Mitrofanov et al., 2009). Initial discrepancies between results for Lunar Prospector GRNS and LRO LEND datasets at the lunar poles have resulted in a mission of opportunity for a low-resource spacecraft mission.

The Lunar Polar Hydrogen Mapper (LunaH-Map) cubesat has been built by Arizona State University and delivered to NASA Kennedy Space Center, with an expected launch date in the early 2020's on NASA's Space Launch System as part of the Artemis 1 mission. LunaH-Map will carry a relatively new type of GRNS, an inorganic Cs_2YLiCl_6:Ce dual detection scintillator, called CLYC. LunaH-Map will map hydrogen abundance via epithermal neutrons at a very low altitude ($\sim$ 10 km) resulting in a spatial resolution of $\sim$ 10 km (Hardgrove et al., 2020). Science results from LunaH-Map will further aid in our understanding of lunar resources. This dissertation reports on the spatial efficiency and calibration details of the miniature neutron spectrometer (Mini-NS) on board the LunaH-Map mission.

1.3.12 A Future Mission to Boldly Go to a Metal World

In 2017, the Psyche mission was chosen as one of two NASA Discovery Class missions to receive funding for flight. The Psyche mission will travel to the asteroid (16) Psyche, located in our solar system's main asteroid belt (Elkins-Tanton et al., 2020). (16) Psyche is hypothesized to be made primarily of iron nickel, with possible silicates lining its surface. The Psyche mission will carry a GRNS, built out of Johns Hopkins Applied Physics Laboratory (APL) and Lawrence Livermore National Lab-

oratory (LLNL). Prior to 2017, I was involved in major contributions to the design of the GRS, a HPGE spectrometer with MESSENGER flight heritage (Burks *et al.*, 2020). The NS on board Psyche shares heritage with the ^{3}He tubes from the Lunar Prospector mission. The GRNS will measure major and trace elemental abundances on Psyche in order to constrain its possible origin, and give insight to planetesimal formation processes.

1.3.13 A Future Mission to Determine the Mystery of Mars' Moons

The Martian Moon eXploration (MMX) JAXA mission aims to return samples from one of Mars' satellites, Phobos, and take additional flyby measurements of Mars' other satellite, Deimos, and aims to constrain the origin(s) of Phobos and Deimos. MMX will carry a veritable Christmas tree of payload instruments to carry out science investigations, including the Mars-moon Exploration with GAmma rays and NEutrons (MEGANE) GRNS instrument (Kuramoto *et al.*, 2022). MEGANE is based on the MESSENGER GRS (HPGe) and LP NS (^{3}He), making it a near-identical GRNS package to that of the NASA Psyche mission (Lawrence *et al.*, 2019).

1.3.14 A Future Mission to Seek Out New Life on an Icy Moon

The Dragonfly mission to Saturn's moon, Titan, was chosen in 2019 as the next NASA New Frontiers Class mission. Titan is Saturn's largest satellite and has been visited by the Cassini mission via the Huygens probe, which landed on Titan's surface in 2013. Images from Huygens show a surface similar to a desert landscape on Earth. Data from Cassini, Huygens, and Earth observations suggest that Titan has an icy surface, rich with ammonia and liquid methane (Barnes *et al.*, 2008, 2021). The NASA Dragonfly mission will land a rotorcopter on Titan which, due to Titan's dense atmosphere and low-gravity, will be able to fly to different measurement locations.

Dragonfly will carry an active GRNS system, with a DT PNG, HPGe and scintillator GRS, and ^{3}He tube NS. The HPGe GRS is of a similar design to the Psyche and MMX HPGe GRS, but will not need a cryocooler to operate, due to Titan's 94K environment (Burks *et al.*, 2020; Barnes *et al.*, 2021; Parsons *et al.*, 2018). This dissertation explores the capabilities of time resolved neutron measurements on an icy world such as Titan.

1.3.15 *A Future Mission to Find Biomarkers on Mars*

The ExoMars (Exobiology on Mars) rover is an astrobiology investigation originally put forth by ESA and Roscosmos. ExoMars will search for signs of past and present life on Mars and characterize the hydrogen environment as a function of depth in the shallow subsurface (Vago *et al.*, 2017). ExoMars will carry a variety of analytical instruments dedicated to exobiology and geochemistry research including the Autonomous Detector of Radiation Of Neutrons onboard Rover at Mars (ADRON-RM), a compact passive NS, similar to the NS on DAN MSL, which will study the abundance and distribution of water and neutron absorption elements (e.g. Cl, Fe, and others) (Mitrofanov *et al.*, 2017).

1.4 Significance and Limitations

This dissertation acknowledges the past while focusing on the future: development of active nuclear detection systems and techniques for future orbital and landed missions are explored, as well as the implications of nuclear environments on non-silicate planetary bodies (i.e. ice). This dissertation presents on different sides of nuclear planetary science: from experiment to simulations, from calibrations to experimental theory, nuclear planetary science is a challenging and rapidly expanding multidisciplinary field. This work aids in the development of future NASA and international

missions by presenting on capabilities and limitations of nuclear detection systems for a variety of planetary bodies. Much of the limitations of GRNS instrumentation and techniques are often due to the elemental composition of a surface and how source particles interact with that surface, these interactions define the nuclear environment.

1.4.1 The Nuclear Environment

The nuclear environment, for the purposes of GRNS planetary science applications, is defined here in terms of the emitted neutron flux as a function of energy, this is termed the *neutron leakage spectrum*. The neutron leakage spectrum is dependent on the initial source particles (GCRs or neutrons) that have penetrated, then interacted with the surface of the planetary target. Mitrofanov *et al.* (2012) describes the neutron leakage spectrum broken out into chunks in time based on a DT neutron pulse for a typical Mars composition. By looking at the neutron leakage spectrum, the general nuclear environment relevant to GRNS can be inferred for other planetary bodies using particle transport codes such as MCNP or GEANT.

Non-silicate planetary bodies are likely to have significantly different nuclear environments than that of primarily silicate bodies (Earth, the Moon, Mars, 433 Eros, etc.). A first-pass simulation study of the nuclear environment using MCNP6.1 for Earth, the Moon, Mars, metallic meteorite samples, and hypothesized Titan surface material was done to demonstrate these differences. Previous studies of the neutron leakage spectrum on these planetary bodies exist in the literature (Feldman *et al.*, 1991; Drake *et al.*, 1991). Figure 1.2 shows the results our studies done using a pulsed DT neutron generator (200 μs pulse) on compositions related to planetary bodies including Earth, Mars, the Moon, Titan, and asteroids (via meteorite samples).
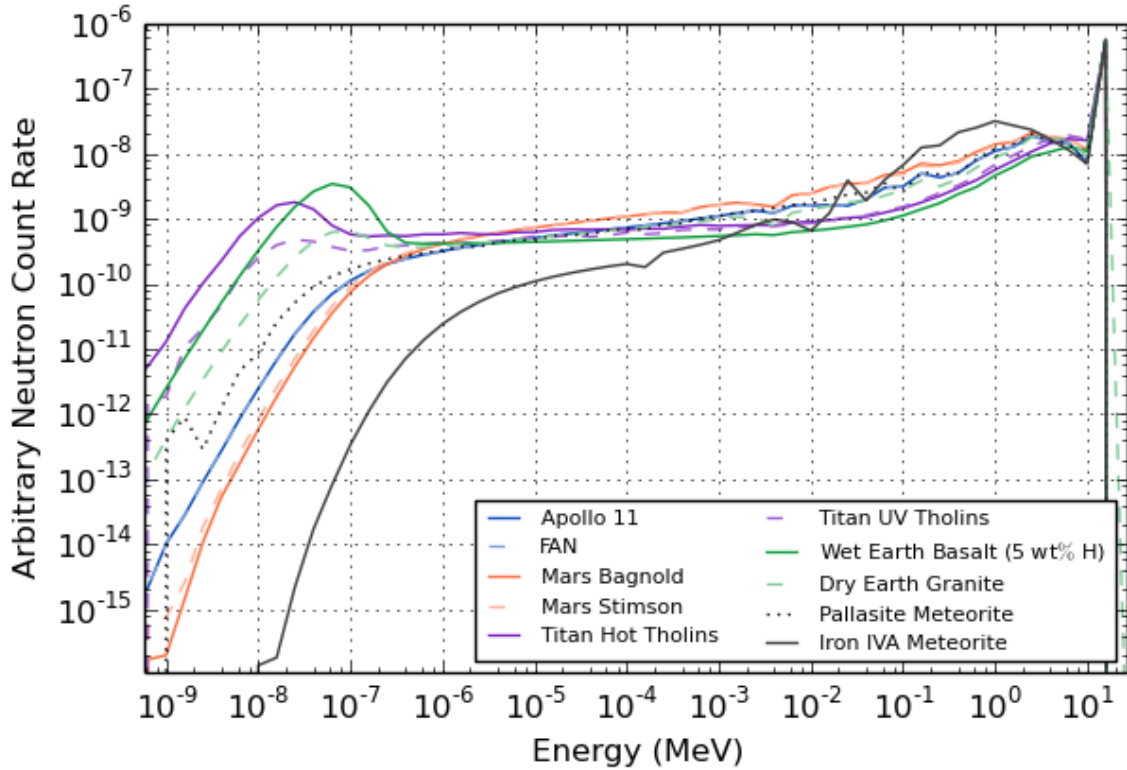
Figure 1.2: Simulated neutron leakage spectra from planetary bodies irradiated by a PNG. Earth materials (green lines) are based on the Colombia River basalt and granite compositions from Bodnarik (2013). Materials for the Moon (blue lines), which appear to overlap, are based on dry ferrositic anorthosite (FAN) and 11 Apollo soils (Prettyman *et al.*, 2003). Two types of Titan Tholins, UV (purple dotted line) and Hot (purple solid line) are based on compositions described in Cable *et al.* (2012). Mars materials (orange lines) are based on the Bagnold and Stimson sites described in Nowicki *et al.* (2017). Finally, the black dotted line is based on an averaged combination of over 40 pallasite meteorites and the black solid line is based on an averaged combination of 25 iron IVA meteorites; both meteorite compositions are based on data from the MetBase database (UG, 2017). The energy corresponding to the thermal neutron peak changes based on the temperature of the planetary body in accordance with the Maxwell-Boltzman distribution. Titan's surface is ~94 K, as compared to Earth (~294 K), the Moon (~234 K), and Mars (~211 K), note that as the temperature of the surface decreases, the energy of the thermal neutron peak shifts down in energy. All simulations were seeded with NPS = 2.5E9 seed particles using MCNP, atmospheres are included. Appendix B contains access information for all material compositions used.

17

These sets of studies show that the neutron environments on non-silicate planetary bodies (metallic, icy) are only moderately different from that of silicate bodies. The iron IVA meteorite study ($\sim$ 81wt% Fe, $\sim$ 3wt% Si, $\sim$ 8wt% Ni, $\sim$ 5wt% O) shows that the high energy neutrons (0.1 MeV +) have a significantly higher overall population compared to the amount of thermal neutrons, this is dramatic even when compared to the pallasite meteorite material study ($\sim$ 16wt% Fe, $\sim$ 16wt% Si, $\sim$ 2wt% Ni, $\sim$ 42wt% O). The high amount of iron (a moderate neutron scatterer and moderate neutron absorber) is what causes these differences from that of a silicate body. The Titan materials contain significant amounts of hydrogen ($> 10wt\%$) which cause an increase in the amount of thermal neutrons; the Titan nuclear environment is similar to highly-hydrated materials on Earth and Mars.

1.5   A Preview of the Following Chapters

The second chapter of this dissertation, in support of a NASA PICASSO funding opportunity, discusses the experimental campaign and results of using the SINGR instrument, a CLYC scintillator, in conjunction with a PNG on Earth. I am the primary contributor to the second chapter and performed the experimental design development, data acquisition, analysis, simulations, writing, and discussion of results. The third chapter focuses on simulation studies of Saturn's moon, Titan, using a NS and PNG to understand the nuclear environment and instrument technique limitations; I am the primary contributor to the third chapter. The fourth chapter, in support of the NASA LunaH-Map mission to the Moon, describes my work for the calibration procedure, data analysis, and angular sensitivity analysis of the Miniature Neutron Spectrometer (Mini-NS). My significant contributions as a co-author focus on the calibration planning, implementation, and analysis at the LANL NFIA facility, as well as data processing and reduction for both the ground calibration data and the

flight spacecraft. The fifth and final chapter, I tie together what has been learned from these projects and where the field may be going in the future. Almost every chapter in this dissertation was completed using a software tool I developed over the course of the doctoral degree, an MCNP Python Toolbox which is described in Appendix B. These chapters present on a subset of the planetary nuclear science field and its many challenges in humanity's ongoing effort to explore strange new worlds.

Chapter 2

ACTIVE NEUTRON INTERROGATION EXPERIMENTS AND SIMULATION VERIFICATION USING THE SINGLE-SCINTILLATOR NEUTRON AND GAMMA-RAY SPECTROMETER (SINGR) FOR GEOSCIENCES

L. E. Heffern[1], C. J. Hardgrove[1], A. Parsons[2], E. B. Johnson[3], R. Starr[4], G. Stoddard[3], R. E. Blakeley[3], T. Prettyman[5], T. S. J. Gabriel[6], H. Barnaby[1], J. Christian[3], M. A. Unzueta[2], C. Tate[7], A. Martin[7], J. Moersch[7]

[1] Arizona State University School of Earth and Space Exploration, Tempe, AZ

[2] NASA Goddard Space Flight Center, Greenbelt, MD,

[3] Radiation Monitoring Devices, Watertown, MA,

[4] Catholic University of America, Washington DC,

[5] Planetary Science Institute, Tuscon, AZ,

[6] United States Geological Society, Flagstaff, AZ,

[7] University of Tennessee, Knoxville, TN

ABSTRACT

We present a new SIngle-scintillator Neutron and Gamma Ray spectrometer (SINGR) instrument for use with both passive and active measurement techniques. Here we discuss the application of SINGR for planetary exploration missions, however, hydrology, nuclear non-proliferation, and resource prospecting are all potential areas where the instrument could be applied. SINGR uses an elpasolite scintillator, Cs_2YLiCl_6:Ce (CLYC), that has been shown to have high neutron efficiency even at small volumes, with a gamma-ray energy resolution of approximately 4% full-width-at-half-maximum at 662 keV. Active gamma-ray and neutron (GRNS) measurements were performed with SINGR at the NASA Goddard Space Flight Center (GSFC) Goddard Geophysical and Astronomical Observatory (GGAO) outdoor test site using a pulsed neutron generator (PNG) to interrogate geologically relevant materials (basalt and granite monuments). These experimental results, combined with simulations, demonstrate that SINGR is capable of generating neutron die-away curves that can be used to reconstruct the bulk hydrogen abundance and the depth distribution of hydrogen within the monuments. We compare our experimental results with Monte Carlo N-Particle (MCNP) 6.1 transport simulations to constrain the uncertainties in depth and hydrogen abundance from the neutron die-away data generated by SINGR. For future planetary exploration missions, SINGR provides a single detector system for interrogating the shallow subsurface to characterize the presence and abundance of hydrated phases and to provide bulk elemental analysis.

21

2.1 Introduction

2.1.1 Background

In planetary exploration, neutron spectrometers are commonly used to constrain the hydrogen abundance and depth distribution within the shallow planetary subsurface, while gamma-ray spectrometers are used to quantify the abundance of major and minor elements within rocks and soils. Passive techniques, which use the galactic cosmic ray proton flux as a source of high-energy neutrons within the surface, have historically been used more frequently on planetary missions. However, the Dynamic Albedo of Neutrons (DAN) instrument - which uses two ^{3}He tubes - on the Mars Science Laboratory Curiosity rover has successfully demonstrated active neutron measurements on the surface of Mars. Active neutron data from DAN has identified hydrogen enrichments throughout the traverse and a hidden, buried volcanoclastic, high-silica layer. DAN measurements have also been used to quantify the abundance of hydrated silica phases within fractures and place constraints on specific hydrated amorphous phase abundances (Kerner *et al.*, 2020; Czarnecki *et al.*, 2020; Gabriel *et al.*, 2018; Litvak *et al.*, 2017). The ability of active neutron techniques to support surface planetary exploration missions has been well demonstrated with DAN, and the development of new active neutron interrogation methods is the goal of several recent and ongoing instrument development programs (Litvak *et al.*, 2017; Bodnarik *et al.*, 2013; Parsons *et al.*, 2013; Nowicki *et al.*, 2017; Hardgrove *et al.*, 2011; Parsons *et al.*, 2018). These development programs use active neutron and gamma-ray measurements to measure the hydrogen content, the depth distribution of hydrogen, as well as the elemental composition of surfaces using a pulsed neutron generator (PNG). The NASA Dragonfly mission to Saturn's moon Titan will also carry an active multiple-detector GRNS instrument (DraGNS) with a neutron generator, these

instruments will take surface measurements of Titan while surrounded by the moon's dense, nitrogen-rich atmosphere (Parsons *et al.*, 2018).

Active neutron techniques generally use a neutron source to bombard a sample, then subsequent neutrons and gamma rays emitted by the sample are measured. The incident neutron energy, activation/bombardment duration time, and area materials (including the target, detectors, neutron source, and surrounding environment) determine the returning measured neutron flux and gamma-ray energy spectrum. The number of neutrons and gamma rays produced by these reactions are also proportional to both the concentration of the elements and the incident flux of neutrons (Nowicki *et al.*, 2017). Therefore, a major advantage of active techniques over passive techniques is reduced measurement time due to the significantly higher source particle flux. Typically, active neutron and gamma-ray techniques use a pulsed neutron generator (PNG) for the neutron source; the emitted PNG neutrons interact in the rocks and soils, become moderated or absorbed, and create characteristic gamma-rays. In active neutron spectroscopy a Deuterium Tritium (DT) PNG can be used due to its high energy neutron output via the $^2H + {}^3H \rightarrow n$ (14.1MeV) + ^4He (3.5MeV) reaction. PNGs used in neutron die-away typically pulse at a low frequency to allow the thermal neutrons to leak back out of the surface between each pulse. The magnitude and shape of the histogram of the neutron arrival in time between each pulse is called "neutron die-away". Neutron die-away experiments bin neutron counts based on their arrival time (time-resolved data) at the detector between each pulse of the PNG. Hydrogen (H), is an efficient neutron moderator; neutron moderators shift the population of fast neutrons towards thermal (2.5×10^{-8} MeV) energies via scattering interactions. With higher H content, more thermal neutrons are produced. DT neutrons travel at 52,000 km/s, whereas thermal neutrons travel at roughly 2,200 m/s, resulting in neutron time-profiles which contain useful information regarding the sub-

surface distribution of moderators. The H abundance, H distribution with depth, and macroscopic absorption cross-section of material surfaces can then be constrained using a neutron die-away curve (Mitrofanov *et al.*, 2012; Litvak *et al.*, 2008). The shape and magnitude of the neutron die-away curve changes as water-equivalent hydrogen (WEH) increases, this has been explored in previous studies (Hardgrove *et al.*, 2011; Kerner *et al.*, 2020). Reconstructing information from a planetary body's subsurface can be accomplished via constraints placed using neutron die-away.

2.1.2 Instrument Utility

Here, we describe a new type of active neutron and gamma-ray instrument for planetary exploration missions that uses just a single sensor coupled with a PNG; we directly compare our experimental measurements to MCNP 6.1 transport code results. We demonstrate that the instrument, the SIngle-scintillator Neutron and Gamma Ray spectrometer (SINGR), is capable of generating time-resolved neutron die-away data and, through simulations, we demonstrate that those data can be used to reconstruct the H content and depth distribution of H within the shallow subsurface (top $\approx$ 15 cm).

SINGR is a single-crystal, Cs_2YLiCl_6:Ce (CLYC), combination neutron and gamma-ray instrument, intended for both passive and active detection. A pulsed neutron generator (PNG) was used with SINGR to collect neutron die-away data at the NASA Goddard Space Flight Center (GSFC) Geophysical and Astronomical Observatory (GGAO) outdoor gamma-ray and neutron instrumentation testing facility. SINGR is capable of detecting and discriminating both neutrons and gamma rays based on differences in the shape of the scintillator light pulse, allowing for segregation using pulse shape discrimination (PSD) in post-data collection (Johnson *et al.*, 2015; Glodo *et al.*, 2012). Previous related studies using high-purity germanium (HPGe) gammma-ray

detectors at the GSFC GGAO were done to study gamma-ray spectra in gated time windows (Bodnarik *et al.*, 2013; Parsons *et al.*, 2013; Nowicki *et al.*, 2017; Parsons *et al.*, 2011, 2012). CLYC crystals have been used in balloon flight passive measurements (Lawrence *et al.*, 2018), and have been implemented for space flight passive measurements (Hardgrove *et al.*, 2020; David Schechtman Stonehill *et al.*, 2016). In this paper we report on successful demonstration and simulation verification of active neutron measurements with SINGR, using the die-away technique for geoscience applications.

Active nuclear technologies have been in use for decades in nuclear nonproliferation and safeguards, as well as geologic applications in hydrogeology, hydrology, agriculture, environmental science, and mining (Knoll, 2010; Attila Vertes, 1998; Ferronsky, 2015). CYLC crystals are in use for commercial devices such as the RIIDEye from ThermoFisher Scientific (ThermoFisher Scientific, 2012). Current Earth applications of CLYC help to facilitate raising the technological readiness level of SINGR and other space sciences detectors; handheld nuclear instruments have a strong heritage of being successfully adapted to planetary science applications - e.g. the GRNS on the NASA Lunar Prospector mission consisted of commercially available ^{3}He tubes and a standard NaI scintillator (Feldman *et al.*, 1999); the NASA Psyche mission will also carry similar ^{3}He tubes and a new GRS that shares development with The Detective X handheld from AMETEK ORTEC (Ametek Inc., 2018; Burks *et al.*, 2020).

The recent development of compact PNGs for use in landed planetary science missions has allowed for more possible uses in a variety of different mission scenarios (Parsons *et al.*, 2013, 2018; Litvak *et al.*, 2008). This work both improves upon previous studies in the field and presents on the response limitations of a new instrument. SINGR has undergone initial experimental characterization with a PNG at the NASA GSFC GGAO outdoor gamma-ray and neutron instrumentation testing facility. In

this paper we will present on neutron die-away results and model comparisons using SINGR.

2.2 Experimental Setup

2.2.1 The SINGR Instrument Package

SINGR uses the ultrabright elpasolite scintillator called CLYC which has a dominant ^{6}Li(n,α)t reaction, allowing for the detection of neutrons (Johnson *et al.*, 2015; Glodo *et al.*, 2012). The signal generated by the alpha-particle (α) and triton (t) produces a light pulse with a transient response different from that of gamma-ray reactions in CLYC ($\approx$ 3.2 MeV full energy gamma-ray equivalent energy, GEE). SINGR was tested using a Radiation Monitoring Devices Inc. (RMD) 2-inch diameter by 2-inch long cylindrical CLYC crystal (2" CLYC), coupled to a R6233-100 Hamamatsu photomultiplier tube (PMT) that has been custom modified with an active voltage divider network designed for high count rates. Typical crystal properties of CLYC are shown in Table 2.1. The data acquisition system (DAQ) used for all experiments is a field-programmable gate array (FPGA) developed by RMD which has a sampling rate of $\approx$250 megasamples per second; Figure 2.1 shows the SINGR detector and the FPGA DAQ in its aluminum housing. The mass of SINGR's CLYC sensor head and PMT is approximately 850 grams, the total instrument including detector, DAQ, and housing is less than 3.5 kilograms. The total volume of the detector, DAQ, and housing is approximately 0.05 m^3.

A commercial ThermoFisher MF Physics Model MP320 DT neutron generator with an approximate mass of 12 kg was used for these experiments (ThermoFisher Scientific, 2007). This neutron generator is capable of operating as a PNG and can produce up to 10^8 neutrons per second with a limited frequency range from 250 to
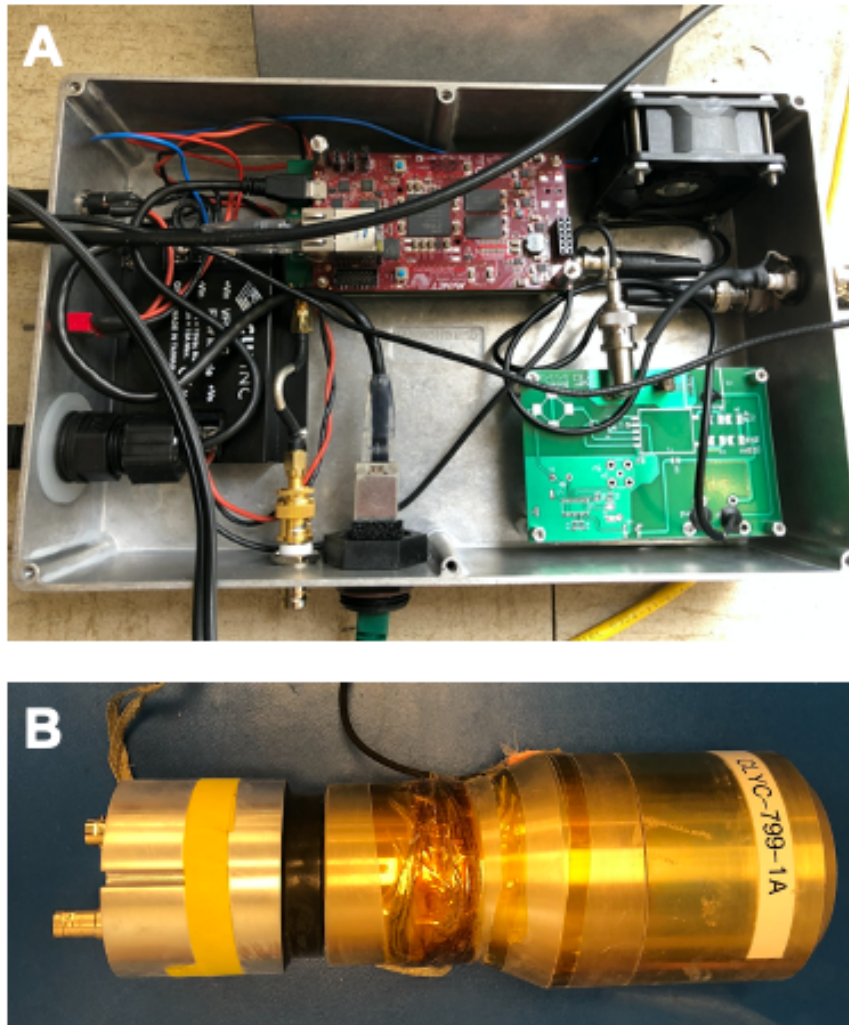
Figure 2.1: Prototype SINGR instrument package: A) RMD data acquisition box with FPGA ($\approx$250 Ms/s) and high-voltage power supply (up to 5 kV via 75 VDC, 15 mA), B) 2-inch crystal CLYC detector.

1000 Hz (50 - 200 μs length pulses). Our experiments used a frequency of 250 Hz which corresponds to a pulse width of 200 μs, we ran the PNG with a current of 60 μA, voltage of 60 kV, and duty factor of 5%, resulting in 2.08x10^7 neutrons per second in 4π. A transistor-transistor logic (TTL) signal (6V pulse ignition, 0V pulse off, 4V during pulse) outputs from the PNG via a BNC output which is connected

Specifications of Cs_2YLiCl_6:Ce	
Density	3.31 g/cm3
2" CLYC Crystal Mass	341 g
Radiation Length	3.42 cm
Melting Point	640° C
Scintillation Light Yield	20,000 ph/MeV
Peak Scintillation Wavelength	370 nm
Decay Constants	1 ns, 50 ns, 1 μs
Decay Time	≈ 400 ns, 1 μs, 6 μs
GEE for Thermal Neutrons	3.2 MeV
Specifications of SINGR (2" CLYC)	
SINGR + DAQ Mass	< 3.5 kg
Thermofisher PNG Mass	≈ 12 kg
DAN PNG Mass	≈ 2.6 kg
Pulsed Intrinsic Neutron Efficiency	20.78 $\pm$ 0.02 % (9.42 $\pm$ 0.02 %)*
Intrinsic Neutron Efficiency (AmBe)	35.5 $\pm$ 0.4 %
Intrinsic Gamma-ray Peak Efficiency (at 662 keV)	25.8 $\pm$ 0.2 %
Energy Resolution (at 662 keV)	4 %

Table 2.1: Basic SINGR Cs_2YLiCl_6:Ce (CLYC) crystal material properties are from (Johnson *et al.*, 2015; Glodo *et al.*, 2012; RMD Inc., 2021). Note that CLYC has three decay constants/times corresponding to the possible allowed energy transition states within the crystal. The efficiency and resolution data were measured during our experiments. The intrinsic pulsed neutron efficiency data (based on PSD value, not GEE peak) was calculated as the total number of measured neutrons of all energies hitting the detector face, divided by the total expected number of neutrons that should be hitting the detector face via MCNP 6.1 simulation. The value in parentheses* denotes the efficiency in the thermal neutron return region only (200 - 2550μs). Note that efficiency can change based on the count rate D'Olympia *et al.* (2013); our pulsed efficiencies are based on the PNG settings described in section 2.2.1. The non-pulsed neutron efficiency was determined using a spontaneous fission source (AmBe) at a distance of 1.5 meters and includes all neutron energies. The gamma-ray efficiency and resolution was determined using ^{137}Cs at 15 inches (cm) and calculated to include attenuation in air and aluminum. Uncertainties are based on Poisson statistics and distance, however these uncertainties may be higher for neutrons due to environmental interactions for non-pulsed efficiency values. Similar, non-pulsed efficiency values can be found in (Glodo *et al.*, 2012; Pérez-Loureiro *et al.*, 2021); the efficiency discrepancy between all neutron energies and thermal region only neutron energies is likely due to the overlap of fast neutrons generated in the ^{35}Cl(n,p)^{35}S reaction in CLYC (Dolympia *et al.*, 2012).

to the SINGR FPGA DAQ. For comparison, the PNG onboard MSL has a mass of 2.6 kg and operates with a higher frequency range with an approximate pulse length of 2 μs (Mitrofanov *et al.*, 2012); future PNGs may be capable of larger frequency ranges (Parsons *et al.*, 2018). The pulse width of the neutron generator affects the magnitude of the neutron count signal seen by SINGR. Ideally, the neutron pulse is short enough that it does not interfere substantially with the relatively low characteristic thermal neutron signal leaking from out of the subsurface after moderating interactions. Following previous active measurement studies done by Bodnarik *et al.* (2013); Parsons *et al.* (2011) we used a 200 μs pulse for studying both neutron and gamma-ray responses in SINGR.

SINGR can be operated at room temperature, so its power consumption is comparable to other scintillators such as NaI, CeBr$_3$, or LaBr$_3$:Ce (Coupland *et al.*, 2016a). However, compared to other scintillators, SINGR has a long light-decay time ($\approx 0.4 - 6\mu s$), meaning that the signal collection of the detector is relatively slow (RMD Inc., 2021). This can be an issue in high-event rate environments, unless the efficiency of the detector is well-known via strict calibration testing and source monitoring. The proportional response of CLYC provides a typical gamma-ray energy resolution of 4% full-width-at-half-maximum (FWHM) at 662 keV, this is a better energy resolution compared to NaI, 7-9% FWHM, despite the emission of fewer photons. The neutron absorption cross-section of the ^{6}Li in CLYC is more than 2 times that of ^{3}He (at 10 atmospheres), as compared on a volume basis, making it an excellent option for neutron detection (Johnson *et al.*, 2015; Glodo *et al.*, 2012).

2.2.2 *Outdoor Instrument Test Site*

SINGR's capabilities have been tested at the NASA GSFC GGAO outdoor gamma-ray and neutron instrumentation testing facility, located a few miles northwest of the

Goddard main campus. The test facility houses two large (1.8- x 1.8- x 0.9 m) rock monuments, one made of Concord Gray Granite and the other made of Columbia River Basalt (hereafter referred to simply as granite and basalt, respectively). The PNG and SINGR instruments were operated from a distance via underground power and communications access. The granite monument has ≈ 0.087 wt% H compared to ≈ 0.05 wt% H in basalt; the macroscopic thermal neutron absorption cross sections (Σ_a) of the two monuments are $\Sigma_a = 0.01785$ cm^{-1} (0.00664 cm^2/g) for basalt and $\Sigma_a = 0.01138$ cm^{-1} (0.00433 cm^2/g) for granite, both of which were calculated from an independent elemental assay of the basalt and granite materials (more detailed information, including composition information about the test site, can be found in Bodnarik *et al.* (2013)). Active measurements with SINGR were performed on both the basalt and granite monuments to demonstrate differences in neutron responses from different target compositions.

The SINGR instrument, electronics, and PNG were mounted onto a 1" x 1" profile extruded aluminum scaffolding that can be moved to sit on top of either the basalt or granite monument. The scaffolding allows for SINGR and the PNG to be adjusted to various heights and relative horizontal distances above the monument. Experiments were performed using the scaffolding, PNG, and detector geometries shown in Figure 2.2.

Six different 24" wide x 24" long x 2" thick high-density polyethylene (HDPE) tile configurations were used (Figure 2.3) to simulate an increase in wt% H abundance; this included one buried HDPE tile configuration to demonstrate H distribution with depth. Active measurements of both the "Bare" and "HDPE top layer" configurations were taken for both basalt and granite monuments; active measurements of all remaining configurations were only performed on the basalt monument. The buried HDPE tile configuration was tested only within the basalt monument at a depth of
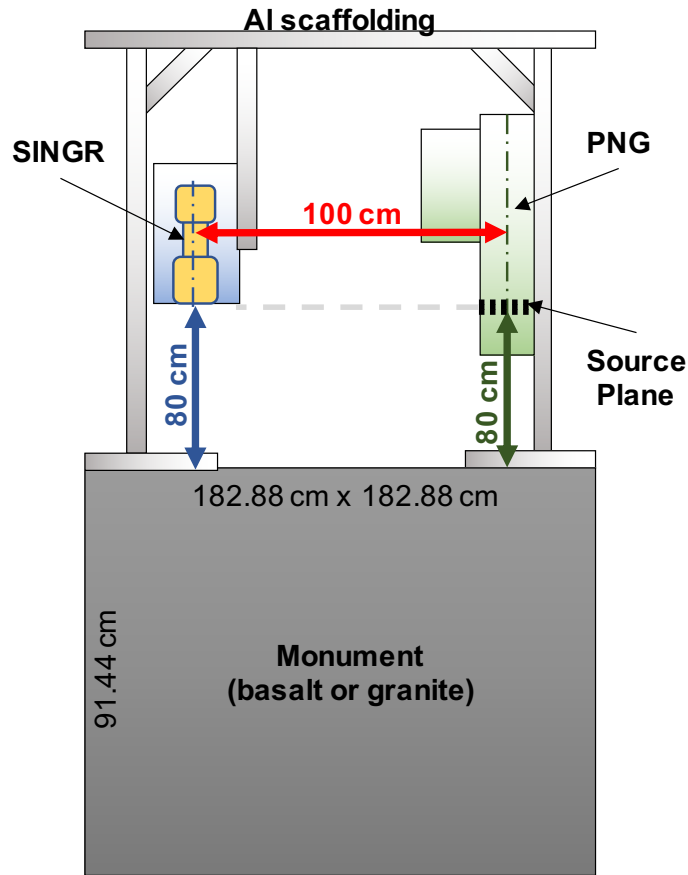
Figure 2.2: Geometry diagram for experiments performed using SINGR at GSFC. The aluminum scaffolding (1" extruded light gray boxes) sits on top of the monument material (182.88- x 182.88- x 91.44 cm dark gray box). The SINGR detector (gold object in blue box) is nested inside an aluminum box which is then mounted to the scaffolding via an extruded aluminum arm. The PNG (green) is mounted opposite the SINGR detector to the other side of the scaffolding. The SINGR detector is concentrically distanced from the PNG by 100 cm and its front detection face is level with the PNG source plane at 80 cm from the top of the monument.
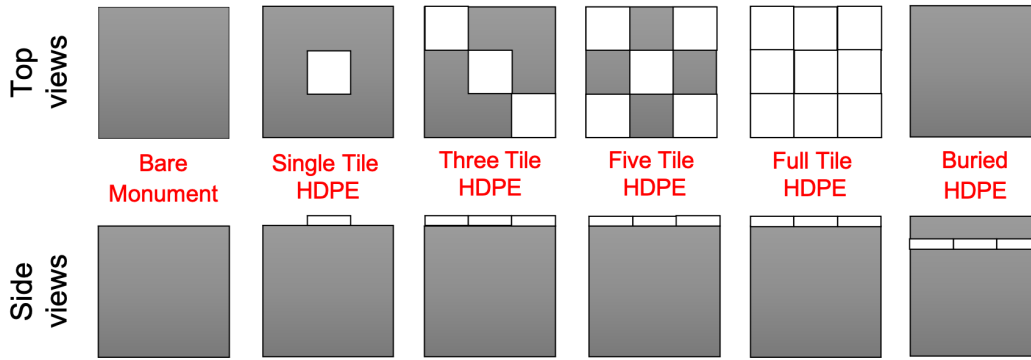
Figure 2.3: The six different top layer high-density polyethylene (HDPE) tile configurations used for the basalt and granite monuments, and the buried configuration used in the basalt monument. The small, white squares represent HDPE while the large, gray squares represent the underlying monument material. The full tile layer of HDPE in the buried configuration can be buried under layers of basalt plates to achieve a variety of burial depths.

| Monument | $Wt\%H$ (WEH) | $Wt\%H$ (WEH) | $Wt\%H$ (WEH) | $Wt\%H$ (WEH) | $Wt\%H$ (WEH) |
Configuration	Bare	Single Tile	Three Tiles	Five Tiles	Full Tiles
Whole Monument	0.050 (0.447)	0.053 (0.475)	0.059 (0.530)	0.065 (0.586)	0.077 (0.697)
Top 15 cm	0.050 (0.447)	0.236 (2.120)	0.593 (5.338)	0.933 (8.398)	1.565 (14.086)

Table 2.2: Calculated H abundances for the HDPE configurations on top of the basalt monument (density of 2.69g/cc) based on volume, elemental abundance, and density of materials. Water-equivalent hydrogen (WEH) values are noted in parentheses. The H contribution from HDPE (density of 9.4g/cc) is calculated using 14 wt% H and 85 wt% C.

6 inches (15.2 cm). The HDPE tiles contain approximately 14 wt% H and 85 wt% C (PNNL Compendium, 2021); when added to a monument, they increase the total wt % H in the topmost layer of the monument. Table 2.2 shows the approximate cal-

culation for wt % H and water-equivalent hydrogen (WEH) in the basalt monument with the HDPE tile configurations. It is important to note that when significantly high amounts of H are present in the first top $\approx$ 15 cm, the neutron sensing depth (neutron number density as a function of depth) will not extend far past the high-H material according to Feldman *et al.* (2000), such that the sensing depth of SINGR does not extend to the base of the monument. Note also, that SINGR and the PNG are positioned on opposite ends of the monument (Figure 2.2) such that SINGR's field of view (FOV) may not encompass the monument's entire top surface.

2.2.3 *Computer Modeling of Test Site*

The monument test site is modeled using MCNP 6.1 (Thompson, 1979) (Figure 2.4) on the Arizona State University *Agave* research computing cluster. The simulation includes the monument (interchangeable as basalt or granite), a simple representation of the aluminum scaffolding on top of the monument, the surrounding atmosphere, an approximation of the ground surrounding the monument, and the SINGR instrument suite. The PNG is fully modeled to include the outer housing and inner materials. The DT reaction within the PNG is modeled as a point source at the approximate location of the source plane within the PNG. The SINGR detector is modeled as a bare 2" tall x 2" diameter cylinder made of CLYC material, (not including the surrounding aluminum housing or surrounding mounting box) which uses a ^{6}Li-neutron reaction neutron tally. HDPE tiles and basalt or granite block layers can be added into the monument as needed depending on the desired simulation. All base material cards used in our simulations are based on information provided in Bodnarik (2013); the weight fraction of H within the base materials (e.g. basalt, granite) is varied and then manually re-normalized using the same methods as Gabriel *et al.* (2018). MCNP 6.1 simulations are run using $3\mathrm{x}10^{10}$ NPS (number

of particle histories) which is sufficient for producing accurate tally statistics in our configuration (LANL, 2003).
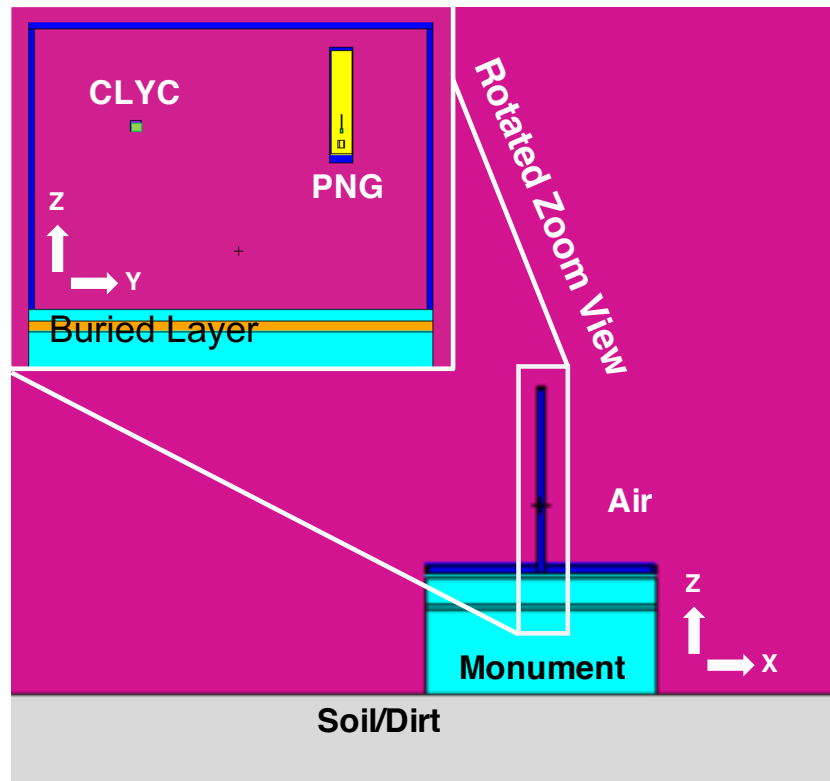
Figure 2.4: MCNP 6.1 simulation geometry of the experimental test site with rotated view inset to show buried polyethylene and instrument package; most materials are color-coded (pink = air, cyan = basalt or granite monument, blue = aluminum alloy, orange = polyethylene), with gray which represents the soil material as well as the PNG and CLYC instrument package.

2.3 Data Processing

Measurements taken at the GSFC GGAO basalt and granite monuments resulted in the collection of temporal neutron and gamma-ray data using SINGR. The data sets require significant reduction post factum to separate the neutron signal from the

gamma-ray signal using pulse shape discrimination. Python 2.7 with various SciPy packages was used to discriminate (PSD), interpret, and visualize all data sets (Van Rossum and Drake, 1995; Virtanen *et al.*, 2020; Mckinney, 2010; Harris *et al.*, 2020). Note that on board data processing can be done for flight electronics, as seen on the CLYC-based spectrometer for the NASA LunaH-Map mission Hardgrove *et al.* (2020).

2.3.1 Pulse-Shape Discrimination

SINGR uses PSD to identify neutrons and gamma rays based on differences in the shape of the scintillator light-pulse. The waveform of the output pulse from the detector is segmented into short (I_s), long (I_L, total in 6 μs), and baseline integrals. I_s and I_L are average baseline integral (B_{avg}) adjusted (the integral divided by the number of samples in the baseline integral) post factum, and then used to determine a pulse shape discrimination ratio. Equation (4.1) describes the calculation of the PSD value used to analyze the SINGR data sets:

$$PSD = \frac{I_s - 73 * B_{avg}}{(I_L - 169 * B_{avg}) - (I_s - 73 * B_{avg})}. \tag{2.1}$$

Note that the values 73 and 169 are the number of samples at 4 ns per sample for the short and long integrals, respectively. Our data sets typically have a neutron PSD ratio ranging from 1.13 to 1.15, whereas gamma-rays tend to have a PSD ratio ranging from 1.15 to 1.19. These values appear slightly distorted in Figure 2.5 due to high event rates occurring from a disproportionate amount of fast neutron events during the pulse. The fast neutron efficiency in CLYC (occurring from neutron reactions with Cl) is on the order of 1 - 2 %, these neutrons span in energy from 0 - 10 MeVee (electron-equivalent energy), which encompasses the thermal neutron peak (Mentana *et al.*, 2016). The thermal neutron and gamma-ray PSD distributions for CLYC are

distinguished from one another based on a figure of merit value (Mesick *et al.*, 2019). More detailed explanations of interactions in CLYC can be found in Johnson *et al.* (2015); Glodo *et al.* (2012); Hardgrove *et al.* (2020); Dolympia *et al.* (2012).

Two Gaussian functions are mapped to the PSD data sets within specified constraints (total PSD ranging 0.5 to 1.5, gamma PSD > 1.15, and 1.11 < neutron PSD < 1.16) using the Python scipy.optimize package (Virtanen *et al.*, 2020); an example of our PSD fit to data is shown in Figure 2.5C, along with energy information in Figure 2.5A. The data is sorted based on the two PSD sets of Gaussian fit parameters to create two new sub-data sets for neutron flux and gamma-ray flux. A combination of the energy, PSD, and total count data is shown in Figure 2.5B. All sub-data sets have their original event-by-event data information preserved, such as a timestamp, full integral (related to particle energy), long integral, short integral, TTL signal (PNG pulse status), and event number. We do not constrain on full integral (energy) events when computing the PSD, as such, fast neutron events are present in our results.

2.3.2 Neutron Data Processing

SINGR neutron flux data is divided into 64 lognormal time bins, adhering to the same methods used by the DAN science team to help provide a direct comparison of our instrument package to a known planetary experiment (Mitrofanov *et al.*, 2012; Litvak *et al.*, 2008). In a single two-hour data set, there can be up to 10^7 total events in the detector. Using the TTL signal from the PNG, each 0 - 2400 μs PNG period (pulse on and pulse off duration) can be co-added based on the TTL signal (i.e. 6V ignition) to produce a smooth neutron response profile, i.e. a *neutron die-away curve*.

Count rates shown in the results section of this paper are normalized to the sum of the output pulse of the PNG (termed *pulse region normalized*), this is done to account for any variability in total time between measurements. Uncertainty in observed count
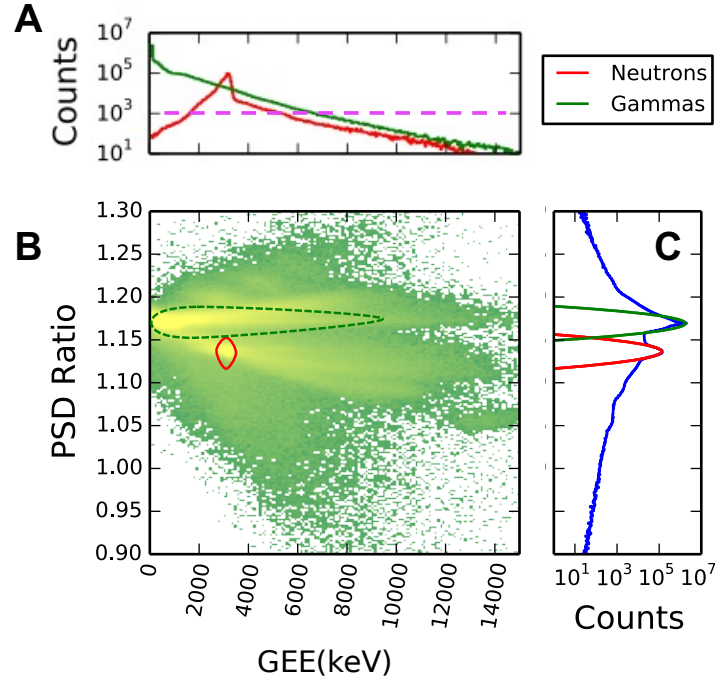
Figure 2.5: Pulse shape discrimination (PSD) plots for the SINGR 2-inch CLYC detector using all data from the detector, including during-pulse events, for a typical two-hour measurement on basalt. A) Counts versus full energy gamma-ray equivalent energy (GEE) of SINGR data for neutrons (red) and gammas (green), with horizontal purple line distinguishing total counts above 1000 (greater than 95% confidence in detecting a peak (Gilmore, 2008)); B) PSD ratio versus gamma-equivalent energy color-mapped for total number of counts on a log-scale, the outlines show the *approximate* locations for neutrons (dotted red, lower outline) and gammas (dotted green, upper outline) based on a 1000 count threshold; C) PSD ratio versus count data including two Gaussian fits to neutrons (red, lower) and gammas (green, upper). Data shown are from an experiment with the basalt monument at GSFC using a 200 μs pulse PNG. Note that much of the counts outside of the red outline for the neutron fit are likely due to fast neutrons (RMD Inc., 2021).

rate ($\sigma_{observed}$) is propagated for each time bin and is determined based on Poisson statistics ($\sqrt{N_{observed}} = \sigma_{observed}$), assuming the accumulated counts ($N_{observed}$) are Poisson random variates (Knoll, 2010).

In this paper, we compare both pulse-region normalized and *thermal region normalized* neutron die-away curves so as to examine die-away profile shape changes which can indicate a difference in bulk neutron cross section. The thermal region normalized method of constructing neutron die-away curves is actively used by members of the MSL DAN science team (Czarnecki *et al.*, 2020, Gabriel *et al.*, 2018, tted). The pulse region normalized methods are similar to that of Mitrofanov *et al.* (2014); Sanin *et al.* (2015), however in our case, we do not include correction factors to account for the rover body. To pulse region normalize a 200 μs pulse, we normalize over the the leading end of the pulse region from 0 to 76 μs which corresponds to time bins from 0 to 10.

Comparison between experimental and MCNP simulated neutron die-away curves are done using the same methods outlined in the supplement of Gabriel *et al.* (2018). However, here, we perform a simple reduced chi-squared (χ^2/m) analysis using the following equation:

$$\frac{\chi^2}{m} = \sqrt{\sum_{Bin_0}^{Bin_f} \frac{N_{observed}^2 - N_{expected}^2}{\sigma_{observed}^2 + \sigma_{expected}^2}}, \tag{2.2}$$

where m is the total number of time bins, $N_{observed}$ is the observed number of normalized counts in a single time bin with normalized uncertainty $\sigma_{observed}$, $N_{expected}$ is the MCNP/simulated output number of normalized counts in the same time bin with normalized uncertainty $\sigma_{expected}$ (based on MCNP relative error), and Bin_0 and Bin_f are the starting time and ending time bins to be compared. Relative errors across our simulations are $< 0.02\%$.

Based on simple neutron time-of-flight calculations, we determined that end-point inclusive time bins 22 through 44 (240 - 1180 μs) best represent the bins in which the majority of thermal neutrons are returning to the detector from within the monument (Bin_0 and Bin_f, respectively); these are the bins used for thermal region normalization. Additional thermals arriving to the detector from 200 - 240 μs are likely back-scattered inside the mechanical structures close to the detectors and/or the neutron generator. Thermal neutrons arriving after 1180 μs are still returning from deep within the target monument but are statistically insignificant compared to additional counts that may be returning from the nearby ground around the monument, objects outside of the monument (piles of basalt bricks, instrument cases, etc. often placed at random), or due to natural background. In our experimental analyses, we did not include background subtraction; in our simulations we did not include small objects placed outside the monument.

2.4 Neutron Die-Away Results

Neutron die-away curves were constructed from SINGR experimental data for all configurations from Figure 2.3 using the basalt monument, and for the bare and full tile HDPE configurations using the granite monument. All data shown in the results section are pulse region normalized. The integrated thermal neutron albedo (total raw counts from 200 - 2250 μs) for all experiments are shown in Table 2.3.

Target	Bare	HDPE Single Tile	HDPE Three Tiles	HDPE Five Tiles	HDPE Full Tiles
Basalt	1.14 ± 0.02	1.86 ± 0.05	2.67 ± 0.05	3.46 ± 0.06	5.79 ± 0.08
Granite	0.60 ± 0.01	N/A	N/A	N/A	4.98 ± 0.02

Table 2.3: GGAO Active Test Configurations, total number of returning neutrons (200 - 2250 μs) per total pulse registered in SINGR using a DT (14.1 MeV neutrons) PNG with a 200μs pulse width (10^7 nps).

2.4.1 Polyethylene Top Layer Configurations

Neutron die-away experiments were performed on the basalt monument for the bare configuration, as well as top layer HDPE configurations listed from Figure 2.3, the results of these experiments are shown in Figure 2.6. As the number of HDPE tiles increases, the total neutron count rate in time bins from 200 - 2250 μs (thermal neutron return region) increases in magnitude; this corresponds to the increase in H abundance.
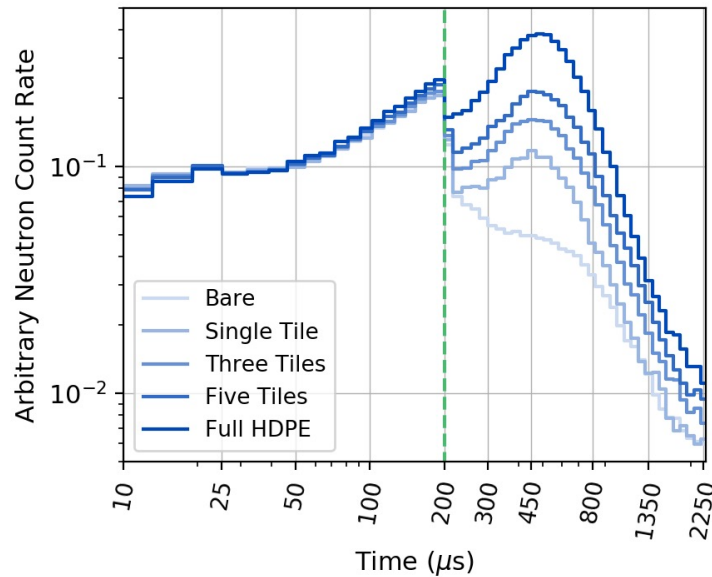
Figure 2.6: Polyethylene configuration experimental neutron die-away results. As more HDPE tiles are added, the total wt% H in the FOV of the SINGR instrument suite increases. The total neutron count rate in the thermal neutron region (time bins 200 - 2250 μs) changes for each configuration, increasing in magnitude as H increases. The green dotted line represents the end of the PNG pulse (≈ 200 μs). The maximum number of thermal neutrons returning to the detector occurs at ≈ 470 μs for the full HDPE tile configuration.

2.4.2 Buried Polyethylene

Figure 2.7 shows the neutron die-away curves for a layer of HDPE tiles (2" thick) buried under 6" of basalt, versus the bare basalt, and the full HDPE tile basalt monument configurations. The basalt in the monument is ≈ 0.05 wt% H based on the elemental assay reported by Bodnarik *et al.* (2013). The maximum count rate of neutrons in the thermal region of the die-away curve for the full HDPE tile configuration occurs at $\approx 470\ \mu$s. The buried HDPE neutron die-away curve has both a lower overall count rate in the thermal neutron region, and the maximum neutron count rate for returning neutrons occurs in later time bins ($\approx 620\ \mu$s) compared to the unburied HDPE. Neutrons have a longer distance to travel within the 6" of basalt, which increases the return time to the detector. The buried HDPE die-away curve is also higher in neutron count rate magnitude for the thermal region compared to the bare monument due to the buried H-rich HDPE tile layer.

2.4.3 Basalt vs. Granite Monument

Experiments of bare and full HDPE top tile were performed on both the basalt and granite monuments. The results of these experiments can be seen in Figure 2.8. The die-away curve for the full HDPE top tile configurations (high-H) are indistinguishable between basalt and granite, whereas the shape of the die-away curve is different between the bare monuments (low-H). The total macroscopic thermal neutron absorption cross sections for basalt and granite have a percent difference of around 44%.
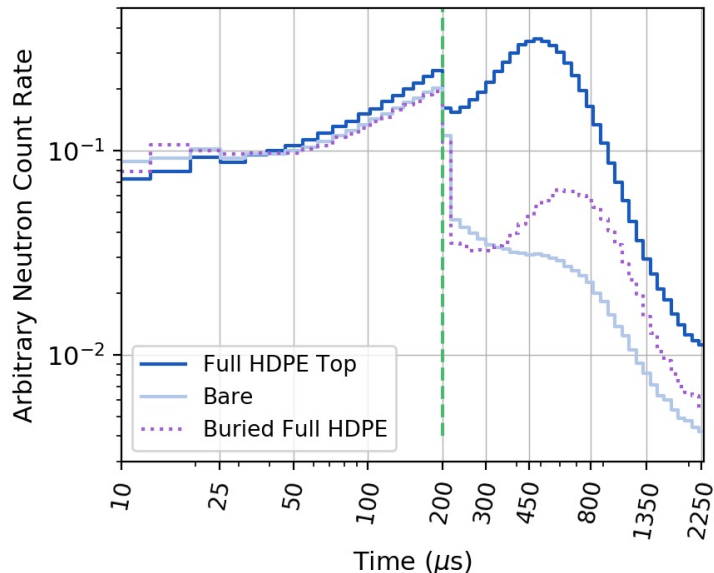
Figure 2.7: Basalt monument neutron die-away curves comparing full HDPE top tiles, buried full HDPE tiles, and bare configurations. Comparison of the peaks (max count rate) of the neutron die-away curves in the thermal region (200 - 2250 μs) show a clear count suppression and time shift from the earlier time bins (full HDPE top, dark blue line, peak $\approx$ 470 μs) to the later time bins (buried full HDPE, purple dotted line, peak $\approx$ 620 μs) due to the buried H-rich material.

2.4.4 Pulse Stability

The pulse variability of the PNG used in these studies (refurbished and calibrated in Fall 2018) was estimated using SINGR to measure the total neutron counts during the pulse. Two bare monument configuration data sets from two different dates (7/16/19, 7/24/19 with aluminum scaffolding raised by 6") were investigated, as well as a more recent measurement (9/1/21) with a CeBr detector, along with HDPE and a $\approx$5 lbs bag of table salt (NaI). For each measurement, two hours of data was taken
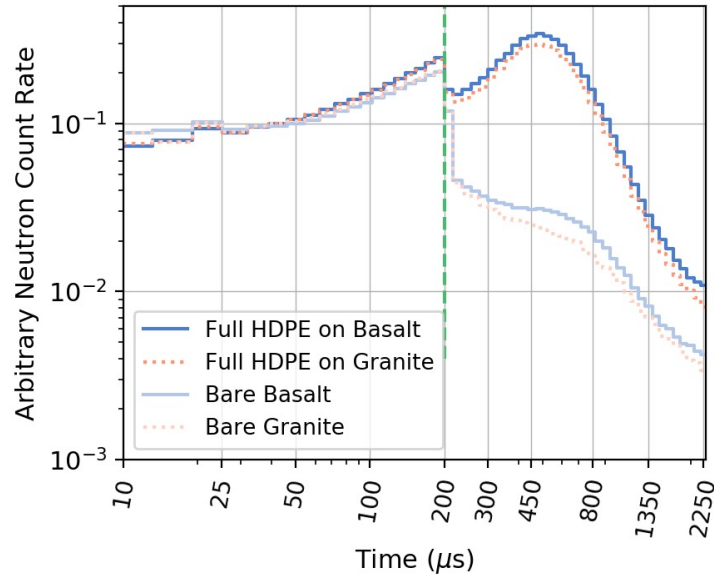
Figure 2.8: Basalt and granite monument neutron die-away curves comparing full HDPE tile and bare configurations. Initial comparison of the magnitude of the neutron die-away curves show that the granite peaks are slightly suppressed for both configurations. Basalt and granite monuments with the full HDPE tile configurations show minor possible differences in shape.

using SINGR, the data was then post-processed into neutron counts using PSD, then divided into 15 minute chunks. These chunks were then divided into the 64 log-normal time bins, then the total number of counts from 0 - 200 μs (during the pulse) were integrated, Figure 2.9(A) shows the results of this study. A five-hour data set was taken with a CeBr detector, which recorded gamma-ray data as a function of time; the total counts in the 2224 keV H peak was monitored in 30 minute chunks, Figure 2.9(B). This specific gamma-ray energy was chosen because it is the most prominent and is well isolated from other peaks. We used this information as a proxy for the stability over time of our PNG. The measurement variations in Figure 2.9 (A) and (B)

are within 3%. The downward trend in Figure 2.9(B) may be due to the diffusion of deuterons or tritons out of the target as the temperature increases, but nevertheless the output is quite stable.

2.5 Comparison to Simulation Studies

Experimental results were compared to simulated results using both thermal (Figure 2.10A - C, Figure 2.11, Figure 2.13, Figure 2.14) and pulse region normalization (Figure 2.10D - F); they are presented with a focus on the thermal neutron region of the die-away curve (200 - 2250 μs).

Our experimental results confirm that the magnitude (Figure 2.10A) and shape (Figure 2.10D) of the neutron die-away curve changes for low amounts of H (0 to 0.25 wt% H in top 10 cm layer with single HDPE tile) for the bare and single HDPE tile configurations on the basalt monument. MCNP 6.1 is used to simulate the HDPE configurations (Figure 2.10B and 2.10E) as well as the bare configuration with variable wt% H throughout the monument (no HDPE tiles, Figure 2.10C and 2.10F). Our simulations confirm that both shape and magnitude of the thermal region of the neutron die-away curve change for low amounts of H ($<$ 0.25 wt% H in top 15 cm layer with single HDPE tile). However, for higher amounts of H ($>$ 0.5 wt% H in top 15 cm layer basalt with HDPE tiles on top) the thermal region normalized curves are no longer distinguishable between experimental measurements with three or more HDPE tiles (Figure 2.10D) or simulated measurements (Figure 2.10E and 2.10F). Our goodness-of-fit testing included over-fitting, potentially due to over-parameterizing the model space (e.g. we did not need to run models of increase in wt% H for the full HDPE tile on top configuration due to neutron sensing depth limits involving high-H content in upper layers). Over-fitting occurs when the experiment and models are within the uncertainties of one another and the reduced chi-squared value is then
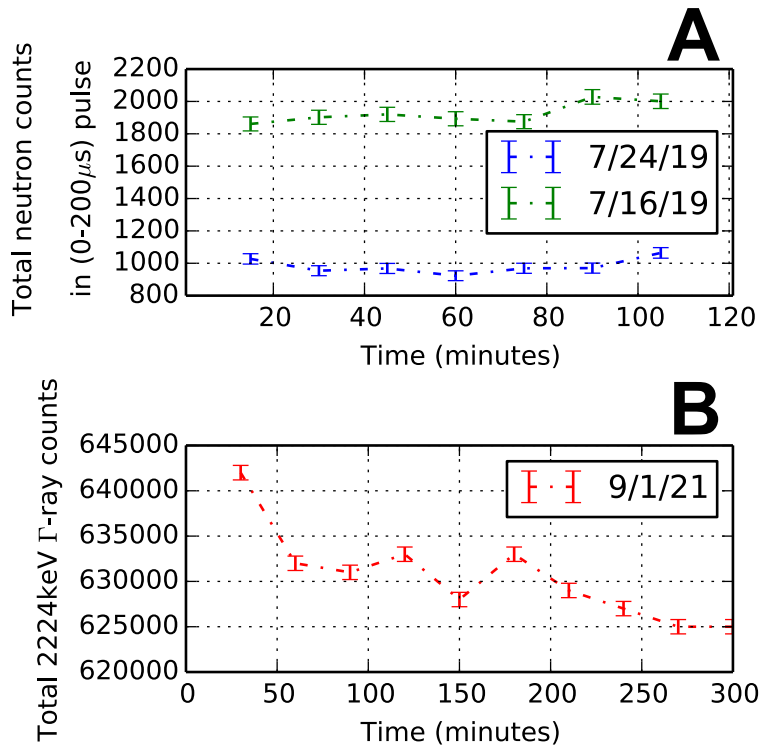
Figure 2.9: Investigation of PNG pulse stability using (A) SINGR (2" CLYC) neutrons and (B) CeBr gamma rays. SINGR data (A) was taken on two different dates (2 hr measurements each) on top of the bare basalt monument, note that the 7/24/19 data was measured from an additional 6" vertical distance compared to the 7/16/19 data. The total neutron counts were divided into 15 minute intervals during the neutron pulse period (0 - 200 μs). The variations between individual measurements/15 minutes in each data set for (A) are within 3%. The CeBr data (B) was taken at a much later date, 9/1/21, and was also taken on top of the bare basalt monument (5 hrs total measurement), along with HDPE and a $\sim$5 lbs bag of table salt (NaI). The total gamma-ray data was divided into 30 minute intervals, tracking the 2224 keV H peak. The measurement variation in (B) is within 3%. See Section 2.4.4 for further details.
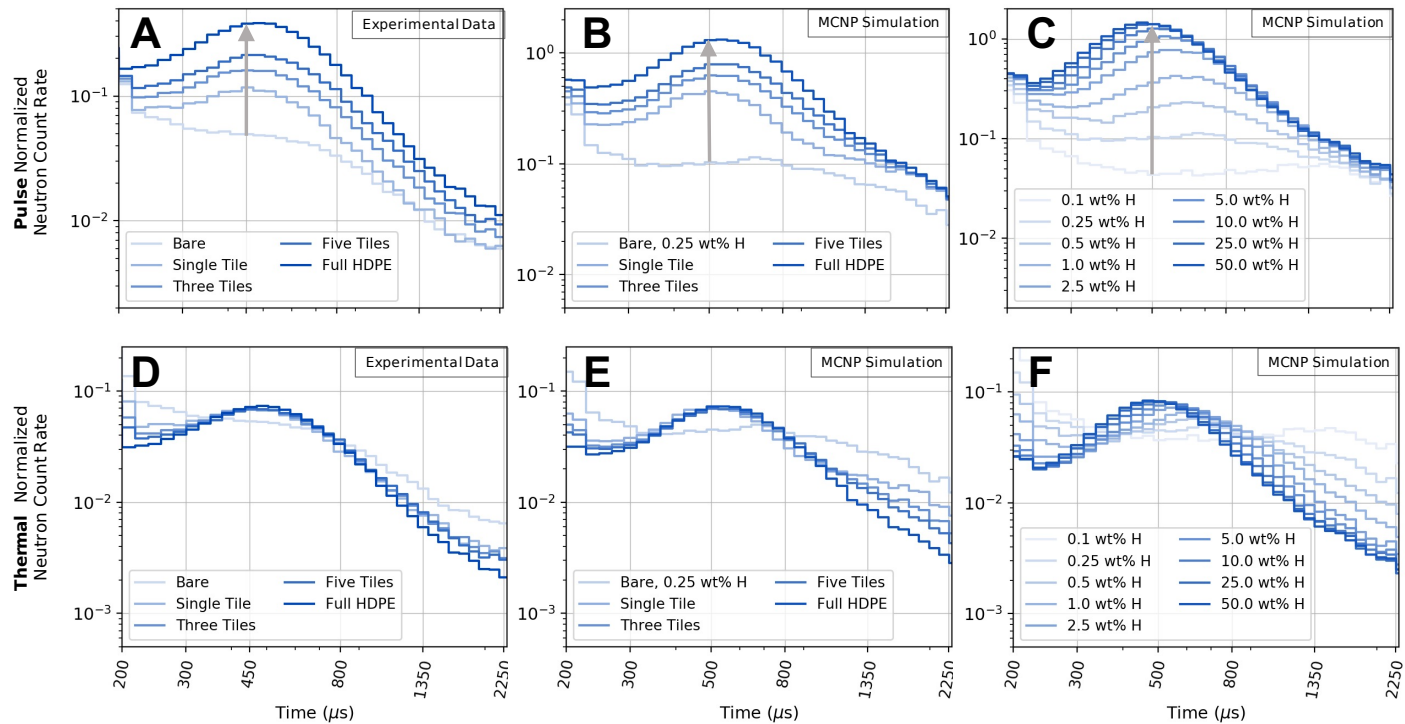
Figure 2.10: Neutron die-away curves showing experimental results and simulated results side-by-side, focused on the neutron die-away region (200 - 2250 μs). (A and D) The basalt monument experiment using the HDPE configurations described in Figure 2.3. (B and E) MCNP 6.1 simulations of the HDPE configurations on the basalt monument with 0.25 wt% H throughout the basalt. (C and F) MCNP 6.1 simulations of the bare (no HDPE tiles modeled) monument with change in H from 0 - 50 wt % throughout the basalt. Note that curves (A) - (C) are normalized to the PNG output pulse region (0 - 200 μs), and curves (D) - (F) are normalized to the thermal neutron return region (330 - 900 μs). The magnitude of the die-away curve in the thermal region is expected to increase as wt% H increases (gray arrows), as shown in the pulse normalized plots (A - C). The shape of the die-away curve is expected to change from 0 - 2.5 wt% H, shifting slightly from right to left time bins. The change in shape is shown in plots D and E between bare and single HDPE tile curves, the change in shape for plot F is seen in light blue curves from 0 - 2.5 wt % H.

interpreted as "fitting to the noise." Alternative statistical methods for avoiding over-fitting with die-away data are discussed in the supplementary materials of Gabriel *et al.* (2018).

2.5.1 HDPE Top Layer Configurations

Figure 2.11 shows the experimental neutron die-away curve from the full HDPE tiles on top of basalt compared to simulations using MCNP of the exact same configuration (full HDPE tiles on top). We found that the wt% H throughout the monument is indeterminable due to all χ^2/m-values < 1.5; these results are consistent with Feldman *et al.* (2000) in regard to neutron sensing depth, such that SINGR's sensing depth does not extend far past the top high-H layer. However, this does show that we can constrain our experimental data using simulations with a high-H top layer. An example of goodness-of-fit results of our MCNP study are shown in Table 2.4, with χ^2/m values visualized in Figure 2.12 to find optimal fits for wt% H and burial depth of the HDPE layer.

2.5.2 Buried HDPE Configuration

We generated MCNP files for parametric studies of burial depth (0 - 24" by 2" increments), total wt% H (0 - 5 wt%) in the basalt, and thermal region normalized neutron count rate via die-away curves. Figures 2.13 and 2.14 show examples of these MCNP neutron die-away outputs for HDPE buried within the basalt monument. Figure 2.13 shows varying 2" thick HDPE layer burial depths (0-10" depths shown) with 1 wt% H throughout all layers of basalt. Figure 2.14 shows varying wt% H (0-5 wt%) throughout all layers of basalt with 2" thick HDPE buried at a depth of 6". Figure 2.15 shows a contour plot from our MCNP parametric study of the 2" thick HDPE layer buried for distances 0-10", versus the wt% H distributed throughout the

wt% H	χ^2	χ^2/m	Average %MCNP error
0.0	20.43	0.97	0.017
0.5	22.35	1.06	0.018
1.0	23.08	1.10	0.018
2.0	25.38	1.21	0.018
3.0	27.33	1.30	0.019
4.0	27.75	1.32	0.019
5.0	27.71	1.32	0.019
6.0	28.34	1.35	0.019

Table 2.4: Best fit (χ^2-values, χ^2/m-values) statistics between experiment for full tile HDPE on top of the basalt monument and the associated MCNP model with variable wt% H in the basalt monument. Bins are endpoint-inclusive normalized from bin 22/63 to bin 44/63, with a total number of degrees of freedom of 23.

basalt monument, versus the χ^2/m-value between MCNP simulation and experiment, both of which were thermal region normalized. The models suggest that the wt% H content of this experiment is between 0.0 - 2 wt% H, with a 2" HDPE depth range of 4 - 10". These simulation results place accurate constraints on the actual experimental configuration (6" burial depth with ≈ 0.05 wt% H) and verify that the neutron die-away method can be used to constrain wt% H and depth for low-H environments ($<$ 0.5 wt% H).

Figure 2.16C shows the result of the homogeneous model comparison of the buried HDPE configuration compared to basalt monument models with varying wt% H that do not contain HDPE. Note that Figure 2.16C is plotted on a linear scale in order to emphasize the thermal neutron peak location. As noted in Section 2.5, the goodness-of-fit (χ^2/m) can suffer from over-fitting, though it may also suffer from sample-size issues, meaning that a larger sample size can cause trivial relationships to appear

48
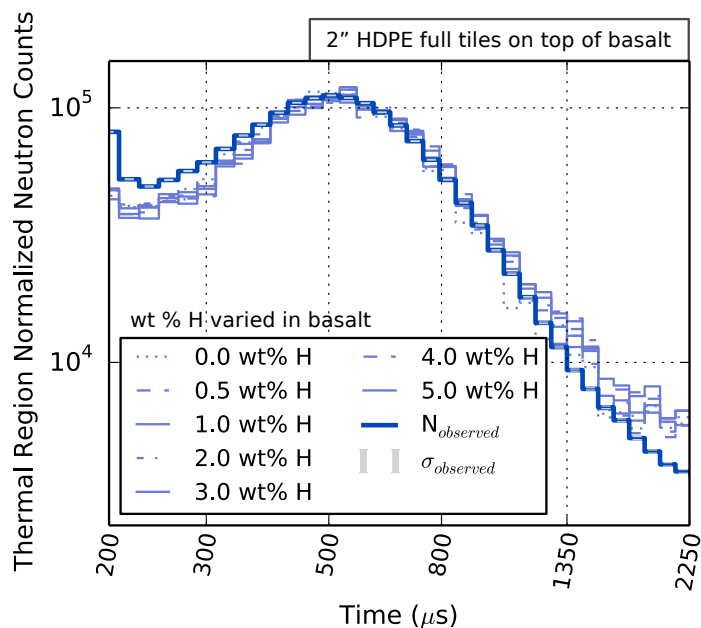
Figure 2.11: Simulations compared to experiment for the full tile HDPE top configuration on basalt. Experimental die-away curve results (deep blue, thick line) compared to MCNP output die-away curves for full tile HDPE top configuration on the basalt monument with varying amounts of H within the monument. The model output line colors reflect the χ^2/m-values when compared to the contour plot of Figure 2.12; in this case all χ^2/m-values < 1.5. The MCNP models include the top layer of full HDPE tiles, wt% H is varied within the underlying basalt. The neutron counts in the time bins from 200 - 300 μs represent neutrons that may not be coming from the target surface, but may be the result of interactions with nearby materials or instrument housings. Uncertainties in counts for simulation results are smaller than the plot line-widths ($< 5\%$ error, $< 0.02\%$ in thermal normalized region).

statistically significant; though outside the scope of this paper, methods discussed in the supplementary materials of Gabriel *et al.* (2018) provide more rigorous methods of analysis to avoid these issues. It is clear in Figure 2.16C that there is a time bin shift
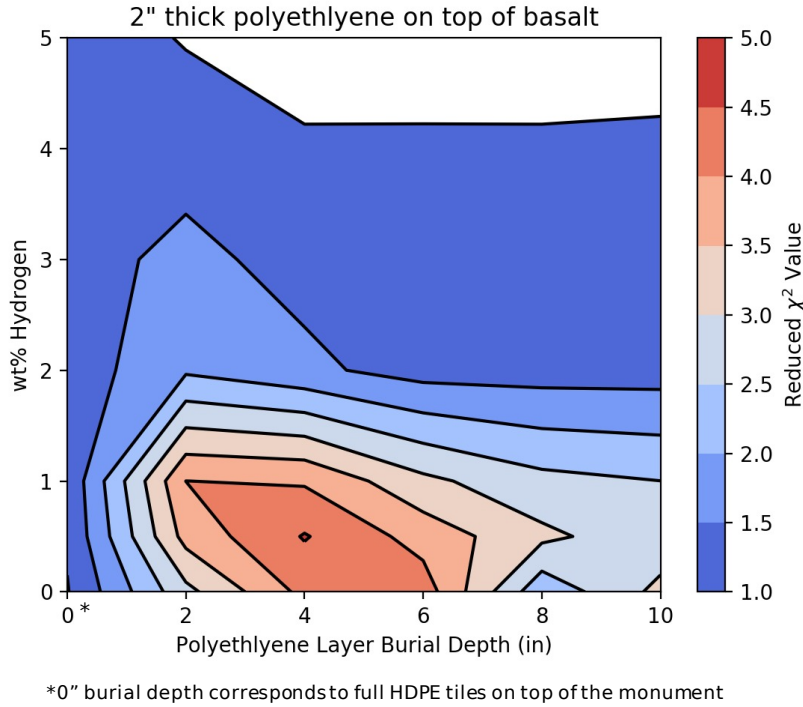
Figure 2.12: Reduced-χ^2 (χ^2/m) contour plot comparison of the full tile HDPE top experiment on basalt and associated MCNP simulations with change in wt% H and burial depth of HDPE. All curves were thermal region normalized. Cooler colors represent lower χ^2/m-values, implying better model-to-measurement fits; values of χ^2/m less than 1.5 are considered good fits between model and experiment. The white region represents an overfitting (Section 2.5) where models and experiment are within the uncertainties of each other (i.e. χ^2/m test is "fitting to the noise"). As seen in Figure 2.10(B), if the amount of H is very large, the shape of the thermal normalized neutron die-away curve becomes indistinguishable between measurements. This plot indicates that there is either 1) a high-H deposit on top of the monument (the experimental match, all χ^2/m-values are close to 1.0 for 2" thick HDPE 0" burial depth) and that there may be greater than 0 wt% H throughout the monument or 2) that there is greater than 2 wt% H throughout the monument regardless of 2" thick HDPE burial depth. This plot also indicates that a buried deposit of H under a dry (< 2 wt% H) layer of basalt is unlikely ($\chi^2/m > 2.5$) within neutron sensing depth limits (≈ 0.5m in basalt, energy-dependent).

to the right (forward in time) due to burying the HDPE tiles, though a χ^2/m-value
of <1.1 corresponds to a homogeneous model (1 wt% H).
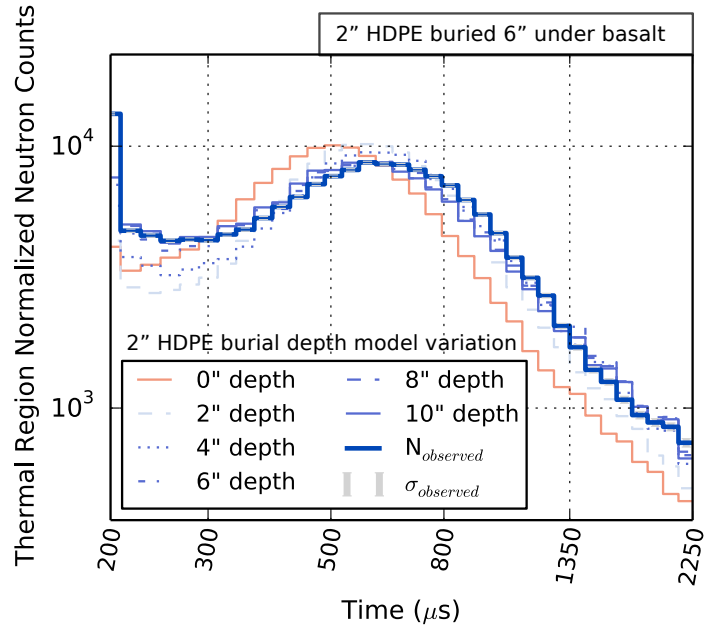
Figure 2.13: Experimental die-away curve results (deep blue, thick line) for HDPE
buried under 6" of basalt compared to MCNP output die-away curves for 2" thick
HDPE under different burial depths of basalt. The model output line colors reflect
the χ^2/m-values when compared to the contour plot of Figure 2.15. All of the basalt
contains 1 wt% H distributed throughout the bottom and top layers of the monument
for this set of models. Values of χ^2/m less than 1.5 are considered good fits between
model and experiment; for this set of models with 1 wt% throughout the basalt, a 2"
HDPE layer is constrained to a depth of 6 - 10".

2.5.3 Bare Monument Configuration

We compare the bare, full tile HDPE on top, and buried HDPE basalt monument
configurations to MCNP simulations of only the bare basalt monument with varying
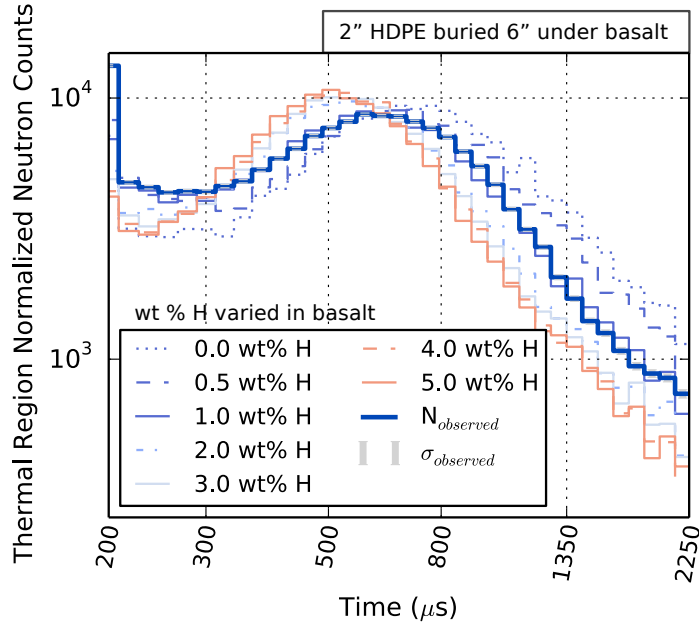
Figure 2.14: Experimental die-away curve results (deep blue, thick line) for HDPE buried under 6" of basalt compared to MCNP output die-away curves. The model output line colors reflect the χ^2/m-values when compared to the contour plot of Figure 2.15. The MCNP models consist of the buried 2" thick HDPE full tile layer under 6" of basalt, with wt% H varied throughout the basalt both above and below the HDPE layer. For this set of models with a 2" HDPE layer modeled at a depth of 6", the wt% H in the basalt is constrained to 0.0 - 1.0 wt%.

wt % H, as shown in Figure 2.16. The χ^2/m-values between MCNP simulations and experiment for the bare basalt monument (Figure 2.16 A) are most consistent (0.9 $< \chi^2$/m < 1.4) with models that have 0.6 - 1.3 wt% H throughout the basalt; this is not consistent with the assay of 0.05 wt% H reported by Bodnarik $et\ al.$ (2013). The experiment for the full HDPE tiles on top of the basalt monument (Figure 2.16 B) are most consistent ($1.5 < \chi^2$/m < 1.8) with models that have 2.5 - 10 wt% H throughout the basalt; all of the χ^2/m-values for this study are greater than 1.0, suggesting that
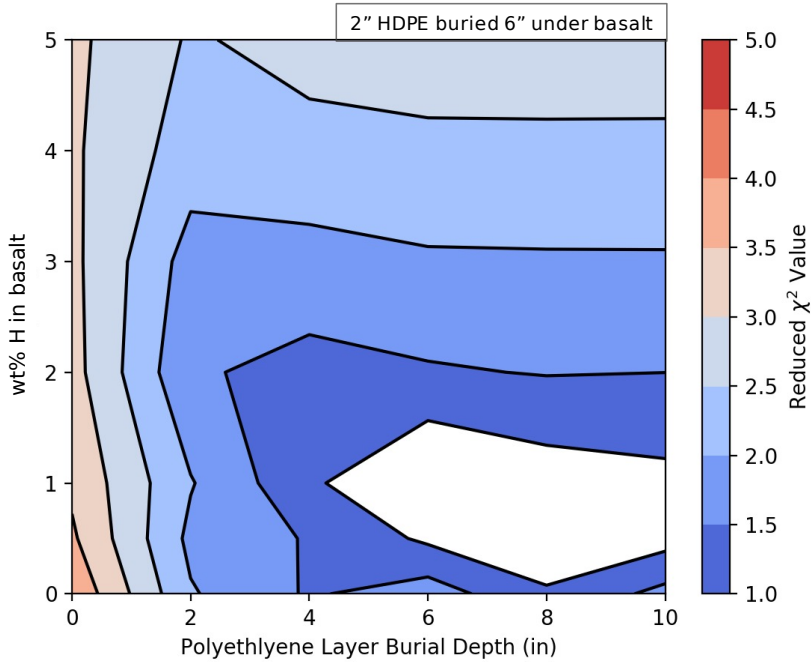
Figure 2.15: Reduced-χ^2 (χ^2/m) contour plot of the 6" buried HDPE experiment in basalt compared to MCNP simulations for change in wt% H versus burial depth of HDPE. The experiment is located at a 6" burial depth with ≈ 0.05wt % H (from elemental assay performed in Bodnarik *et al.* (2013)), which is reflected in the over-fitted region of the contour plot (white area, see Section 2.5 for details). Values of χ^2/m less than 1.5 are considered good fits between model and experiment.

the H is unlikely to be distributed throughout the monument. The experiment for the full HDPE tiles buried 6" under basalt in the monument (Figure 2.16 C) are most consistent ($0.85 < \chi^2/m < 1.26$) with models that have 0.25 - 2.0 wt% H throughout the basalt. This is consistent with the range of H values given in Table 2.2 for the full-tile monument, from 0.08 wt% H in the full monument to 1.57 wt% H in the top 15 cm of the monument.
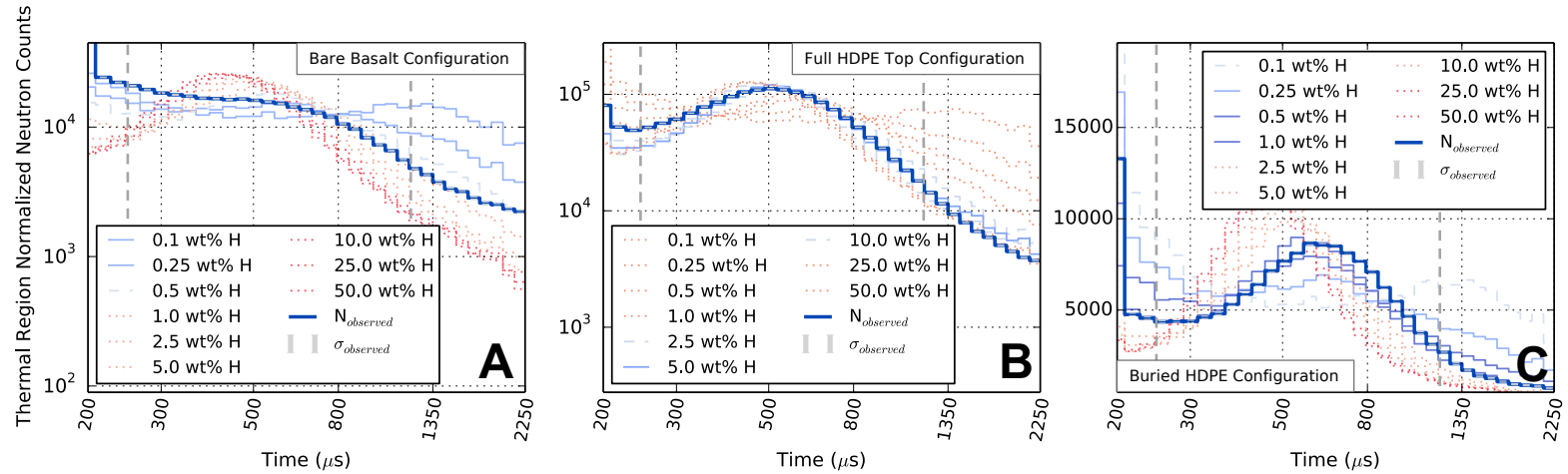
Figure 2.16: MCNP bare basalt monument configuration simulations compared side-by-side to experimental measurements on the basalt monument for (A) the bare configuration, (B) the full HDPE tiles on top configuration, and (C) the buried full HDPE tiles configuration. The basalt monument is modeled with increasing amounts of wt% H from 0.1 - 50.0 throughout the basalt, there is no HDPE present in the models, these are homogeneous, single layer models (see Section 2.5.3). The experimental measurement (observed value) is shown as a deep blue, thick line, the model output line colors reflect the $\chi^2/$m-values using the same color scale as Figures 2.12 and 2.15. The vertical, gray, dotted lines represent time bins 22 - 44 which are used for $\chi^2/$m comparison and thermal region normalization. The bare basalt monument models for 0.1 - 0.5 wt% H agree moderately well ($\chi^2/$m < 2.0) with the bare experimental measurement in (A); this is within the value of the elemental assay (0.5 wt% H) done by Bodnarik (2013). In (B) 2.5 - 10 wt% H model results have $\chi^2/$m-values < 2.0 as compared to the experimental measurement (see Section 2.6.1). In (C) the y-scale is linear to show the shift in the time bins for the thermal neutron peak (see Section 2.5.2); 0.1 - 1.0 wt% H model results have $\chi^2/$m-values < 2.0 as compared to the experimental measurement.

2.6 Discussion

2.6.1 High-Hydrogen Environments

From the HDPE configuration tests (Figures 2.6 and 2.10), we observed that as the wt% H increases beyond 0.25 wt% (2.25 wt% WEH) in the top 15 cm (more than a single HDPE tile), the shape of the neutron die-away curve becomes indistinguishable between measurements and only the magnitude allows for wt% H estimation. This is consistent with our MCNP simulation studies (Figure 2.10) and similar to simulation studies by Kerner *et al.* (2020) for low Σ_a compositions. Studies by Feldman *et al.* (2000) show maximum peak neutron density at a mixture of 3 wt% WEH by mass (0.33 wt% H) in a ferroan-anorthosite material ($\Sigma_a \approx 0.06$ cm^{-1}), this agrees well with our results, given that both the basalt and grante monuments have low Σ_a.

The macroscopic thermal neutron cross sections of the basalt and granite monuments are similar and are considered low in comparison to those calculated for other planetary compositions (Kerner *et al.*, 2020). For measurements with similar low-Σ_a and high-H (HDPE top tiles configuration) compositions, as shown in Figure 2.8, the shape of the neutron die-away curve does not dramatically change. However, as shown in Table 2.3, the bare granite and basalt monuments have clearly different count rates, though both sets of die-away curves are statistically similar when thermal region normalized ($\chi^2/m = 0.99$, $\chi^2/m = 0.73$ for bare and full HDPE tiles, respectively). From our data we infer that materials with more subtle differences ($<$ 0.01 cm^{-1} difference) in absorption cross section may be indeterminable when buried under high-H materials. Simulation studies on Mars compositions ($\Sigma_a > 0.005$ cm^2/g or 0.2 cm^{-1}) done by (Kerner *et al.*, 2020) and data collected by MSL DAN (Czarnecki *et al.*, 2020; Gabriel *et al.*, 2018) have shown that neutron die-away can be used to characterize higher-H (> 2.5 wt% WEH in top 15 cm) abundances when the local

rocks and soils contain materials with higher thermal neutron macroscopic absorption cross-section (i.e. due to elevated Fe and Cl abundances on Mars). As shown in Figure 2.10(C/F), high-H environments begin to show much more subtle changes in the die-away shape, requiring more reliance on the magnitude of the pulse region normalized data.

2.6.2 Simulations Can Be Used to Constrain Results

Figures 2.10B, C, E, and F show the results of our MCNP simulation studies of neutron die-away on the basalt monument. The change in the shape of the neutron die-away curves match well between experiment and simulations as demonstrated with the HDPE full tile on top and buried HDPE configurations. We constrained the HDPE top layer to be in the top 0 - 2" of the monument (for 0 - 2 wt% H), but were unable to fully constrain the underlying H wt% content of the basalt due to neutron sensing depth limitations (Figure 2.12). We constrained the buried HDPE layer to be buried within 4 - 10" with the basalt top layer containing 0 - 2 wt% H within the constrained burial depth of the HDPE (Figure 2.15).

Further discrepancies between simulation and experiment may include small distance uncertainties, atmospheric moisture changes, and the layering of bricks of the basalt and granite monuments (in which rain water can seep and sometimes pool between the brick or buried HDPE layers). This is evident in our experimental comparisons to simulations, where we see a variation of 0.1 - 2 wt% H in bare basalt. Measurements were taken in Maryland, USA, from May - August, when humidity can range from 50 - 90 %, although no measurements were taken during rainfall.

2.6.3 CLYC Benefits and Drawbacks

CLYC's greatest benefit, and therefore SINGR's greatest benefit, is that it is capable of detecting both neutrons and gamma rays. Throughout our experiments we confirmed that CLYC is efficient at both small and large volumes for neutron detection; neutron die-away was easily achievable using 2" CLYC. However, for active dual use on planetary science missions, larger CLYC crystals (> 2") would provide higher count rate statistics (decreasing the necessary integration time) and more efficient high-energy sensitivity to gamma rays. While we were unable to collect active gamma-ray spectra using 2" CLYC with a PNG, we were able to collect typical passive gamma-ray data with standard lab sources (^{60}Co, ^{137}Cs). A preliminary measurement with a larger crystal (3") shows that active gamma-ray acquisition is possible with CLYC (Heffern *et al.*, 2018).

CLYC is not without drawbacks, like many planetary science instruments radiation and thermal damage degrades the detection efficiency of CLYC for both gamma rays and neutrons (light dimming); however, this damage degrades resolution for gammas only. Both damage mechanisms can be partially repaired through the use of room-temperature annealing (Coupland *et al.*, 2016a; Mesick *et al.*, 2019; Vogel *et al.*, 2017; Coupland *et al.*, 2016b; Menge and Richaud, 2011). Unlike HPGE detectors, annealing of scintillator crystals - such as CLYC - does not result in active volume loss and efficiency degradation (Peplowski *et al.*, 2019).

Much of the efficiency loss experienced by the SINGR system was likely due to the high neutron event rate causing pile-up (particles hitting the crystal at the same time saturate the detector and the signals become difficult to individually count); this pile-up effect may also explain the slightly distorted PSD plot shown in Figure 2.5. The decay constants of CLYC are 1-1000 ns (Table 2.1) which are fairly long

in comparison to other GRNS ($NaI(Tl) \approx 250$ns), which is likely why the detector would saturate while taking data during the neutron pulse.

2.7 Summary

We generated neutron die-away curves using SINGR and a PNG. Six different experimental HDPE geometry configurations were used to simulate an increase in wt% H abundance, along with one buried HDPE configuration to demonstrate H distribution with depth. Results show that the measurements can constrain the depth of buried H-rich material.

We conclude that SINGR can be used to inform near-surface (within the top 15 cm) H content in a variety of environments. With a PNG, the integrated thermal neutron albedo can be used to estimate the H abundance. Additional information about the near-surface neutron absorbing elements can be gained through analysis of the neutron die-away curve shape for low-H environments (< 0.25 wt% H) between compositions that have sufficiently different (> 0.01 cm^{-1} difference) macroscopic thermal neutron absorption cross sections.

Qualitatively, we confirm that the shape of the neutron die-away curve changes significantly for low amounts of H (0 - 0.25 wt% H in top 15 cm). However, for high amounts of H (> 0.25 wt% H in top 15 cm) the curves normalized to the thermal neutron count rate are no longer distinguishable between measurements (Figure 2.10 D-F for one or more HDPE tiles) with the same underlying material. At high-H abundance, the total magnitude of the thermal neutron die-away curve is the main indicator of H content. In the absence of information about the neutron output of the PNG, the shape of the thermal neutron die-away curve can be used to determine low-H abundance (< 0.25 wt% H) and inform macroscopic thermal neutron cross section information, however as determined by MSL DAN, normalized curves require

additional counting statistics and longer integration times (Gabriel *et al.*, 2018).

Due to the reduced effect on curve shape in high-H environments, it is important to monitor the neutron output of the PNG for determination of bulk H content. This would enable more robust reduction of raw neutron die-away data without requiring thermal region normalization. Over our two months of measurements, our results did not show significant changes in the PNG output pulse. However, results from the DAN instrument on Mars determined that the PNG neutron output degrades over time due to the degradation of the fill gas and the half-life of Tritium (Gabriel and Hardgrove, 2020). Our results contribute to the argument for a need to monitor the PNG output, during the duration of the mission, to determine the absolute number of neutrons emitted from the PNG during measurements, particularly when analyzing non-normalized data products.

We were unable to generate efficient time-resolved (active) gamma-ray spectra using a 2" CLYC crystal, likely due to the detector's small volume (2" long x 2" diameter). SINGR experienced a saturation of events (likely due to high neutron event rate) during the neutron generator pulse which also contributed to the efficiency degradation for gamma-ray measurements. Larger CLYC crystals for active gamma-ray measurements, as well as similar elpasolite scintillators (e.g., CLLBC ($Cs_2LiLa(Br, Cl)_6 : Ce$) and TLYC ($Tl_2LiYCl_6 : Ce$)) which exist with shorter light decay times, may be required to reduce the significance of pulse pileup in SINGR active gamma-ray data. TLYC also has a higher density than CLYC, making it more likely to be an efficient gamma-ray spectrometer (though its resolution is worse compared to CLYC) (Watts *et al.*, 2019). Still, we conclude that SINGR (2" CLYC) has the potential to be used successfully for active neutron measurements on planetary bodies, with the addition of passive gamma-ray and neutron measurements (Glodo *et al.*, 2012).

Chapter 3

TIME RESOLVED ACTIVE NEUTRON MODELING INVESTIGATIONS ON

ICY PLANETARY SURFACES

L. E. Heffern[1], C. J. Hardgrove[1]

[1] Arizona State University School of Earth and Space Exploration, Tempe, AZ

[2]United States Geological Society, Flagstaff, AZ,

Paper to be submitted to JGR Planets with approval from Co-Author C. J.

Hardgrove.

ABSTRACT

Information about the elemental composition of a planetary surface can be determined through the use of nuclear instrumentation, such as gamma-ray and neutron spectrometers (GRNS). GRNS can be used to determine the elemental abundances and hydrogen content within the top ≈tens of centimeters of planetary surfaces. The first planetary active neutron investigation, the Dynamic Albedo of Neutrons (DAN) instrument on the Mars Science Laboratory Curiosity Rover (MSL), is returning significant scientific results from the surface of Mars; the recently selected Dragonfly mission to Saturn's Titan will also carry an active GRNS instrument (DraGNS). Due to Titan's dense atmosphere and lack of galactic cosmic ray photons at the moon's surface, the addition of a DT (Deuterium-Tritium) pulsed neutron generator (PNG) alongside the GRNS is needed. We used the Monte Carlo N-Particle 6.1 simulation tool from Los Alamos National Laboratory to investigate the use of neutron spectrometers (NS) with a PNG for multiple Titan-like scenarios. Studies in our simulation efforts include 1) determining the effects of Titan's dense atmosphere on the nuclear environment and 2) determining the limits and utility for the neutron die-away technique with a pulsed neutron generator on Titan for both mixed material and layered material (high-N deposits, salts, exposed water ice, tholin layering).

3.1 Introduction

Gamma-ray and neutron spectrometers (GRNS) have a long history of use in planetary science missions ranging from Mercury to the asteroid belt (Surkov, 1977; Lawrence *et al.*, 1998, 2013; Peplowski, 2016; Czarnecki *et al.*, 2020). High energy, galactic cosmic ray protons (GCRs) emitted from cosmic super novae travel through space, eventually penetrating the surfaces of solar system objects that have little or no atmosphere. GCRs liberate neutrons from nuclei within the surface material in a process called spallation, resulting in downscattering of neutrons throughout the subsurface and the emission of gamma-rays, neutrons, and other particles. Using GRNS, we can detect and measure the bulk elemental abundances of a planetary body's surface based on the output of neutrons and gamma-rays (Reedy, 1978). Planetary bodies such as Earth, Venus, and Titan contain dense atmospheres that interact with GCR particles, resulting in fewer GCRs hitting the planetary surface. However, enabling nuclear technologies, such as deuterium-tritium (DT) pulsed neutron generators (PNG), offer a solution for rapid measurements using GRNS technologies on planetary bodies with an atmosphere.

Recent NASA ROSES instrument programs (PICASSO, DALI, etc.) and selected future missions (NASA Dragonfly) use neutron generators (NGs) alongside GRNS to determine the bulk elemental content of unexplored planetary bodies (Parsons *et al.*, 2011; Bodnarik *et al.*, 2013; Nowicki *et al.*, 2017; Parsons *et al.*, 2017; Heffern *et al.*, 2021). The NASA Dragonfly mission will travel to Saturn's Moon, Titan, to explore the moon's surface, it will take measurements of neutrons and gamma-rays to investigate the surface elemental composition (Barnes *et al.*, 2021). As currently planned, the European Space Agency's ExoMars program surface platform will carry an active neutron instrument (ADRON-EM) to investigate subsurface ice and hydrated miner-

als on Mars (Litvak *et al.*, 2017). ADRON-EM is similar to the Dynamic Albedo of Neutrons (DAN) instrument, the only active nuclear instrument on another planetary body, it is currently operating onboard the Mars Science Lab (MSL) Curiosity rover and returning science results to Earth (Mitrofanov *et al.*, 2012; Gabriel *et al.*, 2018; Czarnecki *et al.*, 2020).

This paper is focused on the application of the active neutron die-away technique using a DT PNG and neutron spectrometer (NS) for use near the surface of an unexplored icy planetary body: Titan. Using the Monte-Carlo n-particle (MCNP 6.1) simulation code we performed investigations of hypothesized geologic scenarios on Titan using neutron die-away (LANL, 2003). Using the active neutron technique, we discuss what the expected neutron environments are and their implications for neutron instrument sensitivity limits. Studies in our simulation efforts include determining the effect of Titan's dense atmosphere on the nuclear environment and determining the limits and utility for the neutron die-away technique with a pulsed neutron generator on Titan and other high-H bodies for both mixed material and layered material (high-N deposits, salts, exposed water ice, tholin layering).

3.2 Background

3.2.1 *Planetary Nuclear Measurements*

High energy, galactic cosmic ray protons (GCRs) emitted from cosmic super novae travel through space, eventually interacting with the surfaces of solar system objects that have little or no atmosphere (Mars, Mercury, 4-Vesa, Earth's Moon, etc.). GCRs liberate neutrons from nuclei within the surface material in a process called spallation, resulting in downscattering of neutrons throughout the subsurface and the emission of gamma-rays, neutrons, and other particles. Neutrons can then immediately escape

back into space, or they can interact with the elemental nuclei within that surface resulting in the emission of more gamma rays, neutrons of lower energies, or other particles. Neutrons and gamma rays emitted from a planetary body are a result of characteristic interactions with the subsurface atomic nuclei. By measuring the amount of neutrons and gamma rays emitted from a planetary surface, information about the subsurface composition can be constrained (Reedy *et al.*, 1973; Price Russ *et al.*, 1972). However, the relatively low rate at which GCRs bombard a surface, and the rate at which neutrons and gammas are emitted requires either multiple orbits from space over the same areas, resulting in very large area measurements (e.g. single pixel size of 100'x100's of square kms), or long duration, stationary measurements at the surface of a body (e.g. multiple hours to collect data at 1 m x 1 m).

The probability that a neutron is absorbed by an elemental nucleus is called the microscopic neutron absorption cross section (σ_a). The probability that a neutron is scattered by an elemental nucleus is called the microscopic neutron scattering cross section (σ_s). In a planetary surface, the total effect of the microscopic cross sections of each element and interaction type combine into the macroscopic neutron cross section, which dictates the resulting neutron energy spectrum after initial neutrons interact within that surface. The macroscopic neutron absorption (Σ_a) and scattering (Σ_s) cross sections can be defined as follows (Beckurts and Wirtz, 1964; Elphic *et al.*, 2002):

$$\Sigma_n = \sum_{i=1}^{N} \frac{\sigma_i N_A m_i}{a_i} \tag{3.1}$$

where Σ_n is either the macroscopic neutron absorption or scattering cross section, σ_i is the associated microscopic neutron cross section (absorption or scattering, in barns), N_A is Avogadro's number, m_i is the mass fraction of element i, and a_i is the atomic mass of element i summed over the number of elements, N, contained in

the surface. The macroscopic neutron cross sections are an indicator of the presence of certain elements within the subsurface (Hardgrove *et al.*, 2011). For example, a material with a high macroscopic neutron absorption cross section ($\Sigma_a > 10$ cm^2/g) likely has a high percentage of element(s) with a high microscopic neutron absorption cross section (Cd, B, Cl), depending upon the planetary body and geologic context. Likewise, if a material has a high macroscopic neutron scattering cross section it must have a high percentage of element(s) with a high microscopic neutron scattering cross section (H, Ar). If the neutrons are mostly scattered within the surface, the total energy of the neutron environment will go down (neutron moderation), meaning that the detector will experience a high flux of thermal neutrons. However, if the neutrons are mostly absorbed within the surface, the detector will experience a much lower flux of all energies of neutrons. It is also important to note that neutron cross sections are also energy dependent, such that some elements may absorb low energy neutrons more readily (thermal neutrons, E $\approx 2.5\text{x}10^{-5}$ MeV), while the same element may scatter high energy neutrons (epithermal and fast neutrons, E $>2.5\text{x}10^{-5}$ and 1 MeV, respectively).

Other planetary bodies in our solar system, such as Titan, Earth, or Venus, contain more dense atmospheres. As such, GCRs can not easily penetrate these bodies' atmospheres to interact with surface materials. The idea for using active neutron sources (e.g. ^{252}Cf) or NGs was first postulated by Trombka *et al.* (1970). NGs and PNGs are typically filled with Deuterium (D) gas that is then accelerated via an electric potential inside a sealed tube, into a Tritium (T) or Deuterium target; the result is a fusion reaction which releases 10^5 - 10^8 neutrons at a specific energy per second in 4π. The two reactions can be described as D + T $\rightarrow$ n(14.1 MeV) and D + D $\rightarrow$ n(2.54 MeV). The use of a PNG on another planetary body has already been proven on Mars by the DAN onboard the NASA MSL rover (Mitrofanov *et al.*,

66

2014). The use of a PNG categorizes DAN as an active neutron instrument, meaning that instead of relying on galactic cosmic rays for neutrons, DAN emits them in pulses into the planetary surface using a compact DT PNG (Litvak *et al.*, 2008). Results from DAN have helped with understanding and interpreting processes that have formed and modified rocks on the surface of Mars. Throughout MSL's traverse in Gale Crater DAN has revealed H and Cl enrichments, hydrated silica phases within fractures, and helped place constraints on hydrated amorphous phases (Gabriel *et al.*, 2018; Czarnecki *et al.*, 2020; Litvak *et al.*, 2016).

Hydrogen (H), chlorine (Cl), nitrogen (N), and boron (B) are efficient neutron moderators; neutron moderators shift the population of fast (high-energy) neutrons towards thermal (low) energies. In H-rich environments, fast neutrons emitted by a NG are moderated to lower energies, resulting in higher amounts of thermal neutrons scattered back to the GRNS after each pulse. High-H (>10 wt%) in a planetary subsurface also poses a limitation on the penetration depth of neutrons, limiting the detection depth of the neutron spectrometer (Feldman *et al.*, 2000; Heffern *et al.*, 2021).

Currently, the only future mobile landed mission that uses an active GRNS in NASA's pipeline is the Dragonfly mission to Saturn's moon Titan. Dragonfly will land a rotorcopter on Titan which, due to Titan's dense atmosphere and low-gravity, will fly to measurement locations (Barnes *et al.*, 2021). Dragonfly will carry the Dragonfly Gamma Ray and Neutron Spectrometer (DraGNS), an active GRNS system that includes a DT NG, HPGe and scintillator gamma-ray spectrometers, and ^{3}He tube neutron spectrometers (Parsons *et al.*, 2018; Lawrence *et al.*, 2022). Our high-H time resolved neutron simulation studies are directed towards Dragonfly mission science scenarios to highlight potential applications of PNGs for future missions on Titan.

3.2.2 Geology of Titan

Titan is thought to be primarily composed of C, N, and H compounds, with some small amounts of O incorporated into organics in Titan's upper atmosphere (Barnes et al., 2021). The changing climate on Titan results in a diverse planetary surface, where aeolian transport processes (e.g. wind, storms, etc.) may cause surface gardening of materials (Mitchell and Lora, 2016). Other processes that may cause compositional changes to the surface of Titan include endogenic processes, such as cryovolcanism, as well as external impacts from objects in the Saturnian system and beyond may result in cratering and overturned crustal materials (Barnes et al., 2021). Active nuclear measurements are well-equipped to distinguish between many of these surface changes due to their compositional and depth detection capabilities.

Titan's Dunes

The atmosphere on Titan is dominated by nitrogen with some small amounts of hydrogen and carbon which tend to interact in the atmosphere via irradiation, creating aerosols which later rain down to the surface. These sticky, condensed aerosols have been named "tholins" (Sagan and Khare, 1979; Niemann et al., 2005; Cable et al., 2012). Tholins are thought to make up a majority of the dunes described on Titan's surface (Soderblom et al., 2007; Hörst, 2017). Many attempts have been made to recreate tholins in the lab; these lab-created tholins are termed "Titan tholins." For the purposes of this study, we have used the definition from Cable et al. (2012): *we define a tholin as a complex organic mixture formed specifically in the Titan atmospheric simulation experiments, i.e. synonymous with "Titan tholin".* The possible types of irradiation that can produce tholins in a lab consist of hot plasma discharge, cold plasma discharge, and ultraviolet (UV) radiation. For the purposes of this paper

we have deemed tholins resulting from hot plasma discharge as "hot tholins", these have C/N ratios spanning from 1 - 12; Tholins resulting from cold plasma discharge have been deemed "cold tholins" and have C/N ratios < 5; Tholins resulting from UV radiation have been deemed "UV tholins" and have C/N ratios spanning from 1 - 24, though typical values tend to be much higher from 10 - 24 (Cable et al., 2012). Titan tholin species tend to have different densities depending on how they are produced in the lab (e.g spark plasma vs. UV created, amount of initial C, H, N, etc.) (Hörst and Tolbert, 2013). Active gamma-ray and neutron instruments are able to constrain the C, H, N content of tholin materials on Titan. However, due to gardening and other processes on Titan's surface, these tholin materials may be mixed in or layered with other compounds.

Water-ice and Organics

Titan is thought to have cryovolcanism, such that water-ice, methanol-water, or ammonia-water from Titan's crust may be deposited onto the surface due to eruption (Lopes et al., 2013). Additionally, dissolved salts (Na, K, Mg) may be present in cry-olava deposited on the surface of Titan indicating saltwater eruptions due to water-ice and rocky core cryovolcanic interactions (Lopes et al., 2013; Barnes et al., 2021). A distinct layering of material would indicate deposition as a cohesive layer (i.e. a lava flow), as opposed to material that has been well-mixed and transported by aeolian processes or deposited by atmospheric material. Giant impacts from Saturnian materials or objects outside the Saturnian system may also result in excavated water-ice material from Titan's crust via crater overturn (Barnes et al., 2021). Additional geomorphological information from imaging instruments would assist in distinguishing between lava flows vs. giant impacts. This paper describes how stratification of materials at shallow depths ($\lesssim$ 6 cm) in high-hydrogen environments is detectable and

distinguishable by active neutron instrumentation via the neutron die-away method.

Boron is an efficient neutron moderator (B^{10}, 20% abundance, $\sigma_s = 3835$ barns) making it more detectable at even small amounts ($\sim$ 100's ppm) using nuclear instrumentation. B is an important micronutrient critical to the growth and health of plant life on Earth such that it is considered an Earth biosignature (Pugel et al., 2019). Typical Earth fertilizers use up to 20 wt% B, though natural abundances in soil are on the order of tens of ppm (Whetstone et al., 1941); areas of higher natural B concentrations are likely due to decay of organic matter (Wilcox, 1930). Borate-organic complexes are an important metabolic constituent for life as we know it, such that boron has been suggested as a potential biosignature on other planets (Pugel et al., 2019). We investigate changes in the neutron die-away curve that may indicate the presence of B in simulated Titan surface materials.

Titan's Lakes and Seas

Titan's seas Kraken Mare, Ligeia Mare, and Punga Mare consist of 80% of Titan's liquid surface with the total liquid on the surface making up roughly 1.1% of Titan's global surface area (Hayes, 2016); much of this surface liquid is thought to be methane-dominated, with Ligeia Mare postulated to consist of 71 vol% CH_4, 12 vol% C_2H_6, and 17 vol% N_2 (Glein and Shock, 2013; Mastrogiuseppe et al., 2014). The methane cycle postulated to be present on Titan contributes to the global movement of liquids on the surface of Titan (Atreya et al., 2006). Most of the liquid on Titan's surface is currently located in the northern hemisphere, though it has been postulated that liquid deposits on Titan oscillate between the poles based on Saturn's orbital parameters (Hayes, 2016). These seasonal changes on Titan would likely result in tidal changes at shorelines, exposing lake or sea bed materials over time. Dissolved sulfates may also be present in water-ice deposits, due to early chrondritic sulfur deposition

and dissolution in a possible Titan ocean (Fortes *et al.*, 2007).

Titan's Dense Atmosphere

The density of Titan's atmosphere is ≈ 4.5 times greater than that of Earth (0.00539 g/cc on Titan compared to 0.0012 g/cc on Earth). Titan's atmospheric density and composition (≈ 97 wt% N, 2 wt% C, < 1 wt% H, with trace amounts of O and Ar) were measured at one location during the Cassini-Huygens mission (Fulchignoni *et al.*, 2005; Niemann *et al.*, 2005); many of these measurements were taken using the gas chromatograph mass spectrometer (Niemann *et al.*, 2010). Titan's changing atmospheric weather conditions can lead to density changes near the surface (Mitchell and Lora, 2016; Roe, 2012). These changes in the local atmospheric density affect the total number of neutrons produced in the vicinity of a neutron generator, thereby affecting the background count rate of active nuclear measurements. The relative contributions from planetary atmospheres vs. planetary surfaces are currently not well-characterized. We examine the effects of atmospheric density on detecting surface compositional changes using active neutron die-away in this work.

3.2.3   Nuclear Environments

The planetary scenarios on Titan and other icy bodies are dramatically different from that of silicate-dominated bodies, such as Earth or Mars. To get an idea of the expected neutron environments for different compositions on Titan, we plotted a range of neutron scattering and absorption cross sections for Titan materials in comparison to compositions common on Earth's Moon and Mars, these are shown in Figure 3.1. As expected, the absorption and scattering cross sections for most of the Titan compositions are substantially different from Mars or lunar compositions, with Titan hypothesized macroscopic thermal neutron scattering cross sections ranging

from 0.1 to 50 cm^2/g and macroscopic thermal neutron absorption cross sections ranging from 1e-4 to 0.2 cm^2/g.

3.3   Simulation Methods

We used the Monte Carlo N-Particle 6.1 simulation code from Los Alamos National labs to simulate all scenarios, with studies grouped into three categories (LANL, 2003). Our simulation efforts aim to 1) determine the limits and utility for neutron techniques with a pulsed neutron generator on Titan for both mixed material and layered material (high-N deposits and nutrient signatures, tholin/ice layers); 2) explore temporal (time-stamped) vs. integrated neutron data. MCNP uses a FORTRAN back-end to model nuclear particle transport and material interactions, as such, it uses sections of code that are referred to as *cards*. These cards consist of cell definition (cell card), geometry definition (geometry card), material definitions (materials card), source definitions (source card), physics definition (physics card), time definitions (time card), and particle interaction tallies (tally card).

3.3.1   Description of the Model

Nuclear Source

The source used in our model consists of a DT neutron point source with an associated source distribution definition (*si* and *sp* code identifiers) to simulate pulsing, which creates a PNG within the model. The source card can be set to produce pulses with widths of 3 μs (Hz), 50 μs, and 200 μs. These pulses were explored due to their historic uses in commercial and flight model PNGs (3 μs on MSL DAN (Mitrofanov *et al.*, 2014), 50 μs and 200 μs used in experiments out of GSFC GGAO (Bodnarik *et al.*, 2013).
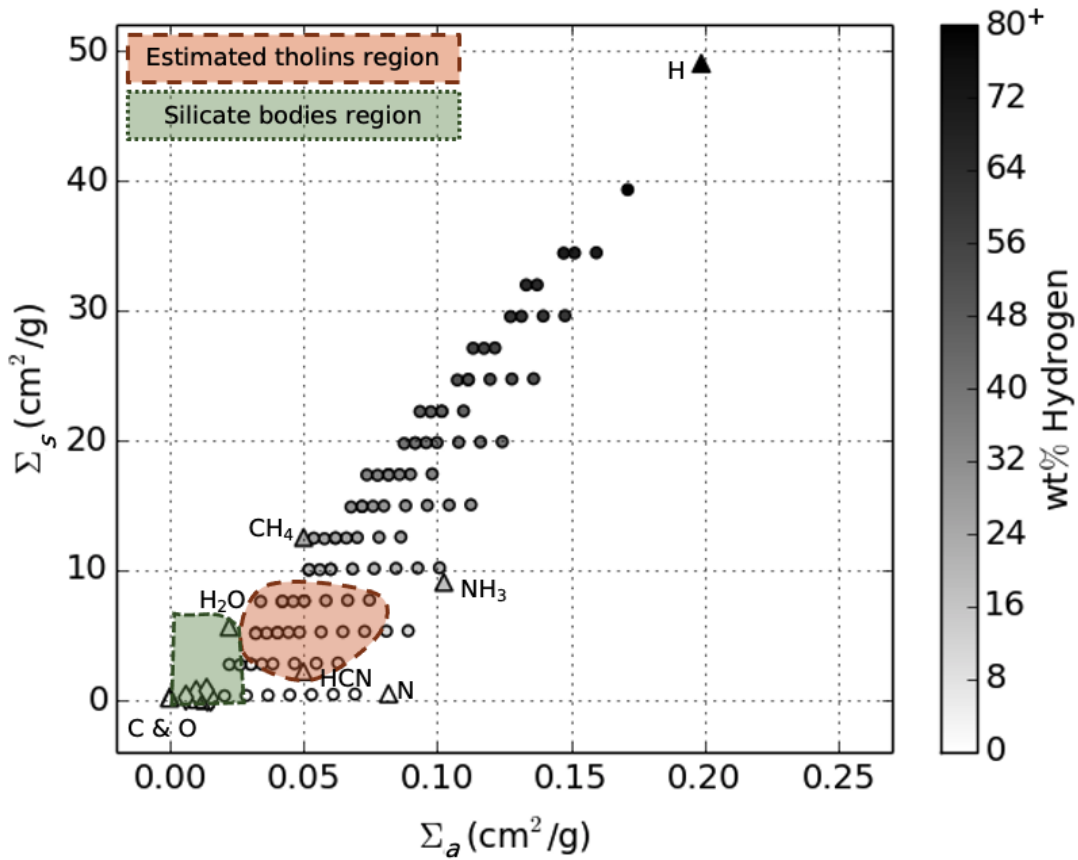
Figure 3.1: Scattering (Σ_s) versus absorption (Σ_a) cross sections for "pure" compositions of Titan-like materials (triangles, e.g. H_2O, CH_4, NH_3, HCN, H, N, C, O) plotted on top of a range of mixed Titan-like materials (circles), silicate body materials are located in the bottom left corner (diamonds). The orange dashed region represents the estimated range of cross section values where Titan tholins are likely; compositions for Titan tholins are based on laboratory studies reported in Cable *et al.* (2012). The green dotted area in the lower left corner represents a range of materials associated with silicate bodies. The comparison of the silicate bodies region and the estimated tholins region show that Titan tholins are likely to have significantly higher values of both Σ_s and Σ_a.

Simulation Structure

Our simulations consist of a simple "bubble world" geometry with half ground material and half atmosphere material inside of a large sphere, a DT-neutron point source is then positioned 100 cm above the ground material surface, and a mass-transparent particle counting surface is placed at 50 cm above the ground material surface (Figure 3.2). These counting surface and source locations can be changed as needed. The tally card is defined using our counting surface ($F2 : n$ surface flux tally type) to track the energy ($E2$ tally type) and time ($F2QTD$ tally type) of neutrons crossing the counting surface. There are no detector or PNG housing materials present in our primary models, however we do present example cases with ^{3}He and CLYC neutron detectors ($F4 : n$ cell flux tally type) in our discussion; these detectors are located a horizontal distance of $\sim$75 cm from the PNG point source.

3.3.2 Model Variations

Initially, we inferred the base composition of Titan's surface material to be a dune-like mixture of methane water-ice ($4CH_4$ $23H_2O$), ammonia water-ice (xN_3H xH_2O), and tholin hydrocarbons (e.g. C_6H_6 and C_3HN) based on studies from (Cable *et al.*, 2012), various hypotheses, and studies of Huygens probe data (Zarnecki *et al.*, 2005; Niemann *et al.*, 2005, 2010; Lorenz, 2006; Soderblom *et al.*, 2007; McCord *et al.*, 2008; Aharonson *et al.*, 2014; Barnes *et al.*, 2008, 2015; Hayes, 2016). Previous studies have been published suggesting that the small amount of O present in Titan's atmosphere is the result of external sources (Hörst *et al.*, 2008). This information has led to the assumption that Titan is likely a low-O world (Rodriguez *et al.*, 2022), such that O-rich areas are likely indicative of water-ice crustal material (Barnes *et al.*, 2021).

Tholins. We used values for cold plasma ($\rho = 1.4$ g/cc, C/H = 3.5, combined mix-
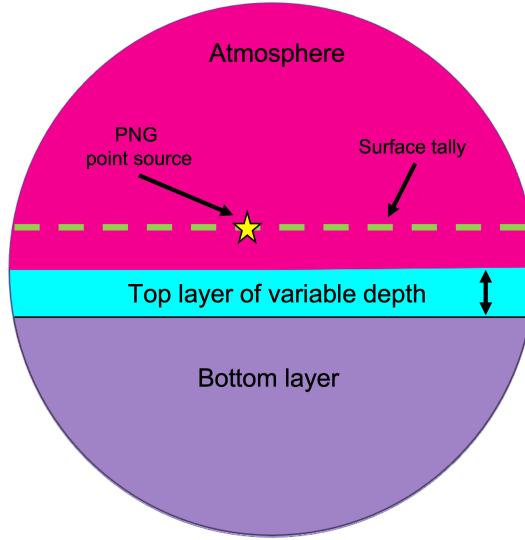
Figure 3.2: MCNP simulation model geometry of the Titan "bubble world". The top magenta pink layer is the atmosphere with a fixed density of 0.00539 g/cc unless otherwise specified. The dashed green line is the neutron flux surface tally. The gold star in the center is the location of the PNG source. The middle blue layer is optional and allows for a varied or fixed top surface layer composition and total deposit depth. The bottom purple layer can be input into the model based on the desired composition and burial depth. All geometries can be varied based on user input, all temperatures in the environment are set at 90K.

ture of HCN, NH$_3$, C$_5$H$_5$N, C$_4$H$_4$NH, HC$_2$N$_3$), hot plasma ($\rho = 1.4$ g/cc, C/H $= 6.5$, combined mixture of HCN, HC$_3$N, C$_2$H$_2$, CH$_4$, C$_2$H$_6$, C$_3$H$_6$, C$_2$H$_4$), and UV radiation ($\rho = 0.8$ g/cc, C/H $= 16.2$, combined mixture of HCN, HC$_3$N, C$_2$H$_2$, N2) generated Titan tholins based on laboratory experiments reviewed in Cable *et al.* (2012) with densities estimated from (Lethuillier *et al.*, 2018; Hörst and Tolbert, 2013). Unless otherwise stated, we used a ground density of 1.4 g/cc, an environmental temperature of 90K, and an atmospheric density of 0.00539 g/cc throughout our models. We expanded the composition parameter space of our simulations by expanding the

possible weight fractions of N, C, and H from 0 to 80 wt%, with O varied from 0 to 5 wt%. Figure 3.1 shows the total parameter space of compositions used in our studies plotted as neutron scattering and absorption cross sections. Table 3.1 and Table 3.2 show the grid sets of compositions and pure molecules, respectively, that were used in our simulations.

Pulse widths. An initial pulse width test was done using three pulse widths (3 μs, 50 μs, and 200 μs) in order to determine the most useful pulse width for studying neutrons in a Titan-like environment. Note that gamma rays have been previously studied on silicate-dominant bodies using longer pulse widths Parsons *et al.* (2011). Thermal neutrons are defined in our simulation as neutrons with energy <0.3 eV, this is based on Cd shielding and not on the actual energy of a thermal neutron on Titan ($\sim$0.008 eV). The temperature on a planetary body dictates the thermal neutron energy in accordance to the Maxwell-Boltzmann distribution (E = kT), such that if a planetary body is very cold (i.e. cryogenic, 94 K) the temporal response (time-of-flight) of neutrons to the detector will be slower than a warmer planetary body (e.g. Earth, 293 K). We define the thermal neutron absorption and scattering cross-sections used throughout this paper as taken at 0.025 eV (i.e. Earth temperature).

Exposed ice, ammonia, liquid methane and other molecules. Titan is thought to have cryovolcanism, such that water-ice from Titan's crust may be deposited onto the surface due to eruption. Seas and lakes made primarily of liquid methane are also thought to be present on Titan's surface. Additionally, exposed crustal material from ejecta blankets due to meteoroid bombardment may cause layering of frozen or liquid water to be present (Artemieva and Lunine, 2003). Table 3.2 shows the details of pure molecules used in our studies broken down into elemental composition, as well as our generalized compositions for Hot, Cold, and UV Titan tholins (Cable *et al.*, 2012). In addition to pure molecules, we also increased the wt%s of H, O, and combined H_2O

wt% H	wt% C	wt% N	wt% O	Σ_S (cm^2/g)	Σ_a (cm^2/g)	C/H ratio	C/N ratio	H/N ratio
0	85	15	0	0.32	0.0124	N/A	5.67	0.00
0	15	85	0	0.46	0.0696	N/A	0.18	0.00
5	80	15	0	2.75	0.0223	16.00	5.33	0.33
5	60	30	5	2.77	0.0346	12.00	2.00	0.17
10	5	85	0	5.33	0.0894	0.50	0.06	0.12
10	75	15	0	5.18	0.0323	7.50	5.00	0.67
15	80	5	0	7.60	0.0340	5.33	16.00	3.00
15	60	25	0	7.64	0.0504	4.00	2.40	0.60
15	50	35	0	7.66	0.0585	3.33	1.43	0.43
15	30	55	0	7.71	0.0749	2.00	0.55	0.27
20	50	25	5	10.07	0.0603	2.50	2.00	0.80
20	5	75	0	10.19	0.1011	0.25	0.07	0.27
25	70	5	0	12.47	0.0539	2.80	14.00	5.00
30	5	65	0	15.04	0.1128	0.17	0.08	0.46
35	60	5	0	17.34	0.0737	1.71	12.00	7.00
35	40	20	5	17.37	0.0860	1.14	2.00	1.75
40	5	55	0	19.89	0.1245	0.13	0.09	0.73
45	50	5	0	22.21	0.0936	1.11	10.00	9.00
50	30	15	5	24.67	0.1117	0.60	2.00	3.33
50	5	45	0	24.74	0.1360	0.10	0.11	1.11
55	40	5	0	27.09	0.1134	0.73	8.00	11.00
60	5	35	0	29.59	0.1479	0.08	0.14	1.71
65	30	5	0	31.96	0.1333	0.46	6.00	13.00
65	20	10	5	31.96	0.1374	0.31	2.00	6.50
80	5	15	0	39.29	0.1712	0.06	0.33	5.33

Table 3.1: Titan ground material grid set of elemental compositions (25 total) used in simulations for this paper. The table is sorted based on the wt% of H present. Additional elements added to these compositions (S, Na, K, Mg, B) were added as a direct wt% forcing a re-normalization of the total composition for input into MCNP. Our composition normalization process is described in Section 3.3.3. This grid set represents possible compositions that lay in between pure molecule end-members hypothesized to exist on Titan.

Material	wt% H	wt% C	wt% N	wt% O	Σ_s (cm^2/g)	Σ_a (cm^2/g)	C/H ratio	C/N ratio	H/N ratio
CO_2	0.00	27.29	0.00	72.71	0.19	0.0001	N/A	N/A	N/A
HC_3N	1.97	70.50	27.52	0.00	1.30	0.0266	35.75	2.56	0.07
UV tholin	3.26	52.91	43.84	0.00	1.96	0.0424	16.25	1.21	0.07
HCN	3.72	44.34	51.93	0.00	2.20	0.0500	11.92	0.85	0.07
$C_{16}H_{10}$	4.98	95.02	0.00	0.00	2.71	0.0101	19.07	N/A	N/A
$C_3H_6N_6$	4.78	28.49	66.73	0.00	2.75	0.0641	5.96	0.43	0.07
C_2H_2	7.74	92.26	0.00	0.00	4.05	0.0155	11.92	N/A	N/A
Cold tholin	10.49	37.06	52.46	0.00	5.50	0.0638	3.53	0.71	0.20
H_2O	11.19	0.00	0.00	88.81	5.62	0.0222	0.00	N/A	N/A
Hot tholin	10.92	70.74	18.33	0.00	5.64	0.0368	6.48	3.86	0.60
CH_2	14.37	85.63	0.00	0.00	7.28	0.0287	5.96	N/A	N/A
$C_{10}H_{22}$	15.58	84.42	0.00	0.00	7.87	0.0311	5.42	N/A	N/A
NH_3	17.69	0.00	82.31	0.00	9.08	0.1025	0.00	0.00	0.21
C_2H_6	20.11	79.89	0.00	0.00	10.08	0.0401	3.97	N/A	N/A
CH_4	25.13	74.87	0.00	0.00	12.52	0.0501	2.98	N/A	N/A

Table 3.2: Titan and Europa molecules broken down into elemental compositions, these compositions are used in simulations throughout this study. The table is sorted based on Σ_s from low to high. Additional elements added to these compositions (S, Na, K, Mg, B) were added as a direct wt% forcing a re-normalization of the total composition for input into MCNP. Our composition normalization process is described in Section 3.3.3. Hot, Cold, and UV tholin species were inferred based on C/N and C/H ratios and molecule descriptions reported in Cable *et al.* (2012).

in our composition card for 1-layer models. H was varied from 0 - 80 wt% in steps of 10 wt%, H_2O was varied from 0 - 80 wt% in steps of 10 wt%, and O was modeled from 0 - 45 wt% in steps of 5 wt%.

Titan's atmosphere. For our studies of Titan's atmosphere, we wanted to determine the possible effect of the atmosphere on the neutron environment. We modeled for comparison 1) a fully atmospheric Titan world and a half atmospheric, half ground material world; 2) a half atmospheric, half ground material world with the DT source and tally surface moving away from the ground material (50 cm to 500 cm); 3) a half

atmospheric, half ground material world with the DT source stationary at 100 cm and only the tally surface moving away from the ground material (50 cm to 500 cm); and 4) a half atmospheric, half ground material world with a changing atmospheric density from 0.003 g/cc to 0.01 g/cc.

Tholin densities. We tested the effects of density changes in the ground materials by modeling the subset grid as a 1-layer model with densities of 0.8 g/cc, 1.4 g/cc, and 2.6 g/cc. Additionally, we modeled a constant material composition (Hot tholin, Table 3.2) with a ground density from 0.8 g/cc to 2.8 g/cc by steps of 2 g/cc. Our tholin density values are within the ranges described by Hörst and Tolbert (2013); Lethuillier *et al.* (2018).

Nutrients. S, Na, K, Mg, and B are all nutrients important to the development of life as we know it on Earth. We modeled S, Na, and Mg from 0.01 to 4 $wt\%$ on a log-scale step, with K and B from 0.01 to 1000 ppm on a log-scale step for 1-layer models using four different base compositions from Table 3.1 based on a range of Σ_a and Σ_s values.

Layered deposits. We studied the possibility of changes in a subsurface layer by creating 2-layer model grids: 1) We held the top layer of material constant (0 wt% O, 10 wt% H, 35 wt% N, 55 wt% C, $\Sigma_a = 6.49$ cm^2/g, $\Sigma_S = 526.95$ cm^2/g, C/H = 5.5, consistent with Hot Tholins), and varied the composition of the lower, buried layer. We used a subset of the composition grid in Table 3.1 – every other composition, starting with the first line for a total of 12 compositions – and then varied the top layer depth from 2 cm to 20 cm in steps of 2 cm, for a total of 120 simulation files. 2) We performed several 2-layer combinations using Titan tholin types as well as pure molecules hypothesized to be present on Titan, these included pure water-ice (H_2O), ammonia (NH_3), methane (CH_4), potassium cyanide (KCN), and the Hot Tholin composition, all modeled at 2cm and 4cm depths for materials listed in Table 3.2.

3.3.3 Composition Renormalization

When a $wt\%$ is added to an MCNP composition card, the FORTRAN back-end of MCNP automatically re-normalizes the composition such that it equals 100 $wt\%$. In order to have better control of the normalization process and overall elemental $wt\%$'s we introduced our own normalization into the python script that generates our MCNP files; this no longer requires MCNP to re-normalize the composition card. As the $wt\%$ of an element ($\Delta element$) is changed or added into the study, we take the total sum of the current elemental composition card and normalize it to 100 $wt\% - \Delta element\ wt\%$. This allows us to control the exact elemental $wt\%$ of that specific added element. In the case of added molecules (e.g. H_2O) we compute the composition card similarly as 100 $wt\% - \Delta molecule\ wt\%$.

3.4 Analysis Methods

All MCNP input simulation files and associated run files were generated with scripts developed in Python 2.7 using numpy, scipy, and matplotlib libraries (Harris et al., 2020; Virtanen et al., 2020; Hunter, 2007). All simulation result files were then analyzed using Python 2.7, such that a full pipeline system was created for MCNP simulation studies using neutron spectrometers on planetary bodies.

3.4.1 Neutron Integrated Counts

Neutron instruments on board planetary science missions have been used to determine the neutron energy flux of a surface, comparing the time-integrated number of counts for total energy, epithermal energy, and thermal energy neutrons, with the exception of the DAN instrument on MSL Curiosity (Lawrence et al., 2013; Prettyman et al., 2019b; Hardgrove et al., 2011; Litvak et al., 2016). We summed the

total number of neutrons for each energy threshold (total, epithermal, thermal) and reported these values in our results. The uncertainty ($\sigma_{observed}$) of the total number of observed counts ($N_{observed}$) is determined based on Poisson statistics ($\sqrt{N_{observed}}$ = $\sigma_{observed}$), assuming the accumulated counts are Poisson random variates (Knoll, 2010).

3.4.2   Temporal Neutron Measurements

Neutron die-away experiments measure the flux of neutrons along with their arrival time (time resolved data) to the detector instrument after the PNG pulse. The only instrument to demonstrate this method on another planetary surface is the DAN instrument on MSL Curiosity (Litvak *et al.*, 2016). We divide the neutron flux data into 64 lognormal time bins, this adheres to the same methods used by the DAN science team which provides a direct comparison of our simulations to a current mission instrument (Mitrofanov *et al.*, 2012; Litvak *et al.*, 2008). The shape of the neutron die-away curve can provide information about the surface composition, this allows further analysis to differentiate changes in composition for neutron data sets that have degenerate cases of integrated neutron count rates. The flux weighted time average (FWTA) can be used as a primary metric to qualitatively describe the shape of the neutron die-away curve for these studies (Hardgrove *et al.*, 2011). The FWTA is calculated as follows:

$$FWTA = \frac{\sum_{m=start}^{M} t_m f_m}{\sum_{m=start}^{M} f_m} \tag{3.2}$$

Where t_m represents the time associated with the mth time bin after the pulse, and f_m represents the number of thermal neutrons counted in the mth time bin. The FWTA is calculated for thermal neutrons only between bins 0 through 40, these correspond with times from 0 μs to 900 μs on the full time-scale.

In order to further quantify changes in the neutron die-away curve shape between

measurements with similar integrated neutron counts and arrival times (and therefore similar FWTAs), we applied the statistical metrics of kurtosis and skew. Kurtosis is the measure of "tailedness" of a probability distribution, the higher the kurtosis value, the heavier the tail is on the distribution. Skew is the measure of the asymmetry or distortion of a probability distribution that deviates from a normal probability distribution about its mean, with negative values skewing to the left of the mean and positive values skewing to the right of the mean. Note that kurtosis and skew are only valid when used with unimodal continuous distributions, such that these may only be used to describe the shape of the neutron die-away curve within the after-pulse region and specific to these simulation studies where walls or other large objects are not in the vicinity (additional objects may cause multimodal distributions). We employed both of these metrics in order to describe the shape of the neutron die-away curve, specifically using the standard definition of kurtosis (κ_1) and the adjusted Fisher-Pearson skewness coefficient (G_1). For neutron counts per bin, x_i, we define κ_1 as:

$$\kappa_1 = \frac{\sum_{m=14}^{M}(x_i - \bar{x})/M}{S^4} \tag{3.3}$$

Where $\bar{x}$ is the mean, S is the standard deviation, and M is the number of data points (number bins for our studies). We define skew using the sample-size adjusted Fisher-Pearson coefficient of skewness, this requires a two step computation as follows, first defining the Fisher-Pearson skewness coefficient, g_1:

$$g_1 = \frac{\sum_{m=14}^{M}(x_i - \bar{x})/M}{S^3} \tag{3.4}$$

Where $\bar{x}$, S, and M are the sample mean, the sample standard deviation, and the sample size (number of bins), respectively. The adjusted Fisher-Pearson skewness coefficient, G_1 is then computed as follows to account for sample size:

$$G_1 = \frac{\sqrt{M(M-1)}}{M-2} * g_1. \tag{3.5}$$

The uncertainty in neutron die-away measurements follows the same convention as integrated neutron count uncertainties. The uncertainty ($\sigma_{observed}$) of the total number of observed counts ($N_{observed}$) *per time bin* is determined based on Poisson statistics ($\sqrt{N_{observed}} = \sigma_{observed}$) (Knoll, 2010).

3.5 Results

3.5.1 Neutron Pulse Width

Three DT (14.1 MeV) neutron generator pulse widths (3 μs, 50 μs, and 200 μs) were briefly studied to determine which pulse width is likely the best candidate for further exploration of temporal neutron measurements, while still being a good option for gamma rays. The result of these simulation studies is shown in Figure 3.3 for thermal neutrons only. Note that gamma-ray measurements typically benefit from longer pulse widths (Bodnarik *et al.*, 2013), hence why longer pulse widths were investigated for this initial study. The total width of the thermal neutron peak is fully returned for all three PNG pulses, though the thermal neutron peak time (TPT, calculated using thermal neutrons only) is shifted to later time bins for longer pulse widths. In order to preserve a balance between gamma-ray and neutron measurements we chose to continue simulation investigations using 50 μs PNG pulse widths to allow for longer irradiation times in favor of gamma rays, using lessons learned from silicate bodies (Bodnarik *et al.*, 2013).

3.5.2 Atmospheric Studies

We studied the effects of Titan's atmospheric density on the neutron environment. We modeled a fully atmospheric Titan world (with density = 0.005 g/cc) and a 1/2 atmospheric, 1/2 dune world and observed effects on the resulting neutron spectra
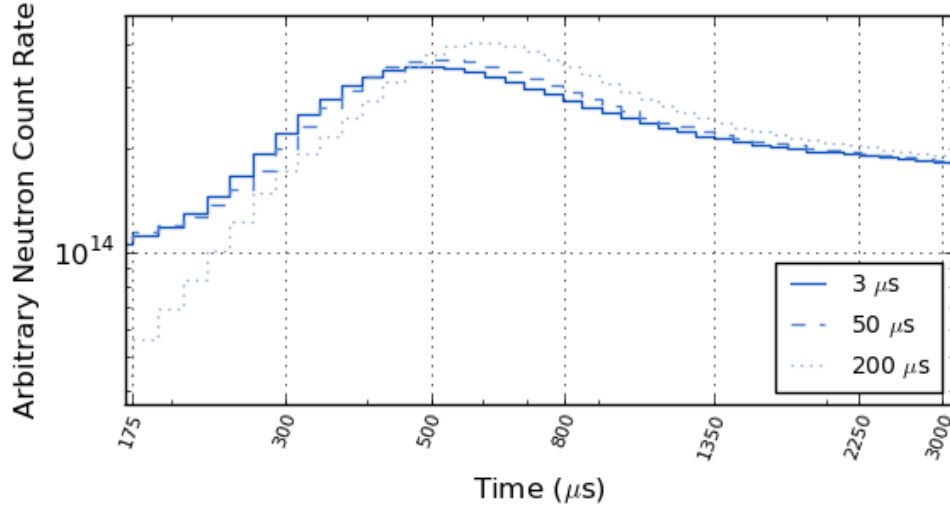
Figure 3.3: Thermal energy neutron die-away curves encompassing only the thermal neutron die-away region for PNG pulses of 3 μs (solid), 50 μs (dashed), and 200 μs (dotted). The time of flight of thermal neutrons (at a Titan temperature of 94 K) from the surface of the body to the tally surface at 50 cm above the ground is $\sim$ 410 μs, this correlates well with the thermal neutron peak times shown above. Our studies use the 50 μs pulse width to allow for slightly longer irradiation for gamma-rays, though any of these pulse widths will work for detecting changes in die-away.

as the density of the atmosphere increased for all 1/2 dune worlds. The contribution from the atmosphere by itself is $\sim$3 orders of magnitude lower than the count rate for the 1/2 dune, 1/2 atmospheric world, regardless of atmospheric density used in the half dune world; relative uncertainty in counts for simulation results are $< 5\%$.

We performed a second study of atmosphere to determine if there are significant changes in the amount of neutron interactions in areas of different atmospheric densities, resulting in a change to the measured count rate. We created a fully atmospheric world, with half of the sphere containing one density (kept constant at 0.005 g/cc) and the other half of the sphere containing a different density (0.5, 0.05, and 0.005

g/cc). For areas of low density (0.005 g/cc) the the order of magnitude (2 - 3 orders) in neutron count rate is significantly lower than that of high density areas (0.5 and 0.05 g/cc).

In our studies of the effects of the Titan environment, we simulated changes in the distances from the tally plane (leaving the PNG source at 100cm from the ground surface) to the ground surface, as well as the distance from the PNG source and tally plane to the ground surface (Figure 3.4). As the distance from the tally to the ground surface increases, the initial neutron pulse lowers in amplitude, and the thermal neutron peak appears in later time bins and is both broader and lower in magnitude. This result is a simple time-of-flight effect, though some interactions with the atmosphere happen in time between the pulse and the thermal neutron peak.

3.5.3   1-layer Modeling with Composition Changes

We performed studies for determining the limits and utility for the neutron die-away technique with a DT pulsed neutron generator on Titan. Figure 3.5 shows a sub-set of the results of our full grid neutron die-away study of MCNP simulations spanning scattering and absorption cross sections throughout the possible ranges on Titan. As Σ_a increases, the magnitude of the neutron die-away curve also increases. Likewise, increasing Σ_s also correlates with an increase in magnitude of the neutron die-away curve.
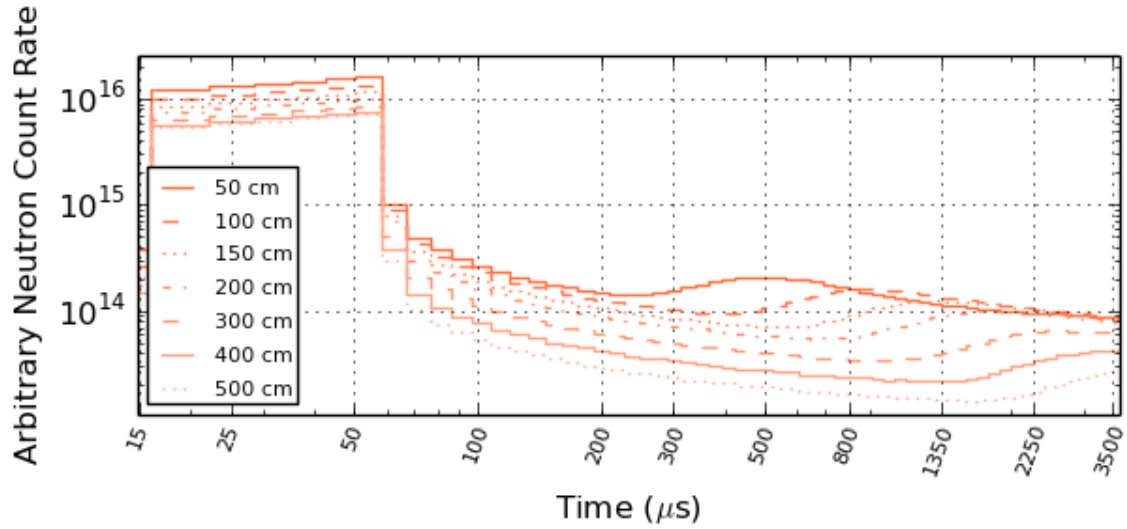
Figure 3.4: Changes in distance affect the thermal neutron return time according to time-of-flight mechanics. Results from MCNP neutron die-away simulations showing the Tally surface (detector position) and PNG source increasing in vertical distance away from the model planetary surface. The count rate in the pulse decreases as a function of distance, which is expected due to particle transport theory. The count rate in the initial portion (58 - 145 μs) of the neutron die-away region is increased in comparison to the pulse due to neutrons interacting with more the atmospheric material before reaching the surface. Additionally, the thermal neutron peak position shifts further in time and broadens.
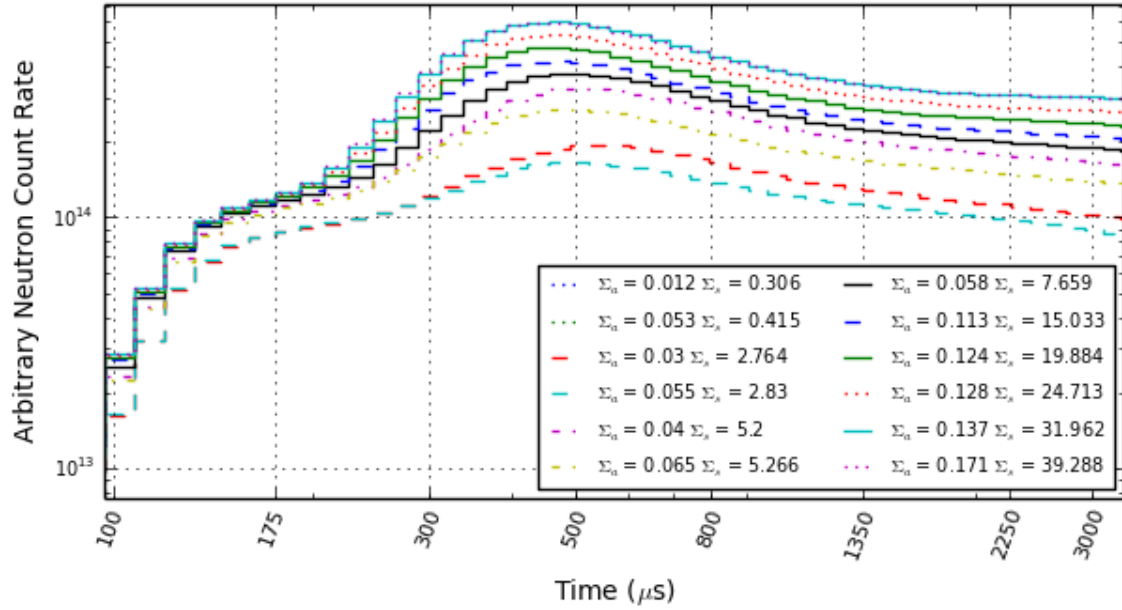
Figure 3.5: Neutron die-away simulations (thermal energies only) of a sub-set grid of possible Titan materials with Σ_a ranging from 0.01 to 0.2 cm^2/g and Σ_s ranging from 0.3 to 40 cm^2/g. As Σ_a and Σ_s increase, the total magnitude of the counts tends to increase. As the value of Σ_s becomes very large ($\gtrsim$ 25 cm^2/g) the neutron die-away peak begins to converge to the same magnitude, peak arrival time, and shape. However, for lower values of Σ_s there are still changes in shape, magnitude, and peak arrival time.

C, H, N, O

Figure 3.6 shows the results of varying the elemental wt % for C, H, N, and O. We represented the change in C, N, and O, as the line color intensity, with less intense colors signifying high overall scattering cross section materials. As the amount of H stays constant, and the values of C and N are allowed to vary, the shape of the neutron die-away curve changes subtly for H values < 25 wt%. Note the range of Σ_a and Σ_s values are dramatic compared to previous studies on Earth and Mars (Kerner *et al.*, 2020; Heffern *et al.*, 2021). As the amount of H increases in the 1-layer model, the thermal neutron peak increases and shifts towards earlier time bins, this is consistent with previous studies by Hardgrove *et al.* (2011); Kerner *et al.* (2020).

We plotted the total epithermal neutron counts versus thermal neutron counts for the 1-layer grid models, distinguishing between C, H, N, and O in Figure 3.7 in increasing wt% abundances. Figure 3.7 shows that as the amount of H increases, the total number of epithermal neutron counts (N_{Epi}) decreases as the number of thermal counts (N_{Th}) increases. Additionally, as the y and x-intercepts of N_{Epi} vs. N_{Th} increase, the wt% N decreases and the wt% C and O increase.

To determine trends in neutron count rate and die-away curve shape for C, H, N, and O, the results of our 1-layer model grid were plotted as follows: FWTA vs. $\%N_{Th}$, Figure 3.8; κ_1 vs. $\%N_{Th}$, Figure 3.9; and G_1 vs. $\%N_{Th}$, Figure 3.10. The FWTA plot shows that H has a large range of possible FWTA values at low wt%'s, whereas at high wt%'s (> 50) there is less than a 1% difference ($\sim$3 μs) between FWTA values within our grid range. The κ_1 plot shows a result similar to FWTA, as the value of H increases, the κ_1 value range decreases ($\sim$4% difference at 50 wt% H) within our grid range. Finally, the G_1 plot shows that as the value of H increases, the G_1 value range also decreases ($\sim$3% difference at 50 wt% H). In contrast, N_{Epi}

shows a difference of $\sim 0.2\%$ and N_{Th} a difference of $\sim 7.7\%$ for the same data points. These results point to an advantage for constraining compositions by using temporal neutron measurements as opposed to epithermal integrated neutron counts.

Tables 3.3 - 3.7 compare several examples from our 1-layer model grid for N_{Th}, N_{Epi}, FWTA, κ_1, G_1, and other metrics using percent differences. The total neutron counts (N_{Tot}), N_{Epi}, and N_{Th} listed in these tables are full time integrated and reported as a raw number of counts, this is equivalent to a 13 hour measurement with a DT PNG (10E8 nps in 4π) at 5% duty factor, 50 μs pulse width, with a 2" CLYC crystal (comparable to two 1" diameter $\times$ 9" long 20 atm ^{3}He tubes). The thermal neutron integrated count rate has the highest percent difference between measurements making it an excellent metric for 1-layer scenarios. The κ_1 value commonly has the next highest % difference value between measurements, making it favorable over N_{Epi} as an indicator of composition change. G_1 and FWTA show less % difference between compared measurements and are comparable to the % differences for N_{Epi}. However, as the amount of O increases, the % difference for both κ_1 and G_1 values increase, this is consistent with Figures 3.9 and 3.10.
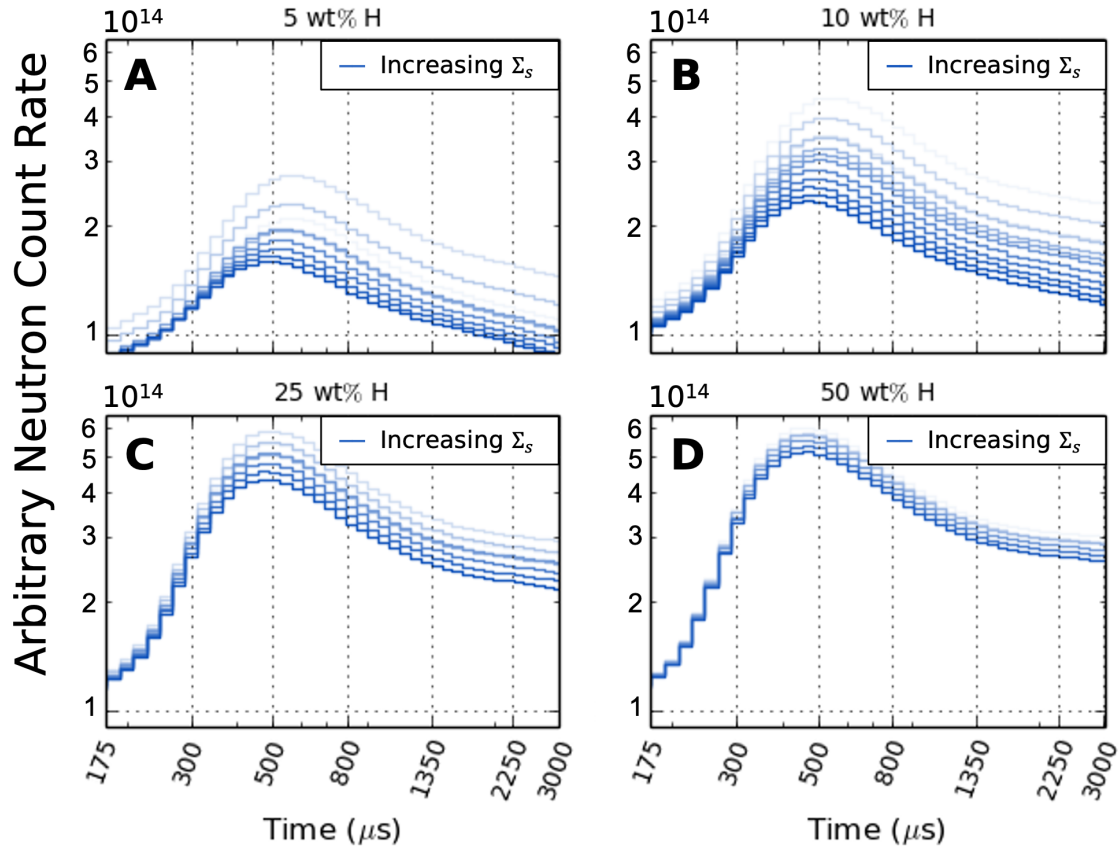
Figure 3.6: Changes in composition can be informed by changes in neutron die-away curve magnitude and shape. 1-layer, heterogeneous thermal neutron die-away curves showing the effect of wt% H with increase in Σ_s represented by blue line increasing intensities, with the lightest colors representing the higher values of Σ_s. The subset grid of compositions from Table 3.1 was modeled with a constant wt% H for each subplot. A and B) For 5 and 10 wt% H held constant, respectively, the magnitude and shape of the neutron die-away curve changes with the underlying change in the total macroscopic scattering cross section. C) For 25 wt% H held constant the shape of the neutron die-away curve is no longer changing, though the magnitude still increases with increasing Σ_s. D) For 50 wt% H and above held constant, the shape and magnitude of the neutron die-away curve begin to converge though changes in the remaining 50 wt% of material are still detectable.
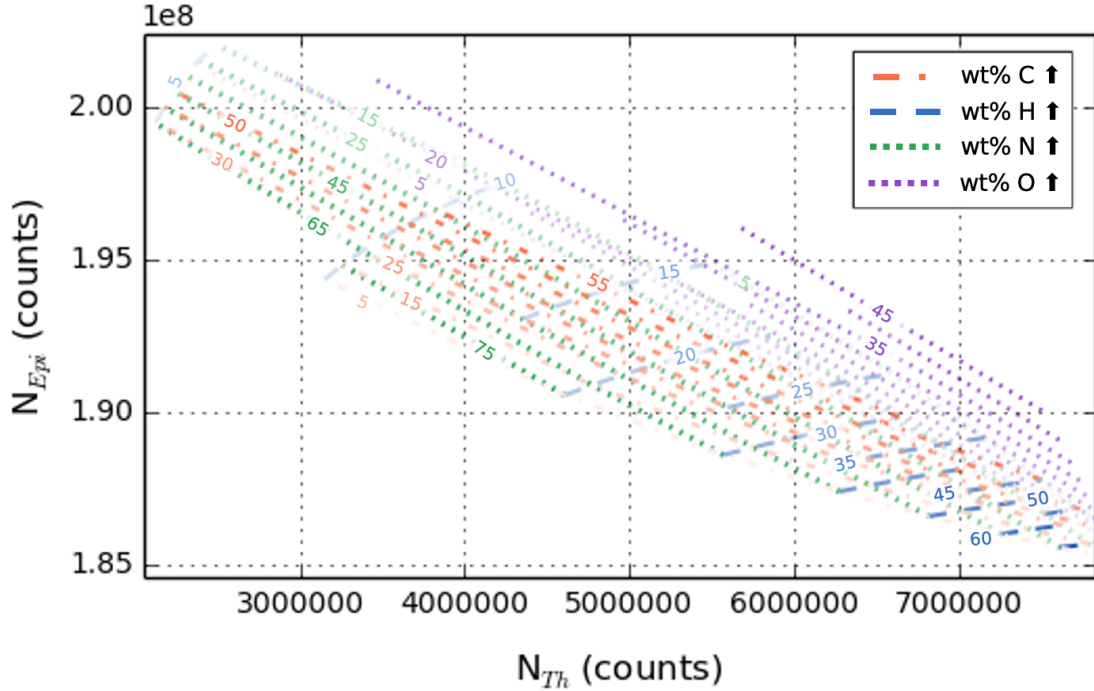
Figure 3.7: Changes in composition can be informed by total neutron count rates. 1-layer, heterogeneous neutron die-away curves for epithermal neutron counts (N_{Epi}) versus thermal neutron counts (N_{Th}), using the grid of compositions from Table 3.1. These simulations were done using an F2 surface flux tally with NPS = 2.5E9 initial particles from the neutron generator, such that the integrated (energy and time) number of neutrons that reach the tally surface is $\lesssim$ 10% compared to the number of input particles. All lines on the plot represent elemental wt%s with increasing amounts denoted by darker shades and decreasing amounts denoted by lighter shades, the exact wt% of each element is labeled in text on a select number of lines. The orange dash-dot lines represent wt% C, the blue dashed lines wt% H, the green dotted lines wt% N, and the purple dotted lines wt% O.
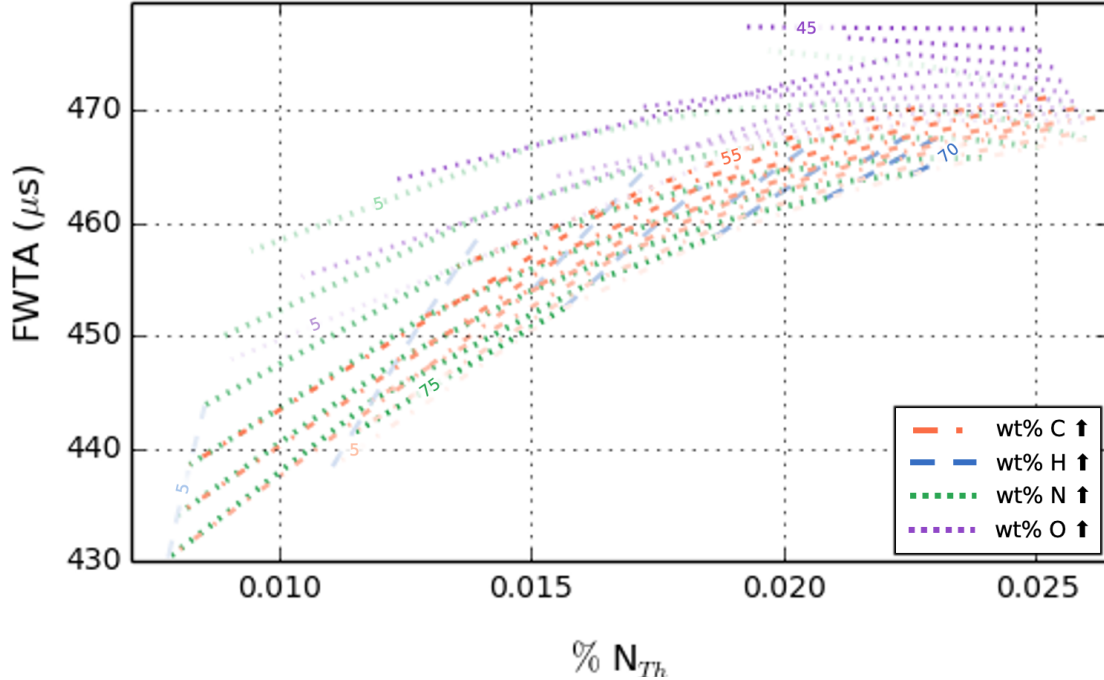
Figure 3.8: Changes in composition can be informed by neutron die-away curve shape via FWTA and thermal neutron count rate. 1-layer, heterogeneous neutron die-away curves for flux weighted time average (FWTA, μs) versus % thermal neutron counts (% N_{Th}), using the grid of compositions from Table 3.1. All lines on the plot represent elemental wt%s with increasing amounts denoted by darker shades and decreasing amounts denoted by lighter shades, the exact wt% of each element is labeled in text on a select number of lines. The orange dash-dot lines represent wt% C, the blue dashed lines wt% H, the green dotted lines wt% N, and the purple dotted lines wt% O. (% N_{Th}) is calculated per data point as $100\% \times N_{Th}/N_{Total}$. As the value of H increases (> 50 wt%), there is less than a 1% difference ($\sim$3 μs) between FWTA values within our grid range.
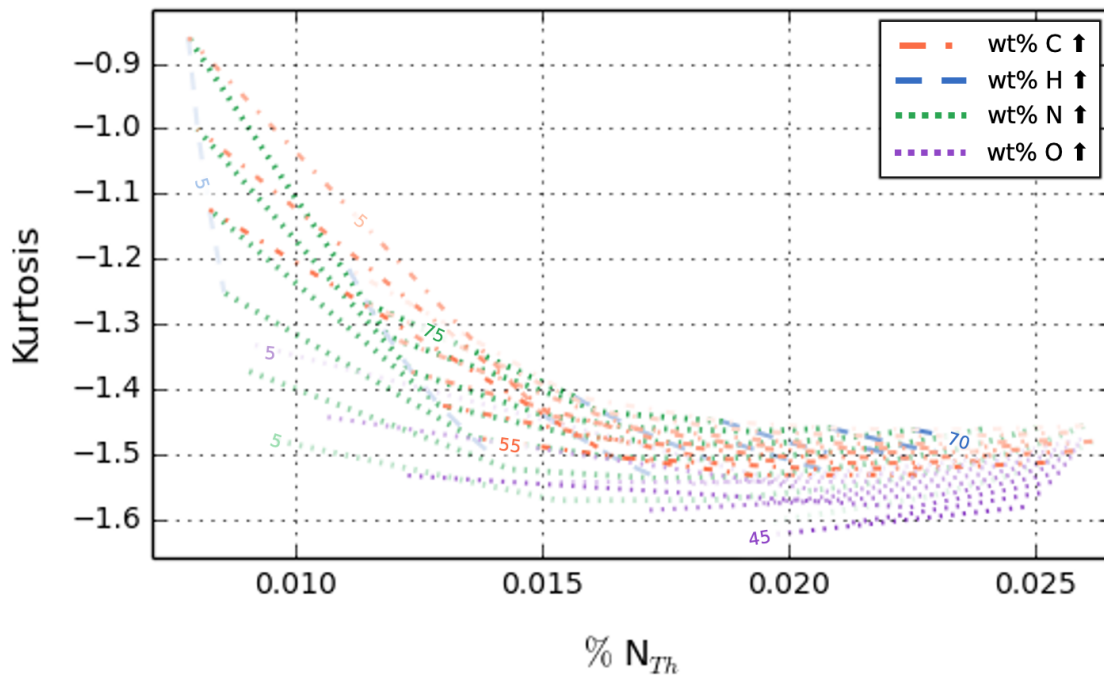
Figure 3.9: Changes in composition can be informed by neutron die-away curve shape via kurtosis (κ_1) and thermal neutron count rate. 1-layer, heterogeneous neutron die-away curves for κ_1 versus % N_{Th}, using the grid of compositions from Table 3.1. All lines on the plot represent elemental wt%s with increasing amounts denoted by darker shades and decreasing amounts denoted by lighter shades, the exact wt% of each element is labeled in text on a select number of lines. The orange dash-dot lines represent wt% C, the blue dashed lines wt% H, the green dotted lines wt% N, and the purple dotted lines wt% O. (% N_{Th}) is calculated per data point as $100\% \times N_{Th}/N_{Total}$. As the value of H increases, the κ_1 value range decreases ($\sim$4% difference at 50 wt% H) within our grid range.

Figure 3.10: Changes in composition can be informed by neutron die-away curve shape via skew (G_1) and thermal neutron count rate. 1-layer, heterogeneous neutron die-away curves for G_1 versus % N_{Th}, using the grid of compositions from Table 3.1. All lines on the plot represent elemental wt%s with increasing amounts denoted by darker shades and decreasing amounts denoted by lighter shades, the exact wt% of each element is labeled in text on a select number of lines. The orange dash-dot lines represent wt% C, the blue dashed lines wt% H, the green dotted lines wt% N, and the purple dotted lines wt% O. (% N_{Th}) is calculated per data point as $100\% \times N_{Th}/N_{Total}$. As the value of H increases, the skew value range decreases ($\sim$3% difference at 50 wt% H) within our grid range.

Metric	κ_1	G_1	**FWTA** (μs)	Σ_a (**cm^2/g**)	Σ_S (**cm^2/g**)	N_{Tot}	N_{Epi}	N_{Th}	**N%**	**C%**	**H%**	**O%**
C/H = 2.8	-1.565	-0.271	473.97	0.05	12.47	1.96E8	1.91E8	4.47E6	5.00	70.00	25.00	0.00
C/H = 1.7	-1.535	-0.305	404.44	0.07	17.34	1.94E8	1.89E8	4.72E6	5.00	60.00	35.00	0.00
% **Difference**	1.935	11.806	15.83	33.33	32.67	1.03	1.05	5.44	0.00	15.38	33.33	0.00

Table 3.3: Comparison of temporal neutron simulation result metrics for two materials taken from Table 3.1. κ_1, G_1, and FWTA describe the shape of the thermal neutron return peak as compared to a normal distribution, these metrics were calculated using thermal neutrons only. The total epithermal neutron counts (N_{Epi}) and thermal neutron counts (N_{Th}) are full time integrated and reported as a raw number of counts, this is equivalent to a 13 hour measurement with a DT PNG at 5% duty factor, 50μs pulse width, with a 2" CLYC crystal. The first material has a higher wt% C and lower wt% H than the second material, with 5 wt% N and 0 wt% O for both materials.

Metric	κ_1	G_1	**FWTA** (μs)	Σ_a (**cm^2/g**)	Σ_S (**cm^2/g**)	N_{Tot}	N_{Epi}	N_{Th}	**N%**	**C%**	**H%**	**O%**
H/N = 0.73	-1.460	-0.363	462.23	0.12	19.88	1.91E8	1.87E8	3.99E6	55.00	5.00	40.00	0.00
H/N = 0.46	-1.449	-0.359	458.80	0.11	15.03	1.92E8	1.89E8	3.59E6	65.00	5.00	30.00	0.00
% **Difference**	0.756	1.108	0.74	8.70	27.79	0.52	1.06	10.55	16.67	0.00	28.57	0.00

Table 3.4: Comparison of temporal neutron simulation result metrics for two materials taken from Table 3.1. The first material has a higher wt% H and lower wt% N than the second material, with 5 wt% C and 0 wt% O for both materials.

Metric	κ_1	G_1	FWTA (μs)	Σ_a (cm^2/g)	Σ_S (cm^2/g)	N_{Tot}	N_{Epi}	N_{Th}	N%	C%	H%	O%
H/N = 2	-1.503	-0.334	468.51	0.10	19.81	1.93E8	1.88E8	4.51E6	20.00	40.00	40.00	0.00
H/N = 1.4	-1.505	-0.328	467.60	0.09	17.38	1.93E8	1.89E8	4.32E6	25.00	40.00	35.00	0.00
% Difference	0.13	1.81	0.19	10.53	13.07	0.00	0.53	4.30	22.22	0.00	13.33	0.00

Table 3.5: Comparison of temporal neutron simulation result metrics for two materials taken from Table 3.1. The first material has a higher wt% H and lower wt% N than the second material, with 40 wt% C and 0 wt% O for both materials.

Metric	κ_1	G_1	FWTA (μs)	Σ_a (cm^2/g)	Σ_S (cm^2/g)	N_{Tot}	N_{Epi}	N_{Th}	N%	C%	H%	O%
O/H = 0.25	-1.535	-0.284	467.19	0.06	10.07	1.96E8	1.92E8	3.83E6	25.00	50.00	20.00	5.00
O/H = 0	-1.532	-0.286	466.65	0.06	10.07	1.96E8	1.92E8	3.78E6	25.00	55.00	20.00	0.00
% Difference	0.20	0.70	0.12	0.00	0.00	0.00	0.00	1.31	0.00	9.52	0.00	200.00

Table 3.6: Comparison of temporal neutron simulation result metrics for two materials taken from Table 3.1. The first material has a higher wt% O and lower wt% C than the second material, with 25 wt% N and 20 wt% H for both materials.

Metric	κ_1	G_1	FWTA (μs)	Σ_a (cm^2/g)	Σ_S (cm^2/g)	N_{Tot}	N_{Epi}	N_{Th}	N%	C%	H%	O%
H/N = 2.5	-1.581	-0.259	477.22	0.06	12.43	1.95E8	1.90E8	4.83E6	10.00	20.00	25.00	45.00
H/N = 1.7	-1.561	-0.274	473.60	0.06	12.45	1.95E8	1.90E8	4.52E6	15.00	30.00	25.00	30.00
% Difference	1.27	5.63	0.76	0.00	0.16	0.00	0.00	6.63	40.00	40.00	0.00	40.00

Table 3.7: Comparison of temporal neutron simulation result metrics for two materials taken from Table 3.1. The first material has a higher wt% O, lower wt% C, and lower wt% N than the second material, with 25 wt% H for both materials.

Pure Materials

Pure materials, such as H_2O, CH_4, NH_3, and others were broken down into their elemental wt% compositions and then used in 1-layer simulation models as ground material, Table 3.2 gives a detailed list of these compositions. Note that these simulations represent possible end-members; the elemental composition of a planetary surface can be inferred based on GRNS, but these methods do not have the capability of directly measuring specific molecules. However, studying end-member cases allows us to look at the neutron response of composition changes (count rate, time shift, etc.) as a function of an idealized or pure composition. Die-away results of our study of pure materials are shown in Figure 3.11 for thermal neutron energies.

The data for each die-away curve is broken down into κ_1, G_1, FWTA, total time-integrated epithermal neutron counts (N_{Epi}) and thermal neutron counts (N_{Th}), and TPT in Table 3.8. Figure 3.7 shows the same N_{Epi} vs. N_{Th} data for all 1-layer grid models from Figure 3.12 with the addition of the "'pure molecule" end-member elemental compositions. We interpolate a line from the expected 11 wt% H to H_2O, as the O in the material increases, the H values for N_{Epi} and N_{Th} have a non-linear trend. End-member results for FWTA, G_1, and κ_1 are not shown, but our modeled grid result values lie within the bounds of expected end-members.
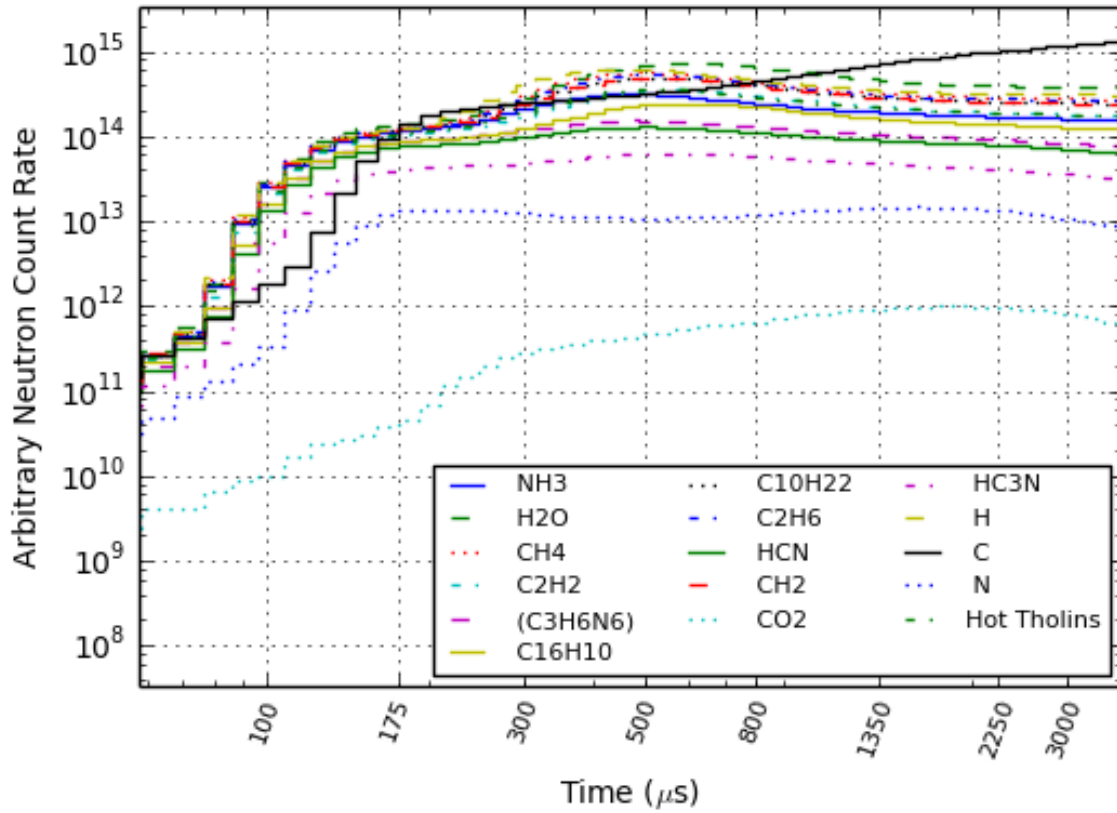
Figure 3.11: Thermal neutron die-away simulation results of elemental compositions representing pure materials. End-member compositions include H_2O (green, solid line), CH_4 (red, dotted line), and NH_3 (blue, solid line). Also included are pure elements such as N (blue, dotted line), H (yellow, dashed line), and C (black, solid line). The behavior of C is due to its high Σ_S value and low Σ_a, shown in Table 3.8 along with other pure materials.

Material	κ_1	G_1	FWTA (μs)	$\%N_{Epi}$	$\%N_{Th}$	TPT (μs)	Σ_a (cm^2/g)	Σ_s (cm^2/g)
CO_2	-1.276	0.016	533.792	99.996	0.004	1749.80	0.0001	0.19
C	-0.467	-0.365	493.588	96.747	3.253	3755.70	0.0002	0.28
N	5.416	-2.283	406.227	99.919	0.081	1537.50	0.0817	0.49
HC_3N	0.150	-0.901	428.718	99.677	0.323	561.78	0.0265	1.29
HCN	-0.636	-0.626	429.079	99.360	0.640	487.43	0.0498	2.20
$C_{16}H_{10}$	-1.606	-0.096	472.477	98.934	1.066	602.54	0.0101	2.70
$C_3H_6N_6$	-0.771	-0.578	428.615	99.244	0.756	453.56	0.0639	2.75
C_2H_2	-1.640	-0.130	477.357	98.509	1.491	561.78	0.0155	4.05
H_2O	-1.720	-0.046	505.616	96.997	3.003	561.78	0.0222	5.62
Hot Tholins	-1.570	-0.222	467.259	98.469	1.531	523.46	0.0368	5.64
CH_2	-1.622	-0.199	478.462	97.985	2.015	523.46	0.0287	7.28
$C_{10}H_{22}$	-1.617	-0.208	478.216	97.928	2.072	523.46	0.0311	7.87
NH_3	-1.378	-0.373	448.955	98.548	1.452	453.56	0.1022	9.07
C_2H_6	-1.596	-0.238	477.111	97.767	2.233	487.43	0.0401	10.07
CH_4	-1.575	-0.263	475.840	97.649	2.351	487.43	0.0501	12.52
H	-1.447	-0.400	467.964	97.280	2.720	421.71	0.1987	49.00

Table 3.8: Temporal neutron simulation result metrics for different pure materials shown in Figure 3.11, table is sorted by Σ_s. κ_1, G_1, and FWTA describe the shape of the thermal neutron return peak as compared to a normal distribution, these metrics were calculated using thermal neutrons only. The total epithermal neutron counts (N_{Epi}) and thermal neutron counts (N_{Th}) are full time integrated and reported as a percentage of the total neutrons such that $N_{Epi} + N_{Th} = 100.0\%$. The thermal neutron peak time (TPT) is reported as the maximum time value for the returning thermal neutron peak in the neutron die-away region, this is also calculated using thermal neutrons only.
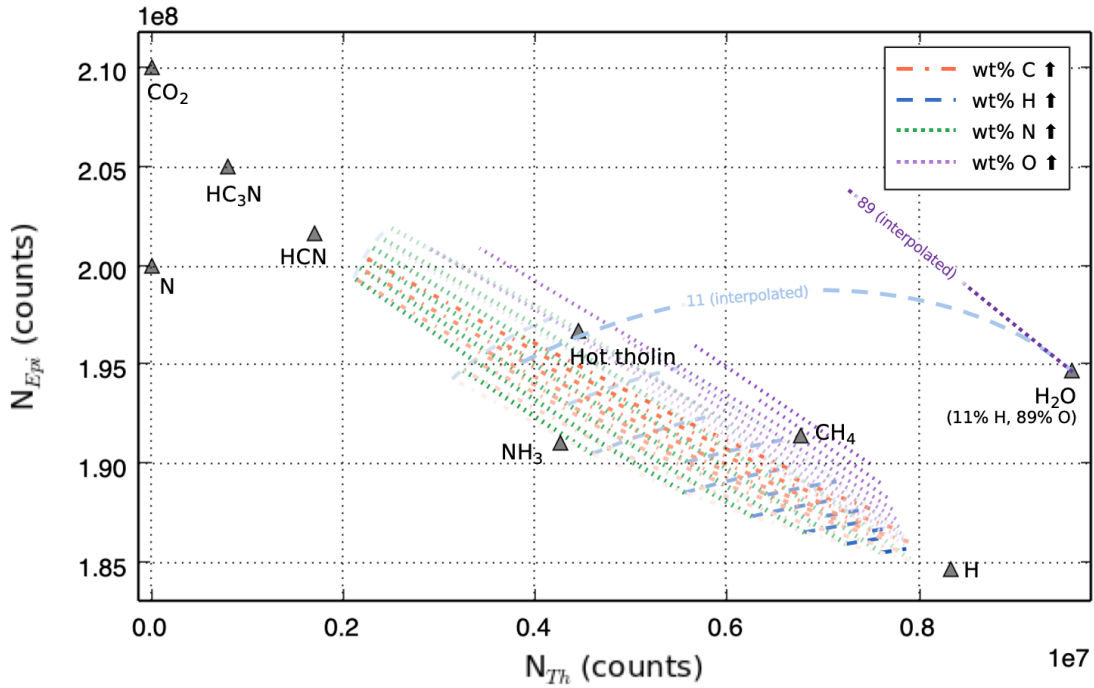
Figure 3.12: Our modeled grid results are for 1-layer models are within the bound of expected end-members. 1-layer, heterogeneous active neutron results for epithermal neutron counts (N_{Epi}) versus thermal neutron counts (N_{Th}), using the grid of compositions from Tables 3.1 and 3.2. All lines on the plot represent elemental wt%s with increasing amounts denoted by darker shades and decreasing amounts denoted by lighter shades. The orange dash-dot lines represent wt% C, the blue dashed lines wt% H, the green dotted lines wt% N, and the purple dotted lines wt% O. End-member compositions are labeled as gray triangles. We interpolate a blue dashed line from the expected 11 wt% H to H_2O, and a purple dotted line for the expected value of 89 wt% O to H_2O. As O increases in a material that contains H, the H values for N_{Epi} and N_{Th} depict a non-linear trend.

Other Nutrients

The high thermal neutron cross-section of B affects the magnitude of the neutron die-away curve, as B increases for large amounts (100's ppm+) the magnitude of the curve is suppressed. Increasing B from 200 to 1000 ppm results in a significant decrease in the magnitude of neutron counts ($\sim 0.5 \times$ order of magnitude), this is consistent with Mars studies by Nowicki *et al.* (2017). Other elements investigated included Na, S, Mg, and K, none of which exhibited any significant change in die-away shape between 1E-4 to 10 wt%. Lower amounts of hydrogen ($<$ 15 wt%) in the bulk composition may allow for more substantial shape changes in the neutron die-away curve, especially for two-layer models.

3.5.4 Surface Density

We modeled a change in the surface density for two 1-layer models, one with a 10 wt% H, 5 wt% C, and 85 wt% N (Σ_s = 5.33 cm^2/g, Σ_a = 0.089 cm^2/g) base surface composition, the other with a 50 wt% H, 5 wt% C, and 45 wt% N (Σ_s = 27.36 cm^2/g, Σ_a = 0.136 cm^2/g) base surface composition. The atmospheric composition and density remain constant, while the surface composition's density is changed from 0.8 to 2.6 g/cc. Studies by Lethuillier *et al.* (2018) constrain specific Titan tholin species to densities between 1.31 and 1.47 g/cc, whereas Earth materials such as pure methane clathrate and water-ice have densities of $\approx$ 1.87 g/cc and 0.92 g/cc, respectively. The total number of counts in the die-away region for each case shown in Figure 3.13 are within less than 1% of each other, though the arrival times are different. For densities from 0.2 - 0.8 g/cc the arrival time changes by several hundred microseconds, as the density increases beyond 1.4 g/cc the arrival time converges. These results are consistent for both simulation sets, with tighter convergence for higher Σ_s materials.
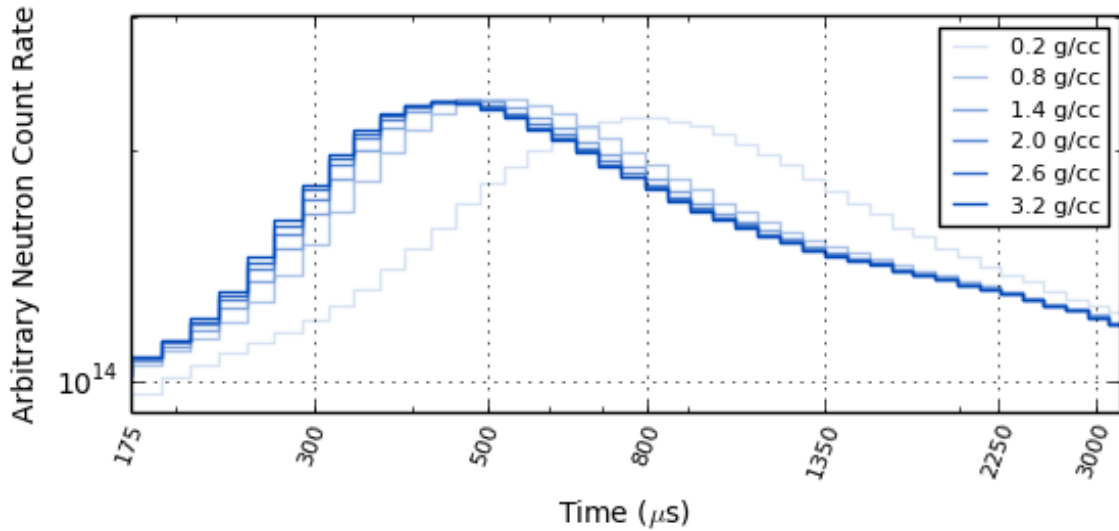
Figure 3.13: Neutron die-away simulation results showing the effects of surface material density on the neutron die-away curve using a 1-layer constant composition of 10 wt% H, 5 wt% C, and 85 wt% N ($\Sigma_s = 5.33$ cm^2/g, $\Sigma_a = 0.089$ cm^2/g). As the density of the surface material increases, the thermal neutron peak arrival time decreases; as atoms in the material are confined in a smaller volume, the probability to stop particles increases. Note that the total number of counts in the die-away region for each case is within less than 1% of each other, though the arrival times are different.

3.5.5 2-layer Modeling of Buried Deposits

We modeled a 2-layer subset grid of 12 different material deposits (Table 3.1) spanning the range of possible icy body cross sections, varying the burial depth of deposit under a layer of Hot Tholin material from 1 - 20 cm, first in steps of 1 cm up to 5 cm, then in steps of 2 cm. A subset of the results of this study are shown in Figure 3.14. As the burial depth increases past 4 cm the neutron die-away signal converges on the response from the top material layer; this behavior is consistent with

other studies describing neutron penetration depth in high-H environments (Feldman *et al.*, 2000; Heffern *et al.*, 2021). Figure 3.14 A has 10 wt% H, matching with the upper layer such that the thermal neutron count rate is nearly identical for all depths beyond 2 cm. Figure 3.14 B has 50 wt% H, such that the thermal neutron count rate is increased at shallow depths, but as the burial depth increases past 4 cm the neutron die-away signal converges on the response from the top material layer.
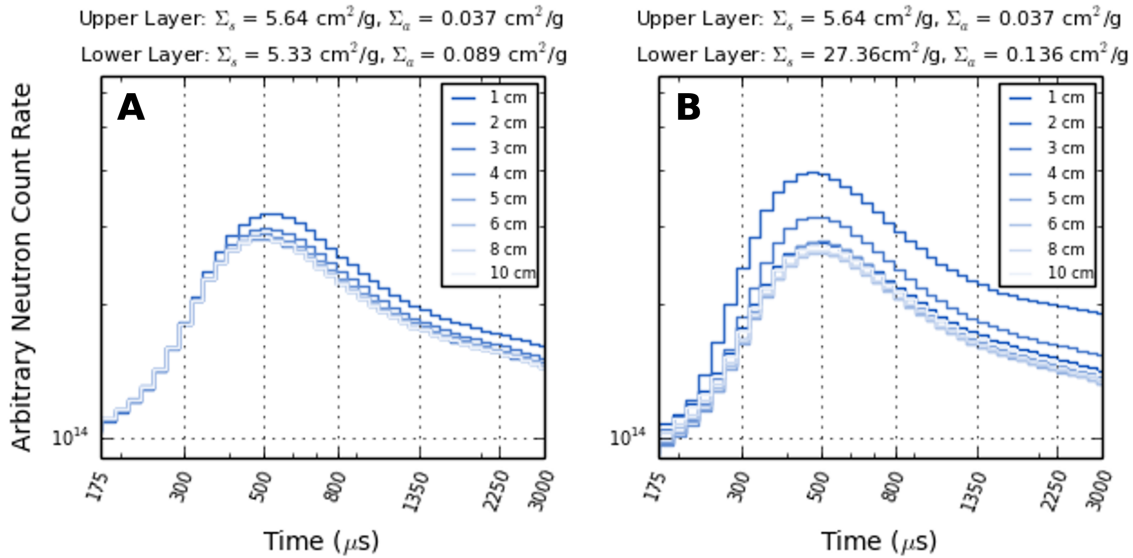
Figure 3.14: Neutron die-away 2-layer simulation results showing the result of change in burial depth (1 - 10 cm) for two different bottom layer materials with a constant top layer material (11 wt% H, 71 wt% C, 18 wt% N, $\Sigma_s = 5.64$ cm^2/g, $\Sigma_a = 0.0368$ cm^2/g). Cross section values are given at the top of each subplot for each material used for upper and lower layers. A) The lower layer consists of 85 wt% C, 10 wt% H and 5 wt% N, resulting in $\Sigma_s = 5.33$ cm^2/g and $\Sigma_a = 0.089$ cm^2/g; B) the lower layer consists of 50 wt% H, 5 wt% C, and 45 wt% N, resulting in $\Sigma_s = 27.36$ cm^2/g and $\Sigma_a = 0.136$ cm^2/g. If the lower layer material's Σ_a and Σ_s are close in value to that of the upper layer (e.g. subplot A) even subtle changes of Σ_a and Σ_s can be detected via changes in the die-away curve for shallow layers (< 3 cm).

To expand more on the possible compositions that may be present on icy bodies, we modeled 2-layer grids of possible end-member materials present on Titan for 2 cm and 4 cm deposit depths. Figure 3.15 shows the die-away results of this study for material buried at a 2 cm depth, Figures 3.16 - 3.17 show example data points for Hot Tholin material (see Table 3.2 for composition) on top of CH_4, NH_3, and H_2O buried deposits at 2 and 4 cm burial depths, overlaid on top of the N_{Epi} vs. N_{Th}, FWTA, κ_1, and G_1 plots. Tables 3.9 and 3.10 report results for 2 cm and 4 cm, respectively, across a range of buried example materials. The shape of the neutron die-away curve is different for most underlying materials, with NH_3 and Hot Tholins having a similar elemental composition. The largest values for TPT and FWTA tend to exist for compositions involving H_2O, due to high Σ_s and low Σ_a.

Table 3.11 compares several examples with from our 2-layer models with a Hot Tholin upper layer for N_{Th}, N_{Epi}, FWTA, κ_1, G_1, and other metrics using percent differences. The total epithermal neutron counts and thermal neutron counts listed in these tables are full time integrated and reported as a raw number of counts, this is equivalent to a 13 hour measurement with a DT PNG (10E8 nps in 4π) at 5% duty factor, 50μs pulse width, with a 2" CLYC crystal. Both κ_1 and G_1 show % differences consistently larger than that of N_{Epi} for these 2-layer models.
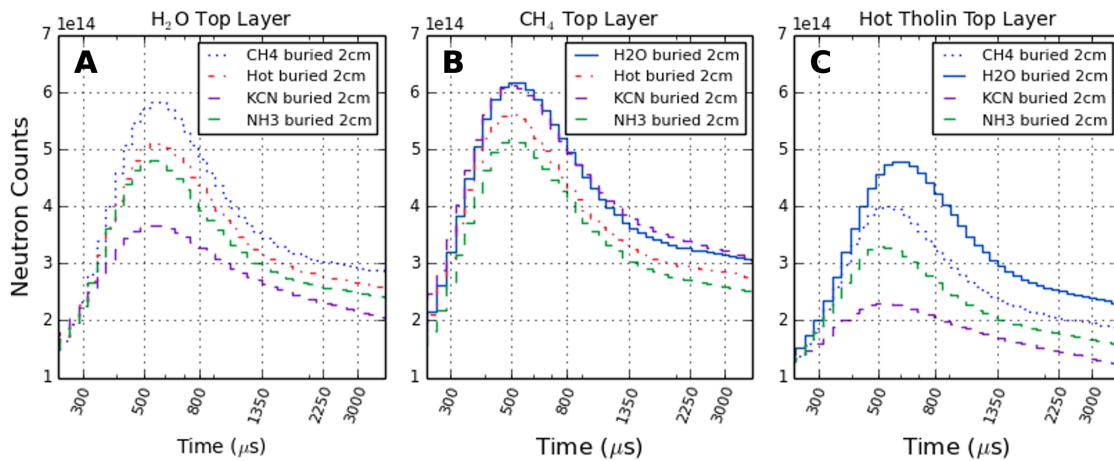
Figure 3.15: Layered composition scenarios have different neutron die-away curves. Thermal neutron die-away results showing the changes in the die-away curve magnitude and shape for 2-layer Titan end-member compositions. A) CH_4, KCN, NH_3, and Hot Tholin materials buried 2 cm under H_2O; the KCN buried deposit is significantly different from other materials due to the lack of H in the buried layer. B) H_2O, KCN, NH_3, and Hot Tholin materials buried 2 cm under CH_4. C) CH_4, KCN, NH_3, and H_2O buried 2 cm under Hot Tholin material.
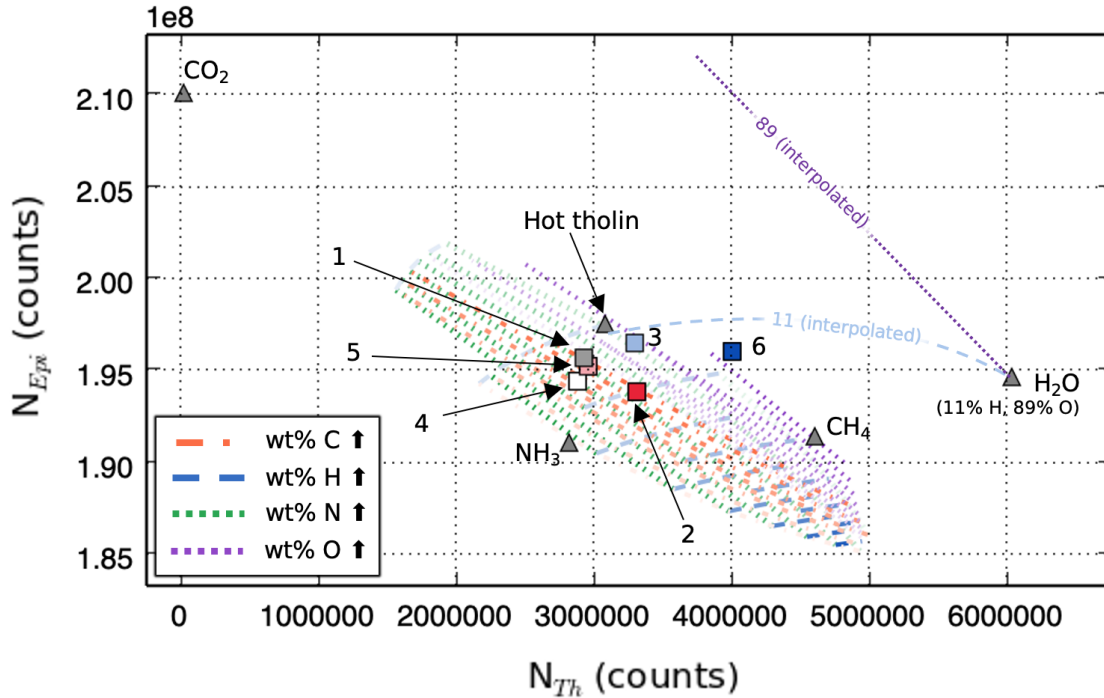
Figure 3.16: Layered composition results using N_{Epi} versus N_{Th} lie within regions where heterogeneous mixing results also lie, resulting in possible degeneracies. 1-layer results for N_{Epi} versus N_{Th}, using the grid of compositions from Tables 3.1 and 3.2, with 2-layer example points (squares) overlaid. All lines on the plot represent elemental wt%s with increasing amounts denoted by darker shades and decreasing amounts denoted by lighter shades. The orange dash-dot lines represent wt% C, the blue dashed lines wt% H, the green dotted lines wt% N, and the purple dotted lines wt% O. End-member compositions are labeled as gray triangles. All buried deposit examples (squares) are buried under a layer of Hot Tholin elemental composition. White (1) and gray (4) squares denote NH_3 buried at 4 cm and 2 cm, respectively; red (2) and pink (5) squares denote CH_4 buried at 4 cm and 2 cm, respectively; and blue (3) and light blue (6) squares denote H_2O buried at 4 cm and 2 cm, respectively. As the depth of the top layer of Hot Tholin increases, the 2-layer data points converge on the Hot Tholin triangle data point on the plot.
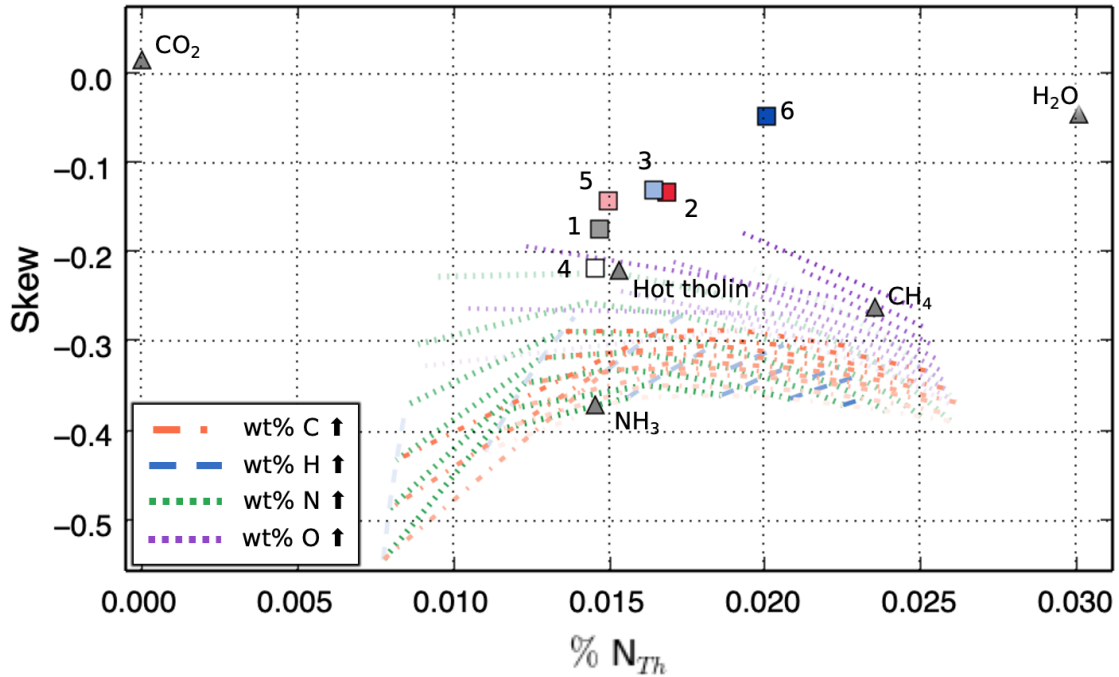
Figure 3.17: Layered composition results for N_{Epi} versus G_1 lie away from regions where similar heterogeneous mixing results lie. 1-layer results for N_{Epi} versus G_1, using the grid of compositions from Tables 3.1 and 3.2, with 2-layer example points (squares) overlaid. All lines on the plot represent elemental wt%s with increasing amounts denoted by darker shades and decreasing amounts denoted by lighter shades. The orange dash-dot lines represent wt% C, the blue dashed lines wt% H, the green dotted lines wt% N, and the purple dotted lines wt% O. All buried deposit examples (squares) are buried under a layer of Hot Tholin elemental composition. Gray (1) and white (4) squares denote NH_3 buried at 4 cm and 2 cm, respectively; red (2) and pink (5) squares denote CH_4 buried at 2 cm and 4 cm, respectively; and blue (3) and light blue (6) squares denote H_2O buried at 4 cm and 2 cm, respectively. As the depth of the top layer of Hot Tholin increases, the 2-layer data points converge on the Hot Tholin triangle data point on the plot.

Top Layer	Bottom Layer	κ_1	G_1	FWTA (μs)	$\%N_{Epi}$	$\%N_{Th}$	TPT (μs)
CH$_4$	NH$_3$	-1.614	-0.224	476.398	97.80	2.20	487.430
CH$_4$	H$_2$O	-1.611	-0.262	481.375	97.39	2.61	487.430
CH$_4$	KCN	-1.576	-0.279	468.247	97.38	2.62	487.430
CH$_4$	Hot Tholin	-1.557	-0.285	472.454	97.63	2.37	487.430
H$_2$O	NH$_3$	-1.653	-0.153	480.034	97.93	2.07	523.460
H$_2$O	CH$_4$	-1.703	-0.076	495.111	97.60	2.40	523.460
H$_2$O	KCN	-1.484	-0.316	457.658	98.28	1.72	523.460
H$_2$O	Hot Tholin	-1.678	-0.107	485.515	97.83	2.17	523.460
Hot Tholin	H$_2$O	-1.701	-0.049	491.626	98.00	2.00	561.780
Hot Tholin	NH$_3$	-1.566	-0.219	463.915	98.54	1.46	487.430
Hot Tholin	KCN	-1.209	-0.464	442.724	98.88	1.12	523.460
Hot Tholin	CH$_4$	-1.649	-0.133	479.045	98.32	1.68	523.460
NH$_3$	Hot Tholin	-1.462	-0.319	453.323	98.53	1.47	487.430
NH$_3$	KCN	-1.313	-0.423	443.200	98.28	1.72	453.560
NH$_3$	CH$_4$	-1.499	-0.287	457.247	98.55	1.45	487.430
NH$_3$	H$_2$O	-1.546	-0.279	462.392	98.38	1.62	523.460

Table 3.9: Temporal neutron simulation result metrics for different 2-layer scenarios at a burial depth of 2 cm, as shown in Figure 3.15; table is grouped by top layer and sorted by FWTA. κ_1, G_1, FWTA, and thermal neutron peak time (TPT) were calculated using thermal neutrons only. The total epithermal neutron counts (N_{Epi}) and thermal neutron counts (N_{Th}) are full time integrated and reported as a percentage of the total neutrons such that $N_{Epi} + N_{Th} = 100.0\%$.

Top Layer	Bottom Layer	κ_1	G_1	FWTA (μs)	$\%N_{Epi}$	$\%N_{Th}$	TPT (μs)
CH_4	NH_3	-1.636	-0.198	480.807	97.72	2.28	487.430
CH_4	H_2O	-1.581	-0.264	476.702	97.58	2.42	487.430
CH_4	KCN	-1.637	-0.200	481.145	97.44	2.56	487.430
CH_4	Hot Tholin	-1.574	-0.265	475.664	97.59	2.41	487.430
H_2O	NH_3	-1.709	-0.044	497.267	97.50	2.50	561.780
H_2O	KCN	-1.686	-0.111	486.184	97.04	2.96	523.460
H_2O	CH_4	-1.718	-0.010	502.980	97.41	2.59	561.780
H_2O	Hot Tholin	-1.712	-0.038	498.313	97.40	2.60	561.780
Hot Tholin	H_2O	-1.656	-0.132	477.324	98.35	1.65	561.780
Hot Tholin	NH_3	-1.602	-0.174	468.536	98.53	1.47	523.460
Hot Tholin	CH_4	-1.628	-0.143	473.106	98.51	1.49	523.460
Hot Tholin	KCN	-1.537	-0.243	459.284	98.26	1.74	523.460
NH_3	Hot Tholin	-1.447	-0.327	452.111	98.55	1.45	487.430
NH_3	CH_4	-1.450	-0.325	452.245	98.61	1.39	487.430
NH_3	KCN	-1.446	-0.328	451.994	98.29	1.71	487.430
NH_3	H_2O	-1.456	-0.324	452.907	98.55	1.45	487.430

Table 3.10: Temporal neutron simulation result metrics for different 2-layer scenarios at a burial depth of 4 cm; table is grouped by top layer and sorted by FWTA. κ_1, G_1, and FWTA were calculated using thermal neutrons only. The total epithermal neutron counts (N_{Epi}) and thermal neutron counts (N_{Th}) are full time integrated and reported as a percentage of the total neutrons such that $N_{Epi} + N_{Th} = 100.0\%$. The TPT is reported as the maximum time value for the returning thermal neutron peak in the neutron die-away region.

Deposit buried under Hot Tholins	% **Diff.** κ_1	% **Diff.** G_1	% **Diff.** FWTA	% **Diff.** N_{Tot}	% **Diff.** N_{Epi}	% **Diff.** N_{Th}
NH_3 from 2cm to 4cm	2.29	22.63	0.99	0.65	0.64	1.40
CH_4 from 2cm to 4cm	1.32	7.59	1.25	0.51	0.70	11.35
H_2O from 2cm to 4cm	2.73	91.66	2.95	0.12	0.24	19.59
Buried deposit compared to 1-layer Hot Tholin material	% **Diff.** κ_1	% **Diff.** G_1	% **Diff.** FWTA	% **Diff.** N_{Tot}	% **Diff.** N_{Epi}	% **Diff.** N_{Th}
CH_4 2cm	4.90	50.08	2.49	2.02	1.52	27.48
CH_4 4cm	3.58	42.90	1.24	1.51	0.82	38.53
H_2O 2cm	8.01	127.45	5.08	0.58	0.40	8.89
H_2O 4cm	5.28	50.54	2.13	0.69	0.15	28.35
NH_3 2cm	0.28	1.37	0.72	1.94	1.21	41.29
NH_3 4cm	2.01	23.98	0.27	1.29	0.57	39.95

Table 3.11: Comparison of temporal neutron simulation result metrics for materials taken from Table 3.2, all results shown are for Hot Tholin top layer models. The first three rows show the % difference between the burial depths (2 cm vs. 4 cm burial depths) of specific deposits (NH_3, CH_4, and H_2O, respectively). The last 6 rows show the % differences between a 1-layer model of all Hot Tholin material versus the 2-layer model with a specific buried deposit CH_4, H_2O, and NH_3, at 2 cm and 4 cm depths, respectively). The % difference between N values (neutron counts) is taken as full integrated counts and is comparable to a 13 hour DT PNG measurement using a 2" CLYC crystal (comparable to two 1" diameter × 9" long 20 atm ^{3}He tubes). Both κ_1 and G_1 show % differences consistently larger than that of N_{Epi} for these 2-layer models (with the exception of NH_3 buried at 2 cm).

3.6 Discussion

3.6.1 Neutron Sources

Three different pulse widths were tested in this study (3 μs, 50 μs, and 200 μs) using DT (14.1 MeV) neutrons. The Dragonfly mission DraGNS originally planned to operate in a pulsed mode, using a large pulse-on duty fraction (>50%) for a nominal 1 ms pulse period Lawrence *et al.* (2022). More recently, plans have been made to run the generator in a continuous mode (priv. comm. A. Parsons). Operating the PNG in this way is beneficial for operating the HPGe detector due to its long shaping time (5–15 μs). We determined that a shorter pulse width ($< 50\mu$s) is more beneficial for neutron die-away operations; the DraGNS PNG operational settings as they are currently planned do not allow for time resolved measurements. However, implementing the addition of a short pulse mode into the electronics may allow for the use of neutron die-away, especially for measurements of shallow subsurface layering (< 4cm) and for use as a back-up measurement of subsurface composition.

Due to the dense atmosphere of Titan and lack of surface sunlight, the main power source onboard any mission to Titan's surface will require a Multi-Mission Radioisotope Thermoelectric Generator (MMRTG), this emits neutrons due to the use of plutonium dioxide. There are graphite sleeves that protect the fuel clads in the MMRTG, the use of graphite may have the potential to cause secondary fissions due to the nature of graphite to facilitate the fission chain reaction, this could result in an even larger contribution to the thermal neutron environment. Experimental characterization of the MMRTG neutron contribution can be done with a passive neutron measurement or by characterizing the later time bins in a neutron die-away curve; temporal measurement bins may be able to better distinguish neutrons as a result of the ground materials versus neutrons from the MMRTG due to time-of-flight

differences via distances (Jun *et al.*, 2013).

3.6.2 Atmospheric Effects

We studied the effects of atmospheric density on a Titan-like MCNP simulation model. As the density of the atmosphere increases for an all-atmospheric Titan model, the total number of neutron counts increases significantly. In our study of atmospheric density, we found that if the density increases by an order of magnitude, then the total number of neutron counts increases by as much as 2.5 orders of magnitude in the thermal neutron die-away region. However, this effect is small when compared to a 1/2 ground material, 1/2 atmospheric Titan model. Neutron interactions with the more-dense ground surface material dominate the total count rate such that the atmospheric effects ($\sigma_{observed}$ for an all-atmospheric model) are less than or on the same order of magnitude as the uncertainty in the total number of counts ($\sigma_{observed}$ in a 1/2 ground 1/2 atmospheric model).

In our studies of the atmospheric effects of a Titan-like world, we generated simulations involving changes in geometry in order to attempt to isolate the effects of the atmosphere from the ground material. By increasing the distance from the target plane to the tally plane (while keeping the source at a constant 100 cm from the surface), we determined that there is a small effect from the atmosphere on the overall shape of the neutron die-away curve, most of the change in the die-away shape is due to the time-of-flight of the neutrons traveling from the surface to the tally plane (counts $\propto 1/\text{distance}^2$), though some interactions likely take place in the atmosphere. Additionally, we investigated a similar scenario where the source is not at a 100 cm distance from the surface, but instead moves with the tally plane a distance away from the surface. This resulted in a gradual decrease in the number of neutrons in the thermal neutron die-away region as the distance increases, this is likely due to

neutrons traveling a further distance to the planetary surface.

Background count rates are dependent on neutrons resulting from an MMRTG as well as some GCRs that penetrate through the atmosphere (Czarnecki *et al.*, 2020). The changes in neutron count rate due to the atmosphere can affect the background count rate. If a rover or rotocopter were to take measurements over the course of months on the surface of Titan, changes in the atmosphere would affect the background count rate during active and passive modes, though the effect is 2-3 orders of magnitude lower than the active neutron mode signal.

Although these studies show that the atmosphere does not have a large effect (multiple orders of magnitude lower than the surface contribution in active mode) we do see change in the neutron die-away curve as a results of scenarios with changing geometry. Current studies involving MSL DAN report on the effects of large cliff walls showing up as additional high count rates in later time bins, suggesting contributions from distant vertical materials, our results support this (Dibb *et al.*, 2019; Berner *et al.*, 2022). These studies further point to a need to characterize the neutron die-away method for non-planar surfaces, which could open the method up to geomorphological applications.

3.6.3 *Composition trends in 1-Layer Models*

As the amount of hydrogen increases in the surface of a planetary body, the amount of thermal neutron counts tends to increase. In our studies we found that as the amount of H increases, the epithermal neutron count decreases and the thermal neutron count increases, as expected. Additionally, the FWTA also decreases, spanning a wide range ($\sim$400 - 560 μs, 0 - 5 wt% H) at low-H and a small range at high-H (398 - 402 μs, 50 - 100 wt% H).

We looked at several examples from our 1-layer model grid to compare N_{Th}, N_{Epi},

FWTA, κ_1, and G_1 (Tables 3.3 - 3.7). The shape of the neutron die-away curve has previously been described by Hardgrove *et al.* (2011) through use of the FWTA, however our results show that the dieaway shape is better described using κ_1 and G_1 metrics due to their consistently higher % differences. We found that integrated thermal neutron counts are the best indicator of composition change but further constraints can be placed upon these measurements using κ_1 and G_1. The integrated epithermal counts is a comparable metric to G_1 when % difference of $\Sigma_a <$ % difference of Σ_s. In other words, when there are more absorbers in the subsurface, the shape of the neutron die-away curve changes more dramatically than the neutron count rate may indicate, this is consistent with studies by Kerner *et al.* (2020); Hardgrove *et al.* (2011).

3.6.4 *Viability of the Die-away Method for Titan-like Materials*

We presented the % difference results for several example scenarios using the neutron die-away method applied to buried deposits: 1) a water-ice layer buried under tholin-like material (Hot Tholin) for 2 cm and 4 cm burial depths, 2) a methane (CH_4) layer buried under tholin-like material for 2 cm and 4 cm burial depths, and 3) an ammonia (NH_3) layer buried under tholin-like material for 2 cm and 4 cm burial depths. We found that there is a dramatic change in the neutron die-away shape (κ_1 and G_1) for these buried materials for depths of 2 cm and 4 cm. As the burial depth of deposit increases, the die-away method for high Σ_a and Σ_s values becomes limited to shallow subsurface depths (< 6 cm) but still allows for further constraints to be put on neutron data for buried deposits. The κ_1 and G_1 metrics were shown to be favorable over FWTA, though changing the time bin widths to favor a less-coarse sampling may aid in more accurate FWTA values. We found that for underlying buried materials with significant compositional changes ($\sim$ 10's+ wt%) the neutron die-away shape

metric FWTA results in values that are closer to that of the underlying layer for shallow deposits, while the shape metrics of κ_1, and G_1 do not clearly follow a trend close to the underlying compositional values (i.e. the κ_1 value for Ch_4 buried at 4 cm does not appear to follow a clear trend back to the pure CH_4 1-layer value). This means that κ_1, and G_1 are likely better indicators of buried deposits than FWTA, N_{Epi}, or N_{Th}. These metrics combined with or in lieu of gamma-ray data may help to better constrain buried deposits of geologically relevant materials on Titan.

We constrain the neutron die-away region to values of Σ_a and Σ_s based on 50% wt H and below for 1-layer compositions, as shown in Figure 3.18, such that changes occurring beyond the estimated die-away detection region are not distinguishable from each other. Results from Kerner *et al.* (2020) show a saturation effect for the average decrease in TPT as Σ_a increases, we expand on this space into Σ_s and do not limit to Mars-like materials. For shallow (< 6 cm) subsurface buried deposits with a high H (10 - 50 wt%) top layer, the neutron die-away method is still able to detect changes in the subsurface so long as the buried material has significantly different Σ_a and Σ_s (e.g. a top layer has a composition value outside of the estimated die-away detection region and the lower layer is buried at 2 cm and has a composition in the middle of the estimated die-away detection region).

3.6.5 Sensitivity and Statistical Metrics

As described in Section 3.4, the uncertainty in neutron measurements is described as $\sqrt{N_{observed}} = \sigma_{observed}$, such that the error bars for sample scenarios which are included on the previous plots are on the order of magnitude of the plot lines. More recent results from the DAN instrument on the MSL Curiosity Rover utilize Markov chain Monte Carlo (MCMC) in their analysis of data sets (Gabriel *et al.*, 2018; Czarnecki *et al.*, 2020; Gabriel and Hardgrove, 2020). MCMC is a hypothesis test method
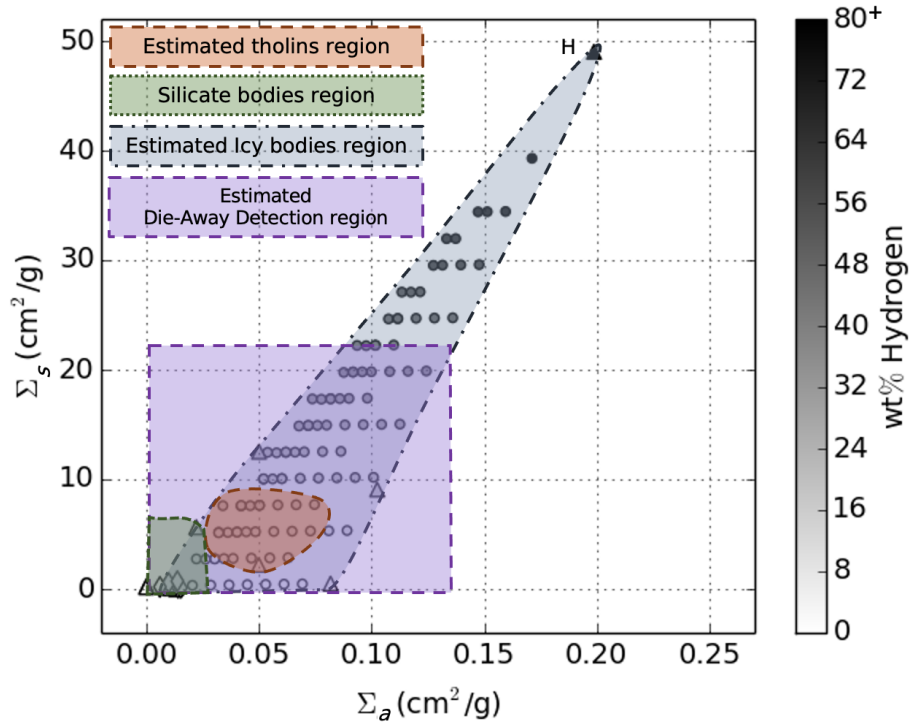
Figure 3.18: The neutron die-away method can be constrained based on Σ_s and Σ_a. Σ_s versus Σ_a for a range of mixed Titan-like materials and "pure molecule" end member compositions (triangles), silicate body materials are located in the bottom left corner (diamonds). Figure 3.1 shows another version of this plot with Titan "pure molecule" end member compositions labeled. The green dotted area in the lower left corner represents a range of materials associated with silicate bodies. The orange dashed region represents our estimated range of values for Titan tholin compositions based on Cable et al. (2012). The blue dash-dot region represents the estimated range of cross sections for an icy body (assumed to be primarily made of C, H, N, and O). Finally, the purple dashed region represents our conservative estimated limit for the neutron die-away method based on 50 wt% H and the dynamic range for values of FWTA, κ_1, and G_1.

rooted in Bayesian statistics and would be much more suitable for result analysis testing using MCNP with the neutron die-away method for future landed missions. Such MCMC analysis results in corner plots that show all the one and two dimensional projections of the posterior probability distributions of a given set of parameters. This type of analysis combined with parameters based on κ_1, G_1, FWTA, N_{Epi}, and N_{Th} would allow for much stricter constraints on neutron data sets as opposed to the traditional two parameters, N_{Epi}, and N_{Th}.

3.7 Conclusions

3.7.1 Implications for Measurements on Titan

One of the main challenges in sending GRNS instrumentation to the outer planets is radiation damage effects. A major challenge exists due to degradation of fill gas for compressed gas instruments, such as ^{3}He and both deuterium and tritium in the PNG. Additionally, the half-life of tritium is 12.3 years, meaning that a PNG may arrive depleted after a long cruise to an outer planetary target. Decay of the tritium in the PNG has the possibility of unstable neutron flux output throughout the mission lifetime (Sanin et $al.$, 2015; Gabriel and Hardgrove, 2020), though this is potentially mitigated with the use of an additional diamond detector for neutron flux monitoring or if an additional reservoir of tritium is available. By using the neutron die-away method, the addition of a diamond detector may not be required for pulse monitoring as the ratio of thermal neutron counts to total counts versus κ_1, G_1, and FWTA can provide enough information for compositional determinations.

The surface of Titan will likely contain large amounts of N, C, H, and small amounts of other elements such as O, Na, K, and Mg. Peplowski et $al.$ (2018) describes a method of elemental depth distribution detection based on multiple gamma-

ray energy lines and their attenuation properties for Si lines (1779 and 3934 keV) that rely on different neutron interaction mechanisms. Low energy (< 3.3 MeV) $^{16}O(n,\gamma)$ gamma-ray lines have low gamma-ray production cross sections ($< 1E-4$ b) which would likely compete with other elemental lines making them difficult to detect, while the 6129 and 5618 keV $^{16}O(n,n'\gamma)$ gamma-ray lines may be difficult to use for determining depth of water-ice deposits due to their high energies and close energy proximity to other lines (N). For gamma-ray instruments, Peplowski *et al.* (2018) successfully demonstrated that high-purity germanium (HPGe) crystals can be annealed and their energy resolution restored from radiation damage effects during cruise, however this is at the cost of the crystal's overall efficiency. The crystal's effective volume decreases over time with multiple anneals, this loss in active volume can cause a loss in gamma ray detection efficiency (e.g. 10% loss for 3 years of modeled flight radiation damage, post-anneal) (Peplowski *et al.*, 2019), an effect which can be dramatic due to the absolute efficiency dependency on detector volumes, especially at high energies (Gilmore, 2008; Knoll, 2010). Increasing the integration time will likely limit this degradation in the number of counts for higher energy peaks, though we argue the use of the neutron die-away technique as a back-up which can provide an alternative, shorter duration measurement for elemental depth distribution detection. Other scintillators, such as $CeBr_3$ and YAP:Ce, are fairly radiation hardened and offer long-term spaceflight solutions but may not have the energy resolution required to perform depth distribution analysis (Kim *et al.*, 2021).

3.7.2 Implications for Other Icy Bodies

We have shown that the neutron die-away method is not entirely limited on icy-bodies. With the rapid development of radiation-hardened electronics and new breakthroughs in radiation-hardened plastics, glasses, and scintillators, the potential for ac-

tive GRNS instrumentation to the outer solar system is not completely out of reach. Other icy worlds, such as Europa, could share in the potential for landed, shallow-subsurface active GRNS measurements. The polar regions of Mars have also been shown to contain large amounts of surface ice (~ 80 wt% or more water-ice) such that a landed mission using active GRNS instrumentation may have similar nuclear environmental conditions to that of Titan (Byrne, 2009).

Chapter 4

CALIBRATION OF THE MINIATURE NEUTRON SPECTROMETER (MINI-NS) FOR THE LUNAR POLAR HYDROGEN MAPPER MISSION (LUNAH-MAP)

Contributions to be submitted as sections of a larger publication to Space Sciences Review with approval from co-authors: C. J. Hardgrove[1] (primary author), L.E. Heffern, E. B. Johnson[2], P. Hailey[1], R. Starr[3], K.E. Mesick[4], D. Coulpand[4], T. Prettyman[5], G. Stoddard[2], J. Christian[2], J. DuBois[1], R. Roebuck[1], S. T. West[1,6]

[1] Arizona State University School of Earth and Space Exploration, Tempe, AZ

[2] Radiation Monitoring Devices, Watertown, MA,

[3] Catholic University of America, Washington DC,

[4] Los Alamos National Laboratories, NM

[5] Planetary Science Institute, Tuscon, AZ,

[6] NASA Goddard Space Flight Center, MD

Individual contributions to the manuscript journal submission are included in this chapter along with associated background information.

ABSTRACT

Nuclear techniques have been used successfully in many previous planetary missions as a remote sensing method from orbit to investigate the water (or hydrogen, H) content in the shallow subsurface and to determine the surface composition of planetary bodies. To understand the presence of water within permanently shadowed regions (PSRs), the Lunar Polar Hydrogen Mapper (LunaH-Map) mission has been designed to provide a high-resolution spatial distribution of the H content over the southern pole from a highly elliptical, low perilune orbit (10 - 15 km altitude). The primary instrument on the LunaH-Map mission is the Miniature Neutron Spectrometer (Mini-NS), which consists of eight 2 cm thick $\times$ 6.3 cm $\times$ 4 cm slabs of Cs_2YLiCl_6:Ce (CLYC). Mini-NS provides a sensitivity similar to 10 atm, 5.7 cm diameter He-3 tubes, as were used in the Lunar Prospector Neutron Spectrometer (LPNS). The Mini-NS has a total active area of 200 cm^2 and is covered with a Gd sheet to ensure measurement of epithermal neutrons ($0.025 - 10^5$ eV). The Mini-NS uses pulse shape discrimination (PSD) techniques implemented in a field programmable gate array (FPGA). Mini-NS was designed as a 1U $\times$ 3U module and has been integrated into a 6U cubesat which will be launched on the Artemis-I vehicle in effort of NASA's Space Launch System (SLS) rocket. In this chapter we demonstrate and report on the calibration of the instrument response and characterization of a compact neutron detector capable of isolating gamma rays and protons from epithermal neutrons.

4.1 Introduction

The Lunar Polar Hydrogen Mapper (LunaH-Map) CubeSat mission is a planetary science investigation sponsored by NASA Science Mission Directorate (SMD). It is the first of its kind in scope and budget, and therefore represents a new type of mission for NASA SMD. The LunaH-Map project structure and funding model are aligned with that of a traditional University-led, low-earth orbit (LEO) CubeSat mission, though it is considered a Class D mission for high risk, high focus science, with high science return. There are inherent major risks associated with this mission, primarily due to its low orbital altitude, as such the cost and schedule are compressed to take advantage of the opportunity.

The Miniature Neutron Spectrometer (Mini-NS) is the primary instrument payload on LunaH-Map. Mini-NS uses eight epasolite scintillators, Cs_2LiYCl_6:Ce (CLYC), coupled to photomultiplier tubes (PMTs). CLYC is enriched to 95% of Li-6, where the ^{6}Li(n,α)t reaction with a Q Value = 4.8 MeV is employed to stop neutrons and generate a large light pulse with a distinguishable transient pulse shape compared to gamma ray interactions (Johnson *et al.*, 2015; Glodo *et al.*, 2012). By detecting suppression in the epithermal neutron count rate from very low perilune altitudes (10 - 15 km), Mini-NS will produce maps of lunar south pole hydrogen enrichments at spatial scales smaller than known permanently shadowed regions (PSRs) (Hardgrove *et al.*, 2020). A careful calibration of the Mini-NS energy-angle response is necessary to properly interpret data acquired at any altitude, regardless of topography, throughout the LunaH-Map mission. The goal of this work is to report on the functional performance and angular response of the Mini-NS instrument.

4.2 Objectives

LunaH-Map's primary objective is to map the uniformity of hydrogen in PSRs by measuring the epithermal neutron signatures in the south polar region of the Moon. In 2009, the LCROSS mission measured $\sim$5 wt% water in an ejecta cloud formed by an impact into Cabeus crater (Colaprete *et al.*, 2010). The water equivalent hydrogen (WEH) seen by the Lunar Prospector Neutron Spectrometer (LPNS) – at spatial scales of $\sim$5-70 km^2 – is only $\sim$0.2 wt% at the LCROSS impact site, assuming the H is uniformly distributed. However, H is likely not uniformly distributed, thus there is a need to assess the heterogeneity at spatial scales less than PSR size ($\lesssim$ 20 km diameter, e.g. Shackleton Crater).

4.2.1 Science

As the Moon is without an atmosphere, galactic cosmic rays can interact with the lunar surface, producing neutrons. As H content increases, the epithermal neutron flux signature decreases. Neutron spectroscopy has become a standard technique in planetary science, the orbital energy distribution of thermal ($<$0.025 eV) and epithermal neutrons ($0.025 - 10^5$ eV) is highly dependent upon the H content in the top $\sim$10's of cms of a planetary surface (Lawrence *et al.*, 2002; Prettyman *et al.*, 2006; Lawrence *et al.*, 2006). The presence of water-ice in PSRs at the lunar poles was first postulated by Harold Urey (1952) and Watson *et al.* (1961). Both the Lunar Prospector and Lunar Reconnaissance Orbiter missions detected changes in the neutron count rate at the poles, indicative of water-ice being present in PSRs (Feldman *et al.*, 1998; Mitrofanov *et al.*, 2010b). The high efficiency of CLYC for epithermal neutrons, coupled with the low spacecraft orbit at the Moon's South Pole will enable LunaH-Map to create maps of H within $\sim$5 degrees of the pole that include

contributions from within PSRs.

4.2.2 Mission

LunaH-Map will identify small regions (<25 km^2) of enriched H within permanently shadowed regions at the lunar South Pole. Near perilune, LunaH-Map will identify <25 km^2 regions with a minimum of 600ppm H $\pm$ 120 ppm (Hardgrove et al., 2020). Thus, the Mini-NS will be designed to measure a minimum H abundance of $\pm 0.6\%$ WEH (600 ppm) $\pm$ 120 ppm with a spatial resolution of < 15 km (within 2-month nominal mission, orbital altitude of $\leq$ 10km). The trajectory and mission design will allow Mini-NS to produce maps at these spatial scales with counts binned once per second. Mini-NS was designed as a 1U $\times$ 3U module and has been integrated into a 6U cubesat which will be launched on the NASA Artemis-I vehicle.

4.3 Mini-NS Instrument Suite

4.3.1 Neutron Spectrometer

New inorganic, ultrabright, elpasolite scintillator materials, such as Cs_2YLiCl_6:Ce (CLYC), Tl_2LiYCl_6:Ce (TLYC), and $Cs_2LiLa(Cl,Br)_6$:Ce (CLLBC) are capable of detecting and discriminating both neutrons and gamma-rays based on differences in the shape of the scintillator light pulse. The Mini-NS instrument uses CLYC, which can achieve a gamma-ray energy resolution of approximately 4% full-width-at-half-maximum at 662 keV. The instrument consists of eight, 2-cm thick $\times$ 4 cm $\times$ 6.3 cm rectangular CLYC crystals, coupled to Hamamatsu PMTs; the individual crystals coupled to PMTs are termed *modules*. The combined eight modules provide a sensitivity similar to the 10 atm, 5.7 cm diameter He-3 tubes which were used for LPNS (Feldman et al., 2004). A comparison of the neutron energy intrinsic efficiency

124

for CLYC vs. He-3 is shown in Figure 4.1.
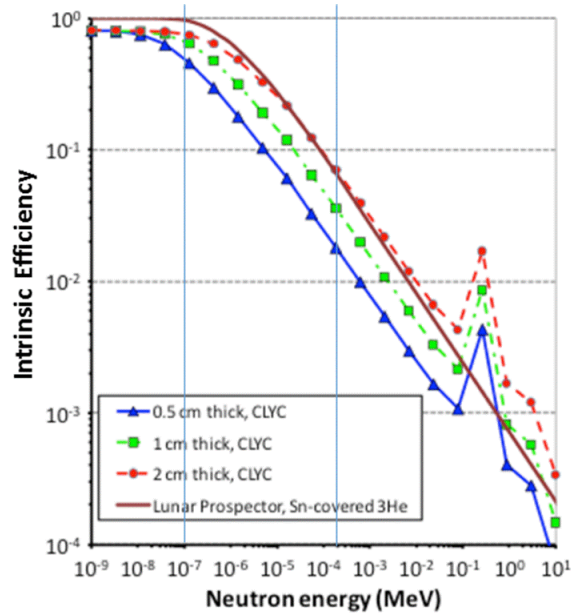
Figure 4.1: Intrinsic efficiency of CLYC compared to the Lunar Prospector Neutron Spectrometer (LPNS). The simulations show the number of ^{6}Li(n,a)^{3}H reactions as a function of neutron energy within a CLYC volume compared to the number of ^{3}He(n,p)^{3}H reactions in the LPNS (priv. comm. T. Prettyman).

A Gd shield (0.5 mm thickness) covers the majority of the CLYC sensor head to significantly reduce the number of thermal neutrons interacting with the scintillators and restricting Mini-NS sensitivity to epithermal neutrons with E > 0.4 eV. Figure 4.2 shows a dimensional schematic of the Mini-NS. The instrument is mounted as a module integral to the mechanical structure of the LunaH-Map cubesat.

The Mini-NS consists of two identical detector units (4 CLYC modules each) and each is equipped with a primary 32 GB SD card and a backup 32 GB SD card; a set of four CLYC crystals coupled to PMTs and readout using one analog to digital converter is defined as one *detector*, Figure 4.2B shows these as CLYC D00 and CLYC D01. A detector consists of the HV supply, amplifier, thermal sensors, relays, readout

125
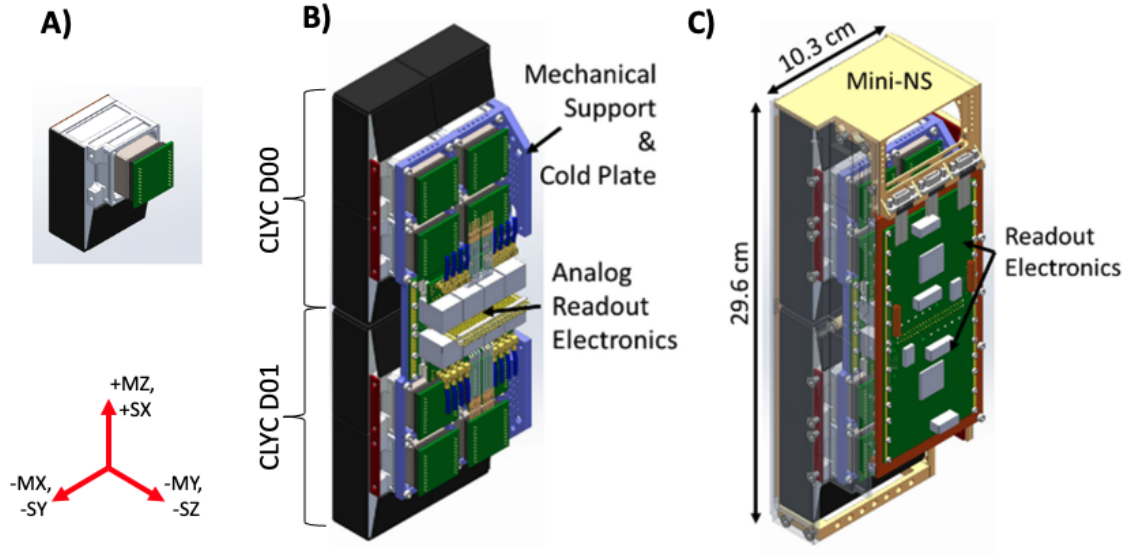
Figure 4.2: A) A CLYC module with PMT. B) The Mini-NS detector system with outer mechanics removed showing the eight CLYC modules and inner analog read-out electronics. C) The full structure of the Mini-NS instrument with housing and digital electronics board. The near-side panel is drawn as transparent to see into the instrument (Hardgrove et al., 2020). The coordinate system shown represents both the Mini-NS instrument coordinates (±M) and the spacecraft coordinates (±S).

electronics. The two detectors are labeled as CLYC-0 and CLYC-1; having two nearly identical detectors minimizes risk, if one were to fail the other can still acquire a useful data set. This configuration supports a possible neutron spectrometer design where one detector may be covered in gadolinium to reject neutrons below 0.4 eV and the other without to accept all neutrons for spectroscopy. As the LunaH-Map mission would have less than 200 orbits to map the southern lunar pole, both detectors were covered in gadolinium to enhance the epithermal signal. The instrument is therefore sensitive primarily to the flux of epithermal neutrons ($0.4 - 10^5$ eV), which varies with H content.

As the focus is on the detection of neutrons, the detector modules are designed

to optimize neutron sensitivity within a compact instrument housing ($\sim$2500 cm^3). The projected area along the +SZ/+MY-axis (Figure 4.2) is 25 cm^2 for each module, providing an effective area of 100 cm^2 per detector, 200 cm^2 in total. The total mass of the instrument is 3.2 kg, and the power consumption for the entire Mini-NS is 15.2 W when acquiring data. Additional specifications for the Mini-NS are shown in Table 4.1.

The Mini-NS uses pulse shape discrimination (PSD) to detect neutrons and gamma rays based on differences in the shape of the scintillator light-pulse. Typical pulse shapes for a neutron and a gamma ray are shown in Figure 4.3. Scintillation is based on core-to-valence luminescence (CVL), a mechanism that is selectively quenched (radiationless de-excitation process whereby energy is typically converted to thermal energy) by high linear energy transfer particles. The ^{6}Li(n,α)t reaction products completely quench the CVL mechanism, resulting in a change to the time profile of the de-excitation process during neutron excitation of the crystal; this time change is measurably distinguishable from gamma rays (Ferrulli *et al.*, 2021).

4.3.2 Data Acquisition System and Signal Processing

The data acquisition system (DAQ) uses a Xilinx Zynq XQ7Z020 field-programmable gate array (FPGA) to digitize waveforms from the scintillators. The signals from the PMTs are summed to a single analog to digital converter (ADC) operated at 250 mega-samples per second (MSPS). There are two signals from each detector module. The primary signal is a summed signal for all of the modules, which is routed through a buffer amplifier and a fast ADC. The ADC produces a signal that will be processed for determining if the event was from a neutron. The other signal is a logic pulse generated from an analog circuit that is triggered when there is a large signal from any of the modules, this is done via the voltage drop from the last dynode stage on
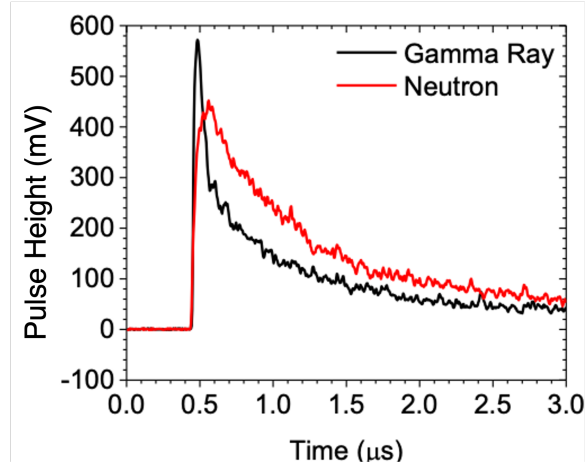
Figure 4.3: Typical CLYC output pulse shapes for a neutron (red) and a gamma ray (black). Note that the neutron pulse is slightly shorter and has less-immediate decay curve such that the two signals can be distinguished based on pulse shape discrimination (PSD). The PSD analysis method is described in Section 4.4.1.

the PMT. This logic pulse identifies which PMT generated the digitized waveform, allowing for data collection on a module by module basis. A basic block diagram of the data acquisition system is shown in Figure 4.4.

4.3.3   Software

The on board software environment operates on a Cortex Arm-9 Processor. The Cortex processor is packaged with the Xilinx FGPA and interfaced using an AXI bus. The FPGA was developed using Xilinx's Software Development Kit Version 2017.4. The system boots from either of the flash devices that contains the software for the processor and bitstream for the FPGA, and uses a polling method for control. Data can be saved onto an onboard SD card ($\sim$30 GB of free space) between orbits.

The algorithm programmed in the FPGA generates four integrals: a baseline integral, a short integral, a long integral, and the full integral; each of the last three

Mini-NS Specifications	
Instrument Dimensions	25 cm × 10 cm × 8 cm (2 Detectors)
CLYC Crystal Module Dimensions	4.0 cm × 6.3 cm × 2 cm
Detector Configuration	2×2 Array of CLYC Crystal Modules
Mass	3.4 kg
Power (both detectors)	3.6 W (standby), 9.6 W (nominal)
Sensitivities	Epithermal (E>0.3 eV) neutrons; Gd shield
Data Acq. Times	Counts binned every 1 second
DAQ Data Rate	14 Bytes/sec (50 kB/Sec stored locally)
Event Data Rate	2 events/sec
Downlink Data Rate	8 (low), 32 (nominal), 128 (high) Kbps
Cs_2YLiCl_6:Ce Specifications	
Density	3.31 g/cm3
Radiation Length	3.42 cm
Melting Point	640° C
Scintillation Light Yield	20,000 ph/MeV
Peak Scintillation Wavelength	370 nm (Temp. dependent)
Decay Constants	1 ns, 50 ns, 1 μs
Decay Time	≈ 400 ns, 1 μs, 6 μs
GEE for Thermal Neutrons	≈ 3.2 MeV
Energy Resolution (662 keV gamma)	4 %

Table 4.1: Basic Cs_2YLiCl_6:Ce (CLYC) crystal material properties are from (Johnson *et al.*, 2015; Glodo *et al.*, 2012; RMD Inc., 2021). Note that CLYC has three decay constants/times corresponding to the possible allowed energy transition states within the crystal. The gamma-equivalent energy (GEE) for thermal neutrons (fundamentally the electron equivalent energy) is approximated. Underlined values indicate dominant mechanisms.
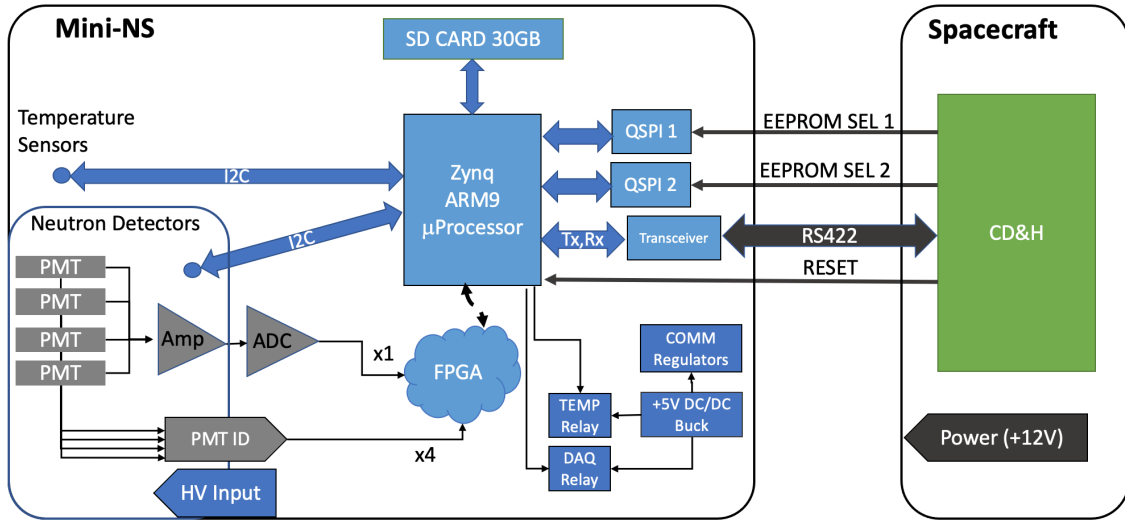
Figure 4.4: Data acquisition system flow block diagram for a Mini-NS detector. Four PMTs signals are summed as a primary signal into a buffer amplifier. The primary signal is sent to a fast ADC, then to the FPGA for processing. Secondary signals from the individual PMTs are tagged as a logic pulse for the PMT ID. The FPGA is a Xilinx Zynq XQ7Z020 with a Cortex Arm-9 Processor which includes onboard SD card storage ($\sim$30 GB of free space). Data is stored for each orbit before being downlinked to Earth. Flash devices contain the software for the processor and bitstream for the FPGA, these are connected to the command and data-handling (C&DH) of the spacecraft bus along with the main RS422 connection for data transfer.

integrals are corrected using the baseline integral. The short and long integrals are used to determine a PSD value and the full integral is used to generate the energy deposition. Details of the PSD calculation are found in Section 4.4.1. Figure 4.5 shows the basic onboard data processing flow programmed onto the FPGA for Mini-NS. Note that the event-by-event data (MNS_EVT) is partially processed onboard the instrument, resulting in 2D histogram data (MNS_2DH). Each detector system is completely separated from the other; there is no file sharing between CLYC D00

130

and CLYC D01 and any files generated by one detector system will not be recorded by the other detector system. Each detector system will continuously back up all the files it creates to the onboard SD card during operation.
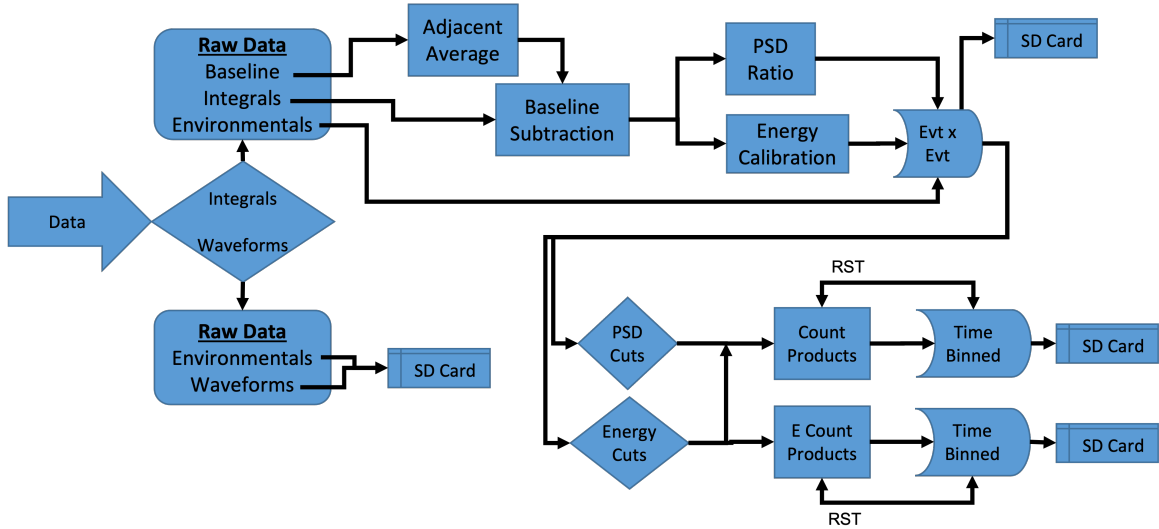
Figure 4.5: Mini-NS onboard data processing flow chart block diagram. The detector signals from the fast ADC are read into the FPGA and converted into raw data. Raw waveform and environmental data (temperature, time) are saved directly to the onboard SD card. The detector pulse signals (integral data) are processed according to the methods described in Section 4.4.1 then saved onboard. Data from the SD card can then be read from the FPGA via RS422 to the command and data handling (C&DH) on the spacecraft bus.

The Mini-NS creates system files and data files during normal operations with the option of acquiring diagnostic waveform files. When a data acquisition run is started, the system uses the detector ID number (D00 or D01) and an internal run number to create folders with a unique names to contain files created during specific DAQ runs. The output from the spacecraft is packetized in Consultative Committee for Space Data Systems (CCSDS) packets; – packets are described in Table 4.2

131

To inform the spacecraft that the Mini-NS is powered on and active, State of Health (SOH) data is generated on the FPGA roughly once per second as a CCSDS packet and sent to the RS422. SOH data packets contain temperature information, the most current neutron count calculation, and the local Mini-NS time. The Mode Byte in payload SOH packets informs the flight computer what mode (also referred to as states) the detector is currently in.

Data ID	Description
CommandSuccess	The input command was successfully executed
CommandFailure	The input command failed somewhere during execution
SOH	Packet contains statement of health information
LSFilesReturn	Packet contains filenames and file sizes for all the file on the Mini-NS SD card
Temperature	Packet with the most current temperatures.
MNS_CPS	Neutron Counts per Second Data
MNS_WAV	Waveform Data
MNS_EVT	Event by Event Data
MNS_2DH	2D Histogram Data (PSD vs. Energy, processed onboard)
MNS_CFG	Configuration File
Log	Log File
DirectoryFile	Directory Contents Metadata File

Table 4.2: Mini-NS CCSDS packet information. Note that MNS_2DH files are generated per individual module and that MNS_EVT data can be split into 4 files – filtered, unfiltered, decompressed, and compressed – depending on the commands sent to the spacecraft during downlink. The MNS_CFG file contains information describing the PSD cuts for all modules. The CommandFailure and CommandSuccess packets contain checksum information to validate the current set of data.

The Xilinx's electrically erasable programmable read-only memory (EEPROM)

can be flashed with non-flight firmware specific for calibration and thermal testing of the Mini-NS instrument at Los Alamos National Laboratory's (LANL) Neutron Free-in-Air Facility (NFIA). This firmware allows for event-by-event and module-by-module data to be read out via RS422 cable directly to a laptop computer from the Mini-NS without having to communicate with the LunaH-Map cubesat (baud rate of 921600 bits/sec for calibration). All calibration and test data exported from the Mini-NS are in binary format and include temperature, calibration, pulse integral (long, short, baseline), power input, computed PSD, module ID, and timing data. This non-flight firmware differs subtly from the flight version in that packets sent in to the Mini-NS system are done using basic .ttl file macros such that instructions are sent directly to the Mini-NS. The calibration software generates up to 20 data files, including a copy of the original binary file. These files also consist of a log file and individual energy ascii, PSD ascii, and Energy/PSD/counts plot files associated with each CLYC module on board the Mini-NS. The log file reports on all commands used in a typical measurement, as well as analog board temperature data, integration time, trigger threshold data, and integral cut data (e.g. baseline, short, long, full).

4.4 Data Processing

Data processing is done following a binary conversion process. Here we describe an analysis of both the MNS_EVT and the 2D histogram (MNS_2DH) data products for the Mini-NS. Note that much of the data processing can be performed onboard Mini-NS via the FPGA, we describe this process in the telemetry data. Ground data processing has been written in Matlab, Origin, and Python languages for ease of use, in this chapter we describe the use of Python 2.7.

4.4.1 Raw Telemetry Data Processing

On-board the Mini-NS, the PSD and energy values are calculated for each event and recorded to the SD card. Mini-NS uses PSD to identify neutrons and gamma rays based on differences in the shape of the scintillator light-pulse. The data is baseline corrected during flight; baseline correction uses a baseline integral to get an average of the baseline to be subtracted from the other integrals.

The waveform of the output pulse from the detector is segmented into short (I_S), long (I_L), full (I_F), and baseline integrals (the baseline signal prior to a pulse). I_S, I_L, and I_F are average baseline integral (B_{avg}) adjusted (the integral divided by the number of samples in the baseline integral), and then used to determine a pulse shape discrimination ratio. Equation (4.1) describes the calculation of the PSD value used to analyze the Mini-NS data sets:

$$PSD = \frac{I_S}{(I_L - I_S)}.$$ (4.1)

Note that I_F is the uncalibrated energy of the incident particle. When the energy of the pulse and the PSD ratio have been calculated, a calibration on the energy may be performed. The equation for this is estimated as a simple linear relation,

$$E = y_0 + \zeta \times I_F$$ (4.2)

Where E is the newly calibrated energy, y_0 is the energy calibration intercept, and ζ is the energy calibration slope. MNS_EVT data consists of all events registered in the Mini-NS and reports on the detector number (D00 or D01), module number (CH00-03), PSD value, energy value, time, and event number. There is no cut to this data, whereas the MNS_2DH data contains specific polygon cuts to the PSD and energy values, which can allow for smaller data transfers, rather than MNS_EVT

134

data.

A series of neutron cuts can be applied to each event to determine if the event resides within the cut window region. The data cuts aim to isolate the neutron count signal from gamma rays and other particles that interact in CLYC. Cutting the data to focus on the neutron signal allows for reduction in the data size, allowing easier transfer back to Earth. The window cut regions are user defined and may be changed (the cut window range is defined using parameters in the configuration file), and additional neutron count totals are determined using an energy cut window. An additional cut on the neutrons with wider (larger region of interest) parameters is also made. The user may define this second, wider window over any region of interest. Another count total is made where events above 10 MeV are aggregated. For overall data collection, the neutron counts are aggregated, and the data is sorted for filling the 2D histograms.

4.4.2 Ground Data Processing

Using Python 2.7, a program was developed to process the binary event-by event (MNS_EVT) data. The MNS_EVT is read in as a binary format (uint8), then converted to ascii via numpy-based scripts (Mckinney, 2010; Harris *et al.*, 2020). Events are tagged based on detector (D00 or D01) then tagged based on module identifier (CH00-03). These are then sorted into individual file sets for each PMT – all information such as PSD, energy, event ID number, and DAQ time are preserved. Table 4.3 lists the processed output files as a result of this program. Details of the Python data processing code can be found in Appendix E. The processed data can then be used to determine the total number of neutron counts per module, create PSD vs. energy heat maps, etc. An additional data visualization program is included with the Python program set for Mini-NS, Figure 4.6 shows the output of an MNS_EVT file

that has been processed for D00, CH00-03.

Filename	Description	Data
MNS[X]PMT0.dat	Detector X, module CH00	PMTid, energy, PSD value, FPGA time, EventID
MNS[X]PMT1.dat	Detector X, module CH01	PMTid, energy, PSD value, FPGA time, EventID
MNS[X]PMT2.dat	Detector X, module CH02	PMTid, energy, PSD value, FPGA time, EventID
MNS[X]PMT3.dat	Detector X, module CH03	PMTid, energy, PSD value, FPGA time, EventID
MNS[X]PMTALLPMTs.dat	Detector X all modules	PMTLogic, energy, PSD value, FPGA time, EventID
MNS[X]PMTALLVALIDPMTs.dat	Detector X all valid events	PMTid, energy, PSD value, FPGA time, EventID
MNS[X]PMTPMTextras.dat	Detector X all invalid events	PMTLogic, energy, PSD value, FPGA time, EventID
MNS[X]Pulser_Set.dat	Detector X, module CH00	FPGA time, EventID
MNS[X]Temp_Set.dat	Detector X, module CH00	EventID, Analog board temp, Digital board temp, Module temp

Table 4.3: List of processed Mini-NS data file names, converted to ascii formats and saved as .dat files. File formats can be switched to ,csv, .txt, etc. formats as user desires. MNS_EVT are downlinked per detector, such that our Python program processes the data per detector, resulting in four individual valid-event PMT files, and other combined PMT files. Temperature and pulser data is also processed into ascii formats. Note that [X] is replaced by 0 for detector 00, and 1 for detector 01. Valid/invalid events are based on the PMT logic pulse, for events shared between detectors the logic pulse is counted as invalid.

4.5 Calibration of the Mini-NS at Los Alamos

4.5.1 Facility Information

Calibration measurements using the Mini-NS flight model were completed at LANL TA-36, Building 214, in the NFIA facility. NFIA is a large room consisting of a tall, loss-mass platform which is ≈3.5 meters in height. The source and instrument, along with all stands, are place on top of the platform; the source location is automated via a tube/track system such that work can be done on the apparatus while the source is shielded and closed off below the platform. The source is ≈ 1 m away
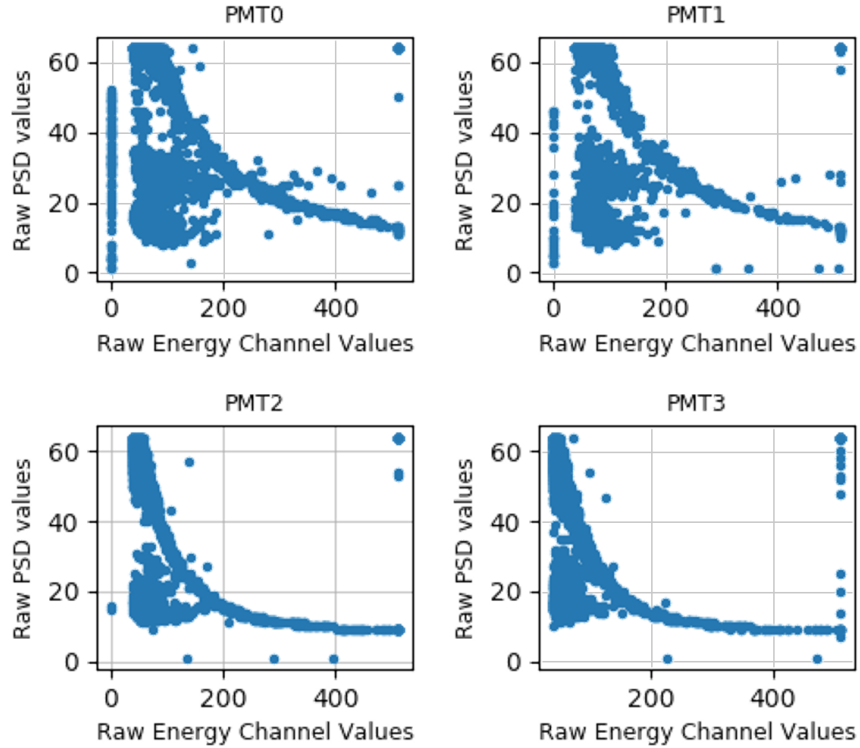
Figure 4.6: Example of the output PSD vs. energy plot of Mini-NS data taken using lab sources pre-flight on detector 00. Note that PSD energy cuts have not been done on this data such that the majority of counts are gamma rays.

from the back wall (Y-direction normal to the wall) and ≈ 2 m away from closest the side wall, while the instrument is located at distances from the Y-direction of the source. The facility houses both a ^{252}Cf source as well as an AmBe source; more details of the sources can be found in RI Scherpelz (2008).

4.5.2 Angular Calibration Procedures

The angular response of the Mini-NS instrument was determined using similar methods outlined for the GRaND (Prettyman *et al.*, 2012) and MESSENGER (Goldsten *et al.*, 2007) instruments, both of which were calibrated at NFIA. The Mini-NS

137

instrument was mounted on a rotating stage (0 - 360º) to enable control of the geometry with respect to the source. Table 4.4 shows a summary of the sets of measurements made with Mini-NS, all of which were done using a ^{252}Cf source, resulting in a total of 140 measurements.

For each set of measurements, the detector was placed a predetermined distance from the face of the source (e.g. 50 cm for LPNS, Mini-NS nominally at 200 cm) at a predetermined angle, and counts were recorded for a predetermined period of time (e.g. 640s for LPNS, Mini-NS nominally for 15 minutes to allow for a minimum of 10,000 counts in the neutron peak). The detector was rotated in place and the next measurement was made for the new relevant angle. This process was repeated for a range of angles from 0 to +180º; the original detailed measurement plan is included in Appendix F. After completing angular sweeps for bare and moderated ^{252}Cf across the Z-rotational axis, the Mini-NS instrument was removed from the rotating stage and reinstalled at a 90º angle from its previous orientation. The calibration was repeated with rotation along this axis (X-rotational axis). Figure 4.7 defines the different axes of the Mini-NS instrument with respect to the spacecraft.

4.5.3 Functional Performance

There are some basic functions required of the Mini-NS instrument for operation: 1) The PMTs must have the correct voltage applied per detector module in order to allow for multiplication of light from the CLYC crystals and therefore pulse signal outputs; 2) The pulse shape (waveform) of the output signal must have a baseline average that reads in an appropriate range such that the pulse shape of neutrons and gamma rays are distinguishable; 3) The gain of the individual modules are matched to within 1% MeV energy channel such that the count rate is consistent across all detector modules. These requirements were met during pre-test of the Mini-NS at

138

Source	Moderator	Distance	Rotation Axis	Angles Covered
^{252}Cf	Bare	2 m	Z	0°, 15°, 30°, 45°, 60°, 90°
^{252}Cf	Bare	2 m	X	0°
^{252}Cf, ^{137}Cs	Bare	1 m	X	0°
^{252}Cf, ^{137}Cs	Bare	1.5 m	X	0°
^{252}Cf, ^{137}Cs	Bare	2 m	X	0°
^{252}Cf, ^{137}Cs	Bare	2.5 m	X	0°
^{252}Cf	2"-thick poly	1 m	Z	0°, 15°, 30°, 45°, 60°, 75°, 90°, 135°, 150°, 180°
^{252}Cf	2"-thick poly	1 m	X	0°, 15°, 30°, 45°, 60°, 75°, 90°, 135°, 150°, 180°
^{252}Cf	2"-thick poly	2 m	Z	0°, 15°, 30°, 45°, 60°, 90°, 135°, 180°
^{252}Cf	2"-thick poly	2 m	X	0°, 15°, 30°, 45°, 60°, 75°, 90°, 135°, 150°, 180°
^{252}Cf	6"-thick poly	2 m	Z	0°
^{252}Cf	6"-thick poly	2 m	X	0°, 60°, 90°
^{252}Cf	Ø22 cm D$_2$O Sphere	2 m	Z	0°
^{252}Cf	Ø22 cm D$_2$O Sphere	2 m	X	0°, 60°, 90°

Table 4.4: Table of measurements taken during the Mini-NS calibration campaign at LANL's NFIA room facility. Sources included ^{252}Cf and ^{137}Cs, with the ^{137}Cs placed at 10" from the center of the Mini-NS face along the Y-axis (normal to the face) in the direction of the ^{252}Cf source. Additional shielding consisting of either 0.25" thick Gd or a LANL-provided "shadow cone" made of steel and high-density polyethylene were used for 0° measurements for bare, 2"-thick poly, and D$_2$O Sphere configurations. A total of 140 measurements were taken for integrated time between 180-1800 seconds. All moderators were placed around the ^{252}Cf source.
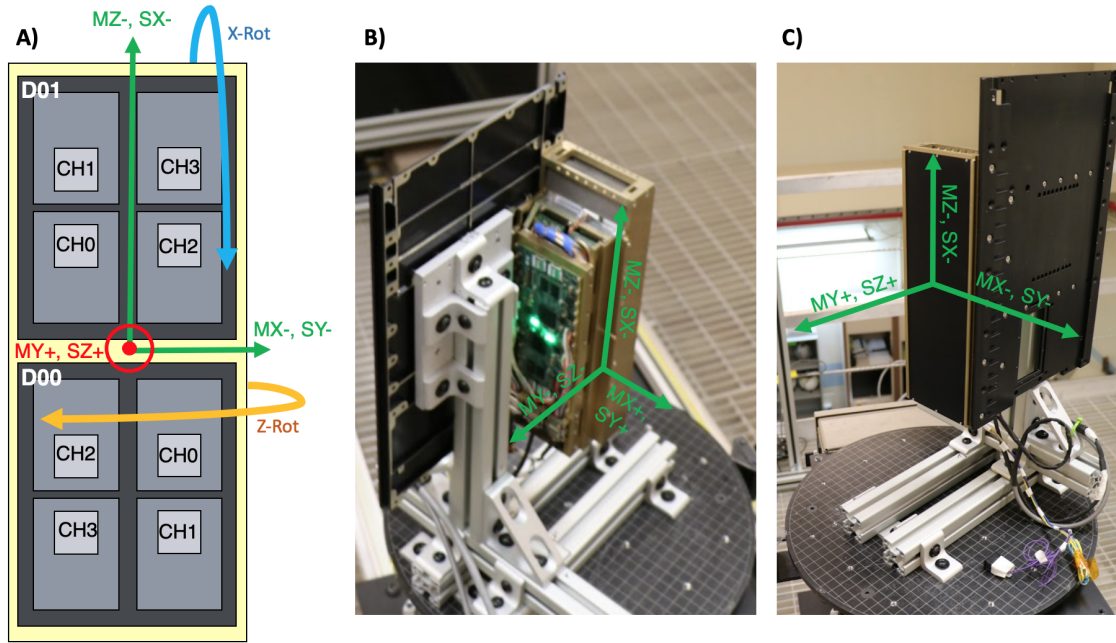
Figure 4.7: A) Diagram of the Mini-NS module (CHX) and detector (D0X) locations oriented to spacecraft (SX, SY, SZ) and Mini-NS instrument (MX, MY, MZ) axes (not to scale). For Z-axis rotations (labeled as Z-rot), measurements are taken as the instrument rotates clockwise about the MZ-/SX- axis according to this diagram. For X-axis rotations (labeled as X-rot), the instrument is remounted 90°, then measurements are taken as the detector rotates into the -ZM-axis and about the -MX-axis. B) Photograph of the back of the Mini-NS mounted on the test stand in Z-rotation mounting position. C) Photograph of the front of the Mini-NS mounted on the test stand in Z-rotation mounting position. The direction MY+/SZ+ will be pointed towards the lunar surface during the science phase.

the LANL NFIA room facility, the results are shown as PSD vs. energy vs. count rate plots in Figure 4.8 for detector 00, modules CH00 - 03.
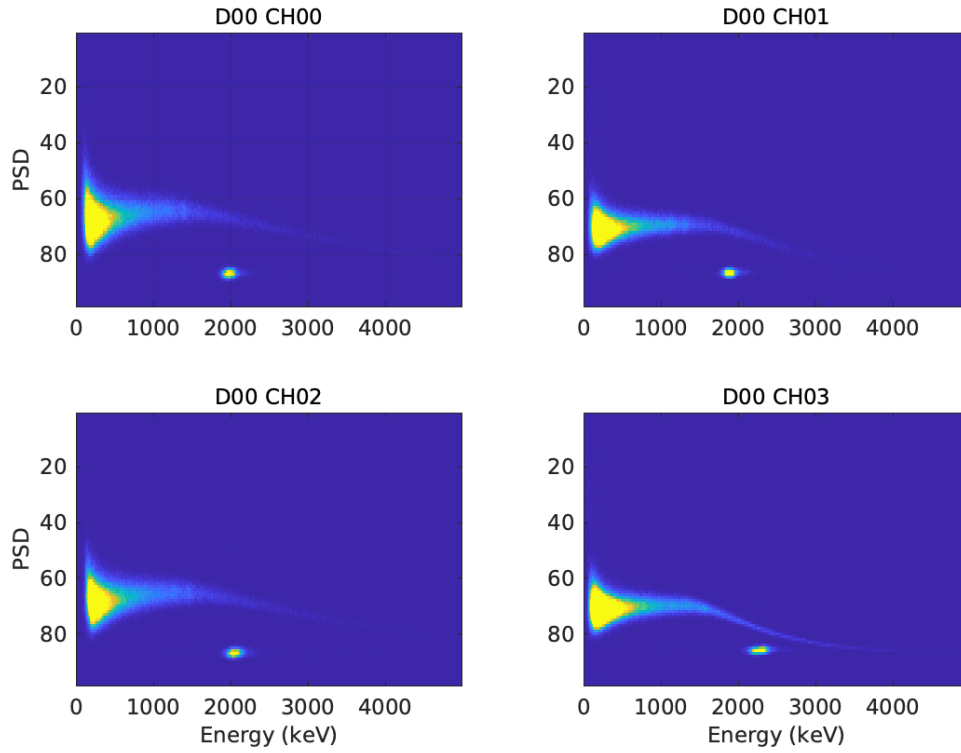
Figure 4.8: PSD vs. energy vs. count rate for the Mini-NS detector D00, modules CH00-03. Gammas rays typically have broad PSD values from $\sim$ 50 - 80 and energies spanning 0 - 4000 keV in this figure. Neutrons typicaly have PSD values centered at $\sim$ 90, with energy centered at 2.3 MeV. The intensity of the plot represents an increase in the count rate. This measurement was for 0° on Z-axis rotation with 2"-thick poly moderation on ^{252}Cf at a distance of 200 cm.

4.5.4   Spatial Resolution

The surface leakage current varies in proportion to the solid angle (Ω) subtended by the surface at a distance ($\vec{r}$). Topographic effects of the lunar surface may be imparted on the data such that a well-known instrument angular response is important for correcting the neutron count rate with the spacecraft orbital altitude and surface

solid angle. The *spatial response function* is determined through either experimental methods (this chapter) or by Monte-Carlo modeling of the detector/spacecraft; this function can be used to back out the actual number of neutron counts emitted from the lunar surface. *Spatial resolution* is represented by the distance apart that two equal point sources must be before they can be distinguished; typically, for orbital altitudes less than a body radius, the spatial resolution is approximately 1.5 × full-width-at-half-maximum arc length along the surface (Prettyman *et al.*, 2019a).

To determine the spatial response function of the Mini-NS instrument, we looked at individual detector modules, their individual angular responses (counts vs. angle), and their location on the instrument with regard to the source, and their distance to the source (R). The 2"-thick poly moderated ^{252}Cf at the 2 m distance was used in Figures 4.9 - 4.10 which show the initial responses of detector 00, modules CH00-03 for Z and X rotational directions, respectively; Figures 4.11 - 4.12 show initial responses of detector 01, modules CH00-03 for Z and X rotational directions, respectively, using the same source configuration.

4.5.5   *Spatial Response Function*

The response function described in Goldsten *et al.* (2007) for the MESSENGER neutron spectrometer assumes the use of a function that is valid for a thin, circular planar detector. Each Mini-NS detector module consists of 2 cm × 4 cm × 6.3 cm CLYC crystals oriented into an array-like configuration, thus the thin planar angular-only response can not be used. Instead, we opted to determine the spatial response function experimentally. The following assumptions for the behavior of the Mini-NS have been made: 1) Off-axes detectors rotation cause a change in the value of R^2 due to forward/backward tilt towards/away from the source; 2) The projected area of the detector changes as a function of angle due to the significant thickness of the

142
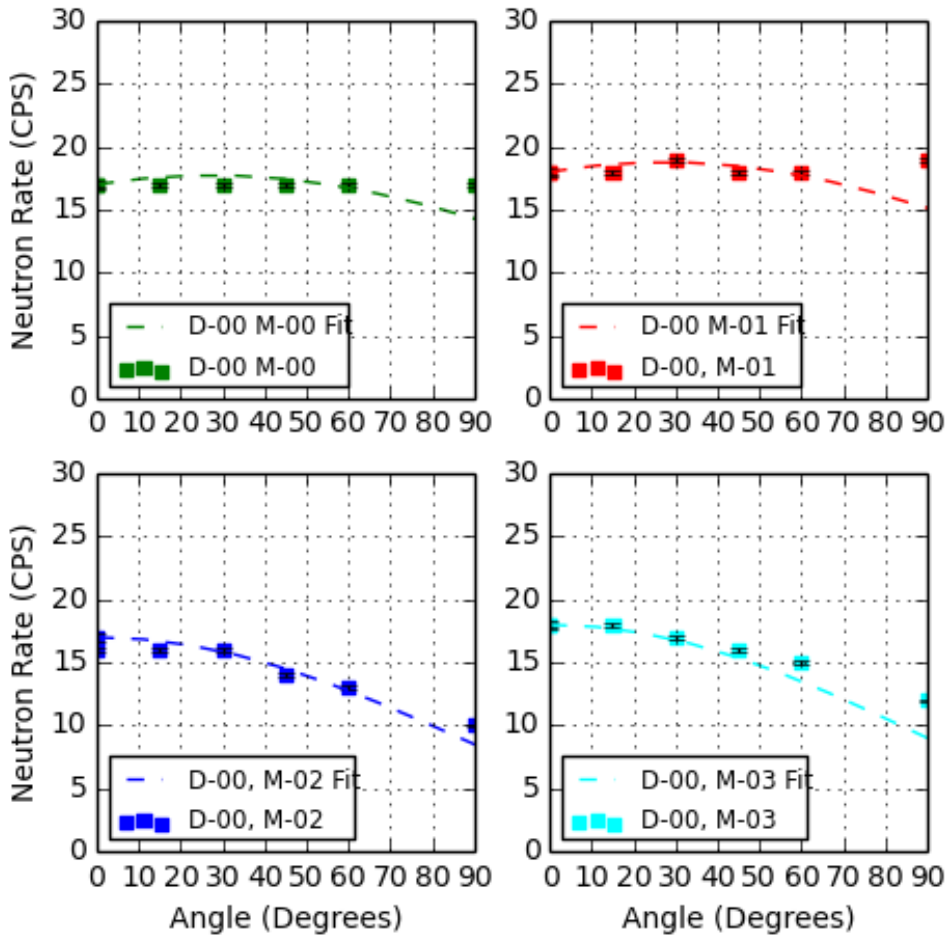
Figure 4.9: Count rate (neutrons/second) vs. incident angle (degrees) plots for detector 00, modules CH00-03 with angle rotating about the Z-axis using 2"-thick poly moderated ^{252}Cf at a 1 m distance from the source. Subplots are labeled in the upper left corner according to which detector and module is plotted. The dotted line on each plot represents the spatial response function for that specific detector module. The spatial response functions are described in section 4.5.5. Note that modules CH00 and CH01 appear to have a more flat and linear response as a function of angle, whereas modules CH02 and CH03 have curved responses.

143
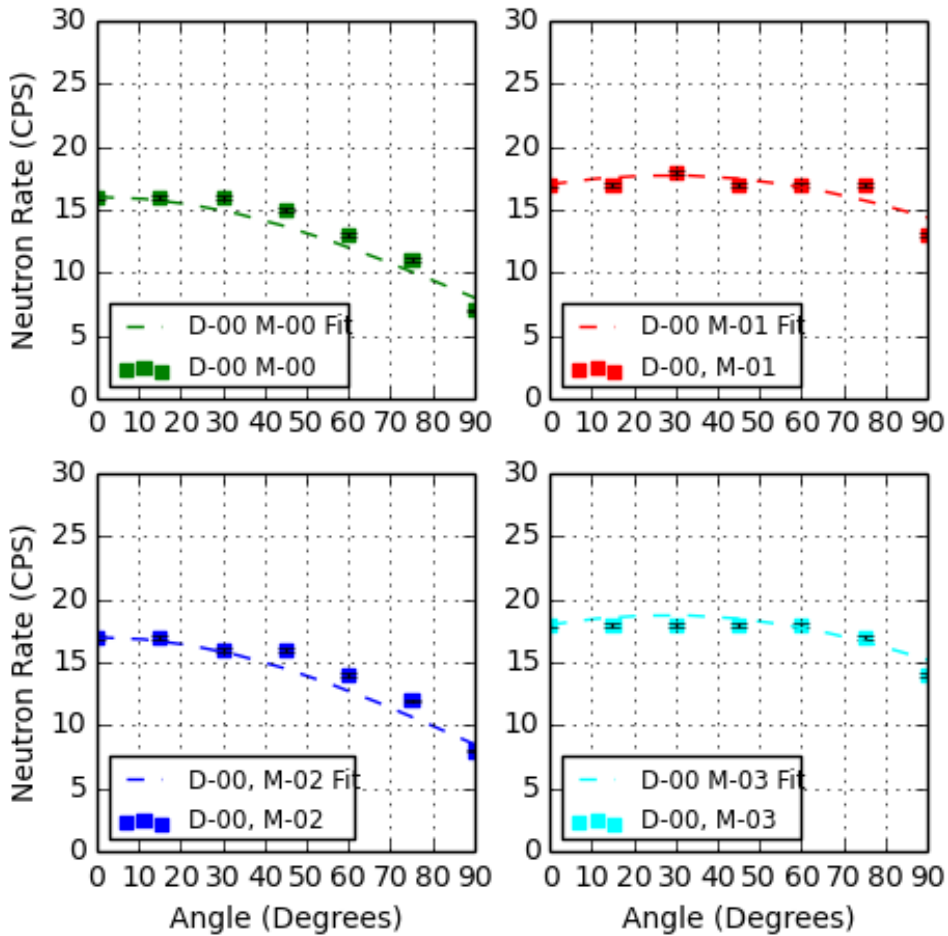
Figure 4.10: Count rate (neutrons/second) vs. incident angle (degrees) plots for detector 00, modules CH00-03 with angle rotating about the X-axis using 2"-thick poly moderated ^{252}Cf at a 1 m distance from the source. Subplots are labeled in the upper left corner according to which detector and module is plotted. The dotted line on each plot represents the spatial response function for that specific detector module. The spatial response functions are described in section 4.5.5. Note that modules CH01 and CH03 appear to have a more flat and linear response as a function of angle, whereas modules CH00 and CH02 have curved responses.
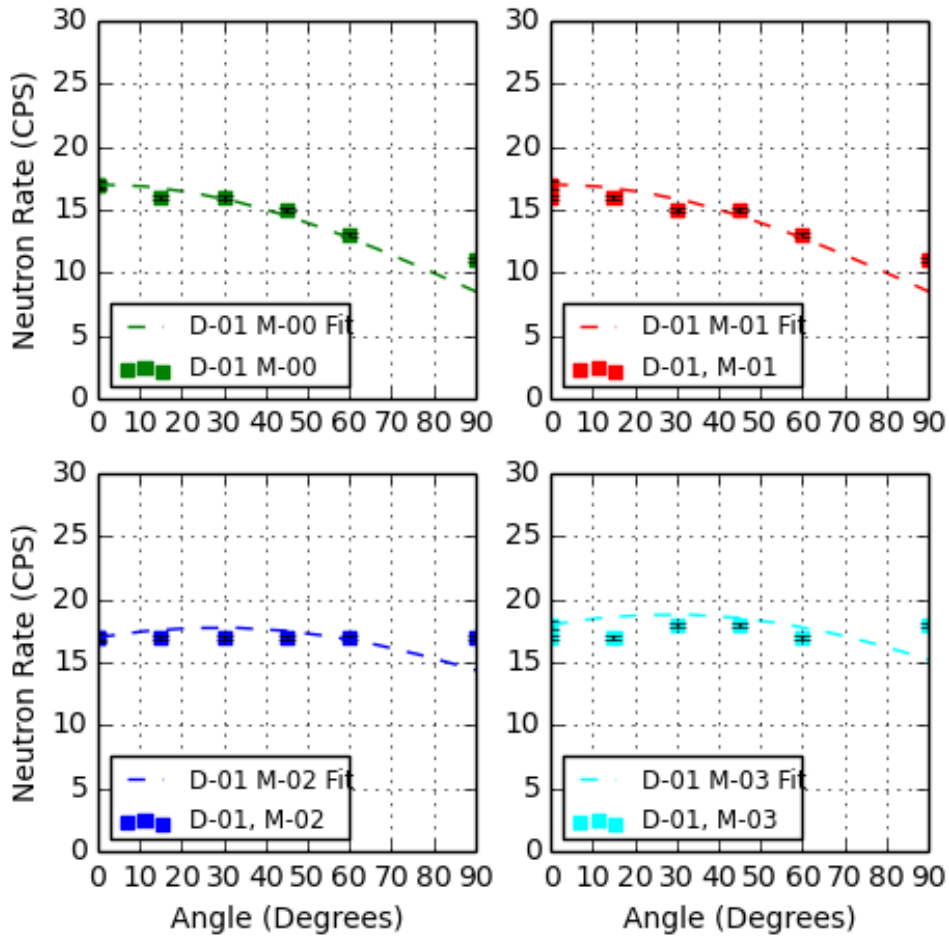
Figure 4.11: Count rate (neutrons/second) vs. incident angle (degrees) plots for detector 01, modules CH00-03 with angle rotating about the Z-axis using 2"-thick poly moderated ^{252}Cf at a 1 m distance from the source. Subplots are labeled in the upper left corner according to which detector and module is plotted. The dotted line on each plot represents the spatial response function for that specific detector module. The spatial response functions are described in section 4.5.5. Note that modules CH02 and CH03 appear to have a more flat and linear response as a function of angle, whereas modules CH00 and CH01 have curved responses.
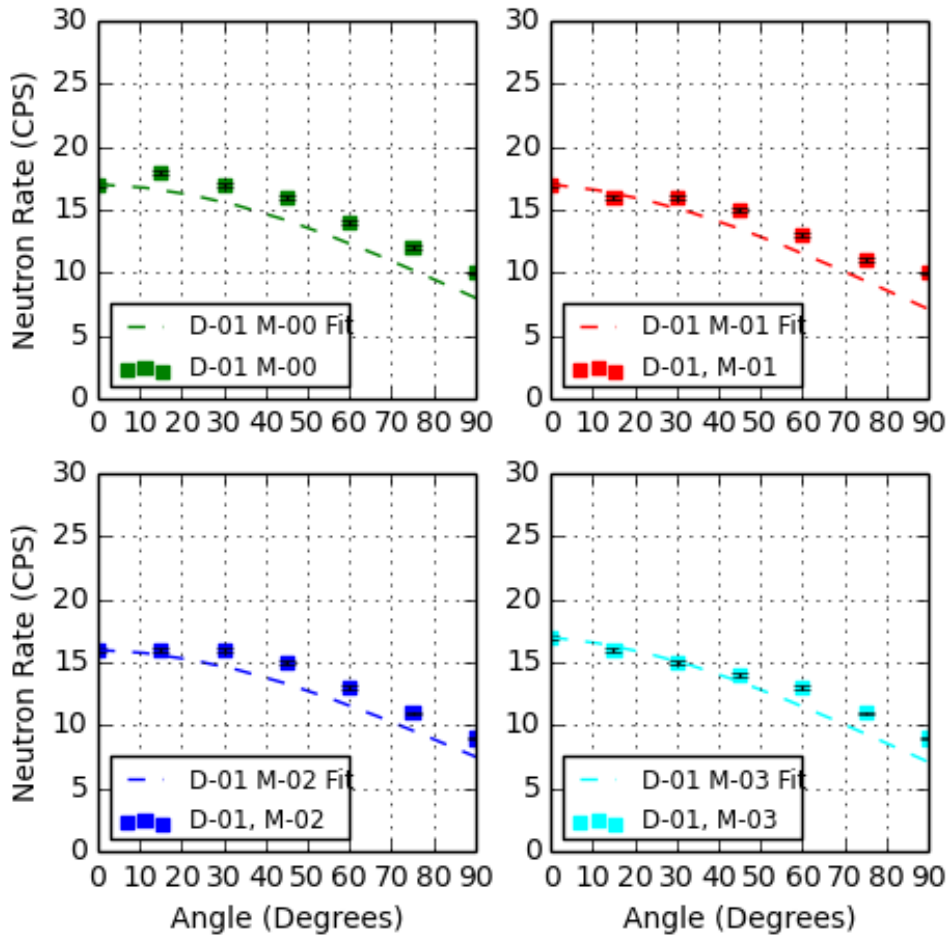
Figure 4.12: Count rate (neutrons/second) vs. incident angle (degrees) plots for detector 01, modules CH00-03 with angle rotating about the X-axis using 2"-thick poly moderated ^{252}Cf at a 1 m distance from the source. Subplots are labeled in the upper left corner according to which detector and module is plotted. The dotted line on each plot represents the spatial response function for that specific detector module. The spatial response functions are described in section 4.5.5. Note that all modules have curved responses as a function of angle.

CLYC crystals; 3) Contributions from the side wall cause an asymmetric increase in the count rate; 4) The volume of crystals at critical angles can cause shadowing onto crystals further away from the source. We will address each of these assumptions and their subsequent contributions to the spatial response function as follows.

Off-axis Correction Factor

As the entire detector rotates, individual modules tilt forwards towards the source, or backwards away from it. Due to the modules being off-axes of the axis of rotation, the change in rotation affects the total distance from an individual module to the neutron source; Figure 4.13 shows a basic concept geometry diagram. If R is the distance from the center of the detector to the source, the total number of counts reaching the detector varies as a function of $1/R^2$ (Knoll, 2010). Since none of the modules are located at the center of the detector, all modules are considered off axis to different extents depending on the orientation of the instrument. For example, in the X-rotational axis modules D01 CH01 and D01 CH03 are a further distance ($\sim$ 9.45 cm) from the center of the instrument compared to modules D01 CH00 and C01 CH02 ($\sim$ 3.15 cm), this allows for a shorter distance to the source when D01 CH01 is rotated inwards toward the source.

The following equation is given as an approximation for the number of counts hitting the detector. For one module, we assume that counts are proportional to the flux (Φ) of neutrons multiplied by the solid angle (Ω) of the module. For a thin, circular planar detector, this is then equal to Φ multiplied by the detector area (A), divided by the distance (R) squared:

$$\frac{Counts}{Crystal} \propto \Phi \times \Omega \propto \frac{\Phi \times A}{R^2} \tag{4.3}$$

The following calculation is then made to account for the change in R as the

detector tilts. We simply make a ratio to account for the slight change in R, whereby the total number of counts must be equal to the original $Counts/Crystal$ multiplied by the Off-Axis Correction Factor (OACF):

$$OACF = \frac{R^2}{(R \pm L_1 \sin \theta)^2} \tag{4.4}$$

$$\frac{Counts_{corrected}}{Crystal} = \frac{Counts}{Crystal} \times OACF \tag{4.5}$$

Where L_1 is the distance to the center of the CLYC module in question and θ is the angle of rotation of the detector; the "$\pm$" is used to designate backward (+) or forward (-) tilt in regard to the distance to the source. Note that as R $\rightarrow \infty$, $L_1 \lll$ R, and the value of OACF $\rightarrow 1$, such that at $\sim$km orbital altitudes, there is no significant off-axis effect. However, this is important to take into account for laboratory calibration measurements (R $\simeq$ 2 m) in order to fully characterize the instrument spatial response.

We take off-axis effects into account in our analysis of lab measurements by dividing the count rate data by the OACF in order to remove any dependency on distance within the data. This allows us to directly compare the data at 1 meter and 2 meter measurements allowing us to determine the spatial response function independent of the distance. As previously stated, as R $\rightarrow \infty$, the OACF = 1.0 such that the distance no longer needs to be taken into account.

Projected Area Correction Factor

Prettyman *et al.* (2019a) describes the efficiency-area product (ϵA) as the product of the intrinsic efficiency (ϵ) and the area of the sensor projected in the direction of the incident particle (A); we relate this to the Projected Area Correction Factor (PACF).
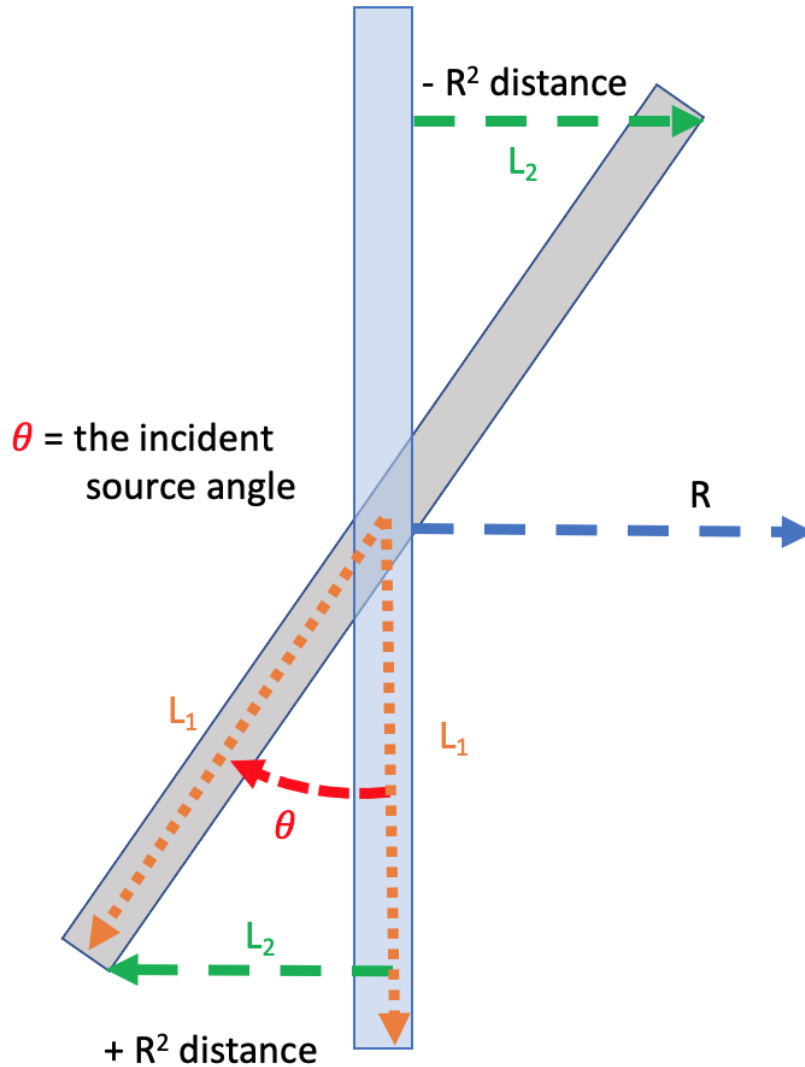
Figure 4.13: OACF geometry diagram: The angle θ represents the angle that the detector rotates into, this is consistent with the rotation angle described throughout the spatial response function results. L_1 is the lever arm in units of cm, typically this is the distance from the center of the detector to the center of a CLYC module, this varies from 2 - 9.45 cm, in the diagram it is shown as the full length. L_2 is the distance a module tilts forwards or backwards, depending on its location in the detector, it is calculated as $L_2 = L_1 \sin \theta$.

As the Mini-NS instrument rotates, the edge closest to the source begins to rotate into the incident source direction causing an increase in projected area, this leads to an increase in the observed count rate for edge module(s). The increase in counts for an edge module is assumed to be the most significant cause of the the "flattening" effect seen in specific modules shown in Figures 4.9 - 4.11. Figure 4.14 shows a simple diagram of the projected area increasing as a module rotates from 0 to 90°. Figure 4.15 shows the module geometry as the detector rotates.

Similar to the OACF, the PAFC is calculated using some assumptions, where again we look at Equation 4.6, but this time we rearrange the location of the area, A:

$$\frac{Counts}{Crystal} \propto \frac{\Phi}{R^2/A} \tag{4.6}$$

Using the geometry provided in Figure 4.15 we can then determine the projected areas of source-facing edge modules, as well as the remaining modules:

$$PACF_{ZRot-edge} = h \times [(d)\cos\theta + (t)\cos(90^o - \theta)] \tag{4.7}$$

$$PACF_{XRot-edge} = d \times [(h)\cos\omega + (t)\cos(90^o - \omega)] \tag{4.8}$$

$$PACF_{ZRot} = h \times (d)\cos\theta \tag{4.9}$$

$$PACF_{XRot} = d \times (h)\cos\omega \tag{4.10}$$

Where θ and ω are the angle of rotation of the instrument with regard to the incident source for Z and X axes, respectively, and d (4 cm), h (6.3 cm), and t (2 cm) are dimensions of the CLYC crystal geometry listed in Table 2.1. For use on the spacecraft, the angle θ must be reassigned for at least one rotational set (hence

150
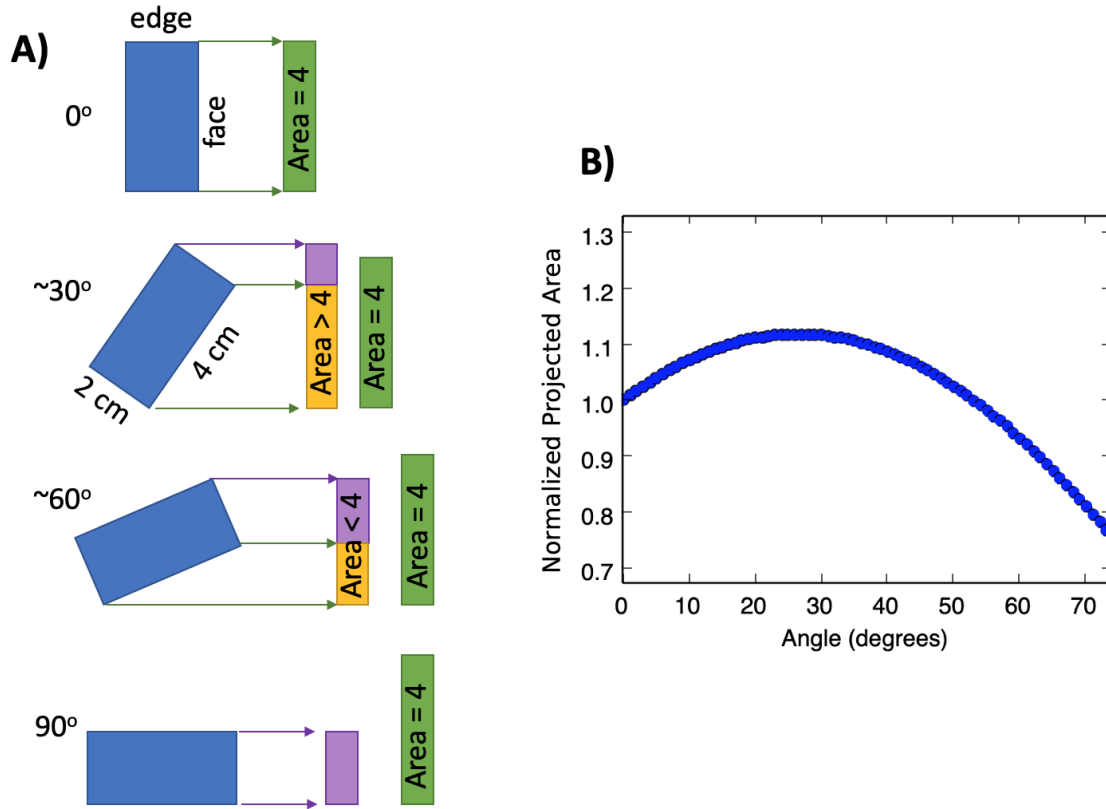
Figure 4.14: A) As the Mini-NS instrument rotates, the edge closest to the source begins to rotate into the incident source direction causing an increase in projected area (purple box), leading to an increase in the count rate for that crystal. The yellow boxes represent the front facing side of the detector's projected area, the purple boxes represents the crystal edge's projected area, the green boxes represent the 0° projected area for comparison. B) If the the combined projected area (purple + yellow) is plotted versus angle, it reaches a maximum at $\approx 27^o$ when the module is going through Z axis rotation. Note that this calculation is normalized to the 0° projected area.

ω instead of θ for the X rotational axis). Note that these functions will result in a combined piece-wise function to describe the total instrument spatial response. We

151
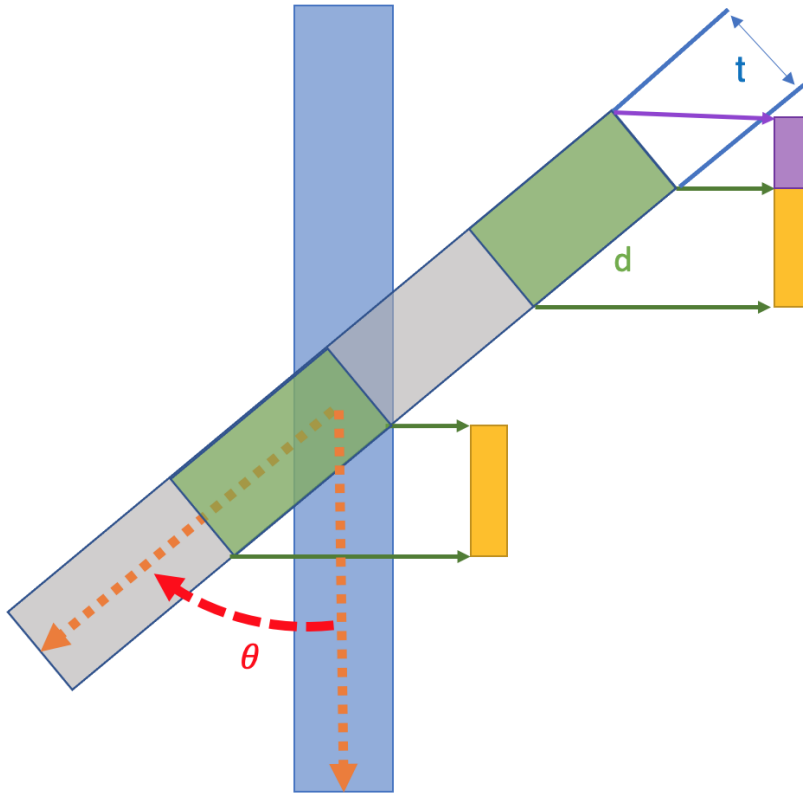
Figure 4.15: As the Mini-NS instrument rotates, the edge closest to the source begins to rotate into the incident source direction causing an increase in projected area (purple box), leading to an increase in the count rate for that crystal. Diagram showing the geometry for calculating the PACF. The angle θ represents the angle that the detector rotates into, this is consistent with the rotation angle described throughout the spatial response function results. The "t" dimension represents the thickness of the CLYC crystal (2 cm), the "d" dimension represents the length of the CLYC crystal (4 cm for Z rotational axis, 6.3 cm for X rotational axis). The last dimension, "h" (not shown), is the height of the CLYC crystal (6.3 cm for Z rotational axis, 4 cm for X rotational axis).

can then apply the PACF to get a corrected count rate:

$$\frac{Counts_{corrected}}{Crystal} = \frac{Counts}{Crystal} \times PACF \tag{4.11}$$

Shadowing Correction Factor

We followed the general functional form of the efficiency equation described by Karge et al. (2017) used to describe shadowing effects in arrays of ^{3}He tubes. The functional form describing the efficiency of a shadowed detector is as follows:

$$\frac{Counts_{shadowed}}{Crystal} = \frac{Counts}{Crystal} \times (-2A_s \sin\theta) \tag{4.12}$$

Where θ is the rotated instrument angle about the Z axis (for X axis use ω), and A_s represents a unitless, combined constant containing the absorption coefficient for an epithermal neutron passing through Cs_2LiYCl_6:Ce, as well as geometric information pertaining to the individual crystal shape (accounting for limits of the particle path).

Applying the Correction Factors

The correction factors must be applied according to the direction that the Mini-NS individual modules are facing with regard to the source, resulting in a piece-wise function. The simplified, resulting orbital spatial response function, which is unique for each individual module, is multiplied by the original number of counts per module dependent on the instrument angle with respect to the location of the lunar surface. A general form of the piece-wise response function is shown as follows:

$$\frac{Counts_{corr}}{Crystal}(\theta,\omega) = \frac{Counts}{Crystal} \times \begin{cases} [PACF(\theta,\omega)_{Edge} - 2A_s \sin(\theta,\omega)], & \text{Edge faces Moon,} \\ & (\theta,\omega) < 90^o \\ [PACF(\theta,\omega) - 2A_s \sin(\theta,\omega)], & (\theta,\omega) < 90^o \end{cases}$$

$$(4.13)$$

Where PACF is determined based on z-rotational angle (θ), x-rotational angle (ω), and whether side edges are facing the lunar surface. The PACF contains geometry information for individual crystals as an initial multiplying constant and is determined via best fit using Python Numpy (Harris *et al.*, 2020), the values are within an expected range of values for the crystal dimensions. For an orbital detector, the room return is removed and in its place is the spacecraft background. The average number of neutrons per second hitting Mini-NS during the cruise phase (prior to orbital insertion) are considered to be a result of GCRs interacting with the spacecraft; this count rate can be subtracted from the count rate taken during the science phase (in orbit). The dead time must also be taken into account and is calculated as a % per degree per module, this will be discussed and applied in a future publication.

Figure 4.16 shows the results of applying the spatial response function for a non-edge module about the Z axis of rotation for both 1 meter and 2 meter measurements for incident angles from 0 - 75°. The figure shows the data normalized to the count rate at 0° incidence. We performed best fits of the spatial response function for the constant for PACF (h, t, and d) and the constant for shadowing (A_s) across all modules.

4.6 Summary and Future Work

The spatial response function of the Mini-NS instrument is more complex than that of a simple planar detector due to its array configuration geometry and thick
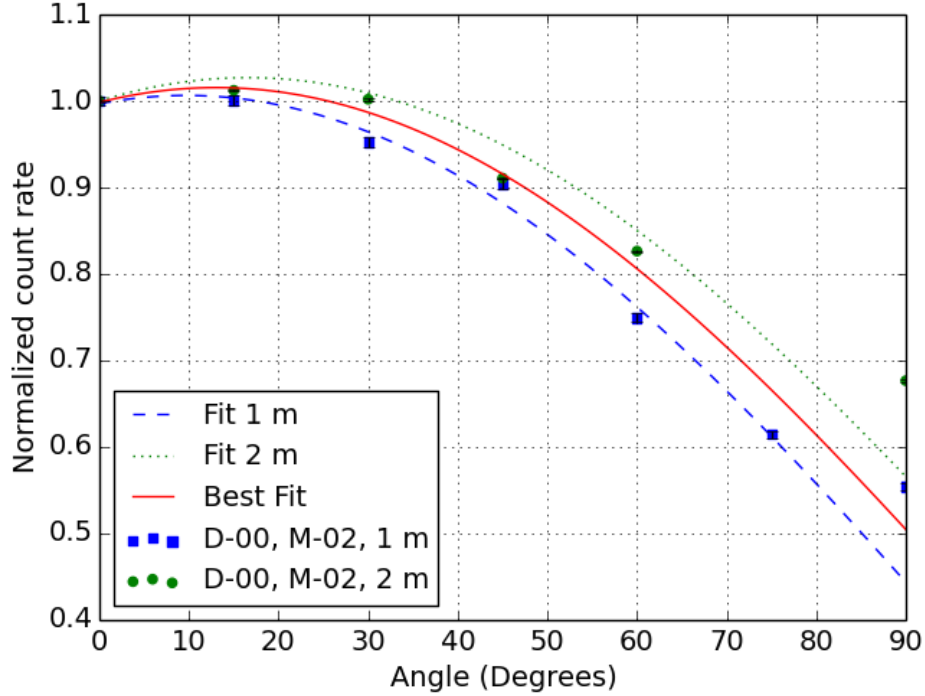
Figure 4.16: Detector 00, Module 03 normalized neutron count rate data from 0 to 90° compared to best fits using the spatial response function described in Eq. 4.13. Data has been normalized to 0° count rates and curves are fit from 0 - 75°, meaning that fits do not account for events hitting the back-side of the detector (some room return is assumed to be hitting at 70 - 90°).

CLYC crystals. We conclude that the spatial response can be estimated from experimental calibration data based on assumptions involving the geometry of the instrument. Improvements can be made to the instrument calibration spatial response function for Mini-NS through the addition of MCNP simulations.

This chapter represents significant contributions done by a single co-author on a space-flight instrument, primarily consisting of the calibration campaign and parts

of the data processing. A full manuscript of this work is intended to be written in the coming year that will include additional details from other co-authors such as: MCNP spatial response modeling, instrument dead time calculations, thermal testing and response functions, vibration testing, C&DH of the instrument, additional details on the software, signal, and data processing, and additional details relevant to the Mini-NS instrument onboard the NASA LunaH-Map mission.

Chapter 5

THE FINAL FRONTIER:

OUTLOOK AND SUMMARY

5.1   Synthesis of Contributions

Space is humanity's final frontier, full of strange new worlds in which we seek to boldly go where no one has gone before, a frontier offering habitation space for humanity's ever-expanding population to live long and prosper. The studies and experiments described in the previous chapters cover new active nuclear technologies and techniques to be used to gather information in the pursuit of efforts to *boldly go*. Our universe contains infinite diversity in infinite combinations and many of the studies presented here tackle very few of these diverse combinations.

In contribution to the development of new technologies, I introduced the SINGR instrument which uses a new type of elpasolite CLYC scintillator capable of detecting both neutrons and gamma rays. I performed experiments at NASA GSFC GGAO using SINGR with a high-energy DT (14.1 MeV) neutron generator in a pulsed-mode operation to collect temporal neutron and gamma-ray data. I was able to complete analysis of experimental neutron data along with MCNP simulation studies for ground-truth verification of the neutron die-away method (Heffern *et al.*, 2021). In addition to the CLYC scintillator on SINGR, I wrote, oversaw, and implemented the calibration plan for the NASA LunaH-Map mission Mini-NS instrument at LANL in the NFIA facility. The Mini-NS is also a CLYC-based instrument and will be the first single scintillator neutron and gamma-ray instrument to orbit the Moon; it is expected to launch in the early 2020's. Mini-NS is an array-type instrument, consisting of

individual CLYC crystals such that the angular response is highly dependent upon the crystals' orientations to a neutron source. In addition to implementation of the calibration procedures, I performed an analysis of the resulting data to determine the experimental spatial efficiency and angular response function of the Mini-NS. This angular information will aid in reporting accurate count rates coming from the lunar surface during the science portion of the mission, thus helping to map the abundance of hydrogen deposits in the south lunar pole.

In contribution to developing new techniques for planetary science, I studied the potential use of temporal neutron measurements on the hypothesized surface of Titan through Monte-Carlo simulation models. Temporal neutron measurements had not been used previously for high-hydrogen environments. The simulations that I performed suggest that shallow sub-surface layering (4 cm) can be identified in high-H environments using the die-away method, though I place limits on the method for use in such environments. The nuclear environment on a high-hydrogen world is unlike that of silicate-dominated bodies, such that detailed planning for the environment is important for instrument operations in the future. Applications of neutron die-away are not limited to dry, silicate dominant environments, in fact studies are underway by LANL for antarctic field tests of active neutron and gamma-ray instruments (priv. comm. S. Nowicki). Sights are set on the martian poles for future landed active neutron geologic investigations.

5.2 The Continuing Mission

As mentioned in Chapter 1, there are many planetary science missions launching in the next decade that will carry GRNS instrumentation designed to map the elemental composition of many different planetary bodies. In the following sections I describe some ideas for future work and and ongoing contributions to the field of nuclear

planetary spectroscopy.

5.2.1   The Mini-NS

The LunaH-Map mission will launch on NASA's Space Launch System in the early 2020's then go on to orbit the south polar region of the Moon in search of water-ice. Data analysis code will need to be fully developed for analyzing mission science data as it comes down from the spacecraft. My contributions to Mini-NS included unpacking and formatting the LunaH-Map flight test data, a NASA program similar to Planetary Data Archiving, Restoration, and Tools (PDART) would be ideal for funding the further development of this mission data analysis code.

In addition to data analysis, the next iteration of the Mini-NS instrument is on the LunaH-Map teams' minds. New dual particle elpasolite scintillators, such as $Cs_2LiLaBr \times Cl_6$ (CLLBC), have higher densities than CLYC meaning that their gamma ray efficiency is higher, and they have shorter decay constants making them more useful for active measurements and high count rates.

5.2.2   Nuclear Imaging

Advancements in silicon photomultipliers (SiPMs) allow for scintillator detectors to be made in smaller packages. More recent developments by LANL, Lawrence Berkeley National Laboratory, and private companies have taken traditional scintillator detectors and packaged them into large arrays of small crystals, enabling neutron and gamma-ray imaging of 3-dimensional rooms and terrain. These imaging detectors are small and robust enough to fly on drones; it is only a matter of time before these innovative technologies appear on landed rover missions to Mars and the Moon. GRNS imaging detectors alongside standard imagers (e.g. MSL's MastCam) could provide detailed composition data (at depth) in a geomorphological context.

5.2.3 Facilities for Active Planetary Investigations

There is a need in the US planetary science community for dedicated active neutron facilities and the funding that goes along with running them and in procuring large well-characterized samples. The GSFC GGAO testing site has been upgraded with large geodesic domes, but still suffers from non-symmetric field-of-view measurement issues. A LLNL dome testing facility is contained within a decommissioned reactor room which is surrounded by thick, cement walls which can interfere with measurements via room return.

One ideal facility for future active GRNS measurements could consist of a large, hangar-like facility with a suspended central support for testing of large geologic materials. Such a facility would need to house neutron generators as well as spontaneous fission sources and alpha neutron sources, along with a variety of both gamma-ray and neutron spectrometers. Ideally, multiple neutron spectrometers would be posted at equidistant locations away from the source material and contain varying layers of shielding so as to create a multi-band neutron spectrum. Proper calibrations and understanding of the responses of GRNS instrumentation are vital for accurate interpretation of orbital and landed results on planetary bodies.

5.2.4 An MCNP Tool for Planetary Science

As mentioned throughout this work, I have developed the beginnings of an MCNP Python program that generates elemental and layering grid models of planetary scenarios. Though still in its infant stage, the outline of that code is included along with a link to its current version in Appendix B of this dissertation. Previous nuclear planetary open-source codes have been reported on but are not currently publicly released online (Peplowski *et al.*, 2018). The ultimate goal of this work is to create a publicly

accessible code which allows a user to generate basic simulations of planetary scenarios and investigate the use of GRNS instrumentation. However, the MCNP back-end of this code is export-controlled such that associated libraries are not fully in the public domain, so running the code requires either access to a cluster that has MCNP installed and available to the user or possession of the source code (limited to US citizens). The intention of this toolkit is for it to be used by non-nuclear experts to get initial first-pass answers as to whether or not GRNS instrumentation may be useful for their mission scenario and which types of specific GRNS instruments may be able to reach their science goals. Such a toolkit is beneficial for the nuclear planetary science field, as it will contribute to increasing demand of these instruments onboard future missions. Additional future work on this toolkit will include implementation of GEANT4, a simulation code similar to MCNP.

REFERENCES

Adler & Trombka, *Geochemical exploration of the moon and planets* (SPRINGER-VERLAG, 1970), 1st ed edn.

Aharonson, O., A. G. Hayes, P. O. Hayne, R. M. Lopes, A. Lucas and J. T. Perron, *Titan's surface geology*, pp. 63–101, Cambridge Planetary Science (Cambridge University Press, 2014).

Ametek Inc., "Detective X Ultra High Resolution HPGe Radioisotope Identification Device The New "Gold Standard" for Mission Critical Detection and Identification", URL https://www.ortec-online.com/ (2018).

Artemieva, N. and J. Lunine, "Cratering on Titan: impact melt, ejecta, and the fate of surface organics", Icarus **164**, 2, 471–480 (2003).

Atreya, S. K., E. Y. Adams, H. B. Niemann, J. E. Demick-Montelara, T. C. Owen, M. Fulchignoni, F. Ferri and E. H. Wilson, "Titan's methane cycle", Planetary and Space Science **54**, 12, 1177–1187 (2006).

Attila Vertes, K., Sandor Nagy, *Nuclear Methods in Mineralogy and Geology* (Springer US, 1998).

Barnes, J. W., R. H. Brown, L. Soderblom, C. Sotin, S. Le Mouèlic, S. Rodriguez, R. Jaumann, R. A. Beyer, B. J. Buratti, K. Pitman, K. H. Baines, R. Clark and P. Nicholson, "Spectroscopy, morphometry, and photoclinometry of Titan's dunefields from Cassini/VIMS", Icarus **195**, 1, 400–414 (2008).

Barnes, J. W., R. D. Lorenz, J. Radebaugh, A. G. Hayes, K. Arnold and C. Chandler, "Production and global transport of Titan's sand particles", PlSci **4**, 1, 1 (2015).

Barnes, J. W., E. P. Turtle, M. G. Trainer, R. D. Lorenz, S. M. Mackenzie, W. B. Brinckerhoff, M. L. Cable, C. M. Ernst, C. Freissinet, K. P. Hand, A. G. Hayes, S. M. Hörst, J. R. Johnson, E. Karkoschka, D. J. Lawrence, A. Le Gall, J. M. Lora, C. P. Mckay, R. S. Miller, S. L. Murchie, C. D. Neish, C. E. Newman, J. Núñez, M. P. Panning, A. M. Parsons, P. N. Peplowski, L. C. Quick, J. Radebaugh, S. C. R. Rafkin, H. Shiraishi, J. M. Soderblom, K. S. Sotzen, A. M. Stickle, E. R. Stofan, C. Szopa, T. Tokano, T. Wagner, C. Wilson, R. A. Yingst, K. Zacny and S. C. Stähler, "Science Goals and Objectives for the Dragonfly Titan Rotorcraft Relocatable Lander", URL https://doi.org/10.3847/PSJ/abfdcf (2021).

Beckurts, K. H. and K. Wirtz, "Neutron Physics", Neutron Physics (1964).

Benkhoff, J., G. Murakami, W. Baumjohann, S. Besse, E. Bunce, M. Casale, G. Cremosese, K. H. Glassmeier, H. Hayakawa, D. Heyner, H. Hiesinger, J. Huovelin, H. Hussmann, V. Iafolla, L. Iess, Y. Kasaba, M. Kobayashi, A. Milillo, I. G. Mitrofanov, E. Montagnon, M. Novara, S. Orsini, E. Quemerais, U. Reininghaus, Y. Saito, F. Santoli, D. Stramaccioni, O. Sutherland, N. Thomas, I. Yoshikawa

and J. Zender, "BepiColombo - Mission Overview and Science Goals", Space Science Reviews **217**, 8, 1–56, URL https://link.springer.com/article/10.1007/s11214-021-00861-4 (2021).

Berner, O. A., S. Czarnecki, C. Hardgrove, P. J. Gasda and K. Mesick, "MEASURING HYDRATION OF NEARBY CLIFFS IN GALE CRATER USING NEUTRON", in "Lunar and Planetary Science Conference", p. 2596 (2022).

Bodnarik, J., D. Burger, A. Burger, L. Evans, A. Parsons, J. Schweitzer, R. Starr and K. Stassun, "Time-resolved neutron/gamma-ray data acquisition for in situ subsurface planetary geochemistry", Nuclear Instruments and Methods in Physics Research Section A: Accelerators, Spectrometers, Detectors and Associated Equipment **707**, 135 – 142 (2013).

Bodnarik, J. G., *PHYSICS USING IN SITU NEUTRON AND GAMMA-RAY SPECTROSCOPY*, Ph.D. thesis, Graduate School of Vanderbilt University (2013).

Boynton, W. V., W. C. Feldman, I. G. Mitrofanov, L. G. Evans, R. C. Reedy, S. W. Squyres, R. Starr, J. I. Trombka, C. D'Uston, J. R. Arnold, P. A. J. Englert, A. E. Metzger, H. Wänke, J. Brückner, D. M. Drake, C. Shinohara, C. Fellows, D. K. Hamara, K. Harshman, K. Kerry, C. Turner, M. Ward, H. Barthe, K. R. Fuller, S. A. Storms, G. W. Thornton, J. L. Longmire, M. L. Litvak and A. K. Ton'chev, "The Mars Odyssey Gamma-Ray Spectrometer Instrument Suite", Space Science Reviews **110**, 1, 37–83, URL https://doi.org/10.1023/B:SPAC.0000021007.76126.15 (2004).

Burks, M. T., O. B. Drury, J. O. Goldsten, L. B. Hagler, L. E. Heffern, N. R. Hines, G.-B. Kim, D. J. Lawrence, K. E. Nelson, P. N. Peplowski and Z. W. Yokley, "GeMini: A High-Resolution, Low-Resource, Gamma-Ray Spectrometer for Planetary Science Applications", Space Science Reviews 2020 216:7 **216**, 7, 1–23, URL https://link.springer.com/article/10.1007/s11214-020-00746-y (2020).

Byrne, S., "The Polar Deposits of Mars", http://dx.doi.org/10.1146/annurev.earth.031208.100101 **37**, 535–560, URL https://www.annualreviews.org/doi/abs/10.1146/annurev.earth.031208.100101 (2009).

Cable, M. L., S. M. Hörst, R. Hodyss, P. M. Beauchamp, M. A. Smith and P. A. Willis, "Titan tholins: Simulating Titan organic chemistry in the Cassini-Huygens era", (2012).

Chin, G., S. Brylow, M. Foote, J. Garvin, J. Kasper, J. Keller, M. Litvak, I. Mitrofanov, D. Paige, K. Raney, M. Robinson, A. Sanin, D. Smith, H. Spence, P. Spudis, S. A. Stern and M. Zuber, "Lunar Reconnaissance Orbiter Overview: The Instrument Suite and Mission", Space Science Reviews **129**, 4, 391–419, URL https://doi.org/10.1007/s11214-007-9153-y (2007).

Colaprete, A., P. Schultz, J. Heldmann, D. Wooden, M. Shirley, K. Ennico, B. Hermalyn, W. Marshall, A. Ricco, R. C. Elphic, D. Goldstein, D. Summy, G. D.

Bart, E. Asphaug, D. Korycansky, D. Landis and L. Sollitt, "Detection of water in the LCROSS ejecta plume", Science **330**, 6003, 463–468, URL https://www.science.org/doi/abs/10.1126/science.1186986 (2010).

Coupland, D. D., B. S. Budden and L. C. Stonehill, "Thermal variance investigation and scintillation mechanisms of Cs2LiLaBr6-xClx:Ce (CLLBC) and Cs2LiYBr6:Ce (CLYB)", in "2015 IEEE Nuclear Science Symposium and Medical Imaging Conference, NSS/MIC 2015", (Institute of Electrical and Electronics Engineers Inc., 2016a).

Coupland, D. D. S., L. C. Stonehill, K. E. Mesick and J. P. Dunn, "The SENSER CLYC experiment", in "2016 IEEE Nuclear Science Symposium, Medical Imaging Conference and Room-Temperature Semiconductor Detector Workshop (NSS/MIC/RTSD)", pp. 1–4 (2016b).

Czarnecki, S., C. J. Hardgrove, P. J. Gasda, T. S. J. Gabriel, M. Starr, M. S. Rice, J. Frydenvang, R. C. Wiens, W. Rapin, S. Nikiforov, D. Lisov, M. Litvak, F. Calef, H. Gengl, H. Newsom, L. Thompson and S. Nowicki, "Identification and Description of a Silicic Volcaniclastic Layer in Gale Crater, Mars, Using Active Neutron Interrogation", Journal of Geophysical Research: Planets **125**, 3, e2019JE006180 (2020).

David Schechtman Stonehill, D., L. Catherine Mesick, K. Elizabeth Dunn, J. Philip and D. D. S, "The SENSER CLYC Experiment", in "IEEE Nuclear Science Symposium and Medical Imaging Conference", (2016).

Dibb, S. D., C. J. Hardgrove, T. S. J. Gabriel and S. M. Czarnecki, "INFLUENCE OF NEARBY TOPOGRAPHY ON PASSIVE NEUTRON COUNT RATES FROM THE DYNAMIC ALBEDO OF NEUTRONS INSTRUMENT ON THE MARS SCIENCE LABORATORY ROVER", in "Lunar and Planetary Science Conference", p. 2908 (2019).

Dolympia, N., P. Chowdhury, C. J. Guess, T. Harrington, E. G. Jackson, S. Lakshmi, C. J. Lister, J. Glodo, R. Hawrami, K. Shah and U. Shirwadkar, "Optimizing Cs2LiYCl6 for fast neutron spectroscopy", Nuclear Instruments and Methods in Physics Research Section A: Accelerators, Spectrometers, Detectors and Associated Equipment **694**, 140–146 (2012).

D'Olympia, N., P. Chowdhury, C. J. Lister, J. Glodo, R. Hawrami, K. Shah and U. Shirwadkar, "Pulse-shape analysis of CLYC for thermal neutrons, fast neutrons, and gamma-rays", Nuclear Instruments and Methods in Physics Research Section A: Accelerators, Spectrometers, Detectors and Associated Equipment **714**, 121–127 (2013).

Drake, D. M., S. A. Wender, R. O. Nelson, D. A. Clark, M. Drosg, W. Amian, J. Brückner and P. A. Englert, "Experimental simulation of martian neutron leakage spectra", Nuclear Instruments and Methods in Physics Research Section A: Accelerators, Spectrometers, Detectors and Associated Equipment **309**, 3, 575–580 (1991).

Elkins-Tanton, L. T., E. Asphaug, J. F. Bell, H. Bercovici, B. Bills, R. Binzel, W. F. Bottke, S. Dibb, D. J. Lawrence, S. Marchi, T. J. McCoy, R. Oran, R. S. Park, P. N. Peplowski, C. A. Polanskey, T. H. Prettyman, C. T. Russell, L. Schaefer, B. P. Weiss, M. A. Wieczorek, D. A. Williams and M. T. Zuber, "Observations, Meteorites, and Models: A Preflight Assessment of the Composition and Formation of (16) Psyche", URL https://doi.org/ (2020).

Elphic, R. C., V. R. Eke, L. F. A. Teodoro, D. J. Lawrence and D. B. J. Bussey, "Models of the distribution and abundance of hydrogen at the lunar south pole", Geophysical Research Letters **34**, 13, URL https://agupubs.onlinelibrary.wiley.com/doi/abs/10.1029/2007GL029954 (2007).

Elphic, R. C., D. J. Lawrence, W. C. Feldman, B. L. Barraclough, O. M. Gasnault, S. Maurice, P. G. Lucey, D. T. Blewett and A. B. Binder, "Lunar prospector neutron spectrometer constraints on TiO2", Journal of Geophysical Research E: Planets **107**, 4 (2002).

Evans, L. G., R. D. Starr, J. Brückner, R. C. Reedy, W. V. Boynton, J. I. Trombka, J. O. Goldsten, J. Masarik, L. R. Nittler and T. J. Mccoy, "Elemental composition from gamma-ray spectroscopy of the NEAR-Shoemaker landing site on 433 Eros", Meteoritics and Planetary Science **36**, 12, 1639–1660, URL https://onlinelibrary.wiley.com/doi/abs/10.1111/j.1945-5100.2001.tb01854.x (2001).

Feldman, W., K. Ahola, B. Barraclough, R. D. Belian, R. K. Black, R. C. Elphic, D. T. Everett, K. R. Fuller, J. Kroesche, D. J. Lawrence, S. L. Lawson, J. L. Longmire, S. Maurice, M. Miller, T. Prettyman, S. A. Storms and G. Thornton, "Gamma-Ray, Neutron, and Alpha-Particle Spectrometers for the Lunar Prospector mission", J. Geophys. Res **109**, 6–7 (2004).

Feldman, W. C., B. L. Barraclough, K. R. Fuller, D. J. Lawrence, S. Maurice, M. C. Miller, T. H. Prettyman and A. B. Binder, "The Lunar Prospector gamma-ray and neutron spectrometers", Nuclear Instruments and Methods in Physics Research, Section A: Accelerators, Spectrometers, Detectors and Associated Equipment **422**, 1-3, 562–566 (1999).

Feldman, W. C., A. B. Binder, G. S. Hubbard, J. McMurry, R. E., M. C. Miller and T. H. Prettyman, "The Lunar Prospector Gamma-Ray Spectrometer", in "Lunar and Planetary Science Conference", vol. 27 of *Lunar and Planetary Science Conference*, p. 355 (1996).

Feldman, W. C., D. J. Lawrence, R. C. Elphic, D. T. Vaniman, D. R. Thomsen, B. L. Barraclough, S. Maurice and A. B. Binder, "Chemical information content of lunar thermal and epithermal neutrons", Journal of Geophysical Research: Planets **105**, E8, 20347–20363 (2000).

Feldman, W. C., S. Maurice, A. B. Binder, B. L. Barraclough, R. C. Elphic and D. J. Lawrence, "Fluxes of Fast and Epithermal Neutrons from Lunar Prospector: Evidence for Water Ice at the Lunar Poles", Science **281**, 5382, 1496–1500, URL https://science.sciencemag.org/content/281/5382/1496 (1998).

Feldman, W. C., M. T. Mellon, O. Gasnault, B. Diez, R. C. Elphic, J. J. Hagerty, D. J. Lawrence, S. Maurice and T. H. Prettyman, "Vertical distribution of hydrogen at high northern latitudes on Mars: The Mars Odyssey Neutron Spectrometer", Geophysical Research Letters **34**, 5, URL https://agupubs.onlinelibrary.wiley.com/doi/abs/10.1029/2006GL028936 (2007).

Feldman, W. C., R. C. Reedy and D. S. McKay, "Lunar neutron leakage fluxes as a function of composition and hydrogen content", GeoRL **18**, 11, 2157–2160, URL https://ui.adsabs.harvard.edu/abs/1991GeoRL..18.2157F/abstract (1991).

Ferronsky, V. I., *Nuclear geophysics: Applications in hydrology, hydrogeology, engineering geology, agriculture and environmental science* (Springer International Publishing, 2015).

Ferrulli, F., M. Caresana, F. Cova, S. Gundacker, N. Kratochwil, R. Pots, M. Silari, A. Vedda, I. Veronese and G. Zorloni, "Analysis and comparison of the Core-to-Valence Luminescence mechanism in a large CLYC crystal under neutron and γ-ray irradiation through optical filtering selection of the scintillation light", Sensors and Actuators A: Physical **332**, 113151 (2021).

Fortes, A. D., P. M. Grindrod, S. K. Trickett and L. Vočadlo, "Ammonium sulfate on Titan: Possible origin and role in cryovolcanism", Icarus **188**, 1, 139–153 (2007).

Fulchignoni, M., F. Ferri, F. Angrilli, A. J. Ball, A. Bar-Nun, M. A. Barucci, C. Bettanini, G. Bianchini, W. Borucki, G. Colombatti, M. Coradini, A. Coustenis, S. Debei, P. Falkner, G. Fanti, E. Flamini, V. Gaborit, R. Grard, M. Hamelin, A. M. Harri, B. Hathi, I. Jernej, M. R. Leese, A. Lehto, P. F. Lion Stoppato, J. J. López-Moreno, T. Mäkinen, J. A. McDonnell, C. P. McKay, G. Molina-Cuberos, F. M. Neubauer, V. Pironello, R. Rodrigo, B. Saggin, K. Schwingenschuh, A. Seiff, F. Simões, H. Svedhem, T. Tokano, M. C. Towner, R. Trautner, P. Withers and J. C. Zarnecki, "In situ measurements of the physical characteristics of Titan's environment", Nature **438**, 7069, 785–791 (2005).

Gabriel, T. S. J. and C. J. Hardgrove, "Analysis of Active Neutron Data for In-Situ Planetary Bulk Geochemistry", in "Lunar and Planetary Science Conference", Lunar and Planetary Science Conference, p. 2888 (2020).

Gabriel, T. S. J., C. J. Hardgrove, C. N. Achilles, E. B. Rampe, W. N. Rapin, S. Nowicki, S. Czarecki, L. Thompson, S. Nikiforov, M. Litvak, I. Mitrofanov, D. Lisov, J. Frydenvang, A. Yen, R. C. Wiens, A. Treiman and A. McAdam, "On an extensive late groundwater event in Gale crater as indicated by water-rich fracture halos", Journal of Geophysical Research: Planets (Submitted).

Gabriel, T. S. J., C. J. Hardgrove, S. Czarnecki, E. B. Rampe, W. Rapin, C. N. Achilles, D. Sullivan, S. Nowicki, L. Thompson, M. Litvak, I. Mitrofanov and R. T. Downs, "Water Abundance of Dunes in Gale Crater, Mars From Active Neutron Experiments and Implications for Amorphous Phases", Geophysical Research Letters **45**, 23, 12,712–766,775 (2018).

Gilmore, G. R., *Practical Gamma-Ray Spectrometry: Second Edition* (John Wiley and Sons, 2008).

Glein, C. and E. Shock, "A geochemical model of non-ideal solutions in the methane–ethane–propane–nitrogen–acetylene system on Titan", Geochimica et Cosmochimica Acta **115**, 217–240 (2013).

Glodo, J., R. Hawrami, E. van Loef, U. Shirwadkar and K. S. Shah, "Pulse Shape Discrimination With Selected Elpasolite Crystals", IEEE Transactions on Nuclear Science **59**, 5, 2328–2333 (2012).

Goldsten, J. O., "The NEAR X-Ray/Gamma-Ray Spectrometer", **19**, 2 (1998).

Goldsten, J. O., E. A. Rhodes, W. V. Boynton, W. C. Feldman, D. J. Lawrence, J. I. Trombka, D. M. Smith, L. G. Evans, J. White, N. W. Madden, P. C. Berg, G. A. Murphy, R. S. Gurnee, K. Strohbehn, B. D. Williams, E. D. Schaefer, C. A. Monaco, C. P. Cork, J. Del Eckels, W. O. Miller, M. T. Burks, L. B. Hagler, S. J. DeTeresa and M. C. Witte, "The MESSENGER Gamma-Ray and Neutron Spectrometer", Space Science Reviews **131**, 1, 339–391, URL https://doi.org/10.1007/s11214-007-9262-7 (2007).

Hardgrove, C., J. Moersch and D. Drake, "Effects of geochemical composition on neutron die-away measurements: Implications for Mars Science Laboratory's Dynamic Albedo of Neutrons experiment", Nuclear Instruments and Methods in Physics Research, Section A: Accelerators, Spectrometers, Detectors and Associated Equipment **659**, 1, 442 – 455 (2011).

Hardgrove, C., R. Starr, I. Lazbin, A. Babuscia, B. Roebuck, J. Dubois, N. Struebel, A. Colaprete, D. Drake, E. Johnson, J. Christian, L. Heffern, S. Stem, S. Parlapiano, M. Wiens, A. Genova, D. Dunham, D. Nelson, B. Williams, J. Bauman, P. Hailey, T. Obrien, K. Marwah, L. Vlieger, J. Bell, T. Prettyman, T. Crain, E. Cisneros, N. Cluff, G. Stoddard and M. Kaffine, "The Lunar Polar Hydrogen Mapper CubeSat Mission", IEEE Aerospace and Electronic Systems Magazine **35**, 3, 54–69 (2020).

Harold Urey, B. C., "On the Early Chemical History of the Earth and the Origin of Life", Proceedings of the National Academy of Sciences **38**, 4, 351–363, URL https://www.pnas.org (1952).

Harrington, T. M., J. Marshall, J. R. Arnold, L. E. Peterson, J. I. Trombka and A. E. Metzger, "The Apollo gamma-ray spectrometer", Nuclear Instruments and Methods **118**, 2, 401–411, URL http://www.sciencedirect.com/science/article/pii/0029554X74906442 (1974).

Harris, C. R., K. J. Millman, S. J. van der Walt, R. Gommers, P. Virtanen, D. Cournapeau, E. Wieser, J. Taylor, S. Berg, N. J. Smith, R. Kern, M. Picus, S. Hoyer, M. H. van Kerkwijk, M. Brett, A. Haldane, J. F. del Río, M. Wiebe, P. Peterson, P. Gérard-Marchant, K. Sheppard, T. Reddy, W. Weckesser, H. Abbasi, C. Gohlke and T. E. Oliphant, "Array programming with NumPy", (2020).

Hayes, A. G., "The Lakes and Seas of Titan", URL www.annualreviews.org (2016).

Heffern, L., C. Hardgrove, E. Johnson, A. Parsons, T. Prettyman, A. Jain, H. Barnaby, J. Christian, C. Tate, G. Stoddard, A. Martin and J. Moersch, "Active Nuclear Investigations of Planetary Surfaces with SINGR (SIngle-Scintillator Neutron and Gamma Ray Spectrometer)", in "Lunar and Planetary Science Conference", p. 2249 (The Woodlands, TX, 2018).

Heffern, L. E., C. J. Hardgrove, A. Parsons, E. B. Johnson, R. Starr, G. Stoddard, R. E. Blakeley, T. Prettyman, T. S. Gabriel, H. Barnaby, J. Christian, M. A. Unzueta, C. Tate, A. Martin and J. Moersch, "Active neutron interrogation experiments and simulation verification using the SIngle-scintillator Neutron and Gamma-Ray spectrometer (SINGR) for geosciences", Nuclear Instruments and Methods in Physics Research Section A: Accelerators, Spectrometers, Detectors and Associated Equipment **1020**, 165883 (2021).

Heilbronn (2015).

Hörst, S. M., "Titan's atmosphere and climate", Journal of Geophysical Research: Planets **122**, 3, 432–482, URL https://onlinelibrary.wiley.com/doi/full/10.1002/2016JE005240https://onlinelibrary.wiley.com/doi/abs/10.1002/2016JE005240https://agupubs.onlinelibrary.wiley.com/doi/10.1002/2016JE005240 (2017).

Hörst, S. M. and M. A. Tolbert, "In situ measurements of the size and density of titan aerosol analogs", Astrophysical Journal Letters **770**, 1 (2013).

Hörst, S. M., V. Vuitton and R. V. Yelle, "Origin of oxygen species in Titan's atmosphere", Journal of Geophysical Research: Planets **113**, E10, 10006, URL https://onlinelibrary.wiley.com/doi/full/10.1029/2008JE003135https://onlinelibrary.wiley.com/doi/abs/10.1029/2008JE003135https://agupubs.onlinelibrary.wiley.com/doi/10.1029/2008JE003135 (2008).

Hunter, J. D., "Matplotlib: A 2D graphics environment", Computing in Science and Engineering **9**, 3, 90 – 95 (2007).

Johnson, E. B., C. Whitney, S. Vogel, J. F. Christian, K. Holbert and P. Chandhran, "High event rate, pulse shape discrimination algorithm for CLYC", in "2015 IEEE International Symposium on Technologies for Homeland Security (HST)", pp. 1–7 (2015).

Jun, I., I. Mitrofanov, M. L. Litvak, A. B. Sanin, W. Kim, A. Behar, W. V. Boynton, L. Deflores, F. Fedosov, D. Golovin, C. Hardgrove, K. Harshman, A. S. Kozyrev, R. O. Kuzmin, A. Malakhov, M. Mischna, J. Moersch, M. Mokrousov, S. Nikiforov, V. N. Shvetsov, C. Tate, V. I. Tret'Yakov and A. Vostrukhin, "Neutron background environment measured by the mars science Laboratory's dynamic albedo of neutrons instrument during the first 100 sols", Journal of Geophysical Research: Planets **118**, 11, 2400–2412, URL https://arizona.pure.elsevier.com/en/publications/neutron-background-environment-measured-by-the-mars-science-labor (2013).

Karge, L., R. Gilles and S. Busch, "Calibrating SANS data for instrument geometry and pixel sensitivity effects: access to an extended Q range", urn:issn:1600-5767 **50**, 5, 1382–1394, URL //scripts.iucr.org/cgi-bin/paper?ks5569 (2017).

Kerner, H. R., C. J. Hardgrove, S. Czarnecki, T. S. J. Gabriel, I. G. Mitrofanov, M. L. Litvak, A. B. Sanin and D. I. Lisov, "Analysis of Active Neutron Measurements From the Mars Science Laboratory Dynamic Albedo of Neutrons Instrument: Intrinsic Variability, Outliers, and Implications for Future Investigations", Journal of Geophysical Research: Planets **125**, 5, e2019JE006264 (2020).

Kim, C., W. Lee, A. Melis, A. Elmughrabi, K. Lee, C. Park and J. Y. Yeom, "A Review of Inorganic Scintillation Crystals for Extreme Environments", Crystals 2021, Vol. 11, Page 669 **11**, 6, 669, URL https://www.mdpi.com/2073-4352/11/6/669/htmhttps://www.mdpi.com/2073-4352/11/6/669 (2021).

Knoll, G. F., *Radiation detection and measurement; 4th ed.* (Wiley, New York, NY, 2010).

Kuramoto, K., Y. Kawakatsu, M. Fujimoto, A. Araya, M. A. Barucci, H. Genda, N. Hirata, H. Ikeda, T. Imamura, J. Helbert, S. Kameda, M. Kobayashi, H. Kusano, D. J. Lawrence, K. Matsumoto, P. Michel, H. Miyamoto, T. Morota, H. Nakagawa, T. Nakamura, K. Ogawa, H. Otake, M. Ozaki, S. Russell, S. Sasaki, H. Sawada, H. Senshu, S. Tachibana, N. Terada, S. Ulamec, T. Usui, K. Wada, S. ichiro Watanabe and S. Yokota, "Martian moons exploration MMX: sample return mission to Phobos elucidating formation processes of habitable planets", Earth, Planets and Space 2021 74:1 **74**, 1, 1–31, URL https://earth-planets-space.springeropen.com/articles/10.1186/s40623-021-01545-7 (2022).

LANL, "MCNP-A General Monte Carlo N-Particle Transport Code, Version 5 Volume I: Overview and Theory X-5 Monte Carlo Team", (2003).

Lawrence, D. J., D. Adams, W. F. Ames, M. Ayllon-Unzueta, B. M. Bronner, M. T. Burks, F. Gicquel, J. O. Goldsten, J. M. Greenberg, N. R. Hines, R. D. Lorenz, S. L. Murchie, C. W. Parker, A. M. Parsons, P. N. Peplowski, C. Z. Sheldon and Z.-a. W. Yokley, "The Dragonfly Gamma-Ray and Neutron Spectrometer (DraGNS): Providing In-situ Measurements of Titan's Elemental Composition", in "Lunar and Planetary Science Conference", (2022).

Lawrence, D. J., W. C. Feldman, B. L. Barraclough, A. B. Binder, R. C. Elphic, S. Maurice and D. R. Thomsen, "Global Elemental Maps of the Moon: The Lunar Prospector Gamma-Ray Spectrometer", Science **281**, 5382, 1484–1489, URL https://www.science.org/doi/abs/10.1126/science.281.5382.1484 (1998).

Lawrence, D. J., W. C. Feldman, R. C. Elphic, J. J. Hagerty, S. Maurice, G. W. McKinney and T. H. Prettyman, "Improved modeling of Lunar Prospector neutron spectrometer data: Implications for hydrogen deposits at the lunar poles", Journal of Geophysical Research E: Planets **111**, 8 (2006).

Lawrence, D. J., W. C. Feldman, R. C. Elphic, R. C. Little, T. H. Prettyman, S. Maurice, P. G. Lucey and A. B. Binder, "Iron abundances on the lunar

surface as measured by the Lunar Prospector gamma-ray and neutron spectrometers", Journal of Geophysical Research: Planets **107**, E12, 13–1, URL `https://onlinelibrary.wiley.com/doi/full/10.1029/2001JE001530https://onlinelibrary.wiley.com/doi/abs/10.1029/2001JE001530https://agupubs.onlinelibrary.wiley.com/doi/10.1029/2001JE001530` (2002).

Lawrence, D. J., W. C. Feldman, J. O. Goldsten, S. Maurice, P. N. Peplowski, B. J. Anderson, D. Bazell, R. L. McNutt, L. R. Nittler, T. H. Prettyman, D. J. Rodgers, S. C. Solomon and S. Z. Weider, "Evidence for water ice near mercury's north pole from MESSENGER neutron spectrometer measurements", Science **339**, 6117, 292–296, URL `https://www.science.org/doi/abs/10.1126/science.1229953` (2013).

Lawrence, D. J., S. Fix, J. O. Goldsten, S. V. Heuer, R. S. Hourani, S. Kerem and P. N. Peplowski, "Near-space operation of compact CsI, CLYC, and CeBr3 sensors: Results from two high-altitude balloon flights", Nuclear Instruments and Methods in Physics Research, Section A: Accelerators, Spectrometers, Detectors and Associated Equipment **905**, 33–46 (2018).

Lawrence, D. J., J. O. Goldsten, P. N. Peplowski and Z. W. Yokley, Earth and Space Science Open Archive (2020).

Lawrence, D. J., P. N. Peplowski, A. W. Beck, M. T. Burks, N. L. Chabot, M. J. Cully, R. C. Elphic, C. M. Ernst, S. Fix, J. O. Goldsten, E. M. Hoffer, H. Kusano, S. L. Murchie, B. C. Schratz, T. Usui and Z. W. Yokley, "Measuring the Elemental Composition of Phobos: The Mars-moon Exploration with GAmma rays and NEutrons (MEGANE) Investigation for the Martian Moons eXploration (MMX) Mission", Earth and Space Science **6**, 12, 2605–2623, URL `https://onlinelibrary.wiley.com/doi/full/10.1029/2019EA000811https://onlinelibrary.wiley.com/doi/abs/10.1029/2019EA000811https://agupubs.onlinelibrary.wiley.com/doi/10.1029/2019EA000811` (2019).

Lethuillier, A., A. Le Gall, M. Hamelin, S. Caujolle-Bert, F. Schreiber, N. Carrasco, G. Cernogora, C. Szopa, Y. Brouet, F. Simões, J. J. Correia and G. Ruffié, "Electrical Properties of Tholins and Derived Constraints on the Huygens Landing Site Composition at the Surface of Titan", Journal of Geophysical Research: Planets **123**, 4, 807–822, URL `https://onlinelibrary.wiley.com/doi/full/10.1002/2017JE005416https://onlinelibrary.wiley.com/doi/abs/10.1002/2017JE005416https://agupubs.onlinelibrary.wiley.com/doi/10.1002/2017JE005416` (2018).

Litvak, M. L., D. V. Golovin, A. B. Kolesnikov, A. A. Vostrukhin, M. V. Djachkova, A. S. Kozyrev, I. G. Mitrofanov, M. I. Mokrousov and A. B. Sanin, "Ground-based measurements with the ADRON active gamma-ray and neutron spectrometer designed for lunar and Martian landing missions", Solar System Research **51**, 3, 171–184 (2017).

Litvak, M. L., I. G. Mitrofanov, Y. Barmakov, A. Behar, A. Bitulev, Y. Bobrovnitsky, E. P. Bogolubov, W. V. Boynton, S. I. Bragin, S. Churin, A. S. Grebennikov, A. Konovalov, A. S. Kozyrev, I. G. Kurdumov, A. Krylov, Y. Kuznetsov, A. V.

Malakhov, M. I. Mokrousov, V. I. Ryzhkov, A. B. Sanin, V. N. Shvetsov, G. A. Smirnov, S. Sholeninov, G. N. Timoshenko, T. M. Tomilina, D. V. Tuvakin, V. I. Tretyakov, V. S. Troshin, V. N. Uvarov, A. Varenikov and A. Vostrukhin, "The Dynamic Albedo of Neutrons (DAN) Experiment for NASA's 2009 Mars Science Laboratory", Astrobiology **8**, 3, 605–612 (2008).

Litvak, M. L., I. G. Mitrofanov, C. Hardgrove, K. M. Stack, A. B. Sanin, D. Lisov, W. V. Boynton, F. Fedosov, D. Golovin, K. Harshman, I. Jun, A. S. Kozyrev, R. O. Kuzmin, A. Malakhov, R. Milliken, M. Mischna, J. Moersch, M. Mokrousov, S. Nikiforov, R. Starr, C. Tate, V. I. Tret'yakov and A. Vostrukhin, "Hydrogen and chlorine abundances in the Kimberley formation of Gale crater measured by the DAN instrument on board the Mars Science Laboratory Curiosity rover", Journal of Geophysical Research: Planets **121**, 5, 836–845, URL https://onlinelibrary.wiley.com/doi/full/10.1002/2015JE004960https://onlinelibrary.wiley.com/doi/abs/10.1002/2015JE004960https://agupubs.onlinelibrary.wiley.com/doi/10.1002/2015JE004960 (2016).

Lopes, R. M. C., R. L. Kirk, K. L. Mitchell, A. Legall, J. W. Barnes, A. Hayes, J. Kargel, L. Wye, J. Radebaugh, E. R. Stofan, M. A. Janssen, C. D. Neish, S. D. Wall, C. A. Wood, J. I. Lunine and M. J. Malaska, "Cryovolcanism on Titan: New results from Cassini RADAR and VIMS", J. Geophys. Res. Planets **118**, 416–435 (2013).

Lorenz, R. D., "Thermal interactions of the Huygens probe with the Titan environment: Constraint on near-surface wind", Icarus **182**, 2, 559–566 (2006).

Mastrogiuseppe, M., V. Poggiali, A. Hayes, R. Lorenz, J. Lunine, G. Picardi, R. Seu, E. Flamini, G. Mitri, C. Notarnicola, P. Paillou and H. Zebker, "The bathymetry of a Titan sea", Geophysical Research Letters **41**, 5, 1432–1437 (2014).

McCord, T. B., P. Hayne, J.-P. Combe, G. B. Hansen, J. W. Barnes, S. Rodriguez, S. Le Mouélic, E. K. H. Baines, B. J. Buratti, C. Sotin, P. Nicholson, R. Jaumann, R. Nelson and the Cassini VIMS Team, "Titan's surface: Search for spectral diversity and composition using the Cassini VIMS investigation", Icarus **194**, 1, 212–242, URL http://www.sciencedirect.com/science/article/pii/S0019103507003855 (2008).

Mckinney, W., "Data Structures for Statistical Computing in Python", Tech. rep. (2010).

McSween, H. Y., R. P. Binzel, M. C. De Sanctis, E. Ammannito, T. H. Prettyman, A. W. Beck, V. Reddy, L. Le Corre, M. J. Gaffey, T. B. Mccord, C. A. Raymond and C. T. Russell, "Dawn; the Vesta–HED connection; and the geologic context for eucrites, diogenites, and howardites", Meteoritics and Planetary Science **48**, 11, 2090–2104, URL https://onlinelibrary.wiley.com/doi/full/10.1111/maps.12108https://onlinelibrary.wiley.com/doi/abs/10.1111/maps.12108https://onlinelibrary.wiley.com/doi/10.1111/maps.12108 (2013).

McSween Jr., H. Y., J. P. Emery, A. S. Rivkin, M. J. Toplis, J. C. Castillo-Rogez, T. H. Prettyman, M. C. De Sanctis, C. M. Pieters, C. A. Raymond and C. T.

Russell, "Carbonaceous chondrites as analogs for the composition and alteration of Ceres", Meteoritics and Planetary Science **53**, 9, 1793–1804, URL https://onlinelibrary.wiley.com/doi/abs/10.1111/maps.12947 (2018).

Menge, P. R. and D. Richaud, "Behavior of Cs2LiYCl6:Ce scintillator up to 175C", in "IEEE Nuclear Science Symposium Conference Record", pp. 1598–1601 (Institute of Electrical and Electronics Engineers Inc., 2011).

Mentana, A., F. Camera, A. Giaz, N. Blasi, S. Brambilla, S. Ceruti, L. Gini, F. Groppi, S. Manenti, B. Million and S. Riboldi, "To cite this article: A Mentana et al", J. Phys.: Conf. Ser **763**, 12006 (2016).

Mesick, K. E., K. D. Bartlett, D. D. Coupland and L. C. Stonehill, "Effects of proton-induced radiation damage on CLYC and CLLBC performance", Nuclear Instruments and Methods in Physics Research, Section A: Accelerators, Spectrometers, Detectors and Associated Equipment **948**, C (2019).

Metzger, A. E., J. I. Trombka, L. E. Peterson, R. C. Reedy and J. R. Arnold, "Lunar Surface Radioactivity: Preliminary Results of the Apollo 15 and Apollo 16 Gamma-Ray Spectrometer Experiments", Science **179**, 4075, 800–803, URL https://www.science.org/doi/abs/10.1126/science.179.4075.800 (1973).

Mitchell, J. L. and J. M. Lora, "The Climate of Titan", Annual Review of Earth and Planetary Sciences **44**, 353–380 (2016).

Mitrofanov, I. G., A. Bartels, Y. I. Bobrovnitsky, W. Boynton, G. Chin, H. Enos, L. Evans, S. Floyd, J. Garvin, D. V. Golovin, A. S. Grebennikov, K. Harshman, L. L. Kazakov, J. Keller, A. A. Konovalov, A. S. Kozyrev, A. R. Krylov, M. L. Litvak, A. V. Malakhov, T. McClanahan, G. M. Milikh, M. I. Mokrousov, S. Ponomareva, R. Z. Sagdeev, A. B. Sanin, V. V. Shevchenko, V. N. Shvetsov, R. Starr, G. N. Timoshenko, T. M. Tomilina, V. I. Tretyakov, J. Trombka, V. S. Troshin, V. N. Uvarov, A. B. Varennikov and A. A. Vostrukhin, "Lunar Exploration Neutron Detector for the NASA Lunar Reconnaissance Orbiter", Space Science Reviews 2009 150:1 **150**, 1, 183–207, URL https://link.springer.com/article/10.1007/s11214-009-9608-4 (2009).

Mitrofanov, I. G., A. S. Kozyrev, A. Konovalov, M. L. Litvak, A. A. Malakhov, M. I. Mokrousov, A. B. Sanin, V. I. Tret'ykov, A. V. Vostrukhin, Y. I. Bobrovnitskij, T. M. Tomilina, L. Gurvits and A. Owens, "The Mercury Gamma and Neutron Spectrometer (MGNS) on board the Planetary Orbiter of the BepiColombo mission", Planetary and Space Science **58**, 1-2, 116–124 (2010a).

Mitrofanov, I. G., M. L. Litvak, S. Y. Nikiforov, I. Jun, Y. I. Bobrovnitsky, D. V. Golovin, A. S. Grebennikov, F. S. Fedosov, A. S. Kozyrev, D. I. Lisov, A. V. Malakhov, M. I. Mokrousov, A. B. Sanin, V. N. Shvetsov, G. N. Timoshenko, T. M. Tomilina, V. I. Tret'Yakov and A. A. Vostrukhin, "The ADRON-RM Instrument Onboard the ExoMars Rover", https://home.liebertpub.com/ast **17**, 6-7, 585–594, URL https://www.liebertpub.com/doi/full/10.1089/ast.2016.1566 (2017).

Mitrofanov, I. G., M. L. Litvak, A. B. Sanin, R. D. Starr, D. I. Lisov, R. O. Kuzmin, A. Behar, W. V. Boynton, C. Hardgrove, K. Harshman, I. Jun, R. E. Milliken, M. A. Mischna, J. E. Moersch and C. G. Tate, "Water and chlorine content in the Martian soil along the first 1900 m of the Curiosity rover traverse as estimated by the DAN instrument", Journal of Geophysical Research: Planets **119**, 7, 1579–1596 (2014).

Mitrofanov, I. G., M. L. Litvak, A. B. Varenikov, Y. N. Barmakov, A. Behar, Y. I. Bobrovnitsky, E. P. Bogolubov, W. V. Boynton, K. Harshman, E. Kan, A. S. Kozyrev, R. O. Kuzmin, A. V. Malakhov, M. I. Mokrousov, S. N. Ponomareva, V. I. Ryzhkov, A. B. Sanin, G. A. Smirnov, V. N. Shvetsov, G. N. Timoshenko, T. M. Tomilina, V. I. Tret'Yakov and A. A. Vostrukhin, "Dynamic Albedo of Neutrons (DAN) experiment onboard NASA's Mars Science Laboratory", Space Science Reviews **170**, 1-4, 559–582, URL https://asu.pure.elsevier.com/en/publications/dynamic-albedo-of-neutrons-dan-experiment-onboard-nasas-mars-scie (2012).

Mitrofanov, I. G., A. B. Sanin, W. V. Boynton, G. Chin, J. B. Garvin, D. Golovin, L. G. Evans, K. Harshman, A. S. Kozyrev, M. L. Litvak, A. Malakhov, E. Mazarico, T. McClanahan, G. Milikh, M. Mokrousov, G. Nandikotkur, G. A. Neumann, I. Nuzhdin, R. Sagdeev, V. Shevchenko, V. Shvetsov, D. E. Smith, R. Starr, V. I. Tretyakov, J. Trombka, D. Usikov, A. Varenikov, A. Vostrukhin and M. T. Zuber, "Hydrogen mapping of the lunar south pole using the LRO neutron detector experiment LEND", Science (New York, N.Y.) **330**, 6003, 483–486, URL https://pubmed.ncbi.nlm.nih.gov/20966247/ (2010b).

Niemann, H. B., S. K. Atreya, S. J. Bauer, G. R. Carignan, J. E. Demick, R. L. Frost, D. Gautier, J. A. Haberman, D. N. Harpold, D. M. Hunten, G. Israel, J. I. Lunine, W. T. Kasprzak, T. C. Owen, M. Paulkovich, F. Raulin, E. Raaen and S. H. Way, "The abundances of constituents of Titan's atmosphere from the GCMS instrument on the Huygens probe", Nature 2005 438:7069 **438**, 7069, 779–784, URL https://www.nature.com/articles/nature04122 (2005).

Niemann, H. B., S. K. Atreya, J. E. Demick, D. Gautier, J. A. Haberman, D. N. Harpold, W. T. Kasprzak, J. I. Lunine, T. C. Owen and F. Raulin, "Composition of Titan's lower atmosphere and simple surface volatiles as measured by the Cassini-Huygens probe gas chromatograph mass spectrometer experiment", Journal of Geophysical Research E: Planets **115**, 12 (2010).

Nowicki, S. F., L. G. Evans, R. D. Starr, J. S. Schweitzer, S. Karunatillake, T. P. McClanahan, J. E. Moersch, A. M. Parsons and C. G. Tate, "Modeled Martian subsurface elemental composition measurements with the Probing In situ with Neutron and Gamma ray instrument", Earth and Space Science **4**, 2, 76–90 (2017).

Parsons, A., J. Bodnarik, L. Evans, S. Floyd, L. Lim, T. McClanahan, M. Namkung, S. Nowicki, J. Schweitzer, R. Starr and J. Trombka, "Active neutron and gamma-ray instrumentation for in situ planetary science applications", in "Nuclear Instruments and Methods in Physics Research, Section A: Accelerators, Spectrometers, Detectors and Associated Equipment", vol. 652, pp. 674–679 (North-Holland, 2011).

Parsons, A., J. Bodnarik, L. Evans, T. McClanahan and R. Starr, "The Probing In-Situ With Neutron and Gamma Rays (PING) Instrument for Planetary Composition Measurements", in "2012 Symposium on Radiation Measurements", (Institute of Electrical and Electronics Engineers Inc., 2012).

Parsons, A., M. Burks, D. J. Lawrence, R. D. Lorenz, R. Miller, P. N. Peplowski, L. Perkins and E. P. Turtle, "The Dragonfly Gamma-Ray and Neutron Spectrometer (DraGNS): Elemental Composition Measurements on the Surface of Titan", in "AGU Fall Meeting Abstracts", pp. P52C–08 (2018).

Parsons, A., T. McClanahan, J. Bodnarik, L. Evans, S. Nowicki, J. Schweitzer and R. Starr, "Subsurface In situ elemental composition measurements with PING", in "IEEE Aerospace Conference Proceedings", (2013).

Parsons, A. M., J. Grau, D. J. Lawrence, T. P. McClanahan, J. Miles, P. N. Peplowski, L. Perkins, J. S. Schweitzer and R. D. Starr, "Pulsed neutron generator - Gamma ray spectrometer measurements of venus elemental composition", 2016 IEEE Nuclear Science Symposium, Medical Imaging Conference and Room-Temperature Semiconductor Detector Workshop, NSS/MIC/RTSD **January** (2017).

Peplowski, P. N., "The global elemental composition of 433 Eros: First results from the NEAR gamma-ray spectrometer orbital dataset", Planetary and Space Science **134**, 36–51 (2016).

Peplowski, P. N., M. Burks, J. O. Goldsten, S. Fix, L. E. Heffern, D. J. Lawrence and Z. W. Yokley, "Radiation damage and annealing of three coaxial n-type germanium detectors: Preparation for spaceflight missions to asteroid 16 Psyche and Mars' moon Phobos", Nuclear Instruments and Methods in Physics Research, Section A: Accelerators, Spectrometers, Detectors and Associated Equipment **942**, 162409 (2019).

Peplowski, P. N., D. J. Lawrence, L. G. Evans, R. L. Klima, D. T. Blewett, J. O. Goldsten, S. L. Murchie, T. J. McCoy, L. R. Nittler, S. C. Solomon, R. D. Starr and S. Z. Weider, "Constraints on the abundance of carbon in near-surface materials on Mercury: Results from the MESSENGER Gamma-Ray Spectrometer", Planetary and Space Science **108**, 98–107, URL http://www.sciencedirect.com/science/article/pii/S0032063315000094 (2015).

Peplowski, P. N., J. T. Wilson, A. W. Beck, M. Burks, J. O. Goldsten and D. J. Lawrence, "Characterizing near-surface elemental layering on Mars using gamma-ray spectroscopy: A proof-of-principle experiment", Nuclear Instruments and Methods in Physics Research Section B: Beam Interactions with Materials and Atoms **415**, 89–99 (2018).

Pérez-Loureiro, D., O. Kamaev, G. Bentoumi, L. Li, C. Jewett and M. Thompson, "Evaluation of CLYC-6 and CLYC-7 scintillators for detection of nuclear materials", Nuclear Instruments and Methods in Physics Research Section A: Accelerators, Spectrometers, Detectors and Associated Equipment **1012**, 165622 (2021).

PNNL Compendium, "Compendium of Material Composition Data for Radiation Transport Modeling — PNNL", URL https://www.pnnl.gov/publications/compendium-material-composition-data-radiation-transport-modeling-1 (2021).

Prettyman, T. H., P. A. Englert, N. Yamashita and M. E. Landis, "Neutron, Gamma-Ray, and X-Ray Spectroscopy of Planetary Bodies", Remote Compositional Analysis: Techniques for Understanding Spectroscopy, Mineralogy, and Geochemistry of Planetary Surfaces pp. 588–603, URL https://www.cambridge.org/core/books/remote-compositional-analysis/neutron-gammaray-and-xray-spectroscopy-of-planetary-bodies/89F275BB366270D5D0D5803B6C6C3BA6 (2019a).

Prettyman, T. H., W. C. Feldman, F. P. Ameduri, B. L. Barraclough, E. W. Cascio, K. R. Fuller, H. O. Funsten, D. J. Lawrence, G. W. McKinney, C. T. Russell, S. A. Soldner, S. A. Storms, C. Szeles and R. L. Tokar, "Gamma-ray and neutron spectrometer for the Dawn mission to 1 Ceres and 4 Vesta", IEEE Transactions on Nuclear Science **50**, 4 II, 1190–1197 (2003).

Prettyman, T. H., W. C. Feldman, H. Y. McSween, R. D. Dingler, D. C. Enemark, D. E. Patrick, S. A. Storms, J. S. Hendricks, J. P. Morgenthaler, K. M. Pitman and R. C. Reedy, *Dawn's Gamma Ray and Neutron Detector*, pp. 371–459 (Springer New York, New York, NY, 2012), URL https://doi.org/10.1007/978-1-4614-4903-4_14.

Prettyman, T. H., J. J. Hagerty, R. C. Elphic, W. C. Feldman, D. J. Lawrence, G. W. McKinney and D. T. Vaniman, "Elemental composition of the lunar surface: Analysis of gamma ray spectroscopy data from Lunar Prospector", Journal of Geophysical Research: Planets **111**, E12, URL https://agupubs.onlinelibrary.wiley.com/doi/abs/10.1029/2005JE002656 (2006).

Prettyman, T. H., N. Yamashita, E. Ammannito, B. L. Ehlmann, H. Y. McSween, D. W. Mittlefehldt, S. Marchi, N. Schörghofer, M. J. Toplis, J.-Y. Li, C. M. Pieters, J. C. Castillo-Rogez, C. A. Raymond and C. T. Russell, "Elemental composition and mineralogy of Vesta and Ceres: Distribution and origins of hydrogen-bearing species", Icarus **318**, 42–55, URL http://www.sciencedirect.com/science/article/pii/S0019103517308643 (2019b).

Price Russ, G., D. S. Burnett and G. J. Wasserburg, "Lunar neutron stratigraphy", Earth and Planetary Science Letters **15**, 2, 172–186 (1972).

Pugel, B., H. Graham, M. Floyd and A. Parsons, "Multimodal investigations of boron as a biosignature - nasa/ads", in "American Geophysical Union, Fall Meeting", pp. abstract P41C–3461 (2019), URL https://ui.adsabs.harvard.edu/abs/2019AGUFM.P41C3461P/abstract.

Reedy, R. C., "Planetary gamma-ray spectroscopy.", Lunar and Planetary Science Conference Proceedings **3**, 2961–2984, URL https://ui.adsabs.harvard.edu/abs/1978LPSC....9.2961R (1978).

Reedy, R. C., J. R. Arnold and J. I. Trombka, "Expected γ ray emission spectra from the lunar surface as a function of chemical composition", Journal of Geophysical Research **78**, 26, 5847–5866, URL `https://onlinelibrary.wiley.com/doi/full/10.1029/JB078i026p05847https://onlinelibrary.wiley.com/doi/abs/10.1029/JB078i026p05847https://agupubs.onlinelibrary.wiley.com/doi/10.1029/JB078i026p05847` (1973).

RI Scherpelz, M. C., "Upgrade of the PNNL TEPC and Multisphere Spectrometer RI Scherpelz MM Conrady", Tech. rep., PNNL-17809, Richland, Washington, URL `https://www.pnnl.gov/main/publications/external/technical_reports/PNNl-17809.pdf` (2008).

RMD Inc., "CLYC Gamma-Neutron Scintillator", URL `https://www.dynasil.com/product-category/scintillators/clyc-gamma-neutron-scintillators/` (2021).

Rodriguez, S., S. Vinatier, D. Cordier, G. Tobie, R. K. Achterberg, C. M. Anderson, S. V. Badman, J. W. Barnes, E. L. Barth, B. Bézard, N. Carrasco, B. Charnay, R. N. Clark, P. Coll, T. Cornet, A. Coustenis, I. Couturier-Tamburelli, M. Dobrijevic, F. M. Flasar, R. de Kok, C. Freissinet, M. Galand, T. Gautier, W. D. Geppert, C. A. Griffith, M. S. Gudipati, L. Z. Hadid, A. G. Hayes, A. R. Hendrix, R. Jaumann, D. E. Jennings, A. Jolly, K. Kalousova, T. T. Koskinen, P. Lavvas, S. Lebonnois, J. P. Lebreton, A. Le Gall, E. Lellouch, S. Le Mouélic, R. M. Lopes, J. M. Lora, R. D. Lorenz, A. Lucas, S. MacKenzie, M. J. Malaska, K. Mandt, M. Mastrogiuseppe, C. E. Newman, C. A. Nixon, J. Radebaugh, S. C. Rafkin, P. Rannou, E. M. Sciamma-O'Brien, J. M. Soderblom, A. Solomonidou, C. Sotin, K. Stephan, D. Strobel, C. Szopa, N. A. Teanby, E. P. Turtle, V. Vuitton and R. A. West, "Science goals and new mission concepts for future exploration of Titan's atmosphere, geology and habitability: titan POlar scout/orbitEr and in situ lake lander and DrONe explorer (POSEIDON)", Experimental Astronomy pp. 1–63, URL `https://link.springer.com/article/10.1007/s10686-021-09815-8` (2022).

Roe, H. G., "Titan's methane weather", Annual Review of Earth and Planetary Sciences **40**, 355–382 (2012).

Sagan, C. and B. N. Khare, "Tholins: organic chemistry of interstellar grains and gas", Nature 1979 277:5692 **277**, 5692, 102–107, URL `https://www.nature.com/articles/277102a0` (1979).

Sanin, A. B., I. G. Mitrofanov, M. L. Litvak, D. I. Lisov, R. Starr, W. Boynton, A. Behar, L. DeFlores, F. Fedosov, D. Golovin, C. Hardgrove, K. Harshman, I. Jun, A. S. Kozyrev, R. O. Kuzmin, A. Malakhov, R. Milliken, M. Mischna, J. Moersch, M. I. Mokrousov, S. Nikiforov, V. N. Shvetsov, C. Tate, V. I. Tret'Yakov and A. Vostrukhin, "Data processing of the active neutron experiment DAN for a Martian regolith investigation", Nuclear Instruments and Methods in Physics Research, Section A: Accelerators, Spectrometers, Detectors and Associated Equipment **789**, 114–127 (2015).

Soderblom, L. A., M. G. Tomasko, B. A. Archinal, T. L. Becker, M. W. Bushroe, D. A. Cook, L. R. Doose, D. M. Galuszka, T. M. Hare, E. Howington-Kraus, E. Karkoschka, R. L. Kirk, J. I. Lunine, E. A. McFarlane, B. L. Redding, B. Rizk, M. R. Rosiek, C. See and P. H. Smith, "Topography and geomorphology of the Huygens landing site on Titan", Planetary and Space Science **55**, 13, 2015–2024, URL http://www.sciencedirect.com/science/article/pii/S0032063307001298 (2007).

Surkov, I. A., "Geochemical studies of Venus by Venera 9 and 10 automatic interplanetary stations.", Lunar and Planetary Science Conference Proceedings **3**, 2665–2689, URL https://ui.adsabs.harvard.edu/abs/1977LPSC....8.2665S (1977).

Surkov, Y. A., F. F. Kirnozov, V. N. Glazov, A. G. Dunchenko, L. P. Tatsy and O. P. Sobornov, "Uranium, thorium, and potassium in the Venusian rocks at the landing sites of Vega 1 and 2", Journal of Geophysical Research: Solid Earth **92**, B4, E537—-E540, URL https://doi.org/10.1029/JB092iB04p0E537 (1987).

Surkov, Y. A., L. P. Moskalyova, V. P. Kharyukova, A. D. Dudin, G. G. Smirnov and S. Y. Zaitseva, "Venus rock composition at the Vega 2 Landing Site", Journal of Geophysical Research: Solid Earth **91**, B13, E215—-E218, URL https://doi.org/10.1029/JB091iB13p0E215 (1986).

ThermoFisher Scientific, "Thermo Scientific MP 320", URL https://www.thermofisher.com/document-connect/document-connect.html?url=https%3A%2F%2Fassets.thermofisher.com%2FTFS-Assets%2FCAD%2FSpecification-Sheets%2FD10497$\sim$.pdf&title=TVAgMzIw (2007).

ThermoFisher Scientific, "Specification Sheet: RIIDEye Series", URL https://www.thermofisher.com/ (2012).

Thompson, W. L., "Mcnp, a general monte carlo code for neutron and photon transport: a summary", Tech. rep., Los Alamos National Laboratory (LANL) (1979).

Trombka, J. I., F. Senftle and R. Schmadebeck, "Neutron radiative capture methods for surface elemental analysis", Nuclear Instruments and Methods **87**, 1, 37–43 (1970).

UG, G., "MetBase: Meteorite Information Database, ", URL http://www.metbase.org (2017).

Vago, J. L., F. Westall, A. J. Coates, R. Jaumann, O. Korablev, V. Rie Ciarletti, I. Mitrofanov, J.-L. Josset, M. C. De Sanctis, J.-P. Bibring, F. Rull, F. Goesmann, H. Steininger, W. Goetz, W. Brinckerhoff, C. Szopa, F. Ois Raulin, H. G. M. Edwards, L. G. Whyte, A. G. Fairé, J. Bridges, E. Hauber, G. G. Ori, S. Werner, D. Loizeau, R. O. Kuzmin, R. M. E. Williams, J. Flahaut, F. Ois Forget, D. Rodionov, H. Kan Svedhem, E. Sefton-Nash, G. Kminek, L. Lorenzoni, L. Joudrier, V. Mikhailov, A. Zashchirinskiy, S. Alexashkin, F. Calantropio, A. Merlo, P. Poulakis, O. Witasse, O. Bayle, S. Bayó, U. Meierhenrich, J. Carter, J. Manuel García-Ruiz, P. Baglioni, A. Haldemann, A. J. Ball, A. Debus, R. Lindner, F. Dé, R. Haessig, D. Monteiro, R. Trautner, C. Voland, P. Rebeyre, D. Goulty,

R. Didot, S. Durrant, E. Zekri, D. Koschny, A. Toni, G. Visentin, M. Zwick, M. Van Winnendael, M. Azkarate and C. Carreau, "ExoMars Rover Mission Habitability on Early Mars and the Search for Biosignatures with the ExoMars Rover Landing Site Selection Working Group", ASTROBIOLOGY **17** (2017).

Van Rossum, G. and F. L. Drake, *The python reference manual*, no. March (Centrum voor Wiskunde en Informatica Amsterdam, 1995), URL www.python.org.

Vertes, S. N., *Nuclear Methods in Mineralogy and Geology* (Springer US, 1998).

Virtanen, P., R. Gommers, T. E. Oliphant, M. Haberland, T. Reddy, D. Cournapeau, E. Burovski, P. Peterson, W. Weckesser, J. Bright, S. J. van der Walt, M. Brett, J. Wilson, K. J. Millman, N. Mayorov, A. R. Nelson, E. Jones, R. Kern, E. Larson, C. J. Carey, I. Polat, Y. Feng, E. W. Moore, J. VanderPlas, D. Laxalde, J. Perktold, R. Cimrman, I. Henriksen, E. A. Quintero, C. R. Harris, A. M. Archibald, A. H. Ribeiro, F. Pedregosa, P. van Mulbregt, A. Vijaykumar, A. P. Bardelli, A. Rothberg, A. Hilboll, A. Kloeckner, A. Scopatz, A. Lee, A. Rokem, C. N. Woods, C. Fulton, C. Masson, C. Häggström, C. Fitzgerald, D. A. Nicholson, D. R. Hagen, D. V. Pasechnik, E. Olivetti, E. Martin, E. Wieser, F. Silva, F. Lenders, F. Wilhelm, G. Young, G. A. Price, G. L. Ingold, G. E. Allen, G. R. Lee, H. Audren, I. Probst, J. P. Dietrich, J. Silterra, J. T. Webber, J. Slavič, J. Nothman, J. Buchner, J. Kulick, J. L. Schönberger, J. V. de Miranda Cardoso, J. Reimer, J. Harrington, J. L. C. Rodríguez, J. Nunez-Iglesias, J. Kuczynski, K. Tritz, M. Thoma, M. Newville, M. Kümmerer, M. Bolingbroke, M. Tartre, M. Pak, N. J. Smith, N. Nowaczyk, N. Shebanov, O. Pavlyk, P. A. Brodtkorb, P. Lee, R. T. McGibbon, R. Feldbauer, S. Lewis, S. Tygier, S. Sievert, S. Vigna, S. Peterson, S. More, T. Pudlik, T. Oshima, T. J. Pingel, T. P. Robitaille, T. Spura, T. R. Jones, T. Cera, T. Leslie, T. Zito, T. Krauss, U. Upadhyay, Y. O. Halchenko and Y. Vázquez-Baeza, "SciPy 1.0: fundamental algorithms for scientific computing in Python", Nature Methods **17**, 3, 261–272 (2020).

Vogel, S., R. Frank, G. Stoddard, J. F. Christian, E. B. Johnson, C. Hardgrove, R. Starr and S. West, "Development of the LunaH-Map miniature neutron spectrometer", in "Hard X-Ray, Gamma-Ray, and Neutron Detector Physics XIX", edited by M. Fiederle, A. Burger, L. Franks, R. B. James and S. A. Payne, vol. 10392, p. 16 (SPIE-Intl Soc Optical Eng, 2017).

Watson, K., B. Murray and H. Brown, "On the possible presence of ice on the Moon", Journal of Geophysical Research **66**, 5, 1598–1600, URL https://onlinelibrary.wiley.com/doi/full/10.1029/JZ066i005p01598https://onlinelibrary.wiley.com/doi/abs/10.1029/JZ066i005p01598https://agupubs.onlinelibrary.wiley.com/doi/10.1029/JZ066i005p01598 (1961).

Watts, M. M., K. E. Mesick, K. D. Bartlett and D. D. S. Coupland, "Thermal Characterization of Tl_2LiYCl_6:Ce (TLYC)", IEEE Transactions on Nuclear Science **67**, 3, 525–533 (2019).

Wetherill, G. W., "ASTEROIDAL SOURCE OF ORDINARY CHONDRITES*", Meteoritics **20**, 1, 1–22, URL https://doi.org/10.1111/j.1945-5100.1985.tb00842.x (1985).

Whetstone, R., W. O. Robinson and H. Byers, "Boron distribution in soils and related data", Tech. rep., US Dept. of Agriculture, URL https://naldc.nal.usda.gov/download/CAT86200792/PDF (1941).

Wilcox, L. V., "Determination of Boron in Natural Waters and Plant Materials: Modification of the Chapin Method", Industrial and Engineering Chemistry - Analytical Edition **2**, 4, 358–361, URL https://pubs.acs.org/sharingguidelines (1930).

Wilson, J., V. Eke, R. Massey, R. Elphic, W. Feldman, S. Maurice and L. Teodoro, "Equatorial locations of water on Mars: Improved resolution maps based on Mars Odyssey Neutron Spectrometer data", Icarus **299** (2017).

Zarnecki, J. C., M. R. Leese, B. Hathi, A. J. Ball, A. Hagermann, M. C. Towner, R. D. Lorenz, J. A. M. McDonnell, S. F. Green, M. R. Patel, T. J. Ringrose, P. D. Rosenberg, K. R. Atkinson, M. D. Paton, M. Banaszkiewicz, B. C. Clark, F. Ferri, M. Fulchignoni, N. A. Ghafoor, G. Kargl, H. Svedhem, J. Delderfield, M. Grande, D. J. Parker, P. G. Challenor and J. E. Geake, "A soft solid surface on Titan as revealed by the Huygens Surface Science Package", Nature **438**, 7069, 792–795 (2005).

APPENDIX A

LIST OF ACRONYMS, SYMBOLS, AND ABBREVIATIONS

Acronym/Symbol/Abbreviation	Meaning
ACS	AntiCoincidence Shield
ADC	Analog to Digital Converter
ADRON-RM	Autonomous Detector of Radiation Of Neutrons onboard Rover at Mars
APID	Application Process Identifier
APL	Applied Physics Laboratory (Johns Hopkins)
BGO	Bismuth Germanate Oxide
BLP	Boron Lithiated Plastic
C&DH	Command and Data Handling
CAD	Computer Assisted Drawing
CCSDS	Consultative Committee for Space Data Systems
CLLBC	$Cs_2LiLa(Br,Cl)_6$:Ce
CLYC	Cs_2LiYCl_6:Ce
CVL	Core-to-Valence Luminescence
DALI	Development and Advancement of Lunar Instrumentation
DAN	Dynamic Albedo of Neutrons
DAQ	Data Acquisition
DD	Deuterium-Deuterium
DraGNS	Dragonfly Gamma Ray and Neutron Spectrometer
DT	Deuterium-Tritium
FPGA	Field Programmable Gate Array
FSW	Flight Software
FWTA	Flux Weighted Time Average
GEANT	GEometry ANd Tracking particle simulation software
GEE	Gamma-Equivalent Energy

Acronym/Symbol/Abbreviation	Meaning
GGAO	Goddard Geophysical and Astronomical Observatory
GRNS	Gamma-Ray and Neutron Spectrometer
GRS	Gamma-Ray Spectrometer
GSFC	Goddard Space Flight Center
HDPE	High-Density PolyEthylene
HEND	High Energy Neutron Detector
HPGE	High-Purity Germanium
HV	High Voltage
JAXA	Japanese Aerospace eXploration Agency
JTAG	USB Programming Cable
LANL	Los Alamos National Laboratory
LEND	Lunar Exploration Neutron Detector
LEO	Low Earth Orbit
LLNL	Lawrence Livermore National Laboratory
LP	Lunar Prospector
LPNS	Lunar Prospector Neutron Spectrometer
MCNP	Monte-Carlo N-Particle (simulation code from LANL)
MEGANE	Mars-moon Exploration with GAmma rays and Neutrons
Mini-NS/MiniNS/MNS	Miniature Neutron Spectrometer
MMRTG	Multi-Mission Radioisotope Thermoelectric Generator
MMX	Martian Moons eXplorer
MOGRS	Mars Odyssey Gamma-Ray Spectrometer
MONS	Mars Odyssey Neutron Spectrometer
MSL	Mars Science Laboratory
NASA	National Aeronautics and Space Administration

Acronym/Symbol/Abbreviation	Meaning
NFIA	Neutron Free-In-Air
NG	Neutron Generator
NS	Neutron Spectrometer
NS	Neutron Spectrometer
OACF	Off-Axis Correction Factor
PACF	Projected Area Correction Factor
PGNAA	Prompt Gamma Neutron Activation Analysis
PICASSO	Planetary Instrument Concepts for the Advancement of Solar System Observations
PMT	Photomultiplier Tube
PNG	Pulsed Neutron Generator
POR	Power On Reset
PSD	Pulse Shape Discrimination
RS422	High speed and/or long distance data transmission
SD	Secure Digital
SINGR	Single Scintillator Neutron and Gamma-Ray spectrometer
SiPM	Silicon PhotoMultiplier
SLS	Space Launch System
SMD	Space Mission Directorate
SNM	Special Nuclear Material
SOH	Statement of Health
SOH	Statement of Health
SPP	Space Packet Protocol
TLYC	Tl_2LiYCl_6:Ce
TPT	Thermal Peak Time

Acronym/Symbol/Abbreviation	Meaning
TTL	Transistor-Transistor Logic
UART	Universal Asynchronous Receiver-Transmitter
USGS	United States Geological Society
WEH	Water-Equivalent Hydrogen
WF	Waveform

APPENDIX B

MCNP PYTHON TOOLBOX FOR PLANETARY APPLICATIONS

Available at https://github.com/lheffern

MCNP base file

- Specific base geometry file (1-layer or 2-layer)

- Specific particle tallys

- Specific time tallys

- Specific source

Python MCNP generator program and library

Program generates all MCNP files, .sh files, and copy/paste files for transferring

to/from Agave ASU cluster

Elemental Grid

Specify base composition from library

Specify elemental abundance to vary

Specify range of abundances

Depth Grid

Specify wt % of a specific element in top layer and bottom layer

Specify range of depth for bottom layer

Python MCNP analysis and stats library

Converts .outputo files into formatted .csv files based on:

Particle type

Energy bin(s)

Imports .csv files into desired programs for data visualization.

Can input experimental file to perform chi-square analysis to compare data with simulation grids

MCNP Material Cards Compendium

All materials cards used throughout this dissertation are located on the gibhub linked above under the Compositions folder. These compositions are formatted in a specific way to allow for easy implementation into MCNP input files, the composition format is as follows:

```
c Concord Grey Granite, rho=2.63 g/cm3, fractions in wt%
m7    8016.70c    -48.69    $O

      14028.70c   -31.91    $Si-28

      14029.70c   -1.62     $Si-29

      14030.70c   -1.07     $Si-30

      19000.70c   -4.27     $K

      ...
```

APPENDIX C

STATEMENT OF CO-AUTHOR APPROVALS FOR PUBLISHED WORK

Chapter 2 has undergone peer review and has been published in the journal Nuclear Instruments and Methods in Physics Research, Section A (Heffern et al., 2021). Chapters 3 is in preparation for a peer-reviewed journal at the time of this dissertation. I, Lena Heffern, affirm that I am the principal author of Chapters 2 and 3 and that all subsequent coauthors approve of the publication of these works. In addition, I am the principle author of Chapter 4 and I will have significant contributions as a co-author to a publication in process for Chapter 4 of which all authors approve for publication.

References

Heffern, L. E., Hardgrove, C. J., Parsons, A., Johnson, E. B., Starr, R., Stoddard, G., Blakeley, R. E., Prettyman, T., Gabriel, T. S. J., Barnaby, H., Christian, J., Unzueta, M. A., Tate, C., Martin, A., & Moersch, J. "Active neutron interrogation experiments and simulation verification using the SIngle-scintillator Neutron and Gamma-Ray spectrometer (SINGR) for geosciences." Nuclear Instruments and Methods in Physics Research, Section A: Accelerators, Spectrometers, Detectors and Associated Equipment, 1020. https://doi.org/10.1016/j.nima.2021.165883 (2021).

APPENDIX D

MINI-NS CALIBRATION PLANS

LunaH-Map Mini-NS Calibration Plan Details & Schedule

Table of Contents

1. Introduction: Calibration at Los Alamos National Laboratory Neutron Free In-Air Facility

Brief Summary

The Miniature Neutron Spectrometer (Mini-NS) flight model (FM) will be calibrated prior to final spacecraft closeout and delivery (NLT 12/15/18). Calibration will be completed at the Los Alamos National Laboratory (LANL) Neutron Free In-Air Facility (NFIA) with the Mini-NS FM. An iodine tank will be available for acquiring secondary measurements to assess the influence of the iodine fuel on the neutron and gamma-ray background after the primary calibration activities are complete. The proposed calibration activities are as follows:

1) Determine the Mini-NS instrument response to a calibrated source of thermal+epithermal neutrons (Figure 1)
2) Determine the Mini-NS instrument response to a calibrated source of epithermal neutrons (Figure 1)
3) Determine the angular response of the Mini-NS instrument
4) Determine the thermal neutron leakage to the detector
5) Determine resulting instrument response functions (efficiency, angular) from calibration
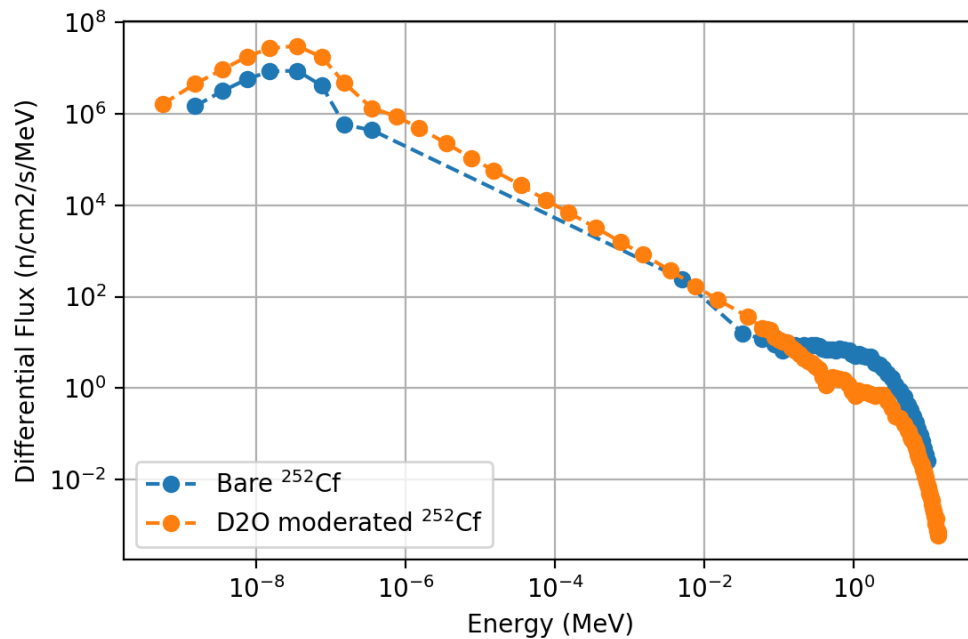
Figure 1: Differential neutron fluxes for the [252]Cf source at the LANL NFIA facility. The source is at a distance of 200 cm from the target. The bare source is shown (blue) along with the D2O moderated sphere (orange) representing a primarily thermal source. Spectra is taken from the ISO Standard ROSPEC excel data file.

Calibration Notes

The angular response of the Mini-NS instrument will be determined using the methods outlined for GRaND (Prettyman et al., 2011) and MESSENGER (Goldsten et al, 2007) in the Neutron Free-in-Air (NFIA) facility. An example of the angular efficiency results from the GRaND instrument is shown in Figure 3.

For calibration, the Mini-NS instrument (Figure 2) will be mounted on a rotating stage to enable control of the geometry with respect to the source (Figure 5). A full set of measurements will be made with a bare [252]Cf source and a D2O moderated [252]Cf source (Cd cover).

For each set of measurements, the detector will be placed a predetermined distance from the face of the source (e.g. 50 cm for LPNS, MiniNS nominally at 200 cm) and counts recorded for a predetermined period of time (e.g. 640s for LPNS, MiniNS nominally for 15 minutes). The detector will be rotated in place and another measurement made. This process will be repeated for a range of angles from -180 to +180 degrees, this is detailed in Section 3. After completing angular sweeps with and without the cadmium/gadolinium shield, the Mini-NS instrument will be removed from the rotating stage and reinstalled at

a 90 degree angle from its previous orientation. The calibration will be repeated with rotation along this axis. Figure 4 defines the different axes of the MiniNS instrument with respect to the spacecraft.

The thermal calibration for the Mini-NS is being handled by RMD Inc. and will be completed before December 31st, 2018.
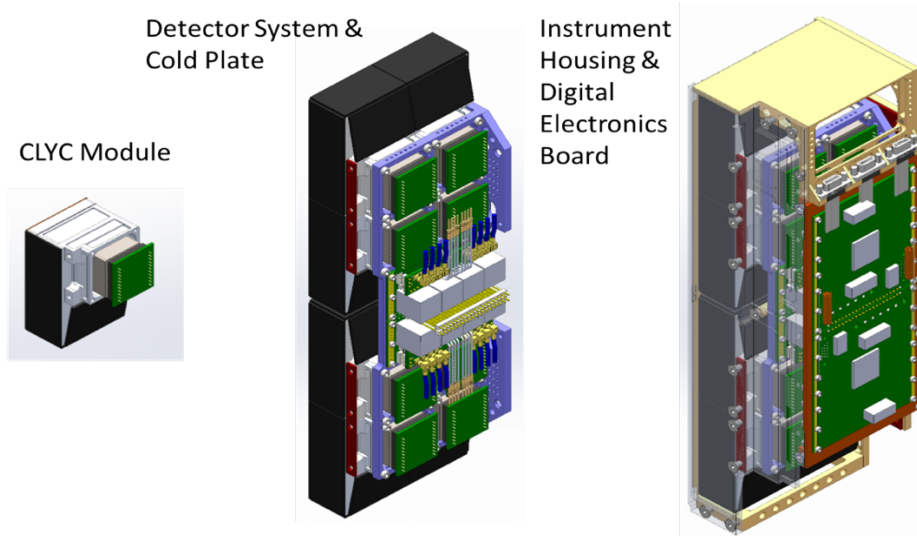
Figure 2: Mini-NS buildup from module to integrated detector. Black B4C shielding shown on all but the nadir face will be replaced with Gd.
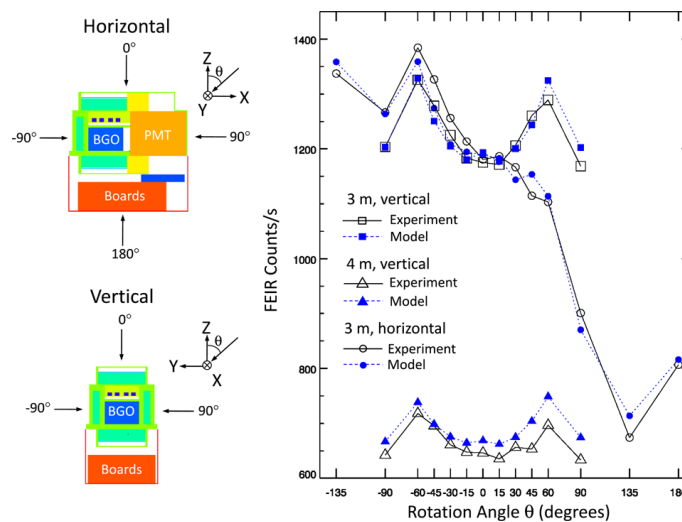
Figure 3: Example of experimental data required for angular response determination from GRaND gamma-ray angular response calibration (Prettyman et al., 2011)

2. Science Background

The Miniature Neutron Spectrometer (Mini-NS) is a neutron spectrometer flying as the primary payload on the Lunar Polar Hydrogen Mapper (LunaH-Map) CubeSat. By detecting suppressions in epithermal neutron count rate from very low perilune altitudes (<15km), Mini-NS will produce maps of lunar south pole hydrogen enrichments at spatial scales smaller than known permanently shadowed regions (PSRs). Due to the desired spatial sensitivities and low altitudes which will likely impart topographic effects on the data, a careful calibration of the Mini-NS energy and angle response is necessary to properly interpret the epithermal count rate suppressions observed throughout the LunaH-Map mission. Mini-NS uses CLYC, an elpasolite scintillator, coupled to PMTs to detect neutrons through the 6-Li(a,t) capture reaction. A gadolinium shield covers the majority of the sensor head to significantly reduce the number of thermal neutrons interacting with the scintillators and restricting Mini-NS sensitivity to epithermal neutrons with $E > \sim 0.3$ eV.

3. Mission Background

The LunaH-Map mission is a planetary science mission sponsored by NASA Science Mission Directorate (SMD). It is, however, the first of its kind in scope and budget, and therefore represents a new type of mission for NASA SMD. While LunaH-Map is a science driven mission, the calibration and tests of sensors and instruments are completed on a best-effort basis as dictated by the Principle Investigator and ASU Project Management. The LunaH-Map project structure and funding model are more aligned with that of traditional University-led, low-earth orbit (LEO) CubeSat mission. The LunaH-Map PI, Dr. Hardgrove, is committed to acquiring the proper calibration data for the Mini-NS and is very excited to foster new partnerships with Los Alamos National Laboratory. Dr. Hardgrove and his research group have recently been working with Drs. Laura Stonehill and Suzanne Nowicki on several neutron and gamma-ray instrument proposals and projects. This included involving LANL in active neutron instrument missions (MSL DAN), proposals (MMX), and summer student work at LANL.

4. Calibration Schedule

Notional Calibration Schedule of Activities
1. Monday - Equipment set up & 5 minute DAQ check ~ 2 hours (EC Macro)
   1.1. Initial source strength test runs ~ 2 hours (DEG Macros - LHMacro)
   1.2. Background ~ 2 hours (DEG Macros - LHMacro)
   1.3. Set up fast response test if time allows
2. Tuesday - Mini-NS installed with X axis of rotation (defined in Fig. 4b & 5b)
   2.1. Mini-NS mounted 200 cm from ^{252}Cf source – Thermal & Epithermal SHORT
      2.1.1. Angular sweep measurements, 900 s integration and ~ 1800 s (in review) data transfer at each (~ 45 minutes each, [5 hours, 7 hours])
      2.1.2. 30 degree increments from 0° to +180° [7 measurements]

2.1.3. If time allows, Thermal & Epithermal LONG

    2.1.3.1.   15°, 45°, 75° increments from 0° [3 measurements]

    2.1.3.2.   15° degree increments from -15° to -90°, and -120°, -150° [7 measurements]

3. Wednesday - Mini-NS installed with X axis of rotation (defined in Fig. 4b & 5b)

    3.1. Mini-NS mounted 200 cm from D2O moderated ^{252}Cf source – Epithermal SHORT

        3.1.1. Angular sweep measurements, 900 s integration and ~ 1800 s (in review) data transfer at each (~ 45 minutes each, [5 hours, 7 hours])

        3.1.2. 30 degree increments from 0° to +180° [7 measurements]

        3.1.3. If time allows, Epithermal LONG

            3.1.3.1.   15°, 45°, 75° increments from 0° [3 measurements]

            3.1.3.2.   15° degree increments from -15° to -90°, and -120°, -150° [7 measurements]

4. Thursday - Mini-NS installed with Z axis of rotation (defined in Fig. 4a & 5a)

    4.1. Mini-NS mounted 200 cm (TBR) from ^{252}Cf source - Thermal & Epithermal SHORT

        4.1.1. Angular sweep measurements, 900 s integration and ~ 1800 s (in review) data transfer at each (~ 45 minutes each, [5 hours, 7 hours])

        4.1.2. 30 degree increments from 0° to +180° [7 measurements]

        4.1.3. If time allows, Thermal & Epithermal LONG

            4.1.3.1.   15°, 45°, 75° increments from 0° [3 measurements]

            4.1.3.2.   15° degree increments from -15° to -90°, and -120°, -150° [7 measurements]

5. Friday - Mini-NS installed with Z axis of rotation (defined in Fig. 4a & 5a)

    5.1. Mini-NS mounted 200 cm (TBR) from D2O moderated ^{252}Cf source – Epithermal SHORT

        5.1.1. Angular sweep measurements, 900 s integration and ~ 1800 s (in review) data transfer at each (~ 45 minutes each, [5 hours, 7 hours])

        5.1.2. 30 degree increments from 0° to +180° [7 measurements]

        5.1.3. If time allows, Epithermal LONG

            5.1.3.1.   15°, 45°, 75° increments from 0° [3 measurements]

            5.1.3.2.   15° degree increments from -15° to -90°, and -120°, -150° [7 measurements]

6. Friday + - If time allows, complete subset (30°) of the X and Z axis tests with an overmoderated ^{252}Cf source (thick polyethylene) and complete the iodine test
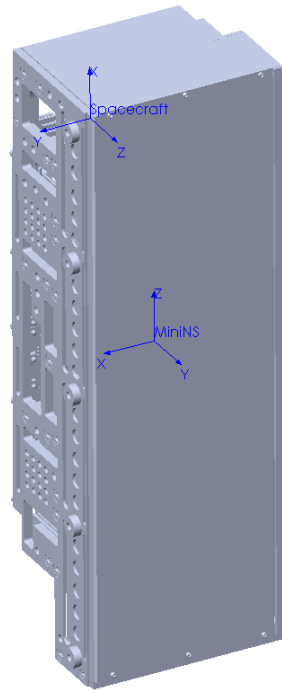
Figure 4(a): Z axis of rotation reference axes for Mini-NS calibration, showing both instrument and spacecraft axes.
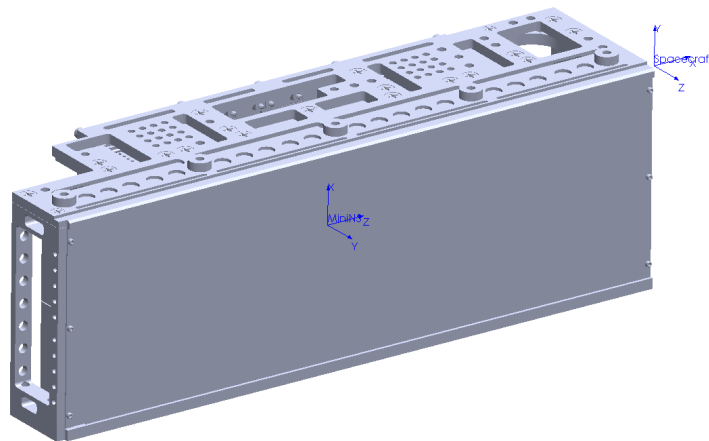
Figure 4(b): X axis of rotation reference axes for Mini-NS calibration, showing both instrument and spacecraft axes.
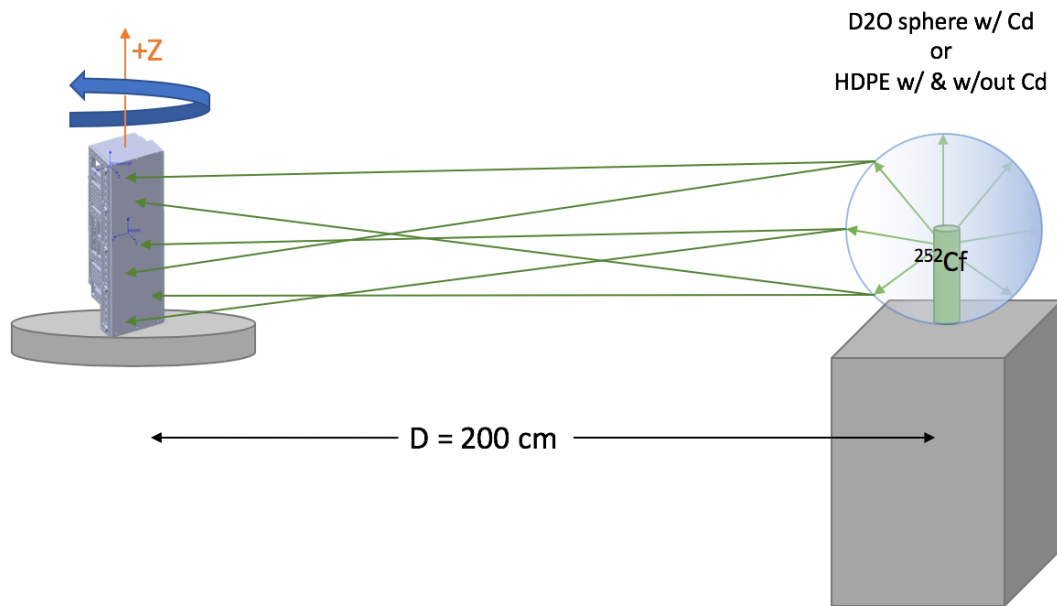
Figure 5(a): Z axis of rotation experimental diagram depicting the [252]Cf neutron source at a distance of 200 cm from the Mini-NS instrument front face.
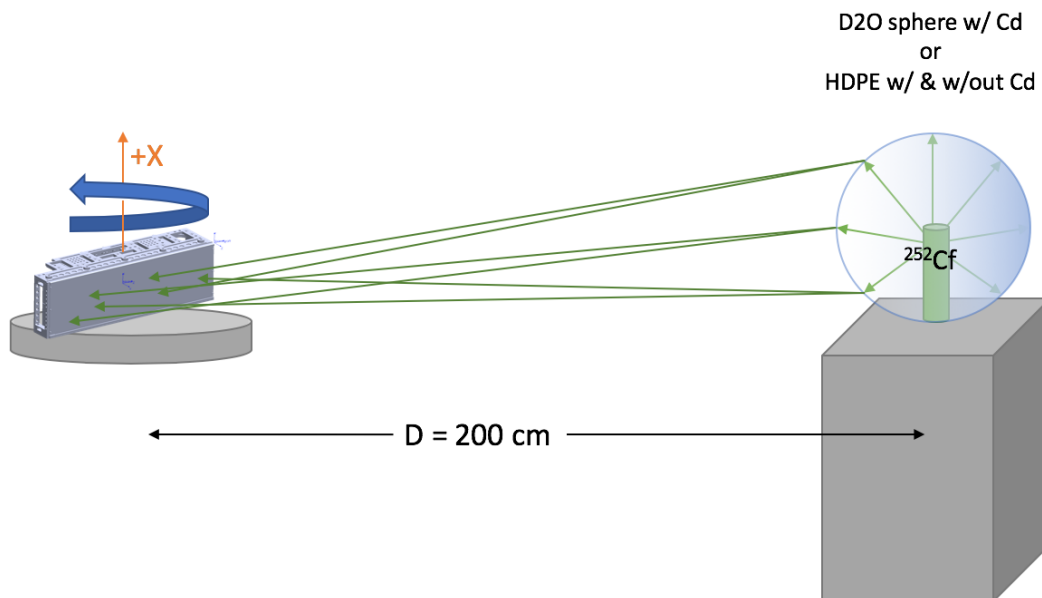
Figure 5(b): X axis of rotation experimental diagram depicting the ^{252}Cf neutron source at a distance of 200 cm from the Mini-NS instrument front face.

5. Mini-NS NFIA MCNP Simulations for Calibration Plan

MCNP6 will be used to determine expected response values for the Mini-NS. An MCNP file of the NFIA facility already exists and has been run for different sources at a variety of distances by Katherine and Dan at LANL, currently we are unsure of *what (if any) simulations have been done with a shadow cone* in place to determine room background response only (source is blocked from direct incidence onto detector).

Desired NFIA Room MCNP Outputs (6 files)
1. Bare ^{252}Cf with instrument/spacecraft at X cm from source
2. D2O covered ^{252}Cf with instrument/spacecraft at X cm from source
3. D2O & Cd covered ^{252}Cf with instrument/spacecraft at X cm from source
4. Bare ^{252}Cf with instrument/spacecraft at X cm from source and Shadow Cone
5. D2O covered ^{252}Cf with instrument/spacecraft at X cm from source and Shadow Cone
6. D2O & Cd covered ^{252}Cf with instrument/spacecraft at X cm from source and Shadow Cone

Starting at X = 200 cm

Instrument Response Bare ^{252}Cf

36 files x 2 spectra x 8 modules

Insert output spectra @ 200 cm into source term of instrument file

Neutron Counts (F1 Tally PRIMARY) rotate instrument/source
- Gamma-ray Counts (F1 Tally, F8 Tally, post process after neutrons)

X-Axis of rotation
- 0°, 15°, 30°, 45°, 60°, 75°, 90°, 120°, 150°, 180°, -15°, -30°, -45°, -60°, -75°, -90°, -120°, -150°

Z-Axis of rotation
- 0°, 15°, 30°, 45°, 60°, 75°, 90°, 120°, 150°, 180°, -15°, -30°, -45°, -60°, -75°, -90°, -120°, -150°

Try to get the n,Cl reaction working to determine a fast neutron count rate

Instrument Response D2O on ^{252}Cf

36 files x 2 spectra x 8 modules

Insert output spectra on source term into instrument file? (double check this)

Neutron Counts (F1 Tally PRIMARY) rotate instrument/source

- Gamma-ray Counts (F1 Tally, F8 Tally)

X-Axis of rotation

- 0°, 15°, 30°, 45°, 60°, 75°, 90°, 120°, 150°, 180°, -15°, -30°, -45°, -60°, -75°, -90°, -120°, -150°

Z-Axis of rotation

- 0°, 15°, 30°, 45°, 60°, 75°, 90°, 120°, 150°, 180°, -15°, -30°, -45°, -60°, -75°, -90°, -120°, -150°

Instrument Response D2O & Cd on ^{252}Cf

36 files x 2 spectra x 8 modules

Insert output spectra on source term into instrument file? (double check this)

Neutron Counts (F1 Tally PRIMARY) rotate instrument/source

- Gamma-ray Counts (F1 Tally, F8 Tally)

X-Axis of rotation

- 0°, 15°, 30°, 45°, 60°, 75°, 90°, 120°, 150°, 180°, -15°, -30°, -45°, -60°, -75°, -90°, -120°, -150°

Z-Axis of rotation

- 0°, 15°, 30°, 45°, 60°, 75°, 90°, 120°, 150°, 180°, -15°, -30°, -45°, -60°, -75°, -90°, -120°, -150°
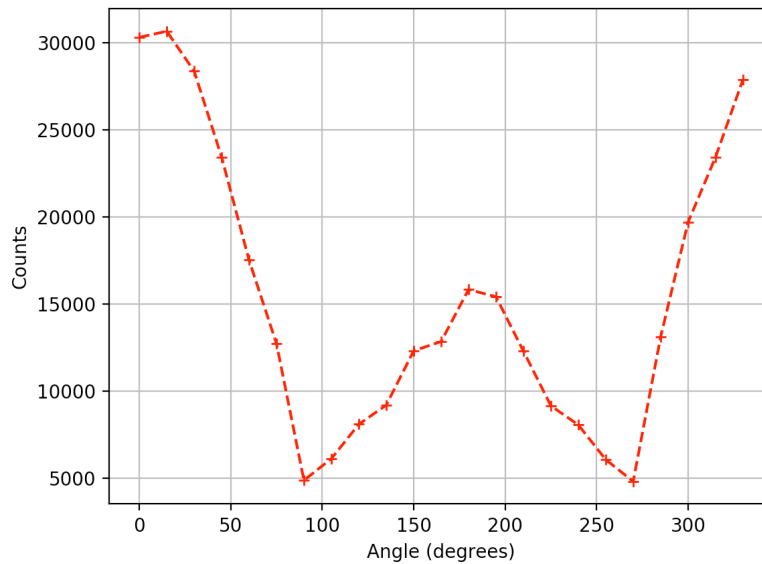
Figure 5: Full instrument (8 modules totaled) angular simulation initial results for the X-axis of rotation of a 40" x 40" source plane rotating about the Mini-NS instrument.

6. Mini-NS NFIA Detailed Calibrations Experimental Test Plan

Ideally, we will be able to pick off integral values (and therefore PSD and channel height histograms) from each individual module. This is a general checklist for the full measurement campaign.

Unpacking Mini-NS (on-site in LANL lab or at NFIA pre-calibration)

      Set up necessary cabling on benchtop

      Verify instrument/spacecraft can power on

          o   Check 12V (+/-20%) power in & vary this to see Mini-NS response - Igor

      Take data with background (15 mins DAQ)

      If weak (class 0 or 1) gamma or neutron source is available (7-8 uC ^{137}Cs), test instrument output to verify gain, 2min & 15 min DAQs. Verify performance against RMD/ASU data using ^{137}Cs pre-ship.

      If gain matching is required, call Erik? Depends on state of instrument/spacecraft

      Verify gain matching if needed

      Power down, move to NFIA facility and NFIA calibration configuration

Initial Set-Up & System Checks in NFIA facility

      Mounting plate attached to NFIA movement stage
      Instrument or Spacecraft secured to mounting plate
      Distance from instrument/spacecraft face and center to NS source measured
      Distance from instrument each NS module center face to NS source measured
      Communication cables secured
      Verify power to instrument/spacecraft (turn on)
      Test communication to instrument/spacecraft
      Run initial test (5 min w/ weakest source) to verify working instrument
      Verify gain matching

Basic Background test

This test is to identify contamination or unexpected sources within the room.

      Remove & secure any sources from the room
      Verify instrument/spacecraft is secure on mount
      If instrument/spacecraft is not powered on, turn it on
      Begin 2-4 hour background measurement acquisition
      Assume 4 hour transfer time minimum
          o   Can we leave the instrument overnight?
          o   Can we come back in the evening to power down?
      Remove source following LANL guidelines

Room return test (optional test, dependent on time allowable)

      Verify instrument/spacecraft is secure on mount in X axis of rotation position
      Align the shadow-cone structure along the axis from the source location to the instrument/spacecraft, blocking the instrument/spacecraft from the source
      If instrument/spacecraft is not powered on, turn it on
      Secure bare ^{252}Cf source following LANL procedure for using the ^{252}Cf source
          o   Check source is bare
      Begin 1 hour measurement acquisition (assume 1 hour transfer time minimum)
      Remove source following LANL guidelines
      Realign & secure instrument/spacecraft on mount in Z axis of rotation position
      If instrument/spacecraft is not powered on, turn it on
      Secure bare ^{252}Cf source following LANL procedure for using the ^{252}Cf source
          o   Check source is bare
      Begin 1 hour measurement acquisition (assume 1 hour transfer time minimum)
      Remove source following LANL guidelines

Epithermal neutron tests X-Axis rotation SHORT (Fig 4b & 5b)

Verify instrument/spacecraft is secure on mount in X axis of rotation position (X fixed axis upwards) with the instrument/spacecraft starting at the 0º position

If instrument/spacecraft is not powered on, turn it on

Secure ^{252}Cf source following LANL procedure for using the ^{252}Cf source
- o Check D2O is mounted
- o Check Cd is mounted

Take data for 900 seconds (15 minutes) per rotation increment (30º) for a total of 7 measurements, starting at 0º and rotating counter-clockwise to 180º
- o (2 hours DAQ time + 1 hour setup time + 2-4 hours transfer time = [5 hours, 7 hours])

The following repeated mounting rotation positions swept from 0º to +180º will be used:
- o Take the first measurement at 0º
- o Follow LANL procedures with ^{252}Cf source before adjusting the rotation mount
- o Adjust angle by +30º, clockwise starting from 0º increasing in +Z up to 180º
    - ▪ 0º, 30º, 60º, 90º, 120º, 150º, 180º (7 total)

Remove source following LANL guidelines

Epithermal neutron tests X-Axis rotation LONG (Fig 4b & 5b)

Verify instrument/spacecraft is secure on mount in X axis of rotation position (X fixed axis upwards) with the instrument/spacecraft starting at the 0º position

If instrument/spacecraft is not powered on, turn it on

Secure ^{252}Cf source following LANL procedure for using the ^{252}Cf source
- o Check D2O is mounted
- o Check Cd is mounted

Take data for 900 seconds (15 minutes) per rotation increment

The following repeated mounting rotation positions swept from -180º to +180º can be used:
- o Take the first measurement at 0º
- o Follow LANL procedures with ^{252}Cf source before adjusting the rotation mount
- o Adjust angle to the following, clockwise starting from 0º increasing in +Z
    - ▪ 15º, 45º, 75º (3 total)
- o Adjust angle to -15º, counter-clockwise starting from 0º decreasing in +Z (-Z direction)
    - ▪ -15º, -30º, -45º, -60º, -75º, -90º (6 total)

- o   Adjust angle by -30°, counter-clockwise starting from -90° increasing in +Z
  - ▪ -120°, -150° (2 total)

Remove source following LANL guidelines

Epithermal & Thermal neutron tests X-Axis rotation SHORT (Fig 4b & 5b)

Verify instrument/spacecraft is secure on mount in X axis of rotation position (X fixed axis upwards) with the instrument/spacecraft starting at the 0° position

If instrument/spacecraft is not powered on, turn it on

Secure ^{252}Cf source following LANL procedure for using the ^{252}Cf source
- o   Check D2O is mounted
- o   Check Cd is removed

Take data for 900 seconds (15 minutes) per rotation increment (30°) for a total of 7 measurements, starting at 0° and rotating counter-clockwise to 180°
- o   (2 hours DAQ time + 1 hour setup time + 2-4 hours transfer time = [5 hours, 7 hours])

The following repeated mounting rotation positions swept from 0° to +180° will be used:
- o   Take the first measurement at 0°
- o   Follow LANL procedures with ^{252}Cf source before adjusting the rotation mount
- o   Adjust angle by +30°, clockwise starting from 0° increasing in +Z up to 180°
  - ▪ 0°, 30°, 60°, 90°, 120°, 150°, 180° (7 total)

Remove source following LANL guidelines

Epithermal & Thermal neutron tests X-Axis rotation LONG (Fig 4b & 5b)

Verify instrument/spacecraft is secure on mount in X axis of rotation position (X fixed axis upwards) with the instrument/spacecraft starting at the 0° position

If instrument/spacecraft is not powered on, turn it on

Secure ^{252}Cf source following LANL procedure for using the ^{252}Cf source
- o   Check D2O is mounted
- o   Check Cd is removed

Take data for 900 seconds (15 minutes) per rotation increment

The following repeated mounting rotation positions swept from -180° to +180° can be used:
- o   Take the first measurement at 0°
- o   Follow LANL procedures with ^{252}Cf source before adjusting the rotation mount
- o   Adjust angle to the following, clockwise starting from 0° increasing in +Z

- 15°, 45°, 75° (3 total)
  - o Adjust angle to -15°, counter-clockwise starting from 0° decreasing in +Z (-Z direction)
    - -15°, -30°, -45°, -60°, -75°, -90° (6 total)
  - o Adjust angle by -30°, counter-clockwise starting from -90° increasing in +Z
    - -120°, -150° (2 total)

Remove source following LANL guidelines

Epithermal neutron tests Z-Axis rotation SHORT (Fig 4a & 5a)

Verify instrument/spacecraft is secure on mount in Z axis of rotation position (Z fixed axis upwards) with the instrument/spacecraft starting at the 0° position

If instrument/spacecraft is not powered on, turn it on

Secure ^{252}Cf source following LANL procedure for using the ^{252}Cf source
  - o Check D2O is on
  - o Check Cd is on

Take data for 900 seconds (15 minutes) per rotation increment (30°) for a total of 7 measurements, starting at 0° and rotating *counter-clockwise* to 180°
  - o (2 hours DAQ time + 1 hour setup time + 2-4 hours transfer time = [5 hours, 7 hours])

The following repeated mounting rotation positions swept from 0° to +180° will be used:
  - o Take the first measurement at 0°
  - o Follow LANL procedures with ^{252}Cf source before adjusting the rotation mount
  - o Adjust angle by +30°, *counter-clockwise* starting from 0° increasing in +X up to 180°
    - 0°, 30°, 60°, 90°, 120°, 150°, 180° (7 total)

Remove source following LANL guidelines

Epithermal neutron tests Z-Axis rotation LONG (Fig 4a & 5a)

Verify instrument/spacecraft is secure on mount in Z axis of rotation position (Z fixed axis upwards) with the instrument/spacecraft starting at the 0° position

If instrument/spacecraft is not powered on, turn it on

Secure ^{252}Cf source following LANL procedure for using the ^{252}Cf source
  - o Check D2O is on
  - o Check Cd is on

Take data for 900 seconds (15 minutes) per rotation increment

The following repeated mounting rotation positions swept from -180° to +180° can be used:

- o Take the first measurement at 0°
- o Follow LANL procedures with ^{252}Cf source before adjusting the rotation mount
- o Adjust angle to the following, *counter-clockwise* starting from 0° increasing in +X
  - § 15°, 45°, 75° (3 total)
- o Adjust angle to -15°, *clockwise* starting from 0° decreasing in +X (-X direction)
  - § -15°, -30°, -45°, -60°, -75°, -90° (6 total)
- o Adjust angle by -30°, *clockwise* starting from -90° increasing in +X
  - § -120°, -150° (2 total)

Remove source following LANL guidelines

Epithermal & Thermal neutron tests Z-Axis rotation SHORT (Fig 4a & 5a)

Verify instrument/spacecraft is secure on mount in Z axis of rotation position (Z fixed axis upwards) with the instrument/spacecraft starting at the 0° position

If instrument/spacecraft is not powered on, turn it on

Secure ^{252}Cf source following LANL procedure for using the ^{252}Cf source

- o Check D2O is on
- o Check Cd is removed

Take data for 900 seconds (15 minutes) per rotation increment (30°) for a total of 7 measurements, starting at 0° and rotating *counter-clockwise* to 180°

- o (2 hours DAQ time + 1 hour setup time + 2-4 hours transfer time = [5 hours, 7 hours])

The following repeated mounting rotation positions swept from 0° to +180° will be used:

- o Take the first measurement at 0°
- o Follow LANL procedures with ^{252}Cf source before adjusting the rotation mount
- o Adjust angle by +30°, *counter-clockwise* starting from 0° increasing in +X up to 180°
  - § 0°, 30°, 60°, 90°, 120°, 150°, 180° (7 total)

Remove source following LANL guidelines

Epithermal & Thermal neutron tests Z-Axis rotation LONG (Fig 4a & 5a)

Verify instrument/spacecraft is secure on mount in Z axis of rotation position (Z fixed axis upwards) with the instrument/spacecraft starting at the 0° position

If instrument/spacecraft is not powered on, turn it on

Secure ^{252}Cf source following LANL procedure for using the ^{252}Cf source

- o Check D2O is on

- o   Check Cd is removed

Take data for 900 seconds (15 minutes) per rotation increment

The following repeated mounting rotation positions swept from -180° to +180° can be used:

- o   Take the first measurement at 0°
- o   Follow LANL procedures with ^{252}Cf source before adjusting the rotation mount
- o   Adjust angle to the following, *counter-clockwise* starting from 0° increasing in +X
    - ▪   15°, 45°, 75° (3 total)
- o   Adjust angle to -15°, *clockwise* starting from 0° decreasing in +X (-X direction)
    - ▪   -15°, -30°, -45°, -60°, -75°, -90° (6 total)
- o   Adjust angle by -30°, *clockwise* starting from -90° increasing in +X
    - ▪   -120°, -150° (2 total)

Remove source following LANL guidelines

Long fast neutron test - optional

Verify instrument/spacecraft is secure on mount in X axis of rotation position

If instrument/spacecraft is not powered on, turn it on

Secure bare ^{252}Cf source following LANL procedure for using the ^{252}Cf source

- o   Check source is bare

Begin 4-6 hour bare ^{252}Cf measurement acquisition (Goldsten et al, 2007)

- o   Dependent on whether source can be kept up overnight without supervision

Remove source following LANL guidelines

Over-moderated neutron test - optional

Verify instrument/spacecraft is secure on mount in X axis of rotation position

If instrument/spacecraft is not powered on, turn it on

Secure ^{252}Cf source following LANL procedure for using the ^{252}Cf source

- o   Check source has D2O and extra poly surrounding it

Begin 2 hour over-moderated ^{252}Cf measurement acquisition

Remove source following LANL guidelines

Iodine sensitivity test - optional

Verify instrument/spacecraft is secure on mount in X axis of rotation position

If instrument/spacecraft is not powered on, turn it on

Place the iodine near the instrument, record location of iodine with respect to Mini-NS

Secure ^{252}Cf source following LANL procedure for using the ^{252}Cf source
- o   Check D2O is on
- o   Check Cd is removed

Take data for 900 seconds (15 minutes) at 0° of rotation

Transfer from NFIA neutron testing room to ASU

TBD location

Make sure source is shielded/removed

Make sure instrument/spacecraft is powered OFF

Disconnect all cabling

Dismount instrument/spacecraft from mounting bracket

Unbolt mounting bracket from rotational stage

Pack instrument/spacecraft into container

Pack cables and DAQ PC

7. Data Post-Processing

Simulation Data

Tally analysis is already written in a Python program, this pulls the F8 tallies module by module and converts them in CPS

CPS on individual modules per rotational degree
- o   Thermals
- o   Epi + Thermals
- o   Epis

Combination of all modules together per rotational degree
- o   Thermals
- o   Epi + Thermals
- o   Epis

Gammas (F8)
- o   Only a count rate is needed for gammas to determine possible pile-up issues

Sensitivity
- o   Change in count rate 5%, minimum 10k counts per measurement

Experimental Data

Instrument specific equations are laid out in Prettyman, et al., 2011. & Goldsten, et al., 2007

Estimated flux equations

Angular counts/efficiency (cosine) equation

Emission spectrum from ^{252}Cf for expected neutron energies

CPS on individual modules per rotational degree (if possible)
- Thermals
- Epi + Thermals
- Epis
- Fast?

Combination of all modules together per rotational degree
- Thermals
- Epi + Thermals
- Epis
- Fast?

8. Hand Calculations for Estimated Count Rate

LunaH-Map Mini-NS Known Values

- Source ^{252}Cf, A_n = 6158692.06468338 neutrons/second

- Detector Module Length, L = 6.3 cm

- Detector Module Width, W = 4.0 cm

- Distance from Source, R = 200.0 cm

- 2 cm thick CLYC efficiency epithermals (0.4 - 100 keV), EFF_{epi} = 0.4140

- 2 cm thick CLYC efficiency thermals (0 - 0.4 eV), EFF_{therm} = 0.7710

- 2 cm thick CLYC efficiency fasts (1 MeV), EFF_{fast} = 0.0085

Basic Hand Calculations: One Module

Solid Angle (Ω):

$$\Omega = \frac{LW}{4\pi R^2} = 5.0134\text{x}10^{-5}$$

Individual module neutrons/s incident ($\text{N}_{MODcounts}$):

$$\text{N}_{MOD} = \Omega \text{ x } \text{A}_n = 308.759 \text{ neutrons/s per module}$$

We're going to assume all neutrons incident are of one energy type for each case (thermal, epi, fast), which is a big overestimate. Counts/s per module for fast neutrons ($\text{CPS}_{MODfast}$):

$$\text{CPS}_{MODfast} = N_{MODcounts} \text{ x } \text{EFF}_{fast} = 0.5127 \text{ neutrons/second per module}$$

Counts/s per module for epithermal neutrons (CPS_{MODepi}):

$$\text{CPS}_{MODepi} = N_{MODcounts} \text{ x } \text{EFF}_{epi} = 127.826 \text{ neutrons/second per module}$$

Counts/s per module for thermal neutrons ($\text{CPS}_{MODtherm}$):

$$\text{CPS}_{MODtherm} = N_{MODcounts} \text{ x } \text{EFF}_{therm} = 238.053 \text{ neutrons/second per module}$$

Basic Hand Calculations: Eight Modules

Whole detector (8 modules) neutrons/s incident ($\text{N}_{NScounts}$):

$$\text{N}_{NS} = 8 * \text{N}_{MOD} = 8 * \Omega \text{ x } \text{A}_n = 2470.072 \text{ neutrons/s on detector}$$

We're going to assume all neutrons incident are of one energy type for each case (thermal, epi, fast), which is a big overestimate. Counts/s on detector for fast neutrons (CPS_{NSfast}):

$$\text{CPS}_{NSfast} = N_{NScounts} \text{ x } \text{EFF}_{fast} = 4.1016 \text{ neutrons/second on detector}$$

Counts/s on detector for epithermal neutrons (CPS_{NSepi}):

$$\text{CPS}_{NSepi} = N_{NScounts} \text{ x } \text{EFF}_{epi} = 1022.608 \text{ neutrons/second on detector}$$

Counts/s on detector for thermal neutrons ($\text{CPS}_{NStherm}$):

$$\text{CPS}_{NStherm} = N_{NScounts} \text{ x } \text{EFF}_{therm} = 1904.424 \text{ neutrons/second on detector}$$

As a quick estimate, the number of gammas should be about $\approx$X10 as many as neutrons.

References

Feldman, W.C., Ahola, K., Barraclough, B.L., Belian, R.D., Black, R.K., Elphic, R.C., Everett, D.T., Fuller, K.R., Kroesche, J., Lawrence, D.J., Lawson, S.L., Longmire, J.L., Maurice, S., Miller, M.C., Prettyman, T.H., Storms, S.A., Thornton, G.W., 2004. Gamma-Ray, Neutron, and Alpha-Particle Spectrometers for the Lunar Prospector mission. J. Geophys. Res. E Planets 109, 1–19. doi:10.1029/2003JE002207

Prettyman, T.H., Feldman, W.C., McSween, H.Y., Dingler, R.D., Enemark, D.C., Patrick, D.E., Storms, S.A., Hendricks, J.S., Morgenthaler, J.P., Pitman, K.M., Reedy, R.C., 2011. Dawn's Gamma Ray and Neutron Detector, Space Science Reviews. doi:10.1007/s11214-011-9862-0

Goldsten, J.O, Rhodes, E.A., Boynton, W.V., Feldman, W.C., Lawrence, D.J., Trombka, J.I., et al.. 2007. The MESSENGER Gamma-Ray and Neutron Spectrometer. Space Science Reviews. doi:10.1007/s11214-007-9262-7

APPENDIX E

MINI-NS DATA PROCESSING CODE

```python
# MiniNS_Functions.py
'''
LunaH-Map Mini-NS downlinked data processing tool for Python V.1.0.1.
Start: May 1, 2021 by L. E. Heffern
Last Edit: April 11, 2022
(c) 2021 ASU SESE & NASA LunaH-Map Mission
Required libraries include: numpy, matplotlib, struct, os.
For use with the Miniature Neutron Spectrometer flight software.
Updated 04/11/2022 by L. Heffern
Partially based on Matlab code by I. Lazbin
See Mini-NS ICD for more details
'''
import numpy as np
import struct
import os


'''
# ========================================================
# READ BINARY FILES
# ========================================================
'''

class BinaryReaderEOFException(Exception):
    def __init__(self):
        pass

    def __str__(self):
        return 'Not enough bytes in file to satisfy read request'


class BinaryReader:
    # Map well-known type names into struct format characters.
    typeNames = {
        'int8': 'b',
        'uint8': 'B',
        'int16': 'h',
        'uint16': 'H',
        'int32': 'i',
        'uint32': 'I',
        'int64': 'q',
        'uint64': 'Q',
        'float': 'f',
        'double': 'd',
        'char': 's'}

    def __init__(self, fileName):
        self.file = open(fileName, 'rb')

    def read(self, typeName):
        typeFormat = BinaryReader.typeNames[typeName.lower()]
        typeSize = struct.calcsize(typeFormat)
        value = self.file.read(typeSize)
        if typeSize != len(value):
            raise BinaryReaderEOFException
        return struct.unpack(typeFormat, value)[0]

    def __del__(self):
        self.file.close()


'''
# ========================================================
# PSD FUNCTIONS
# ========================================================
'''
```

```python
def avebaseline(aaBaselineInt):
    Q=len(aaBaselineInt)
    AVGbaseline=[]
    for i in range(0,Q):
        AVGbaseline.append((aaBaselineInt[i]/(38.0*Q)))
    AVGbaseline=sum(AVGbaseline)
    return AVGbaseline


# Computes the PSD for every usable value (non-negative integrals) and assigns a zero to
# negative integral values, added in the PSD0 to ignore non-usables
def makePSD(AVGbaseline,aaShortInt,aaLongInt):
    M = len(aaShortInt)
    PSD=np.zeros(M)
    PSD0=[]
    for i in range(0,M):
        if (aaShortInt[i]-AVGbaseline*73.0)>0:
            if (aaLongInt[i]-AVGbaseline*169.0)>0:
                if (aaLongInt[i]-AVGbaseline*169.0)-(aaShortInt[i]-AVGbaseline*73.0)>0:
                    PSD[i]=((aaShortInt[i]-AVGbaseline*73.0)/((aaLongInt[i]-AVGbaseline*169.0)-
(aaShortInt[i]-AVGbaseline*73.0)))
                    PSD0.append(PSD[i])
    return PSD, PSD0


def psdfilter(psdratio):
    M = len(psdratio)
    PSD2=[]
    for i in range(0, M):
        if psdratio[i] > 0:
            if psdratio[i] < 1:
                PSD2.append(psdratio[i])
    return PSD2

'''
# ========================================================
# GENERATE NEW DATA FILES
# ========================================================
'''

# Writes out MCNP data file
def writeoutLunaHfile(newfilename,topline,nameslist, countlist,cpslist,compareeff):
    outfile=open(newfilename, 'w')
    outfile.write('#'+str(topline))
    for i in range(0,len(nameslist)):
        outfile.write(str(nameslist[i]))
        outfile.write('\t')
    outfile.write('\r')
    for i in range(0, len(countlist)):
        outfile.write(str(countlist[i]))
        outfile.write('\t')
    outfile.write('\r')
    for i in range(0, len(cpslist)):
        outfile.write(str(cpslist[i]))
        outfile.write('\t')
    outfile.write('\r')
    for i in range(0, len(compareeff)):
        outfile.write(str(compareeff[i]))
        outfile.write('\t')
    outfile.close()


# writes out PMT files
def write_PMTfile(path,PMT,PMTnumber,inputfilename):
    newpath=path+'/'+inputfilename
    filename1=newpath+'/'+inputfilename.split('_')[0]+'PMT'+PMTnumber+'.dat'
```

```python
    try:
        os.makedirs(newpath)
    except OSError:
        if not os.path.isdir(newpath):
            raise
    outfile=open(filename1, 'w')
    toplines='# '+str(inputfilename)+' \r# PMTid,  energybin,  PSDvalue,  FPGA_time_new2,
tageventID \r'
    outfile.write('#'+str(toplines))
    for i in range(0,len(PMT)):
        outfile.write((str(PMT[i]).strip('[]')))
        outfile.write('\r')
    outfile.close()

# writes out pulser files
def write_Pulserfile(path,inputfilename,pulser_set):
    newpath = path + '/' + inputfilename
    filename1=newpath+'/'+inputfilename.split('_')[0]+'Pulser_Set.dat'
    try:
        os.makedirs(newpath)
    except OSError:
        if not os.path.isdir(newpath):
            raise
    outfile=open(filename1, 'w')
    toplines='# '+str(inputfilename)+' Pulser File \r# FPGA_time \r'
    outfile.write('#'+str(toplines))
    for i in range(0,len(pulser_set)):
        outfile.write((str(pulser_set[i])))
        outfile.write('\r')
    outfile.close()

# writes out temperature files
def write_Tempfile(path,inputfilename,temp_set):
    newpath=path + '/' + inputfilename
    filename1=newpath+'/'+inputfilename.split('_')[0]+'Temp_Set.dat'
    try:
        os.makedirs(newpath)
    except OSError:
        if not os.path.isdir(newpath):
            raise
    outfile=open(filename1, 'w')
    toplines='# '+str(inputfilename)+' Temp File \r# EventID, T_Analog, T_Digital, T_Module \r'
    outfile.write('#'+str(toplines))
    for i in range(0,len(temp_set)):
        outfile.write((str(temp_set[i])))
        outfile.write('\r')
    outfile.close()


# writes out cfg files
def write_cfgfile(path,inputfilename,cfgints):
    newname=inputfilename.split('/')[-1].strip('.bin')
    newpath=path + '/' + newname
    filename1=newpath+'_ascii.dat'
    outfile=open(filename1, 'w')
    toplines='# '+str(inputfilename)+ ' \r'
    outfile.write('#'+str(toplines))
    for i in range(0,len(cfgints)):
        outfile.write((str(cfgints[i])))
        outfile.write('\r')
    outfile.close()

'''
# =========================================================
# READ NEW DATA FILES
# =========================================================
'''
```

```python
# read in a PMT file from MNSXPMTX.dat file type
def read_PMTfile(filename):
    file = open(filename, 'r')
    # Read and ignore header line
    data = file.readline()
    data=data.split('\r')
    file.close()
    # PMTid,  energybin,  PSDvalue,  FPGA_time_new2, tageventID
    PMTid=[]
    energybin=[]
    PSDvalue=[]
    FPGA_time_new2=[]
    tageventID=[]
    for i in range(2,len(data)-1):
        columns=data[i].split(',')
        PMTid.append(float(columns[0]))
        energybin.append(float(columns[1]))
        PSDvalue.append(float(columns[2]))
        FPGA_time_new2.append(float(columns[3]))
        tageventID.append(float(columns[4]))
    return PMTid, energybin, PSDvalue, FPGA_time_new2, tageventID

# read in a temperature file from MNSXTemp_Set.dat file type
def read_Tempfile(filename):
    file = open(filename, 'r')
    # Read and ignore header line
    data1 = file.readline()
    data=data1.split('\r[')
    file.close()
    # EventID, T_Analog, T_Digital, T_Module
    EventID=[]
    T_Analog=[]
    T_Digital=[]
    T_Module=[]
    for i in range(2,len(data)-1):
        columns=(data[i].strip(']')).split(',')
        EventID.append(float(columns[0]))
        T_Analog.append(float(columns[1]))
        T_Digital.append(float(columns[2]))
        T_Module.append(float(columns[3]))
    return EventID, T_Analog, T_Digital, T_Module

# read in a cfg file from mns_X_cfg_IDXX_Rxx_ascii.dat file type
def read_cfgfile(filename):
    file = open(filename, 'r')
    # Read and ignore header line
    data1 = file.readline()
    data=data1.split('\r')
    file.close()
    line=[]
    for i in range(1,len(data)-1):
        line.append(float(data[i]))
    return line

'''
=======================================================
=== MINI-NS POST-PROCESSING FUNCTIONS
=======================================================
'''

'''
=======================================================
=== Sort the data into specific sets based on the ICD ===
This for loop sorts out the First event data product, the pulser data product, the temperature
data product,
then finally the event data product. Tables 24-28 in the ICD describe the different event
```

216

```
formats in detail.
=========================================================
'''
def sort_minins_bindata(asciiout):
    set221=[]
    pulser_set=[]
    temp_set=[]
    event_set=[]
    for i in range(0,(len(asciiout))):
        if asciiout[i] != 255: # number to designate any event that is NOT real event data
            if asciiout[i] == 221: # number designation for a false trigger event
                set221.append(asciiout[i:i+7]) # pulls the first false triggered event set out
                i=i+7
            elif asciiout[i] == 238: # number designation for a temp or pulser event
                if asciiout[i+1] == 238:
                    if asciiout[i+2] == 238: # if 238 is repeated x3 then its pulser
                        pulser_settmp=asciiout[i:i+8] # pulls the pulsar event sets out
                        FPGA_time_new=(pulser_settmp[-1] + pulser_settmp[-2] * 256 +
pulser_settmp[-3] * 256 * 256)
                        pulser_set.append(FPGA_time_new)
                        FPGA_time=FPGA_time_new
                        i=i+8
                else:
                    temp_settmp=(asciiout[i:i + 4]) # pulls the temperature event sets out
                    FPGA_time_new=(temp_settmp[-1] + temp_settmp[-2] * 256 + temp_settmp[-3] *
256 * 256)
                    FPGA_time=FPGA_time_new

temp_set.append([FPGA_time_new,temp_settmp[1],temp_settmp[2],temp_settmp[3]])
                    i=i+4
            else:
                i=i+1
        else: # any remaining events must be real event data
            if len(asciiout) - i > 8: # pulls the actual event-by-event sets out
                event_settmp = (asciiout[i:i + 8])
                FPGA_time_new = (event_settmp[-1] + event_settmp[-2] * 256 + event_settmp[-3] *
256 * 256)
                event_set.append(
                    [event_settmp[0], event_settmp[1], event_settmp[2], event_settmp[3],
event_settmp[4],FPGA_time_new])
                i = i + 8
            else:
                break
    return (set221,pulser_set,temp_set,event_set,FPGA_time)


'''
=========================================================
======== Post-process the event-by-event sets =========
This section performs the bit conversions for: MNS_EVTS    Value(0x77) Event by Event Data
Tables 24 - 28 in the ICD describe this in more detail.
This pulls the data one event packet at a time, bit-flips/switches to the correct ascii format,
then appends to a new array. The arrays are then sorted based on PMT number in the second for
loop.

Bit operators in python are described as:

x << y
Returns x with the bits shifted to the left by y places (and new bits on the right-hand-side
are zeros).
This is the same as multiplying x by 2**y.

x >> y
Returns x with the bits shifted to the right by y places. This is the same as //'ing x by 2**y.

x & y
Does a "bitwise and". Each bit of the output is 1 if the corresponding bit of x AND of y is 1,
```

```python
otherwise it's 0.
=======================================================
'''
def sort_eventsets(event_set):
    event_packets = event_set
    item0_event = []  # event identifier
    PMTid = []  # PMT ID number
    item2_event = []  # total number of events?
    energybin = []  # Energy Bin
    PSDvalue = []  # PSD Bin
    FPGA_time_new2 = []
    tag_count = 0
    tageventID = []
    for i in range(0, len(event_packets)):
        item0_event.append(event_packets[i][0])
        tst = event_packets[i][1] & 240 # identifies the PMT ID
        PMTid.append(tst >> 4) # converts the PMT from binary to int
        tst1 = event_packets[i][3] << 1 # converts the first bit in the energy set, bitshift
down
        tst2 = event_packets[i][4] >> 7 # converts the second bit in the energy set, bitshift
up
        energybin.append(tst1 + tst2) # calculates the energy value from the two bits
        tst3 = event_packets[i][4] & 126 # grabs the psd value, bitwise and
        psd_bin = tst3 >> 1 # converts the psd value from binary to float
        tag_bit = event_packets[i][4] & 1
        tag_count = tag_count + tag_bit
        item2_event.append(event_packets[i][2])
        PSDvalue.append(psd_bin + 1) # assigns the psd value
        FPGA_time_new2.append((event_packets[i][5])) # FPGA time
        tageventID.append(i)
    return (item0_event,PMTid,item2_event,energybin,PSDvalue,FPGA_time_new2,tageventID)

# ===== Post-process the event-by-event sets by PMT =======
def sort_PMTevents(PMTid,energybin,PSDvalue,FPGA_time_new2,tageventID):
    ALLPMTs=[]
    ALLVALIDPMTs=[]
    PMT0=[]
    PMT1=[]
    PMT2=[]
    PMT3=[]
    PMTextras=[]
    for i in range(0,len(PMTid)):
        ALLPMTs.append([PMTid[i], energybin[i], PSDvalue[i], FPGA_time_new2[i],tageventID[i]])
        if PMTid[i] == 1: # PMT0 ->> now 0
            PMT0.append([PMTid[i],energybin[i],PSDvalue[i],FPGA_time_new2[i],tageventID[i]])
            ALLVALIDPMTs.append([PMTid[i], energybin[i], PSDvalue[i], FPGA_time_new2[i],
tageventID[i]])
        elif PMTid[i] == 2: # PMT1 ->> now 1
            PMT1.append([PMTid[i], energybin[i], PSDvalue[i], FPGA_time_new2[i],tageventID[i]])
            ALLVALIDPMTs.append([PMTid[i], energybin[i], PSDvalue[i], FPGA_time_new2[i],
tageventID[i]])
        elif PMTid[i] == 4: #PMT2 ->> now 2
            PMT2.append([PMTid[i], energybin[i], PSDvalue[i], FPGA_time_new2[i],tageventID[i]])
            ALLVALIDPMTs.append([PMTid[i], energybin[i], PSDvalue[i], FPGA_time_new2[i],
tageventID[i]])
        elif PMTid[i] == 8: # PMT3 ->> now 3
            PMT3.append([PMTid[i], energybin[i], PSDvalue[i], FPGA_time_new2[i],tageventID[i]])
            ALLVALIDPMTs.append([PMTid[i], energybin[i], PSDvalue[i], FPGA_time_new2[i],
tageventID[i]])
        else: # there may be 3, 5, 6, 7, etc. values up to 16 -> these are overlapped PMTs
            PMTextras.append([PMTid[i], energybin[i], PSDvalue[i],
FPGA_time_new2[i],tageventID[i]])
    return (ALLPMTs,ALLVALIDPMTs,PMT0,PMT1,PMT2,PMT3,PMTextras)

# Future program TO DO: add in PMT sort that accounts for the overlapped PMTs.

# ======== Post-process the tmperature sets =========
```

```python
#MiniNS_CreateDataProducts.py


'''
LunaH-Map Mini-NS downlinked data processing tool for Python V.1.0.1.
Start: May 1, 2021 by L. E. Heffern
Last Edit: April 11, 2022
(c) 2021 ASU SESE & NASA LunaH-Map Mission
Required libraries include: numpy, matplotlib, struct, os, and the file MiniNS_Functions.py
For use with the Miniature Neutron Spectrometer flight software.
This code generates .dat files and .png plot images of event-by-event data from the Mini-NS.
'''
import numpy as np
import matplotlib.pyplot as plt
import MiniNS_Functions as lh
import os
from matplotlib import gridspec


'''
========================================================
========= Select the data you want to process =========
========================================================
'''

#testfile:
#filename='/Users/lenaheffern/Documents/Grad/Projects/LunaHmap/PreShip_May2021/mns_0_evt_filter
ed_decompressed_pkt_ID70_R22.bin'


print "Enter the location of the folders: "; directory = raw_input()

path = r"%s" % directory

datatype='.bin'
settype='evt_filtered_decompressed'

filelist=[]

MNS0paths=[]
MNS1paths=[]

current_folder = os.listdir(path)
for i in range(0,len(current_folder)):
    if '.' in current_folder[i]:
        pass
    elif 'MNS0' in current_folder[i]:
        MNS0paths.append(current_folder[i])
    elif 'MNS1' in current_folder[i]:
        MNS1paths.append(current_folder[i])

for folder in range(0,len(MNS0paths)):
    for file in os.listdir(path+'/'+MNS0paths[folder]):
        current_file = os.path.join(path+'/'+MNS0paths[folder], file)
        fileIDinfo=MNS0paths[folder]+'_processed'
        if '.bin' in current_file:
            if settype in current_file:
                filelist.append(current_file)
    print 'Processing ' + str(len(filelist)) + ' filtered event files.'
#========================================================
#============ Pick what you want to output =============
#========================================================
#============ FILE OUTPUTS
    #print "Enter the desired file outputs (can list w/ commas): "; fileinputs = raw_input()
    FileOuts=[1,1,1,1,1]
    #for word in range(0,len(str(fileinputs))):
        #if 'PMT' in fileinputs or 'PMTS' in fileinputs or 'pmts' in fileinputs:
        #    FileOuts[0]=1
        #elif 'Pulser' in fileinputs:
```

```python
    #     FileOuts[1]=1
    #elif 'Temp' in fileinputs or 'Temperature' in fileinputs or 'temp' in fileinputs or
'temperature' in fileinputs:
    #     FileOuts[2]=1
    #elif 'All files' in fileinputs or' all' in fileinputs or 'All' in fileinputs or 'ALL'
in fileinputs:
    #     FileOuts = [1, 1, 1, 1, 1]
    #elif 'none'in fileinputs or 'NONE' in fileinputs or 'None' in fileinputs:
    #     FileOuts = [0, 0, 0, 0, 0]
# ============ PLOT OUTPUTS
# for PMTs, options are: PMT0, PMT1, PMT2, PMT3, ALLPMTS, PMTextras
    PlotOuts=[1,1,1,1,1]
#======================================================
#========== Read in the binary files as uint8 =========
#======================================================
    for k in range (0,len(filelist)):
        filename=filelist[k]
        mainfilename=str(filename.split('/')[-2]) + '/' + str(filename.split('/')[-1])
        shortfilename=(str(((filename.split('/')[-1]))).split('.bin'))[0].split('_')[-2]+'
'+(str(((filename.split('/')[-1]))).split('.bin'))[0].split('_')[-1]
    #============ Read in the binary files as uint8 ==========
        binaryReader = lh.BinaryReader(filename)
        asciiout = []
        try:
            binlen = 50000000
            for i in range (0,binlen):
                asciiout.append(binaryReader.read('uint8'))
        except lh.BinaryReaderEOFException:
            print 'Binary read in past length... ignoring.'
        asciiout=np.array(asciiout)
        if len(asciiout) == 0:
            print 'Binary file '+str(filename.split('/')[-1]) +' in '
+str(filename.split('/')[-2]) + ' is empty...\r ...continuing to next file.'
            continue
    #
    #=== Sort the data into specific sets based on the ICD ===
    #
        (set221, pulser_set, temp_set, event_set, FPGA_time)=lh.sort_minins_bindata(asciiout)
    #
    # ========= Post-process the event-by-event sets =========
    #
        (item0_event, PMTid, item2_event, energybin, PSDvalue, FPGA_time_new2,
tageventID)=lh.sort_eventsets(event_set)
    #
    # ===== Post-process the event-by-event sets by PMT =======
    #
        (ALLPMTs, ALLVALIDPMTs, PMT0, PMT1, PMT2, PMT3, PMTextras)=lh.sort_PMTevents(PMTid,
energybin, PSDvalue, FPGA_time_new2, tageventID)
    #
    # ========= Post-process the temperature sets =========
    #
        (item0_temp, atemp, dtemp, mtemp)=lh.sort_tempdata(temp_set)
    #
    # ========= Save datasets =========
    #
        if FileOuts[0] == 1: #PMT flag
            lh.write_PMTfile(path, PMT0, '0', fileIDinfo)
            lh.write_PMTfile(path, PMT1, '1', fileIDinfo)
            lh.write_PMTfile(path, PMT2, '2', fileIDinfo)
            lh.write_PMTfile(path, PMT3, '3', fileIDinfo)
            lh.write_PMTfile(path, ALLVALIDPMTs, 'ALLVALIDPMTs', fileIDinfo)
            lh.write_PMTfile(path, PMTextras, 'PMTextras', fileIDinfo)
            lh.write_PMTfile(path, ALLPMTs, 'ALLPMTs', fileIDinfo)
            print 'Data has been written.'
        if FileOuts[1] == 1: #pulser flag
            lh.write_Pulserfile(path,fileIDinfo,pulser_set)
        if FileOuts[2] == 1: #temperature flag
```

```python
            lh.write_Tempfile(path, fileIDinfo, temp_set)
        if PlotOuts[0] == 1:
            print 'Plot wanted'
            if PlotOuts[1] == 1:
            # ========== Plot the data ==========
            # for PMTs, options are: PMT0, PMT1, PMT2, PMT3, ALLPMTS, PMTextras
            # ========== First histogram
                title1 = 'PSD vs. Energy Channel Standard PMTs ' + (fileIDinfo)
                title11 = 'PSDvEnergy_StandardPMTs_' + fileIDinfo
                PMTchoice = np.array([PMT0,PMT1,PMT2,PMT3])
                PMTchoicename=(['PMT0','PMT1','PMT2','PMT3'])
                fig = plt.figure(title11, figsize=(6, 5), dpi=100, facecolor='w',
                            edgecolor='k')  # adjust dpi & figsize for size adjust
                gs = gridspec.GridSpec(2, 2)
                ax1 = fig.add_subplot(gs[0,0])
                ax4 = fig.add_subplot(gs[1, 1])
                ax2 = fig.add_subplot(gs[0, 1])
                ax3 = fig.add_subplot(gs[1, 0])
                ax1.plot([row[1] for row in PMTchoice[0]], [row[2] for row in PMTchoice[0]],
'.')
                ax1.set_title(PMTchoicename[0], fontsize = 9)
                ax1.set_ylabel('Raw PSD values', fontsize = 9)  # labelpad adjusts how close
the text is to the plot edges
                ax1.set_xlabel('Raw Energy Channel Values', fontsize = 9)
                ax2.plot([row[1] for row in PMTchoice[1]], [row[2] for row in PMTchoice[1]],
'.')
                ax2.set_title(PMTchoicename[1], fontsize = 9)
                ax2.set_ylabel('Raw PSD values', fontsize = 9)  # labelpad adjusts how close
the text is to the plot edges
                ax2.set_xlabel('Raw Energy Channel Values', fontsize = 9)
                ax3.plot([row[1] for row in PMTchoice[2]], [row[2] for row in PMTchoice[2]],
'.')
                ax3.set_title(PMTchoicename[2], fontsize = 9)
                ax3.set_ylabel('Raw PSD values', fontsize = 9)  # labelpad adjusts how close
the text is to the plot edges
                ax3.set_xlabel('Raw Energy Channel Values', fontsize = 9)
                ax4.plot([row[1] for row in PMTchoice[3]], [row[2] for row in PMTchoice[3]],
'.')
                ax4.set_title(PMTchoicename[3], fontsize = 9)
                ax4.set_ylabel('Raw PSD values', fontsize = 9)  # labelpad adjusts how close
the text is to the plot edges
                ax4.set_xlabel('Raw Energy Channel Values', fontsize = 9)
                plt.subplots_adjust(left=0.2,
                                    bottom=0.2,
                                    right=0.9,
                                    top=0.9,
                                    wspace=0.4,
                                    hspace=0.6)
                plt.grid(True, which="major", linewidth=0.5)
                plt.suptitle(title1)
            # plt.xscale('log', nonposy='clip')
            # plt.tight_layout
                plt.rcParams.update({'font.size': 10})  # this updates the overall plot font
size
            #plt.gcf().subplots_adjust(bottom=0.2, left=0.2)
                fig.savefig(os.path.join(path+'/'+fileIDinfo, title11+'.png'))
                plt.show()
            # ========== Second histogram
                title2 = 'PSD vs. Energy Channel Misc. ' + (fileIDinfo)
                title21 = 'PSDvEnergy_miscPMTs_' + fileIDinfo
                PMTchoice = np.array([PMT0,PMT1,PMT2,PMT3])
                PMTchoicename=(['ALLVALIDPMTs','PMTextras','ALLPMTs'])
                fig2 = plt.figure(title21, figsize=(6, 5), dpi=100, facecolor='w',
                            edgecolor='k')  # adjust dpi & figsize for size adjust
                gs1 = gridspec.GridSpec(2, 2)
                ax11 = fig2.add_subplot(gs1[0,0])
                ax21 = fig2.add_subplot(gs1[0, 1])
```

```python
                ax31 = fig2.add_subplot(gs1[1, 0:])
                ax11.plot([row[1] for row in PMTchoice[0]], [row[2] for row in PMTchoice[0]],
'.')
                ax11.set_title(PMTchoicename[0], fontsize = 9)
                ax11.set_ylabel('Raw PSD values', fontsize = 9)  # labelpad adjusts how close
the text is to the plot edges
                ax11.set_xlabel('Raw Energy Channel Values', fontsize = 9)
                ax21.plot([row[1] for row in PMTchoice[1]], [row[2] for row in PMTchoice[1]],
'.')
                ax21.set_title(PMTchoicename[1], fontsize = 9)
                ax21.set_ylabel('Raw PSD values', fontsize = 9)  # labelpad adjusts how close
the text is to the plot edges
                ax21.set_xlabel('Raw Energy Channel Values', fontsize = 9)
                ax31.plot([row[1] for row in PMTchoice[2]], [row[2] for row in PMTchoice[2]],
'.')
                ax31.set_title(PMTchoicename[2], fontsize = 9)
                ax31.set_ylabel('Raw PSD values', fontsize = 9)  # labelpad adjusts how close
the text is to the plot edges
                ax31.set_xlabel('Raw Energy Channel Values', fontsize = 9)
                plt.subplots_adjust(left=0.2,
                                    bottom=0.2,
                                    right=0.9,
                                    top=0.9,
                                    wspace=0.4,
                                    hspace=0.6)
                plt.suptitle(title2)
                # plt.xscale('log', nonposy='clip')
                # plt.tight_layout
                plt.rcParams.update({'font.size': 10})  # this updates the overall plot font
size
                #plt.gcf().subplots_adjust(bottom=0.2, left=0.2)
                fig.savefig(os.path.join(path + '/' + fileIDinfo, title21 + '.png'))
                plt.show()

        else:
            break


print 'Files completed for MNS0.'


for folder in range(0,len(MNS1paths)):
    for file in os.listdir(path+'/'+MNS1paths[folder]):
        current_file = os.path.join(path+'/'+MNS1paths[folder], file)
        fileIDinfo=MNS1paths[folder]+'_processed'
        if '.bin' in current_file:
            if settype in current_file:
                filelist.append(current_file)
    print 'Processing ' + str(len(filelist)) + ' filtered event files.'
#=======================================================
#============ Pick what you want to output =============
#=======================================================
#============ FILE OUTPUTS
    #print "Enter the desired file outputs (can list w/ commas): "; fileinputs = raw_input()
    FileOuts=[1,1,1,1,1]
    #for word in range(0,len(str(fileinputs))):
        #if 'PMT' in fileinputs or 'PMTS' in fileinputs or 'pmts' in fileinputs:
        #    FileOuts[0]=1
        #elif 'Pulser' in fileinputs:
        #    FileOuts[1]=1
        #elif 'Temp' in fileinputs or 'Temperature' in fileinputs or 'temp' in fileinputs or
'temperature' in fileinputs:
        #    FileOuts[2]=1
        #elif 'All files' in fileinputs or' all' in fileinputs or 'All' in fileinputs or 'ALL'
in fileinputs:
        #    FileOuts = [1, 1, 1, 1, 1]
        #elif 'none'in fileinputs or 'NONE' in fileinputs or 'None' in fileinputs:
```

```python
        #      FileOuts = [0, 0, 0, 0, 0]
# ============ PLOT OUTPUTS
# for PMTs, options are: PMT0, PMT1, PMT2, PMT3, ALLPMTS, PMTextras
    PlotOuts=[1,1,1,1,1]
#=======================================================
#========== Read in the binary files as uint8 ==========
#=======================================================
    for k in range (0,len(filelist)):
        filename=filelist[k]
        mainfilename=str(filename.split('/')[-2]) + '/' + str(filename.split('/')[-1])
        shortfilename=(str(((filename.split('/')[-1]))).split('.bin'))[0].split('_')[-2]+'
'+(str(((filename.split('/')[-1]))).split('.bin'))[0].split('_')[-1]
        #============= Read in the binary files as uint8 ==========
        binaryReader = lh.BinaryReader(filename)
        asciiout = []
        try:
            binlen = 50000000
            for i in range (0,binlen):
                asciiout.append(binaryReader.read('uint8'))
        except lh.BinaryReaderEOFException:
            print 'Binary read in past length... ignoring.'
        asciiout=np.array(asciiout)
        if len(asciiout) == 0:
            print 'Binary file '+str(filename.split('/')[-1]) +' in '
+str(filename.split('/')[-2]) + ' is empty...\r ...continuing to next file.'
            continue
    #
    #=== Sort the data into specific sets based on the ICD ===
    #
        (set221, pulser_set, temp_set, event_set, FPGA_time)=lh.sort_minins_bindata(asciiout)
    #
    # ========= Post-process the event-by-event sets =========
    #
        (item0_event, PMTid, item2_event, energybin, PSDvalue, FPGA_time_new2,
tageventID)=lh.sort_eventsets(event_set)
    #
    # ===== Post-process the event-by-event sets by PMT =======
    #
        (ALLPMTs, ALLVALIDPMTs, PMT0, PMT1, PMT2, PMT3, PMTextras)=lh.sort_PMTevents(PMTid,
energybin, PSDvalue, FPGA_time_new2, tageventID)
    #
    # ========= Post-process the temperature sets =========
    #
        (item0_temp, atemp, dtemp, mtemp)=lh.sort_tempdata(temp_set)
    #
    # ========= Save datasets =========
    #
        if FileOuts[0] == 1: #PMT flag
            lh.write_PMTfile(path, PMT0, '0', fileIDinfo)
            lh.write_PMTfile(path, PMT1, '1', fileIDinfo)
            lh.write_PMTfile(path, PMT2, '2', fileIDinfo)
            lh.write_PMTfile(path, PMT3, '3', fileIDinfo)
            lh.write_PMTfile(path, ALLVALIDPMTs, 'ALLVALIDPMTs', fileIDinfo)
            lh.write_PMTfile(path, PMTextras, 'PMTextras', fileIDinfo)
            lh.write_PMTfile(path, ALLPMTs, 'ALLPMTs', fileIDinfo)
            print 'Data has been written.'
        if FileOuts[1] == 1: #pulser flag
            lh.write_Pulserfile(path,fileIDinfo,pulser_set)
        if FileOuts[2] == 1: #temperature flag
            lh.write_Tempfile(path, fileIDinfo, temp_set)
        if PlotOuts[0] == 1:
            print 'Plot wanted'
            if PlotOuts[1] == 1:
            # ========== Plot the data ==========
            # for PMTs, options are: PMT0, PMT1, PMT2, PMT3, ALLPMTS, PMTextras
            # ========== First histogram
                title1 = 'PSD vs. Energy Channel Standard PMTs ' + (fileIDinfo)
```

```
                title11 = 'PSDvEnergy_StandardPMTs_' + fileIDinfo
                PMTchoice = np.array([PMT0,PMT1,PMT2,PMT3])
                PMTchoicename=(['PMT0','PMT1','PMT2','PMT3'])
                fig = plt.figure(title11, figsize=(6, 5), dpi=100, facecolor='w',
                            edgecolor='k')  # adjust dpi & figsize for size adjust
                gs = gridspec.GridSpec(2, 2)
                ax1 = fig.add_subplot(gs[0,0])
                ax4 = fig.add_subplot(gs[1, 1])
                ax2 = fig.add_subplot(gs[0, 1])
                ax3 = fig.add_subplot(gs[1, 0])
                ax1.plot([row[1] for row in PMTchoice[0]], [row[2] for row in PMTchoice[0]],
'.')
                ax1.set_title(PMTchoicename[0], fontsize = 9)
                ax1.set_ylabel('Raw PSD values', fontsize = 9)  # labelpad adjusts how close
the text is to the plot edges
                ax1.set_xlabel('Raw Energy Channel Values', fontsize = 9)
                ax2.plot([row[1] for row in PMTchoice[1]], [row[2] for row in PMTchoice[1]],
'.')
                ax2.set_title(PMTchoicename[1], fontsize = 9)
                ax2.set_ylabel('Raw PSD values', fontsize = 9)  # labelpad adjusts how close
the text is to the plot edges
                ax2.set_xlabel('Raw Energy Channel Values', fontsize = 9)
                ax3.plot([row[1] for row in PMTchoice[2]], [row[2] for row in PMTchoice[2]],
'.')
                ax3.set_title(PMTchoicename[2], fontsize = 9)
                ax3.set_ylabel('Raw PSD values', fontsize = 9)  # labelpad adjusts how close
the text is to the plot edges
                ax3.set_xlabel('Raw Energy Channel Values', fontsize = 9)
                ax4.plot([row[1] for row in PMTchoice[3]], [row[2] for row in PMTchoice[3]],
'.')
                ax4.set_title(PMTchoicename[3], fontsize = 9)
                ax4.set_ylabel('Raw PSD values', fontsize = 9)  # labelpad adjusts how close
the text is to the plot edges
                ax4.set_xlabel('Raw Energy Channel Values', fontsize = 9)
                plt.subplots_adjust(left=0.2,
                                    bottom=0.2,
                                    right=0.9,
                                    top=0.9,
                                    wspace=0.4,
                                    hspace=0.6)
                plt.grid(True, which="major", linewidth=0.5)
                plt.suptitle(title1)
            # plt.xscale('log', nonposy='clip')
            # plt.tight_layout
                plt.rcParams.update({'font.size': 10})  # this updates the overall plot font
size
            #plt.gcf().subplots_adjust(bottom=0.2, left=0.2)
                fig.savefig(os.path.join(path+'/'+fileIDinfo, title11+'.png'))
                plt.show()
            # =========== Second histogram
                title2 = 'PSD vs. Energy Channel Misc. ' + (fileIDinfo)
                title21 = 'PSDvEnergy_miscPMTs_' + fileIDinfo
                PMTchoice = np.array([PMT0,PMT1,PMT2,PMT3])
                PMTchoicename=(['ALLVALIDPMTs','PMTextras','ALLPMTs'])
                fig2 = plt.figure(title21, figsize=(6, 5), dpi=100, facecolor='w',
                            edgecolor='k')  # adjust dpi & figsize for size adjust
                gs1 = gridspec.GridSpec(2, 2)
                ax11 = fig2.add_subplot(gs1[0,0])
                ax21 = fig2.add_subplot(gs1[0, 1])
                ax31 = fig2.add_subplot(gs1[1, 0:])
                ax11.plot([row[1] for row in PMTchoice[0]], [row[2] for row in PMTchoice[0]],
'.')
                ax11.set_title(PMTchoicename[0], fontsize = 9)
                ax11.set_ylabel('Raw PSD values', fontsize = 9)  # labelpad adjusts how close
the text is to the plot edges
                ax11.set_xlabel('Raw Energy Channel Values', fontsize = 9)
                ax21.plot([row[1] for row in PMTchoice[1]], [row[2] for row in PMTchoice[1]],
```

```python
'.')
                ax21.set_title(PMTchoicename[1], fontsize = 9)
                ax21.set_ylabel('Raw PSD values', fontsize = 9)   # labelpad adjusts how close
the text is to the plot edges
                ax21.set_xlabel('Raw Energy Channel Values', fontsize = 9)
                ax31.plot([row[1] for row in PMTchoice[2]], [row[2] for row in PMTchoice[2]],
'.')
                ax31.set_title(PMTchoicename[2], fontsize = 9)
                ax31.set_ylabel('Raw PSD values', fontsize = 9)   # labelpad adjusts how close
the text is to the plot edges
                ax31.set_xlabel('Raw Energy Channel Values', fontsize = 9)
                plt.subplots_adjust(left=0.2,
                                    bottom=0.2,
                                    right=0.9,
                                    top=0.9,
                                    wspace=0.4,
                                    hspace=0.6)
                #plt.grid(True, which="major", linewidth=0.5)
                plt.suptitle(title2)
                # plt.xscale('log', nonposy='clip')
                # plt.tight_layout
                plt.rcParams.update({'font.size': 10})   # this updates the overall plot font
size
                #plt.gcf().subplots_adjust(bottom=0.2, left=0.2)
                fig.savefig(os.path.join(path + '/' + fileIDinfo, title21 + '.png'))
                plt.show()

        else:
            break


print 'Files completed for MNS1.'

print 'Reading in cfg file...'

cfgfilelist=[]
newpaths=[]
for folder in range(0,len(MNS0paths)):
    for file in os.listdir(path+'/'+MNS0paths[folder]):
        current_file = os.path.join(path+'/'+MNS0paths[folder], file)
        if '.bin' in current_file:
            if 'cfg' in current_file:
                cfgfilelist.append(current_file)
                newpaths.append(path+'/'+MNS0paths[folder] + '_processed')
print 'Processing ' + str(len(cfgfilelist)) + ' filtered event files for MNS0.'

if len(cfgfilelist) > 1:
    for i in range(0,len(cfgfilelist)):
        binaryReader = lh.BinaryReader(cfgfilelist[i])
        asciiout = []
        newpath=cfgfilelist[i]
        try:
            binlen = 50000000
            for i in range (0,binlen):
                asciiout.append(binaryReader.read('uint8'))
        except lh.BinaryReaderEOFException:
            print 'Binary read in past length... ignoring.'
        lh.write_cfgfile(newpaths[i],cfgfilelist[i],asciiout)
else:
    binaryReader = lh.BinaryReader(cfgfilelist[0])
    asciiout = []
    newpath = cfgfilelist[0]
    try:
        binlen = 50000000
        for i in range(0, binlen):
            asciiout.append(binaryReader.read('uint8'))
    except lh.BinaryReaderEOFException:
```

```
            print 'Binary read in past length... ignoring.'
        lh.write_cfgfile(newpaths[0], cfgfilelist[0], asciiout)
        print 'Ignore the error.'

cfgfilelist=[]
newpaths=[]
for folder in range(0,len(MNS1paths)):
    for file in os.listdir(path+'/'+MNS1paths[folder]):
        current_file = os.path.join(path+'/'+MNS1paths[folder], file)
        if '.bin' in current_file:
            if 'cfg' in current_file:
                cfgfilelist.append(current_file)
                newpaths.append(path+'/'+MNS1paths[folder] + '_processed')
print 'Processing ' + str(len(cfgfilelist)) + ' filtered event files for MNS1.'

if len(cfgfilelist) > 1:
    for i in range(0,len(cfgfilelist)):
        binaryReader = lh.BinaryReader(cfgfilelist[i])
        asciiout = []
        newpath=cfgfilelist[i]
        try:
            binlen = 50000000
            for i in range (0,binlen):
                asciiout.append(binaryReader.read('uint8'))
        except lh.BinaryReaderEOFException:
            print 'Binary read in past length... ignoring.'
        lh.write_cfgfile(newpaths[i],cfgfilelist[i],asciiout)
else:
    binaryReader = lh.BinaryReader(cfgfilelist[0])
    asciiout = []
    newpath = cfgfilelist[0]
    try:
        binlen = 50000000
        for i in range(0, binlen):
            asciiout.append(binaryReader.read('uint8'))
    except lh.BinaryReaderEOFException:
        print 'Binary read in past length... ignoring.'
    lh.write_cfgfile(newpaths[0], cfgfilelist[0], asciiout)
    print 'Ignore the error.'
```

```python
#MiniNS_PlotDataProducts.py

'''
LunaH-Map Mini-NS downlinked data processing tool for Python V.1.0.1.
Start: May 1, 2021 by L. E. Heffern
Last Edit: April 11, 2022
(c) 2021 ASU SESE & NASA LunaH-Map Mission
Required libraries include: numpy, matplotlib, struct, os, and the file MiniNS_Functions.py
For use with the Miniature Neutron Spectrometer flight software.
This code generates plots based on user inputs for desired PMTs or other parameters.
'''
import numpy as np
import matplotlib.pyplot as plt
import MiniNS_Functions as lh
import os
from matplotlib import gridspec

'''
=======================================================
========= Select the data you want to plot =========
=======================================================
'''


print "Enter the folder location of the files: "; directory = raw_input()

path = r"%s" % directory

print "Enter the desired plot outputs (can list w/ commas, e.g. histogram, temp, pulser,
timing): "; plotinputs = raw_input()


print "Enter the desired PMTs to make histogram plots (as PMT0, PMT1, PMT2, PMT3, ALLVALIDPMTs,
etc.): "
PMTplotchoice = raw_input()


filelist=[]

for file in os.listdir(path):
    current_file = os.path.join(path, file)
    if '.dat' in current_file:
        if 'PMT' in current_file:
            filelist.append(current_file)
        elif 'Temp' in current_file:
            filelist.append(current_file)
        elif 'Pulser' in current_file:
            filelist.append(current_file)

print 'Processing ' + str(len(filelist)) + ' filtered event files.'



neutronpolygonX=np.array([1,125,280,360,280,125,50,1])
neutronpolygonY=np.array([10,7,7,9,15,24,24,10])

PMTchoicename=[]
PMTchoice=[]
Otherchoicename=[]
for k in range (0,len(filelist)):
    filename=filelist[k]
    if 'PMT0' in filename:
        PMT0=lh.read_PMTfile(filename)
        PMTchoicename.append('PMT0')
        PMTchoice.append(PMT0)
    elif 'PMT1' in filename:
```

```python
            PMT1 = lh.read_PMTfile(filename)
            PMTchoicename.append('PMT1')
            PMTchoice.append(PMT1)
        elif 'PMT2' in filename:
            PMT2 = lh.read_PMTfile(filename)
            PMTchoicename.append('PMT2')
            PMTchoice.append(PMT2)
        elif 'PMT3' in filename:
            PMT3 = lh.read_PMTfile(filename)
            PMTchoicename.append('PMT3')
            PMTchoice.append(PMT3)
        elif 'ALLVALIDPMTs' in filename:
            ALLVALIDPMTs = lh.read_PMTfile(filename)
            PMTchoicename.append('ALLVALIDPMTs')
            PMTchoice.append(ALLVALIDPMTs)
        elif 'PMTextras' in filename:
            PMTextras = lh.read_PMTfile(filename)
            PMTchoicename.append('PMTextras')
            PMTchoice.append(PMTextras)
        elif 'ALLPMTs' in filename:
            ALLPMTs = lh.read_PMTfile(filename)
            PMTchoicename.append('ALLPMTs')
            PMTchoice.append(ALLPMTs)
        #elif 'Pulser' in filename:
         #    Pulser = lh.read_PMTfile(filename)
          #    Otherchoicename.append('Pulser')
        elif 'Temp' in filename:
            EventID, T_Analog, T_Digital, T_Module = lh.Temp_filter_zeros(filename)
            Otherchoicename.append('Temp')


PlotOuts=[0,0,0,0,0]
plotinputs2=str(plotinputs).split(',')
for x in range(0,len((plotinputs2))):
    for y in range(0, len(lh.histnames)):
        if lh.histnames[y] in plotinputs2[x]:
            PlotOuts[1]=1
    for y in range(0, len(lh.pulsernames)):
        if lh.pulsernames[y] in plotinputs2[x]:
            PlotOuts[2]=1
    for y in range(0, len(lh.tempnames)):
        if lh.tempnames[y] in plotinputs2[x]:
            PlotOuts[3]=1
    for y in range(0, len(lh.timenames)):
        if lh.timenames[y] in plotinputs2[x]:
            PlotOuts[4]=1
    if 'None' in plotinputs2[x]:
        PlotOuts = [0, 0, 0, 0, 0]
    else:
        PlotOuts=PlotOuts

PMTchoicename2=np.array([PMT0,PMT1,PMT2,PMT3,ALLVALIDPMTs,PMTextras,ALLPMTs])


fileIDinfo=filelist[0].split('/')[-2]

if PlotOuts[1] == 1:
    PMThistplot=PMTplotchoice
    for f in range(0,len(PMTchoicename)):
        if PMThistplot in PMTchoicename[f]:
            print 'PMT choice valid.'
            break
        else:
            print 'PMT choice invalid. Restart program.'
    if 'PMT0' in PMThistplot:
        PMTchoice = PMTchoicename2[0]
        title1 = 'PSD vs. Energy Channel ' + (fileIDinfo) +' ' + str(PMThistplot)
```

```python
            title11 = 'PSDvEnergy_StandardPMTs_' + fileIDinfo + str(PMThistplot)
            fig = plt.figure(title11, figsize=(6, 5), dpi=100, facecolor='w',
                             edgecolor='k')  # adjust dpi & figsize for size adjust
            plt.plot(PMTchoice[1], PMTchoice[2], '.')
            plt.ylabel('Raw PSD values', fontsize=9)  # labelpad adjusts how close the text is to
the plot edges
            plt.xlabel('Raw Energy Channel Values', fontsize=9)
            plt.title(PMTchoicename[0], fontsize=9)
            plt.grid(True, which="major", linewidth=0.5)
            plt.suptitle(title1)
            # plt.xscale('log', nonposy='clip')
            # plt.tight_layout
            plt.rcParams.update({'font.size': 10})  # this updates the overall plot font size
            # plt.gcf().subplots_adjust(bottom=0.2, left=0.2)
            # fig.savefig(os.path.join(path + '/' + fileIDinfo, title11 + '.png'))
            plt.show()
    if 'PMT1' in PMThistplot:
            PMTchoice = PMTchoicename2[1]
            title1 = 'PSD vs. Energy Channel ' + (fileIDinfo) +' ' + str(PMThistplot)
            title11 = 'PSDvEnergy_StandardPMTs_' + fileIDinfo + str(PMThistplot)
            fig = plt.figure(title11, figsize=(6, 5), dpi=100, facecolor='w',
                             edgecolor='k')  # adjust dpi & figsize for size adjust
            plt.plot(PMTchoice[1], PMTchoice[2], '.')
            plt.ylabel('Raw PSD values', fontsize=9)  # labelpad adjusts how close the text is to
the plot edges
            plt.xlabel('Raw Energy Channel Values', fontsize=9)
            plt.title(PMTchoicename[0], fontsize=9)
            plt.grid(True, which="major", linewidth=0.5)
            plt.suptitle(title1)
            # plt.xscale('log', nonposy='clip')
            # plt.tight_layout
            plt.rcParams.update({'font.size': 10})  # this updates the overall plot font size
            # plt.gcf().subplots_adjust(bottom=0.2, left=0.2)
            # fig.savefig(os.path.join(path + '/' + fileIDinfo, title11 + '.png'))
            plt.show()
    if 'PMT2' in PMThistplot:
            PMTchoice = PMTchoicename2[2]
            title1 = 'PSD vs. Energy Channel ' + (fileIDinfo) +' ' + str(PMThistplot)
            title11 = 'PSDvEnergy_StandardPMTs_' + fileIDinfo + str(PMThistplot)
            fig = plt.figure(title11, figsize=(6, 5), dpi=100, facecolor='w',
                             edgecolor='k')  # adjust dpi & figsize for size adjust
            plt.plot(PMTchoice[1], PMTchoice[2], '.')
            plt.ylabel('Raw PSD values', fontsize=9)  # labelpad adjusts how close the text is to
the plot edges
            plt.xlabel('Raw Energy Channel Values', fontsize=9)
            plt.title(PMTchoicename[0], fontsize=9)
            plt.grid(True, which="major", linewidth=0.5)
            plt.suptitle(title1)
            # plt.xscale('log', nonposy='clip')
            # plt.tight_layout
            plt.rcParams.update({'font.size': 10})  # this updates the overall plot font size
            # plt.gcf().subplots_adjust(bottom=0.2, left=0.2)
            # fig.savefig(os.path.join(path + '/' + fileIDinfo, title11 + '.png'))
            plt.show()
    if 'PMT3' in PMThistplot:
            PMTchoice = PMTchoicename2[3]
            title1 = 'PSD vs. Energy Channel ' + (fileIDinfo) +' ' + str(PMThistplot)
            title11 = 'PSDvEnergy_StandardPMTs_' + fileIDinfo + str(PMThistplot)
            fig = plt.figure(title11, figsize=(6, 5), dpi=100, facecolor='w',
                             edgecolor='k')  # adjust dpi & figsize for size adjust
            plt.plot(PMTchoice[1], PMTchoice[2], '.')
            plt.ylabel('Raw PSD values', fontsize=9)  # labelpad adjusts how close the text is to
the plot edges
            plt.xlabel('Raw Energy Channel Values', fontsize=9)
            plt.title(PMTchoicename[0], fontsize=9)
            plt.grid(True, which="major", linewidth=0.5)
            plt.suptitle(title1)
```

```python
        # plt.xscale('log', nonposy='clip')
        # plt.tight_layout
        plt.rcParams.update({'font.size': 10})  # this updates the overall plot font size
        # plt.gcf().subplots_adjust(bottom=0.2, left=0.2)
        # fig.savefig(os.path.join(path + '/' + fileIDinfo, title11 + '.png'))
        plt.show()
    if 'ALLVALIDPMTs' in PMThistplot:
        PMTchoicename = (['PMT0', 'PMT1', 'PMT2', 'PMT3'])
        #PMTchoice = PMTchoicename2[4]
        # ========== Plot the data ==========
        # for PMTs, options are: PMT0, PMT1, PMT2, PMT3, ALLPMTS, PMTextras
        # ========== First histogram
        title1 = 'PSD vs. Energy Channel Standard PMTs ' + (fileIDinfo)
        title11 = 'PSDvEnergy_StandardPMTs_' + fileIDinfo
        PMTchoice = np.array([PMT0, PMT1, PMT2, PMT3])
        fig = plt.figure(title11, figsize=(6, 5), dpi=100, facecolor='w',
                         edgecolor='k')  # adjust dpi & figsize for size adjust
        gs = gridspec.GridSpec(2, 2)
        ax1 = fig.add_subplot(gs[0, 0])
        ax4 = fig.add_subplot(gs[1, 1])
        ax2 = fig.add_subplot(gs[0, 1])
        ax3 = fig.add_subplot(gs[1, 0])
        ax1.plot(PMTchoice[0][1], PMTchoice[0][2], '.')
        ax1.set_title(PMTchoicename[0], fontsize=9)
        ax1.set_ylabel('Raw PSD values', fontsize=9)  # labelpad adjusts how close the text is
to the plot edges
        ax1.set_xlabel('Raw Energy Channel Values', fontsize=9)
        ax2.plot(PMTchoice[1][1], PMTchoice[1][2], '.')
        ax2.set_title(PMTchoicename[1], fontsize=9)
        ax2.set_ylabel('Raw PSD values', fontsize=9)  # labelpad adjusts how close the text is
to the plot edges
        ax2.set_xlabel('Raw Energy Channel Values', fontsize=9)
        ax3.plot(PMTchoice[2][1], PMTchoice[2][2], '.')
        ax3.set_title(PMTchoicename[2], fontsize=9)
        ax3.set_ylabel('Raw PSD values', fontsize=9)  # labelpad adjusts how close the text is
to the plot edges
        ax3.set_xlabel('Raw Energy Channel Values', fontsize=9)
        ax4.plot(PMTchoice[3][1], PMTchoice[3][2], '.')
        ax4.set_title(PMTchoicename[3], fontsize=9)
        ax4.set_ylabel('Raw PSD values', fontsize=9)  # labelpad adjusts how close the text is
to the plot edges
        ax4.set_xlabel('Raw Energy Channel Values', fontsize=9)
        plt.subplots_adjust(left=0.2,
                            bottom=0.2,
                            right=0.9,
                            top=0.9,
                            wspace=0.4,
                            hspace=0.6)
        plt.grid(True, which="major", linewidth=0.5)
        plt.suptitle(title1)
        # plt.xscale('log', nonposy='clip')
        # plt.tight_layout
        plt.rcParams.update({'font.size': 10})  # this updates the overall plot font size
        # plt.gcf().subplots_adjust(bottom=0.2, left=0.2)
        # fig.savefig(os.path.join(path + '/' + fileIDinfo, title11 + '.png'))
        plt.show()
    if 'PMTextras' in PMThistplot:
        PMTchoice = PMTchoicename2[5]
        title1 = 'Invalid Events, PSD vs. Energy Channel ' + (fileIDinfo) +' ' +
str(PMThistplot)
        title11 = 'PSDvEnergy_StandardPMTs_' + fileIDinfo + str(PMThistplot)
        fig = plt.figure(title11, figsize=(6, 5), dpi=100, facecolor='w',
                         edgecolor='k')  # adjust dpi & figsize for size adjust
        plt.plot(PMTchoice[1], PMTchoice[2], '.')
        plt.ylabel('Raw PSD values', fontsize=9)  # labelpad adjusts how close the text is to
the plot edges
        plt.xlabel('Raw Energy Channel Values', fontsize=9)
```

```python
        plt.title(PMTchoicename[0], fontsize=9)
        plt.grid(True, which="major", linewidth=0.5)
        plt.suptitle(title1)
        # plt.xscale('log', nonposy='clip')
        # plt.tight_layout
        plt.rcParams.update({'font.size': 10})  # this updates the overall plot font size
        # plt.gcf().subplots_adjust(bottom=0.2, left=0.2)
        # fig.savefig(os.path.join(path + '/' + fileIDinfo, title11 + '.png'))
        plt.show()
    if 'ALLPMTs' in PMThistplot:
        PMTchoice = PMTchoicename2[6]
        title1 = 'PSD vs. Energy Channel ' + (fileIDinfo) +' ' + str(PMThistplot)
        title11 = 'PSDvEnergy_StandardPMTs_' + fileIDinfo + str(PMThistplot)
        fig = plt.figure(title11, figsize=(6, 5), dpi=100, facecolor='w',
                         edgecolor='k')  # adjust dpi & figsize for size adjust
        plt.plot(PMTchoice[1], PMTchoice[2], '.')
        plt.ylabel('Raw PSD values', fontsize=9)  # labelpad adjusts how close the text is to
the plot edges
        plt.xlabel('Raw Energy Channel Values', fontsize=9)
        plt.title(PMTchoicename[0], fontsize=9)
        plt.grid(True, which="major", linewidth=0.5)
        plt.suptitle(title1)
        # plt.xscale('log', nonposy='clip')
        # plt.tight_layout
        plt.rcParams.update({'font.size': 10})  # this updates the overall plot font size
        # plt.gcf().subplots_adjust(bottom=0.2, left=0.2)
        # fig.savefig(os.path.join(path + '/' + fileIDinfo, title11 + '.png'))
        plt.show()

if PlotOuts[3] == 1:
    tempnames=( 'EventID', 'T_Analog', 'T_Digital', 'T_Module')
    title1 = 'Temperature on all PMTs, all boards ' + (fileIDinfo)
    title11 = 'Temps_StandardPMTs_' + fileIDinfo
    fig = plt.figure(title11, figsize=(6, 5), dpi=100, facecolor='w',
                     edgecolor='k')  # adjust dpi & figsize for size adjust
    gs = gridspec.GridSpec(2, 2)
    ax1 = fig.add_subplot(gs[0, 0])
    ax4 = fig.add_subplot(gs[1, 1])
    ax2 = fig.add_subplot(gs[0, 1])
    ax3 = fig.add_subplot(gs[1, 0])
    ax1.hist(EventID,100)
    ax1.set_yscale('log')
    ax1.set_title(tempnames[0], fontsize=9)
    ax1.set_ylabel('Counts', fontsize=9)
    ax1.set_xlabel('EventID number', fontsize=9)
    ax2.hist(T_Analog,100)
    ax2.set_yscale('log')
    ax2.set_title(tempnames[1], fontsize=9)
    ax2.set_ylabel('Counts', fontsize=9)
    ax2.set_xlabel('Analog Board Temperature (K)', fontsize=9)
    ax3.hist(T_Digital,100)
    ax3.set_yscale('log')
    ax3.set_title(tempnames[2], fontsize=9)
    ax3.set_ylabel('Counts', fontsize=9)
    ax3.set_xlabel('Digital Board Temperature (K)', fontsize=9)
    ax4.hist(T_Module,100)
    ax4.set_yscale('log')
    ax4.set_title(tempnames[3], fontsize=9)
    ax4.set_ylabel('Counts', fontsize=9)
    ax4.set_xlabel('Module Temperature (K)', fontsize=9)
    plt.subplots_adjust(left=0.2,
                        bottom=0.2,
                        right=0.9,
                        top=0.9,
                        wspace=0.4,
                        hspace=0.6)
    plt.suptitle(title1)
```

```python
    # plt.tight_layout
    plt.rcParams.update({'font.size': 10})  # this updates the overall plot font size
    # plt.gcf().subplots_adjust(bottom=0.2, left=0.2)
    # fig.savefig(os.path.join(path + '/' + fileIDinfo, title11 + '.png'))
    plt.show()


if PlotOuts[4] == 1:
    PMTtimingplot=PMTplotchoice
    print "Enter the desired PMT to make timing plots (as PMT0, PMT1, ALLPMTs, etc.): "
    PMTtimingplot = raw_input()
    for f in range(0,len(PMTchoicename)):
        if PMTtimingplot in PMTchoicename:
            print 'PMT choice valid.'
            break
        else:
            print 'PMT choice invalid. Restart program.'
    if 'PMT0' in PMTtimingplot:
        PMTchoice = PMTchoicename2[0]
    if 'PMT1' in PMTtimingplot:
        PMTchoice = PMTchoicename2[1]
    if 'PMT2' in PMTtimingplot:
        PMTchoice = PMTchoicename2[2]
    if 'PMT3' in PMTtimingplot:
        PMTchoice = PMTchoicename2[3]
    if 'ALLVALIDPMTs' in PMTtimingplot:
        PMTchoice = PMTchoicename2[4]
    if 'PMTextras' in PMTtimingplot:
        PMTchoice = PMTchoicename2[5]
    if 'ALLPMTs' in PMTtimingplot:
        PMTchoice = PMTchoicename2[6]
```

APPENDIX F

SPACE INSPIRED

The title of this dissertation (and many of the subtitles) is in homage to the television show *Star Trek* which has doubtlessly inspired countless scientists and engineers throughout their careers. This dissertation expands on human knowledge of nuclear planetary science technologies and techniques, a field that owes its existence to the creation of the atomic bomb during WWII. Nuclear technology has been used historically in efforts of both destruction and exploration. The fictitious "warp reactor" in *Star Trek* can be used for exploration purposes and as a weapon; warp is analogous to nuclear energy, particularly nuclear fusion. While finishing revisions, the newest iteration of *Star Trek* was released, titled "Star Trek: Strange New Worlds." I end this dissertation with a monologue from the pilot episode that I find to be fitting to the nuclear science field applied to space exploration, in hopes that others choose to work together and *reach for the stars:*

> *"Hi. Sorry to interrupt. I'm Christopher Pike. My world is called Earth. And though it's far from here, uh, my people and yours are, uh, very much alike. This is my world today. But we were not always peaceful. This is Earth in our 21st century. Before everything went wrong. It's a lot like your world today.*
>
> *Recently I was treated to a glimpse of my future. It was not all I'd hoped. After all, what good is there in knowing your future? A friend of mine asked me that recently and... I didn't understand what he meant. Until now. I've seen my future. Let me show you yours.*
>
> *Our conflict also started with a fight for freedoms. We called it the Second Civil War, then the Eugenics War, and finally just World War III. This was our last day. The day the Earth we knew ceased to exist.*

What began as an eruption in one nation, ended in the eradication of 600,000 species of animals and plants and 30% of Earth's population. Global suicide. What we gave you is the means to exterminate yourselves. And from the looks of you, you're gonna do it. You'll use competing ideas of liberty to bomb each other to rubble, just like we did, and then your last day will look just like this. Perhaps, somewhere, all your ends are written as indelibly as mine. But I choose to believe that your destinies are still your own.

Maybe that's why I'm here– to remind you of the power... of possibility. Maybe that's the good in-in seeing my future– that I might remind you that, right up until the very end, life is to be worn gloriously. Because, till our last moment... the future's what we make it. So... go to war with each other. Or... join our Federation of Planets... and reach for the stars. The choice is yours."

Citation: Goldsman A. (Director, Writer), Kurtzman A. (Writer), Lumet J. (Writer). (May 5, 2022). "Strange New Worlds" (Season 1, Episode 1) [TV series episode]. Roddenberry, E. (Producer). *Star Trek: Strange New Worlds.* Secret Hideout, Weed Road Pictures, H M R X Productions, Roddenberry Entertainment, CBS Studios.